Nanosized Titania Composites for Reinforcement of Photocatalysis and Photoelectrocatalysis

Maksym Zahornyi
Georgii Sokolsky

Nanosized Titania Composites for Reinforcement of Photocatalysis and Photoelectrocatalysis

Nanosized Titania Composites for Reinforcement of Photocatalysis and Photoelectrocatalysis

By

Maksym Zahornyi and Georgii Sokolsky

Cambridge Scholars Publishing

Nanosized Titania Composites for Reinforcement of Photocatalysis and Photoelectrocatalysis

By Maksym Zahornyi and Georgii Sokolsky

This book first published 2022

Cambridge Scholars Publishing

Lady Stephenson Library, Newcastle upon Tyne, NE6 2PA, UK

British Library Cataloguing in Publication Data
A catalogue record for this book is available from the British Library

ISBN (10): 1-5275-7786-4
ISBN (13): 978-1-5275-7786-2

CONTENTS

ABSTRACT

Today, innovative technologies using organic-inorganic composite materials are driving rapid progress in the development of novel water purification technologies. The unique surface, optical, and catalytic properties of nanomaterials based on oxide nanoparticles with varied natures has found widespread application in wastewater treatment.

Nanosized titanium dioxide and its composites are the most promising photocatalytically active materials and this book gives an overview of their application in photocatalysis and photoelectrocatalysis. In light of the continuing COVID-19 global emergency, this monograph also discusses the antimicrobial and antiviral activity of TiO_2 nanoparticles. A number of semiconducting and bioactive catalysts based on conjugated polymers and TiO_2-MnO_2, which have a redox function in water purification, are introduced.

The aim of this monograph is to analyse the state-of-the-art in this rapidly developing research area. As such, the authors' original research data are presented and composites based on polyaniline, polypyrrole, and nanosized TiO_2 nanoparticles are investigated.

Keywords: nanomaterials, TiO_2, photocatalyst, photoelectrocatalysis, conducting polymer, PANI, PPy.

Codes: PNRD, PNNP, PNN, PH

PREFACE

Photocatalysis using nanomaterials is fast becoming an effective strategy for environmental remediation. The activity of semiconductor nanomaterials predetermines their photocatalytic performance. Numerous photocatalysts have been studied and the results presented in papers and patents, including UV, visible, and full-spectrum light response photocatalysts for the treatment of contaminants of emerging concern (organic dyes, pesticides, and pharmaceutical pollutants, etc.). The optimization principles for efficient photocatalysts concern their high light response, utilization ability, excellent physicochemical stability, low cost, and environmental friendliness (Sabu et al. 2018).

The following three issues need to be addressed in future studies of these photocatalysts: efficiency in fast recombination of photogenerated electron-hole pairs; limited visible light response; and low specific surface area. On the one hand, strategies for existing materials need to be investigated further; on the other, the synthesis of new photocatalysts is urgently needed. Furthermore, to optimize the treatment of contaminants, different processes can be combined, including the strategies of adsorption, photocatalysis, and electrophotocatalysis. Additionally, the study of the morphological architecture of photocatalysts and their properties has significance for the design of stable photoelectrocatalytic materials. Important aspects in the preparation of photocatalytic materials are presented in this book.

This book is composed of five chapters. The first chapter is devoted to titanium dioxide (TiO_2) nanoparticles and covers: their occurrence in nature; technologies of their synthesis; their physical and thermodynamic properties; and their application. Nanosized polymorphs have been shown to improve the photocatalytic activity of TiO_2 particles. The shift in their capacity to absorb light, from UV to the visible region, is presented along with the positive and negative effects of impurities introduced into the TiO_2 structure. The influence of doping elements on the optical and photocatalytic activity of TiO_2 is also presented. The second chapter covers the application of nanoparticles in the reinforcement of photoactive TiO_2 composites.

The third chapter describes the preparation, physicochemical properties, and applications of polyaniline-TiO_2(C_3N_4) nanocomposites. We

demonstrate the structural features and optical properties of C_3N_4 semiconductor systems. Graphite-like carbon nitride (g-C_3N_4) shows high potential for biohazard removal and photoelectrocatalytic hydrogen generation. However, due to its bandgap of 2.7 eV, g-C_3N_4 utilizes solar light at a wavelength below 460 nm. The engineering strategies used to resolve these issues, such as doping with oxygen, are described in this chapter. We present the oxidative polymerization kinetics of monomers; the relationship between the parameters of synthesis; and the structure of the PANI polymer. The self-organization process of polyaniline nanoparticles on substrates is presented and the monomer polymerization mechanism is studied. Optimal polymer synthesis parameters, as well as the role of the oxidizing agent, are also described.

Analysis of the literature has demonstrated that nanosized TiO_2, as an anatase polymorph, possesses high photoactivity; TiO_2 concentration has some influence on thermoplastic photodegradation too. Currently, there is only fragmentary information concerning the polymerization of aqueous solutions of methyl methacrylate. Acrylate oligomers and rubber-methacrylate solutions hold the promise of new composites produced in situ under the action of UV light. TiO_2 additives have an influence on the photopolymerization process. This growing body of knowledge is proving useful in the development of efficient and highly stable photocatalysts for the purification of pathogenic microorganisms from water and air.

Chapter 4 presents experimental results that have been discussed by the authors at forums in France and Portugal. PANI has been used to prepare PANI-TiO_2($C_3N_4O_x$) and TiO_2-Ag nanocomposite photocatalysts. The IR, Raman, SEM, and EPR techniques were used to elucidate the mechanism of electron interaction in PANI-TiO_2, TiO_2-Ag nanocomposites. These PANI-TiO_2 composites exhibit significantly higher photocatalytic activity than PANI in the degradation of an MB (methylene blue) aqueous solution under UV irradiation. The results of XRD and EPR analysis have confirmed the strong interaction between TiO_2 and PANI nanoparticles. The PANI-TiO_2 photocatalyst (anatase, anatase-rutile) demonstrates high efficiency in photocatalytic applications and investigation of the ultraviolet-visible (UV-vis) characteristics, elemental composition, and chromatography of PANI-TiO_2 nanocomposites has confirmed the physicochemical interactions between the polymer and TiO_2 nanoparticles. The high photocatalytic activity of PANI-TiO_2 is seen in the rapidity of phenol degradation under UV and visible light irradiation. Phenol degradation occurs in the first 10–20 min. with a constant rate of k $1 \cdot 10^{-2}$ – $3 \cdot 10^{-2}$ min^{-1}.

Current aspects of TiO_2 photoelectrocatalysis (PEC) are the focus of the Chapter 5. The role of PEC phenomena, depending on the TiO_2 composite semiconductor/electrolyte interface and the influence of TiO_2's polymorphic nature and potential gradient, have all been studied and the results are presented here. Unlike with electrocatalysis, semiconductor electrodes based on TM oxides are among the best available PEC materials. They have the advantages of low price and environmental abundance. The different strategies for doping TiO_2 in PEC include "co-doping". Amino azo-dye methyl orange (MO) degradation under UV irradiation is also discussed in terms of the Ti^{3+} self-doping effect.

This book will be of use for students in areas closely oriented to materials science, chemistry, physics, and biology, as well as also for virologists and specialists in environmental pollution.

The authors have focused on semiconducting nanosized TiO_2 and its composites for the following reasons:

1. The TiO_2 semiconductor is stable in a wide pH range of 0 to 14.
2. Alongside its geometric-morphological and dimensional effects, its quantum-dimensional ones are also important because of the Mott-Wannier exciton radius, which can vary in the range of 0.8–1.9 nm depending on the size of the crystallite TiO_2.
3. The migration time (τ_{migr}) of photogenerated charges from the bulk of the particles to the surface is short (10 pcs) compared to the time (τ_{rec}) of electron-hole recombination (100 ns).
4. The electron transfer time to the adsorbed substrates occurs in the range 50–200 picoseconds.
5. Being excellent oxidizing agents, photogenerated holes can mineralize organic pollutants directly. Additionally, the holes (h+) can also form hydroxyl radicals (•OH) with strong oxidizing properties. Photoexcited electrons, on the other hand, can produce superoxide radicals (O_2•−) and •OH. These free radicals and e-/h+ pairs are highly reactive and can induce a series of redox reactions. In terms of water splitting, photogenerated electrons are captured by H+ in water to generate hydrogen, while holes will oxidize H_2O to form O_2.
6. The TiO_2 photocatalyst has been widely used in the fields of renewable energy and environmental clean-up. However, the large bandgap of TiO_2, along with the fast recombination of charge carriers, significantly lowers its photocatalytic

performance. Studies of light absorption and charge recombination of doped TiO_2 particles are limited by the entangled parameters introduced in experimental conditions. Theoretical approaches have provided useful insights through the systematic modelling of TiO_2 particles.

7. The greatest challenge in PEC research is the development of stable semiconductor nanomaterials based on TiO_2 that are activated by solar radiation. This will lead to their application in the oxidation of organics, anion reduction, and CO_2 reduction, as well as in the electrosynthesis, disinfection, and generation of radicals through the photoelectrocatalytic process, which brings some particular issues. Noble metal nanoparticles combine both catalytic activity and chemical inertness in an electrolyte medium and usually display the best electrocatalytic performance; sometimes there are no alternatives.
8. The origin, dispersion, and particle shape of the material has a strong influence on the functional properties of non-stoichiometric oxides; this has stimulated our interest in new titanium dioxide preparation methods. Our aim is to study the activity of composite electrodes based on titanium dioxide of various origins and phase composition during photoelectrocatalytic degradation of MO under UV irradiation and then to analyze the efficiency of TiO_2 samples synthesized from domestically produced Ukrainian raw materials (in the form of a hydrated titanium dioxide $TiO(OH)_2$ suspension).

ACKNOWLEDGEMENTS

We would like to acknowledge the engineers and scientists (depart. 48, 35, 58) of the institute, with whom we have been associated for 16 years and have published the results of our research.

The authors wish to express their gratitude to Patsui V., Lobunets T., Tyschenko N., Prof. Ragulya A., Tomila T., Ievtushenko A., Kasumov A., Lavrynenko O., Kornienko O., Bondarenko M., Silenko P. (Institute for Problems of Materials Science, IPMS), Prof. Strelchuk V., Yuhimchuk V. (V.Ye. Lashkarev Institute of Semiconductor Physics, NASU), Prof. Christophe Colbeau-Justin, PhD. Ghazzal M.N., Teseer Bahry, Prof. H. Remita of Laboratory photocatalysis at Université Paris-Sud.

Some experiments and efforts would have been almost impossible without the valuable support of Prof. Ivanov S. (National Academy of Culture and Art Management, Kyiv, Ukraine), Prof. Ivanova N. (Institute of General and Inorganic Chemistry of NASU), and postgraduate students L. Zudina and N. Gayuk (National aviation university, Kyiv, Ukraine).

The authors also wish to thank Pankivska Yu., Biliavska L., Povnitsa O., Zahorodnia S. (Zabolotny Institute of Microbiology and Virology, NAS Ukraine) for the helpful anti-adenovirus activity study of TiO_2 nanoparticles and NAS Ukraine “Development of innovative photocatalytic nanostructured materials based on ZnO and TiO_2” (528/IPM-11/20) and the nano-program “The development of photocatalytic nanocomposites for viral inactivation in the air” (№ 40/20-H) for supporting this book.

.

LIST OF ABBREVIATIONS AND SYMBOLS

NPs – nanoparticles
LED – light-emitting diode
APS – ammonium persulfate
An – aniline
CFU – colony forming unit
MB – methylene blue
SBM – surfactant binder modifier
MMA – methyl methacrylate
PMMA – polymethyl methacrylate
PANI – polyaniline
PPy – polypyrrole
PC – polyvinylchloride
DBSA – dodecylbenzenesulfonic acid
PAA – polyacrylic acid
DMF – N, N-dimethylformamide
Q – quinoid
Ox – oxidizer
EtOH – ethanol
h+ – holes
C – concentration
TGA – thermogravimetric analysis
LUMO – lowest unoccupied molecular orbital
CB – conductivity band
VB – valence band
n – refractive index
GO – graphene oxide
PA – polyacrylate
PVA – polyvinyl alcohol
CVD – chemical vapour deposition
ORR – oxygen reduction reaction
N-CPs – nitrogen-containing conjugated polymers
PEC – photoelectrocatalysis
EPC– electro-photocatalytic
AOP – advanced oxidation process
BDD – boron doped diamond

BET – Brunauer-Emmett-Teller (method)
CBD – chemical bath deposition process
CMD – chemically synthesized MnO_2
CVA – cyclic voltammetry
DSA – dimensional stable anode
EDX – energy-dispersive X-ray spectroscopy
EMD – electrochemically obtained MnO_2
HRTEM – high resolution transmission microscopy (study)
ITO – indium-doped tin oxide
LAB – Lithium-air battery
LPD – liquid phase deposition
MCE – mineralization current efficiency
MO – methyl orange
MS – molecular sieves
NP – nanoparticle
NTAs – nanotube arrays
NT – nanotube
OER – oxygen evolution reactions
OMS – octahedral molecular sieves
ORR – oxygen reduction reaction
PJSC – Private Joint Stock Company
PTFE – polytetrafluoroethylene (emulsion)
PV – photovoltaic
PC – photocatalysis (photocatalytic)
RhB – Rhodamine B
SCE – standard calomel electrode
SEM – scanning electronic microscopy
SHE – standard hydrogen electrode
STH – solar-to-hydrogen efficiency
TA – terephthalic acid
TAOH – 2-hydroxyterephthalia acid
TM – transition metal
TMO – transition metal oxide
XPS – X-ray photoelectron spectroscopy
XRD – X-ray diffraction
VSM – vibrating sample magnetometer
WOCs – water oxidation cocatalysts

INTRODUCTION

Novel nanoscale composite materials with a polymer matrix are fast becoming an essential part of meeting current and future needs for clean water and air. The unique properties of nanomaterials and their convergence with current treatment technologies present great opportunities to revolutionize wastewater treatment (Sabu et al. 2018).

Semiconductor photocatalytic (PC) and electrophotocatalytic (EPC) technologies have been the object of many research efforts due to their applications in the fields of renewable energy and environmental protection and remediation. A number of studies have been devoted to the development of highly-efficient PC and EPC systems and the exploration of the fundamental parameters that can modify their performance. Semiconductors, such as TiO_2, ZnO, and C_3N_4, have proved to be excellent photocatalysts, capable of the absorption of natural sunlight as nanomaterials. The fast recombination rate of photogenerated electrons and holes has led to the utilization of green solar energy and a reduction in photocatalytic activity.

Titanium dioxide photocatalysis is a physicochemical process used in water and wastewater treatment. Its potential for advanced oxidation and disinfection of refractory pollutants and resistant pathogens has been highlighted in many works over the last 30 years. TiO_2 displays numerous benefits, such as low cost, durability, photostability, and non-toxicity. The most challenging issues concern how the heterogeneous phase of photocatalysts make it difficult to describe the physicochemical processes involved and the low yields for other established advanced oxidation processes needed for the development of technological applications at full-scale.

Nowadays, different methods, including shape, size, and facet control, and element doping have been developed to enhance photocatalytic performance by increasing their capacity for broad absorption of sunlight, prolonging the lifetime of photoinduced carriers, and enhancing photocatalytic stability. For example, greater efficiency has been achieved through shape control; doping with metal or non-metal elements; dye-sensitization; and the construction of heterostructured photocatalyst systems by combining them with novel plasmonic metals (i.e. Ag, Au, Pd, and Pt) or other semiconductors with polymers. Among these, the construction of

plasmonic metal-semiconductor heterojunctions is an effective strategy due to the effects of surface plasmon resonance (SPR) and Schottky junctions, which endow the heterojunction with the desirable properties. Noble metal nanoparticles (NPs) can show SPR, which can be tailored by engineering the shape, size, and surroundings. Therefore, noble metal NPs do not only strongly absorb visible light, but can also serve as electron sinks and as a source of active reaction sites. Accordingly, under irradiation with light, the photogenerated electron-hole pairs can be separated and the carriers can be transported efficiently at the interfaces of the metal-semiconductor. Over the last few years, one of the most closely investigated types of plasmonic metal-semiconductor heterostructured photocatalyst is a semiconductor decorated with plasmonic metal nanoparticles. The metal nanoparticles on the outside are exposed to the reactants and the surrounding medium, leading to corrosion and detachment from the semiconductor photocatalyst. An alternative option is to construct core-shell metal-semiconductor structures. As an important type of photocatalyst, one-dimensional (1D) semiconductor nanostructures and their hybrids with metal, as well as conducting polymer heterostructures, have been intensively explored (Sabu et al. 2018).

Morphology-controlled rutile titanium (IV) oxide (TiO_2) and anatase TiO_2 are prepared by the hydrothermal method and their surfaces are selectively loaded with Au, Ag, and Au-Ag bimetallic nanoparticles (NPs) through photodeposition to obtain visible light-responsive photocatalysts. With the help of local surface plasmon resonance (LSPR) noble metal NPs, the photocatalytic activity of noble metal-loaded TiO_2 under visible-light irradiation has been improved compared to that of bare TiO_2. The enhancement of LSPR on the photocatalytic activity of rutile TiO_2 has been shown to be larger than that of anatase TiO_2 with an optimum amount of Au or Au-Ag. In addition, the reusability (stability) of Au-Ag-loaded TiO_2 has been shown to be much better than that of Ag-loaded TiO_2. Double-beam photoacoustic results have confirmed how different trap energy level distributions lead to different electron transfer ways, resulting in different oxidizing capabilities; this presents an important strategy in the design of visible-light responsive TiO_2 (Zheng and Murakamia 2020).

The synthesis of 1D nanostructures and their potential applications in solar energy conversion has attracted much recent interest because of their unique 1D geometry with fast and long-distance electron transfer, good electron conductivity and mobility, large specific surface area, high light-harvesting efficiency, favourable length-to-diameter ratios, and high adsorption capacity. Taking into account the shortcomings of single component nanomaterials, such as ineffective utilization of visible light, low

quantum efficiency, and poor stability during photocatalysis, multicomponent 1D-based nanohybrids are expected to overcome such drawbacks and, accordingly, are being studied for heterogeneous photocatalysis.

The PEC process has the advantages of simplicity, rapidity, and controllable transformation inherent to electrochemical methods with a further rate increase due to catalytic effects on electrode materials in the presence of solar radiation. Pioneering work (Fujishima and Honda 1972, 238) on the discovery of TiO_2 PEC water splitting has been the cornerstone of this phenomenon, particularly for green and sustainable hydrogen production. Various applications of PEC technologies have been introduced in wastewater treatment.

CHAPTER 1

TITANIUM DIOXIDE PRODUCTION, PROPERTIES, AND APPLICATIONS: A BRIEF OVERVIEW

The development of nanotechnology has led to tremendous growth in the application of NPs for drug delivery systems, antibacterial materials, cosmetics, sunscreens, and electronics. In October 2011, the European Union defined nanomaterials as natural, incidental, or manufactured materials containing particles in an unbound state or as an aggregate or agglomerate, and where 50 % or more of the particles exhibit one or more external dimensions in the size range of 1–100 nm. Others have defined NPs as objects with at least one of their three dimensions in the range of 1–100 nm. NPs possess dramatically different physicochemical properties compared to fine particles of the same composition. The small size of NPs ensures that a large portion of atoms will be on the particle surface. Since surface properties, such as energy level, electronic structure, and reactivity are different from interior states, the bioactivity of NPs differs from that of fine size analogues (Shi and Magaye 2013, 15).

1.1 Occurrence in Nature

Pure TiO_2 is a colourless crystalline solid powder. Despite being colourless, in large quantities, if it is well cleaned, titanium dioxide is a white pigment. TiO_2 does not absorb incident light in the visible spectrum and so light is either transmitted or refracted through a crystal or reflected on to surfaces. TiO_2 is a stable, non-volatile substance that is insoluble in acids, alkalis, and solutions under normal conditions. Titanium dioxide is highly reactive to various compounds, including toxic ones contained in the air. Due to its inertness, titanium dioxide is non-toxic and, in general, is considered a very safe substance. TiO_2 does not dissolve in water, or in dilute mineral acids (except hydrofluoric acid) and dilute alkali solutions.

Our company, Nanotechcenter LLC (IPMS NASU), produces anatase of 10–20 nm (fig. 1.1) with the ability to absorb light in the UV

region (http://ntc.co.ua/en/). In its pure form, TiO_2 is found in nature in the form of the minerals rutile, anatase, and brookite (the first two are tetragonal in structure and the last is a rhombic phase), with rutile constituting the main part. The third-largest rutile deposit in the world is located in Rasskazovsky district in the Tambov region. Large deposits are also located in Chile (Cerro Bianco) and the Canadian province of Quebec (Woodruff and Bedinger 2017, 1802).

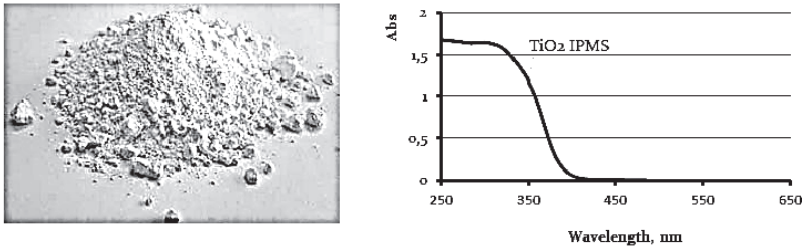

Fig. 1.1 The spectrum optical absorbance of TiO_2 (IPMS NASU).

Titanium-oxide minerals are denser than quartz and are left behind during erosion and weathering as lighter minerals are more rapidly transported away or broken down. Typical mineral assemblages in heavy-mineral deposits can include rutile and ilmenite (and minerals produced from the weathering of ilmenite, such as anatase, leucoxene, and pseudorutile), as well as other high-density, erosion-resistant minerals, such as chromite, garnet, kyanite, monazite, staurolite, tourmaline, and zircon. Heavy-mineral deposits develop when relatively resistant iron-titanium-oxide minerals and other heavy minerals, such as monazite and zircon, are eroded from the parent rocks, transported and sorted, and finally deposited in fluvial (alluvial) settings. Many productive heavy-mineral locations, such as the east coast of the United States, the east and west coasts of South Africa, and the east and west coasts of Australia, are located on passive continental margins backed by elevated and metamorphic or mafic igneous hinterlands (Force 1991, 259).

Titanium is the ninth most abundant element in the earth's crust, with an average TiO_2 abundance of 0.7 weight percent (wt%) (Rudnick and Fountain 1995, 3). Titanium can be found in nearly all rocks and sediments at more than one percent. Thus, unlike many other elements of economic interest, it is considered to be a major element rather than a trace element. Titanium is a transition element with the atomic number 22 and atomic mass of 47.867 atomic mass units. Titanium's chemistry shows

similarities to those of silicon and zirconium. The main oxidation state is Ti^{4+}, although Ti^{2+} and Ti^{3+} exist too. Titanium is a lithophilic element with a strong affinity for oxygen and it typically forms oxide minerals. It is not found as a pure metal in nature. Titanium metal is a high-strength metal with low density—as strong as steel but 45 percent lighter—and has excellent corrosion resistance.

1.2 Production Methods

Pigment TiO_2 is produced from titanium-containing concentrates using chloride and sulfate methods. In the chloride method, rutile is converted to titanium tetrachloride ($TiCl_4$) by chlorination in the presence of petroleum coke. In the sulfate process (48 % of world production capacity), ilmenite concentrates or titanium slag is decomposed by sulfuric acid. Precursor $TiCl_4$ is hydrolysed to hydroxide in the liquid phase with heat treatment of the precipitate by hydrolysis in water vapour, or burning in a stream of oxygen.

The sulfate method was developed in 1931, starting with the release of the anatase form of TiO_2 and followed by the synthesis of rutile in 1941. With this technology, an ore containing titanium is dissolved in sulfuric acid to form a solution of titanium sulfates, iron, and other metals. Then, as a result of a sequence of operations including chemical reduction, purification, precipitation, washing, and calcination, intermediate pigment-sized TiO_2 fractions are obtained.

$$FeTiO_3 + 2H_2SO_4 \rightarrow TiOSO_4 + FeSO_4 + 2H_2O;\ TiOSO_4 + H_2O \rightarrow TiO_2 + H_2SO_4$$

DuPont developed and implemented the chloride method in 1948. Under reducing conditions, titanium ore interacts with gaseous chlorine to produce titanium chloride and other metal bichlorides, which are then separated. Subsequently, the finely purified $TiCI_4$ is oxidized at high temperatures to obtain high brightness intermediate titanium dioxide. At the oxidation stage, as part of the chlorination process, it is possible to tightly control the particle size distribution, as well as the type of crystal, making it possible to obtain titanium dioxide with excellent hiding and whitening properties.

$$2FeTiO_3 + 7Cl_2 + 3C \rightarrow 2TiCl_4 + 2FeCl_3 + 3CO_2;\ TiCl_4 + O_2 \rightarrow TiO_2 + 2Cl_2$$

In both technological processes, the sulfate and chloride methods give intermediates with TiO_2 crystal congestion and are separated (crushed) to obtain optimal optical characteristics. Depending on the end-user requirements, various processing methods are used to modify TiO_2, including deposition of silicon, aluminium, zirconium, or zinc oxides on the surface of pigment fractions. Oxide treatment methods can be used in an aqueous or anhydrous medium to optimise performance for specific applications. Additionally, organic additives can be used to improve individual pigment characteristics.

Our laboratory obtained the titanium dioxide required for experimentation through the thermal decomposition of a precursor. The raw material was a suspension of hydrated titanium dioxide $TiO(OH)_2$ (metatitanic acid)—a product of titanium concentrates and slags from "Sumykhimprom" (a Ukrainian company). The suspension was heated to 600 °C with a heating rate of 5 °C/min to obtain anatase. This production method promotes the formation of additional active centres on the surface of the TiO_2. This process improves the optical and photocatalytic properties of anatase (https://doi10.15421/081914).

A critical part of the production of TiO_2 is the supply of titanium ore. Titanium is one of the ten most common chemical elements on Earth and it is necessary to introduce rational methods for the extraction and enrichment of this mineral.

1.3 Physical and Thermodynamic Properties

Hydrated $TiO_2 \cdot nH_2O$ dioxide (titanium (IV) hydroxide), depending on the preparation conditions, may contain various numbers of OH groups bound to Ti, structural water, acid residues, and adsorbed cations. Freshly precipitated $TiO_2 \cdot nH_2O$ obtained in the cold is highly soluble in dilute mineral and strong organic acids, but insoluble in alkali solutions. It easily peptized with the formation of stable colloidal solutions. After the drying process, it forms a voluminous white powder with a density of 2.6 g/cm³ and a composition formula of $TiO_2 \cdot 2H_2O$ (acid). When heated, and with prolonged drying in a vacuum, it is gradually dehydrated, approaching the formula $TiO_2 \cdot H_2O$ (metatitanic acid). This powder is obtained through precipitation from hot solutions using the interaction of titanium metal with HNO_3 acid. The density of the powder is ~3.2 g/cm³ or more.

As they age, $TiO_2 \cdot nH_2O$ precipitates gradually turn into anhydrous dioxide, which keeps adsorbed cations and anions bound. The maturation of the powder is accelerated by the boiling water suspension. The structure of TiO_2 formed during aging is determined by the deposition conditions.

When the powder precipitates in acid solutions of pH <2, samples of anatase are formed
(http://www.plasma.com.ua/chemistry/chemistry/dioxid_titana.html).

The melting point of rutile is 1870 °C (according to other sources: 1850 °C and 1855 °C). The boiling point for rutile is 2500 °C and its density is 4.235 g/cm³. For anatase this is 4.05 g/cm³ (3.95 g/cm³), while for brookite it is 4.1 g/cm³. The decomposition temperature for rutile is 2900 °C. The melting, boiling, and decomposition temperatures for other modifications are not presented, because they become rutile after heating (see above).

Table 1.1 Average isobaric heat capacity Cp ($J \cdot mol^{-1} \cdot K^{-1}$)

type	Temperature interval, K					
	298-500	298-600	298-700	298-800	298-900	298-1000
rutile	60.71	62.39	63.76	64.92	65.95	66.89
anatase	63.21	65.18	66.59	67.64	68.47	69.12

Table 1.2 Thermodynamic properties

type	$\Delta H°_{f,\,298}$, $kJ \cdot mol^{-1}$	$\Delta G°_{f,\,298}$, $kJ \cdot mol^{-1}$	$C°_{p,\,298}$, $J \cdot mol^{-1} \cdot K^{-1}$
rutile	-944.75 (-943.9)	-889.49 (-888.6)	55.04 (55.02)
anatase	-933.03 (-938.6)	-877.65 (-888.3)	55.21 (55.48)

Anatase is mainly stable at low temperatures, while the rutile phase is stable at high temperatures (tables 1.1 and 1.2). The Gibbs free energy of the anatase phase is lower than that of the rutile phase; TiO_2 initially prefers to nucleate into the anatase phase rather than into rutile. The phase transformation (anatase-rutile) is controlled by the annealing temperature, anatase nanocrystallites, and grain boundary defects (Choudhury 2013, 3). The particle arrangement and packing also influence the thermal stability and phase transformation behaviour of TiO_2 nanoparticles.

The metastability of TiO_2

TiO_2 forms three crystalline polymorphs—rutile (tetragonal), anatase (tetragonal), and brookite (rhombic). Rutile displays thermostability, while anatase reveals a metastable state with brookite when heating (Satoh and Nakashima 2013, 3). The pattern formation of TiO_2 metastable modifications at atmospheric pressure is currently insufficiently studied. Several models explaining the stabilization of metastable phases at low

temperatures have been developed. The approach in which the main factor determining the phase composition of TiO_2 is the size factor (the amount of excess surface energy) has become widespread and thus the thermodynamic analysis of TiO_2 phase stability is presented. Anatase is more stable than rutile when the crystallite size is lower than 14 nm. This trend is also extended to brookite. Apparently, in different situations, various mechanisms of stabilization of anatase or brookite at low temperatures prevail, or the action of these mechanisms appears. After rutile phase formation at low temperatures, the transition to anatase or brookite is absent fig. 1.2).

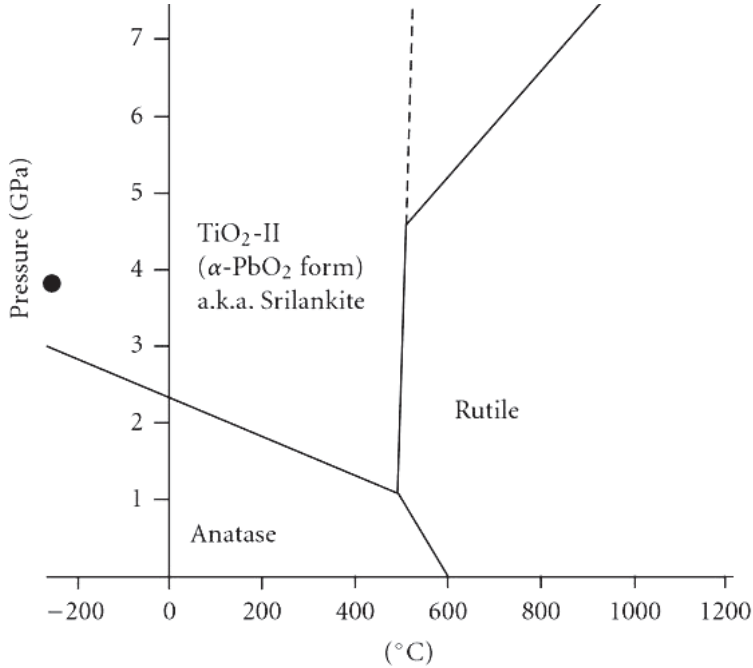

Fig. 1.2 Phase P-T diagram of TiO_2.

1.4 TiO_2 Nanoparticle Safety Evaluation. Risks, Toxicity, and Application

Nanoparticles, nanotechnologies, and nanofabrication characterise the current stage of scientific and technological progress and are factors significantly influencing the further acceleration of this field (Yavorovsky and Tkachyshyn 2016, 3).

Nanoparticles and nanotechnologies have penetrated the fields of business, medicine, science, and even everyday life. On the one hand, these technologies allow us to obtain new materials, modified foods, and medicines, etc.; on the other they have potentially harmful and dangerous impacts on human health, the environment, and the biosphere as a whole (Zeinalov and Kombarova 2016, 3). Semiconductor NPs are characterised by special physicochemical properties that give them high reactivity and the ability to penetrate through biological barriers; as a consequence, they can affect the internal organs and systems of the body, causing pathological changes. The degree of toxicity of NPs depends on their chemical structure, shape, size, permeability, and surface area.

Proper toxicological evaluation of nanomaterials, as well as an understanding of the processes that occur on the surface of nanoparticles when in contact with living systems, is crucial to determining possible toxicological effects. The dose of the nanomaterials is important for identifying hazards and assessing the risks of using nanotechnologies (Zaroddu and Medici 2014, 33).

To date no standards have been developed for safe levels of nanomaterials in environmental objects in such areas as manufacturing, special workers' remedies, and methods for the safe handling of new materials based on nanostructures. As such, they should be handled with the utmost care as they are potentially dangerous to health (Demetska 2010, 4; Zavgorodnii and Dmuhovskaya 2013, 3). Here, the development of new toxicological approaches are required that consider the unique toxicity features of nanomaterials (Balbus and Maynard 2007, 11; Smith and Brown 2014, 2; Koivitso and Kling 2017, 6).

According to the literature, a nanoparticle's toxicity is related to its: 1) chemical composition; 2) surface properties; 3) biotransformation products; and 4) development in terms of influence on apoptosis or necrosis of cells (Ghosh and Roy 2014, 6) or cell lysis (Simon and Saez 2017, 1). The mechanisms of toxicity are associated with oxidative stress, impaired mitochondrial function, and increased membrane permeability (Bosquet and Guaita-Esteruelas 2016, 249).

Scientists have determined lethal doses for nanoparticles in the form of solutions or oral suspensions (Wojcik and Szwajgier 2019, 193). Toxicological studies of TiO_2 (20 nm) introduced to rats by inhalation have shown that particles with a size of 20 nm are capable of accumulating in lymphoid tissue (Ostiguy 2006, 52). They have been shown to have a damaging effect on the DNA of lymphocytes and brain cells (Jiang and Oberdörster 2008, 1). In mice, the LD50 of TiO_2 was found to be 1200 mg/kg and the long-term action of titanium dioxide led to the accumulation of nanoparticles in the brain, oxidative stress, excessive proliferation of glial cells, tissue necrosis, cell apoptosis, and neurogenic disease states (Ze and Hu 2014, 2).

The morphology and concentration of TiO_2 and ZnO nanoparticles leads them to significantly affect human organs. Exposure to fibre nanoparticles with a dose of 5–40 μg/ml results in cell death in the human bronchial epithelium. ZnO nanoparticles hold significant dangers because they are so widespread and are even found in antiseptic agents for children. Studies of *in vitro* toxicity of TiO_2, ZnO, and Al_2O_3 (30–47 nm) nanoparticles, used or proposed for use in some industries, suggest that ZnO has high toxicity, TiO_2 has moderate toxicity, and Al_2O_3 nanoparticles exhibit low toxicity at concentrations greater than 200 μg/ml (Zeinalov and Kombarova 2016, 3). The presence of ZnO nanoparticles (50 to 100 μg/ml) suppresses the mitochondrial function of Neuro-2A (murine neuroblastoma) cells. The relationship of organ-systemic toxicity to particle size may be due to the complex and often counter-directional dependencies between these sizes, the mechanisms of biological aggressiveness of the nanoparticles, and their toxicokinetics.

Analysis of the literature has allowed us to draw the following conclusions:

- Nanotechnologies, nanomaterials, and nanoparticles are seeing widespread use in various fields of economic activity, science, technology, medicine, and everyday life; however, there is a certain lag in biomedical research in assessing the risk of their impact on the human body.
- In the scientific literature, there is no unambiguous dependence shown in the protective and pathological reactions of organisms to the action of oxide semiconductor nanoparticles in terms of their particle size and nature.
- With decreasing size at the nanoscale, toxicity at the cellular level increases.

TiO_2 is used in the manufacture of fibreoptic products, medical equipment, and electronics. Titanium dioxide serves as a standard ingredient in ultrapure glass manufacture. It is also indispensable to the production of heat-resistant and optical glass and as a refractory protective coating for welding. In the manufacture of ceramics, titanium dioxide gives maximum whiteness to shards or enamels. Other areas of usage include: wood preservation (improving weather resistance by optical filtration of solar radiation); filling rubber; glass enamels; glass and glass ceramics; electroceramics; air purification; welding fluxes; hard alloys; chemical intermediates; and titanium dioxide-containing materials suitable for use at high temperatures (for example, fire protection in forced draft furnaces) and the analytical and experimental chromatography of liquids (Shi and Magaye 2013, 15).

Unfortunately, the process for obtaining TiO_2 nanomaterials (rods, tubes, and fibres) from the aqueous solution of precursor Ti(IV) is not well understood.

The technique used involves hydrothermal synthesis of titanium, zirconium, and hafnium dioxide at high-pressures of up to 4.0 GPa, which can give fundamentally novel results, revealing differences in the phase composition of hydrothermal treatment products as amorphous hydroxide gels and the solutions of corresponding compounds. It is interesting to study the process of obtaining one-dimensional (1D) nanostructures using titanium dioxide by the hydrothermal method, which should also lead to new results.

High temperatures in heat treatment allow us to increase the size of crystals, thereby reducing the number of surface defects of the material. This reduces the rate of recombination of electron pairs and promotes high photocatalytic activity. However, anatase can be transformed into the rutile phase and increasing the thermal stability of anatase is a priority task.

1.5 TiO_2 Synthesis

Titanium dioxide is a popular material with unique properties (Wang and Lin 2008, 20). Research has shown how the electrochemical anodizing of high-purity Ti foil allows the production of titanium dioxide membrane nanotubes with a high length to diameter ratio (approximately 1500). Anodizing occured at room temperature and a platinum foil acted as a contoured electrode with a constant potential of 60 V. A membrane was formed of 135 μm thickness. The pore diameter, wall thickness, and length of the TiO_2 nanotubes were 90 nm, 15 nm, and 135 μm, respectively.

In another study, mesoporous titanium dioxide nanoparticles were synthesized by the aerosol-gel method (sol-gel) (Ahh and Cheou 2012, 188). Sodium chloride solutions (the amount of NaCl varying) in distilled water (90 ml) and titanium tetrabutoxide (17.15 ml) in ethanol (72.85 ml) were prepared separately. These solutions were combined and sonicated for 1 h. Next, the joint precursor was aerosolised, after being dried at 25 °C, and then nanostructured TiO_2-NaCl particles were formed at 500 °C, with sodium chloride acting as a template. The resulting TiO_2-NaCl composite nanoparticles were collected on a membrane filter and washed with deionized water using a centrifuge (3600 rpm for 10 min). The purification process was repeated twice to ensure complete removal of the NaCl. The specific surface area of the obtained nanoparticles was 286 and 184 m^2/g, and the average pore size was 1.9 and 4.8 nm, respectively.

The synthesis of high-purity nanosized TiO_2 films by the sol-gel method has also been investigated (Sucio and Marian 2014, 384). Tetrabutoxy titanium (1 mmol) and propionic acid (1 mmol) were mixed for 3 h at 25 °C and part of the solution was used to obtain titanium dioxide in powder form. Heat treatment for 1 h at 450 °C led to the formation of TiO_2 with the structure of anatase and an average crystallite size of 17 nm. The second part of the solution was applied to ITO substrates (25x25 mm) by spin-coating (time 60 s, rotation speed 2000 rpm). The deposited layer was heated in the air for 2 h at a temperature of 450 °C. This gave a coating thickness of 72.33±20 nm and an average crystallite size of 11 nm.

A microemulsion was made consisting of cyclohexane (156 g), Triton X-100, hexanol (33 g), and hydrochloric acid (5 ml, 37 %). This mixture was used for TiO_2 nanoparticle synthesis (Khomane 2011, 1). After examination under a transmission electron microscope (TEM), the diameter of the synthesized particles was found to be 20–25 nm and the length exceeded 100 nm. The specific surface area was 135 m^2/g and the average pore size was 10 nm.

Titanium dioxide nanoparticles can be in the form of one-dimensional structures (Wang and Li 2014, 19). Synthesis using the hydrothermal method (180 °C, 48 hours) yielded nanorods, needles, and smooth microspheres of titanium dioxide (Wei and Zang 2008). Due to the interaction of $TiCl_4$ with water, TiO_2 nanorods formed with a diameter of 60 nm and a length of 500–800 nm. $FeCl_3$ was added and needle microspheres formed with a diameter of 1–2 μm. Smooth microspheres formed only in the presence of the Span-80 surfactant and their size increased to 5–7 μm. In the X-ray diffraction patterns of both types of microspheres, the reflexes belonged to titanium dioxide with a rutile

structure, but anatase and brookite phases were also present. There were no crystalline phases containing iron in the X-ray diffraction patterns.

Use of the sol-gel method made it possible to obtain stable titanium dioxide fibres (You and Zhang 2012, 8) with a thickness of approximately 30 μm and a length of several metres. A solution of tetrabutoxy titanium in ethanol was prepared with a molar ratio of 1:3. This solution was slowly added dropwise to a solution of hydrochloric acid (6 mol/L) in water and absolute ethanol. After stirring for 2 h, it was heated in an oil bath at 110–140 °C. From the colloidal solution (sol) obtained, fibres were pulled by blowing nitrogen. The crystallization of TiO_2 fibres was performed at 500 °C for 1.5 h. The best fibre formation was observed for a sol with the ratio (TiO_2):n $(H_2O) \leq 2$. The continuous fibres consisted of titanium dioxide with anatase and a rutile crystal lattice with a layered structure and an average particle size of 30 nm.

Titanium dioxide nanopowders were obtained by the hydrothermal method and the precipitation method at room temperature (El-Sherbiny and Fetma 2014). In the hydrothermal method, a TiO_2 ethanol solution was added dropwise to concentrated hydrochloric acid, diluted with water, and then subjected to intense stirring for 30 min. The mixture was placed in an autoclave, sealed, and heated to 120 °C. The nanoparticles were a mixture of crystalline phases with anatase and brookite (100 °C, 24 h), and a pure phase of anatase (120 °C, 24 h), for which the average particle size was 6.2 nm. In the precipitation method, a tetrabutoxy titanium ethanol solution was added dropwise and stirred into a mixture of urea with hydrochloric acid at 0 °C. After 4 h of stirring, the mixture was left for 2 weeks at 25 °C. As a result, TiO_2 with a rutile structure was formed with an average particle size of 9.2 nm, confirmed by TEM analysis. Analysis showed that pure TiO_2 with an anatase structure had a specific surface area of 140.74 m^2/g and pore volume of 0.237 cm^3/g, while for TiO_2 with a rutile structure, these parameters were reduced to 60.621 m^2/g and 0.122 cm^3/g, respectively.

TiO_2 films were obtained by nonaqueous electrodeposition (Chigane and Shinagawa 2017). The source of titanium was orthotitanic acid n-hydrate $(Ti(OH)_4 \cdot nH_2O)$. Next, a galvanic solution consisting of titanium, electrolytes (tetramethylammonium chloride), and organic solvents (DMF and ethanol) were prepared. Glass (10x30 mm) was coated with a layer of titanium (20 nm thickness) and platinum (100 nm thickness) by spraying. A titanium plate was used as a counter electrode and a reference electrode. Films were deposited with a controlled potential of -1.8 V for 1 min. Then, the annealed electrodeposited samples were placed in a muffle furnace (600 °

C, 1 h). Films of titanium dioxide with anatase structure were obtained with a thickness of 350 nm.

A rutile titanium dioxide powder (Amano and Nakata 2016, 14) was obtained by heating commercially-sourced P25 powder. The initial powder was a mixture of crystalline phases of TiO_2-anatase and rutile. This powder was heated at 300, 500, and 700 °C in a hydrogen atmosphere for 2 h at atmospheric pressure. The transition from anatase to rutile occured after heating to 700 °C. At this temperature, the specific surface area decreased from 55 to 16 m^2/g and the average crystallite size was 52 nm.

The conditions of hydrothermal synthesis and TiO_2 morphology were studied. A tetrabutoxy titanium (1 ml) solution was mixed with an aqueous solution of sodium hydroxide (60 ml, 0.2 M) containing 0.05 wt% hydrogen peroxide; following this, the solution was stirred (Tian and Luo 2016). Then, the solution was placed in an autoclave and heated to 180 °C, maintained for 24 h. The white product was washed in hydrochloric acid, deionized water, and acetone to clear the sodium cations. This process was followed by drying (70 °C, 24 h) and crystallization (400 °C, 1 h). The resulting particles had a spherical morphology. According to the results of SEM and TEM, the spheres consisted of various nano-objects of TiO_2. Nanoribbons formed after 2 h of heating and twisted nanosheets formed after 6 h of heating. Nanotubes formed after 18 and 24 h. X-ray diffraction patterns of the products confirmed the formation of TiO_2 with an anatase structure.

A restricting factor when using coatings with special properties is their low resistance to long-term operation. As such, a number of different approaches are used (Sakai and Kato 2016, 1). A hydrophobic coating was obtained using an epoxy resin to realize biomimetic self-healing abilities and titanium dioxide and fluoropolymer acted as the photocatalyst. A mixture of epoxy resin, amine, polyethylene glycol, titanium dioxide, and fluoropolymer particles was prepared. Stirring and heating were carried out to remove the amine and the mixture was washed to remove the polyethylene glycol before the powder was dried at 75 °C for 4 h. As a result, a super-hydrophobic surface was formed. This coating had high wear resistance—it retained its resistant properties after two years in the open air and for 6000 h with an accelerated atmospheric exposure test.

Pure titanium dioxide is not active in visible light. As such, a luminescent agent $Er^{3+}YAlO_3$ was added to oxide nanoparticles to activate them (Wang and Li 2009, 4). Tetrabutoxy titanium provided the titanium source, acetic acid was used as the polymerization catalyst, and ethanol was the dispersion medium. A solution was prepared of tetrabutoxy

titanium diluted with ethanol (solution A); then a mixture of $Er_{0.01}Y_{0.99}AlO_3$ powder, water, acetic acid, and ethanol was created (solution B). Solution B was added by the drop to solution A, initiating hydrolysis and polycondensation of tetrabutoxy titanium. A Ti-containing gel coating formed on the surface of the $Er_{0.01}Y_{0.99}AlO_3$ particles. The final product crystallized after heating at 500–700 ºC for 50 min. The resultant TiO_2 film thickness was 50–70 nm.

Thin nanocrystalline films of TiO_2 were prepared by the sol-gel method (Muthukrishnan and Vanaraja 2015, 7). Titanium tetrachloride (1.8 ml) mixed with isopropanol (20 ml), deionized water (30 ml), and a sodium carboxymethyl cellulose solution displayed increased viscosity after 24 hours of stirring. Then, the precursor film was obtained on a glass substrate using the dip coating method. After drying, the procedure was repeated 20 times to achieve a uniform nanoparticle film on the substrate. The crystallization of TiO_2 occurred at 450 °C. The X-ray diffraction pattern demonstrated that the titanium dioxide with an anatase structure had an average crystallite size of 31 nm. According to TEM analysis, the particles had a spherical shape and their average size was in the range 30–40 nm. The maximum sensor response was at 100 ppm with a minimum detectable acetaldehyde concentration of 5 ppm.

The synthesis of titanium dioxide submicron spheres has been proposed (Huang and Zhu 2016, 12). After continuous stirring for 16 h, the product obtained was centrifuged and washed twice with ethanol to remove unreacted substances. After stirring for 1 h, the suspension was transferred to an autoclave, sealed, and heated at 160 °C for 16 h to obtain completely crystallized titanium dioxide. The product was separated and washed three times with ethanol. As a result, TiO_2 submicron sphere powder was formed, which was mixed with ethyl cellulose and α-terpineol to form a paste.

Thin films of titanium dioxide were produced by gas-phase deposition (Khalita and Muhmoud 2017). Titanium tetraisopropoxide acted as a precursor. The coating was formed on a glass substrate at 250–450 °C with a pressure of 15 Torr. The film thickness did not exceed 350 nm. TiO_2 with an anatase structure was obtained. With an increase in the deposition temperature, the average crystallite size decreased from 45 nm (250 °C) to 20 nm (450 °C). As has been described, sol-gel technology can be used effectively for the formation of titanium dioxide, especially in the form of thin films (Niemelä and Marin 2017). However, scientists still do not pay enough attention to the rheological properties of precursor solutions on which the functional characteristics of the products substantially depend.

The high temperatures of heat treatments allow us to increase the size of crystallites and reduce the number of surface defects. However, during this treatment, anatase can quickly turn into rutile. As such, obtaining stable photocatalysts remains an important task.

The scientific group of Lopez, Gomez, Quintana, and Gonzales in the Departmento de Qu´ımica, Universidad Autónoma Metropolitana-Iztapalapa (Mexico) and Instituto Nacional de Neurologıa y Neurocirugıa (Mexico) have developed this topic further. The aims of their work are the sol-gel synthesis of titanium dioxide and the study of its photocatalytic properties, as well as the possibilities of using titanium dioxide as a transport component for treating cancer and epilepsy.

At the University of Cincinnati, USA, under the supervision of Dionysios D. Dionysiou, studies are being conducted into the photocatalytic activity of titanium dioxide in the form of films, nanoparticles doped with nitrogen, fluorine, and sulfur exposed to visible light to purify water of pollutants.

A group of Japanese scientists (Atsunori, Tsutomu, Masahiro, and Kiyoharu) at Toyohashi University of Technology, Osaka Prefecture University, and Nippon Sheet Glass Co Ltd have produced super-hydrophobic and super-hydrophilic materials using thin films of titanium dioxide.

In China, the Yang Hui group at Zhejiang University has engaged in the production of titanium dioxide-based aerogels and the formation and study of the photocatalytic activity of TiO_2 upon doping with gold in the presence of block copolymers. The research team led by Wang Jun of Liaoning University, whose work is primarily aimed at increasing the photocatalytic activity of titanium dioxide doped with amorphous Er^{3+}:$Y_3Al_5O_{12}$, is also worth noting.

In Ukraine, the scientific group Nanotechcenter, under the leadership of Prof. Ragulya A.V. (IPMS NASU), has produced mesoporous TiO_2 nanopowders.

.

CHAPTER 2

PHOTOCATALYTIC APPLICATIONS OF TiO_2 NANOPARTICLES: INACTIVATION OF PATHOGENIC MICROORGANISMS AND DEGRADATION OF DYES

Titanium dioxide nanoparticles increase the photocatalytic activity of composite materials. A high probability of charge release onto the catalyst surface is the advantage of nanoparticles over microparticles. The separation of photogenerated charges in nano-TiO_2 proceeds effectively under UV irradiation (Zahornyi 2017, 56). TiO_2 nanopowders have chemical resistance, are non-toxic, and are effective reagents for the purification of organic and inorganic substances and pathogens of various types in the environment (Mandal 2016).

2.1 Defects in Titanium Dioxide as Catalytic Doping Centres

Further study of the interaction of O_2 molecules with titanium dioxide is of great importance. The formation of non-stoichiometric sites on the surface of TiO_2 makes it possible to reduce its bandgap and shift its absorption spectrum into the visible range of electromagnetic radiation (EMR).

The Ti–O bond is defined as a covalent polar bond, the valence band of TiO_2 is formed by external p-electrons of oxygen, and the wave function of conduction electrons is present on O_2^- ions. The excited titanium ion orbitals form the conduction band bottom. Thus, two isolated energy bands observed in the band structure of titanium oxide allow us to calculate the energy of the valence and conduction bands. The authors have found that the interband transition energy is independent of particle size with particle sizes of 1, 2, 2.5, and 3 nm for optically active anatase.

The optical bandgap is 3.2 eV. For particles with the smallest diameter, a shift of 0.17 eV is observed. The titanium atom in TiO_2 can exist in the form of ions with different oxidation states: Ti^{3+}, Ti^{2+}, and Ti^{+}. The appearance of these charged centres is due to oxygen vacancies present in the crystal structure of the oxide. One oxygen vacancy leads to the formation of two charged Ti^{3+} centres on the surface of the TiO_2. What is more, O_3^- and O^- anions can be present on the surface of titanium dioxide as well (Smirnova and Grebenyuk 2017, 24).

Currently, titanium dioxide in combination with other elements is the most promising approach for the modification of nanoparticles. Doping allows us to expand the absorption spectrum of TiO_2 and increase its photocatalytic activity. The essence of cationic doping is the introduction of metal cations into the crystal structure of titanium dioxide at the position of Ti^{4+} ions. Rare-earth, noble, and transition metal cations can be used (Yalçın and Murat 2010, 3-4). Doping with cations significantly expands the absorption spectrum of TiO_2, increases the redox potential of the formed radicals, and increases the quantum efficiency by reducing the degree of recombination of electrons and holes. The nature and concentration of the doping impurity changes the charge distribution on the TiO_2 surface and affects the degree of photocorrosion and photocatalytic activity. Researchers have found that the concentration and valency of doping cations (In^{3+}, Zn^{2+}, W^{6+}, Nb^{5+}, Li^{+}, etc.) determines the photocatalytic properties of TiO_2 (Karakitsou and Verikios 1993, 6).

An increase in visible light absorption does not lead to increased photocatalytic activity. After doping with cations, a certain number of defects appear in the structure of TiO_2 and these can act as charge recombination centres. After doping, annealing of the photocatalytic process occurs in an oxygen-containing atmosphere (Yalçın and Murat 2010, 3-4).

Compared to pure TiO_2, samples doped with metal cations have higher conductivity. For example, in the case of doping with cations of metals with a lower oxidation state (Fe^{3+}), an electrically neutral state is achieved due to the transfer of electrons from the valence band with the creation of holes, which increases electrical conductivity (p-type conductivity). For comparison, in the case of doped TiO_2 with cations having a higher oxidation state (Nb^{5+}), an electrically neutral state in the system is achieved by transferring electrons to the conduction band, which increases electrical conductivity (n-type conductivity) (Furubayashi and Hitosugi 2005, 25).

Doping of TiO_2 samples with rare-earth metal cations also leads to an increase in TiO_2 photocatalytic activity. The doping of TiO_2 with

cerium (Ce^{3+}/Ce^{4+}) slows the growth rate and increases photocatalytic activity. Cerium can also act as an electron acceptor and can increase photocatalytic activity (El-Baly and Ismail 2009, 1).

The photocatalytic activity of TiO_2-Ce through degradation of the dye methylene blue when irradiated with UV and visible light sources was studied by Magesh and Viswanathan. Here, the size of the ions is different between Ce (Ce^{4+} 0.093 nm, Ce^{3+} 0.103 nm) and titanium (Ti^{4+} 0.068 nm). The bandgap of CeO_2 is 2.76 eV at 450 nm. The mechanism of photocatalytic activity upon irradiation with visible light sees the introduction of Ce into the titanium dioxide lattice and the formation of mixed oxides. This is the result of the formation of an additional energy state that belongs to partially filled 4f Ce levels between the conduction band and the valence band of TiO_2. Visible light can excite electrons from the valence band to 4f Ce levels or from 4f Ce levels to the conduction band, leading to the formation of holes and electrons. X-rays have shown that the introduction of Ce into the TiO_2 lattice increases the interplanar distance *d*.

Doping of samples with cations of other rare earth elements, such as Ce, La, Gd (Wang and Zeng 2019, 2), has also been shown to increase photocatalytic activity. The increase in the photocatalytic activity of TiO_2 by doping with rare-earth metals is mainly associated with the transition of 4f electrons, decreasing the bandgap by transferring the charge between the valence band of TiO_2 and the conduction band through the 4f level of rare-earth metals (El-Baly and Ismail 2009, 1).

The disadvantages of doping in the Ti^{4+} position are primarily found in increased charge recombination, which decreases photocatalytic activity even under UV light. Recent studies have confirmed that it is better to use anionic impurities rather than cationic ones to reduce the band gap of TiO_2 (Choi and Termin 1994, 51).

TiO_2 samples doped by non-metallic elements, such as carbon, sulfur, fluorine, and nitrogen in the oxygen anionic position, demonstrate high photocatalytic activity in the visible and UV regions of the solar spectrum. Among these anions, carbon and nitrogen are of the greatest interest. The substitution of oxygen atoms for carbon leads to the formation of new levels (C2p) above the ceiling of the valence band of TiO_2 (O 2p), which reduces the bandgap and shifts the absorption spectrum (Chen and Jiang 2007, 9). The inclusion of carbon in TiO_2 can also lead to the formation of carbon compounds on the surface of the photocatalyst, which act as absorption centres of visible radiation (Bondarenko and Khalyavka 2018, 1).

Doping with nitrogen atoms is the most popular way of improving the photocatalytic activity parameters of TiO_2 (Li and Zhang 2019, 11). The introduction of nitrogen into TiO_2 shifts the absorption spectrum into the visible region of the solar spectrum. Changes in the refractive index, an increase in hardness, an increase in electrical conductivity, an increase in the elastic modulus, and an increase in activity concerning visible light also occur. After oxygen replacement, a new level is formed above the ceiling of the valence band of TiO_2. After embedding in the lattice internode, the level is formed at 0.76 eV above the valence band (Peng and Cai 2008, 1657-1664). Doping with nitrogen at the oxygen position is difficult since the ionic radius N (1.71 Å) is much larger than O (1.4 Å) (Guo and Zhang 2007, 18). To maintain electroneutrality and the formation of oxygen vacancies, three oxygen atoms are replaced by two nitrogen atoms.

It has been found that the presence of nitrogen narrows the bandgap of TiO_2 to 2.5 eV, which contributes to the absorption of photons with lower energy (Ao and Xu 2009, 1-3). Upon doping, Ti–N and N–O bonds were formed in the structure of the samples. The presence of partially reduced titanium (Ti^{3+}) was also noted. According some published data, the introduction of fluorine at the oxygen position in TiO_2 leads to the formation of Ti^{3+} (Cheng and Geng 2009, 2). Thus, during the capture of a photogenerated electron by an oxygen vacancy, the formation of an F centre occurs, which contributes to the absorption of visible radiation. Here, a defective N2p level arises, which is located at 0.14 eV above the valence band of TiO_2. Thus, nitrogen atoms can act as hole traps and contribute to the separation of free charge carriers. They act as centres of charge recombination and contribute to a decrease in photocatalytic activity. It is worth noting that electron transfer between the N2p level and the oxygen vacancy leads to absorption in the visible range of solar radiation (Guo and Zhang 2007, 18).

Fluorine atoms constitute another promising dopant in the anionic positions of TiO_2. Doping with fluorine atoms leads to the conversion of Ti^{4+} ions into Ti^{3+}. Recent studies have shown that doping with fluorine can also cause absorption in the visible part of the solar spectrum due to the creation of oxygen vacancies. Unlike nitrogen, fluorine atoms replace oxygen due to the close ion radius (1.33 Å for F-, 1.4 Å for O_2-) (Li and Haneda 2005, 1).

Thermolysis of $(NH_4)_2TiF_6$ is a promising approach for producing titanium dioxide containing fluorine and nitrogen ions (Cheng and Geng 2009, 2):

$$(NH_4)_2TiF_6 + 2H_2O \rightarrow TiO_2 + 4HF + 2NH_4F$$

TiO_2 synthesized by this method has high photocatalytic activity in the visible range of the solar spectrum. It is worth noting that there is evidence of the formation of $TiO_xN_yF_z$ particles during the thermolysis of compound $(NH_4)_2TiF_6$.

The application of metal particles offers an alternative approach to the modification of photocatalysts. The noble metals, including Pt, Ag, Au, Pd, Ni, Cu, and Rh, significantly increase the photocatalytic activity of TiO_2 (Rupa et al. 2013, 1-2). The Fermi levels of these metals are lower than those of TiO_2, photoexcited electrons can pass from the conduction band of TiO_2 to metal particles deposited on its surface and photogenerated holes remain in the valence band of TiO_2. The properties of these photocatalysts depend on the dispersion of the metal particles. When the particle size of the metal is less than 2.0 nm, the composites exhibit high catalytic activity. A high concentration of metal particles blocks the surface of TiO_2, reducing the degree of absorption of photons; metal particles themselves also act as electron-hole recombination centres, which decrease the efficiency of photocatalysts.

Sakthivel and Shankar (2004, 13) synthesized TiO_2 nanoparticles doped with particles (1 wt%) of noble metals (Me/TiO_2, Me = Ag, Au, and Pt) using the sol-gel method. The activity of the studied catalysts decreased in the following order: Au/TiO_2 > Ag/TiO_2 > Pt/TiO_2 > synthesized TiO_2 > TiO_2 (P25). Rather than the previously proposed approach, the authors studied the effect of rare elements on TiO_2 activity and doping with palladium was found to increase the activity of the TiO_2 (Papp and Shen 1993, 5).

Rutile phase tantalum-modified titanium oxide ($Ta_{0.3}Ti_{0.7}O_2$) was synthesized and studied using electrochemical and spectroscopic methods to evaluate its efficacy as a corrosion-resistant electrocatalyst material. A 20 wt% Pt supported on the $Ta_{0.3}Ti_{0.}7O_2$ catalyst was prepared. The existence of strong metal-support interactions in 20 % $Pt/Ta_{0.3}Ti_{0.7}O_2$ was ascertained using X-ray absorption near-edge structure analysis. The number of unfilled *d* states in 20 % $Pt/Ta_{0.3}Ti_{0.7}O_2$ was ∼1.47, which was lower than the value of ∼1.60 found in both the carbon-supported Pt catalysts. The decrease in the number of unfilled *d* states confirmed electron donation from the $Ta_{0.3}Ti_{0.}7O_2$ support to the Pt atoms, resulting in increased electron density on the Pt. This interaction enhanced both electrocatalytic activity and catalyst stability (Kumar and Ramani 2014, 5).

The synthesis of H_2 was reported by the photoreduction of an aqueous methanol solution with the Cu/TiO_2 photocatalyst. Later, the authors increased the yield of hydrogen by producing a photocatalyst

using copper precipitation with TiO_2 particles (Wong and Malati 1986, 2).

The specific coupling of different semiconductors with different energy levels has become another approach for modifying photocatalysts. Systems consisting of several semiconductor particles are active in the visible spectrum of solar radiation and, due to the high degree of charge separation, have high photocatalytic activity. Good agreement between the conduction band and the valence band of the two semiconductors ensures efficient transfer of charge carriers from one to the other. A semiconductor with a narrow bandgap acts as a sensitizer to visible radiation for TiO_2. The energy gap between the corresponding band levels ensures the transfer of charge carriers to adjacent particles and promotes the separation of electrons and holes (Zhang and Chen 2009, 29).

Photocatalytic water and air purification systems with artificial UV radiation have been on the market for several years. Additionally, the combination of photocatalysis and membrane cleaning can reduce the pollution of a filter membrane, thereby significantly increasing the efficiency of water treatment.

Roy and Varghese (2010, 3) used TiO_2 nanotubes obtained by anodic oxidation of titanium, which was modified with Cu or Pt nanoparticles, as a photocatalyst. The total productivity for all hydrocarbons obtained in the laboratory was 160 µl/h per gram of nanotubes. These results are 20 times higher than all previously described methods, but still too low for direct practical application.

2.2 TiO_2 Nanoparticle Antimicrobial and Antiviral Activity

Organisms, including humans, animals, and birds, determine the relevance of tools and methods for the decontamination and removal of microorganisms from the environment. Viral infections spread in several ways, among which the most dangerous are airborne infection and waterborne infection. The water environment supports great vitality in nature, including enteroviruses, hepatitis A, adenoviruses, and avian flu. In the early twenty-first century, infection with human and animal viruses such as avian influenza (H5N1, H7N7, H7N3, H9N2, and H7N9), swine flu (H1N1), norovirus, and coronavirus (fig. 2.1) brings the risk of new and variant epidemics (doi: 10.1179/2047773213Y.0000000103).

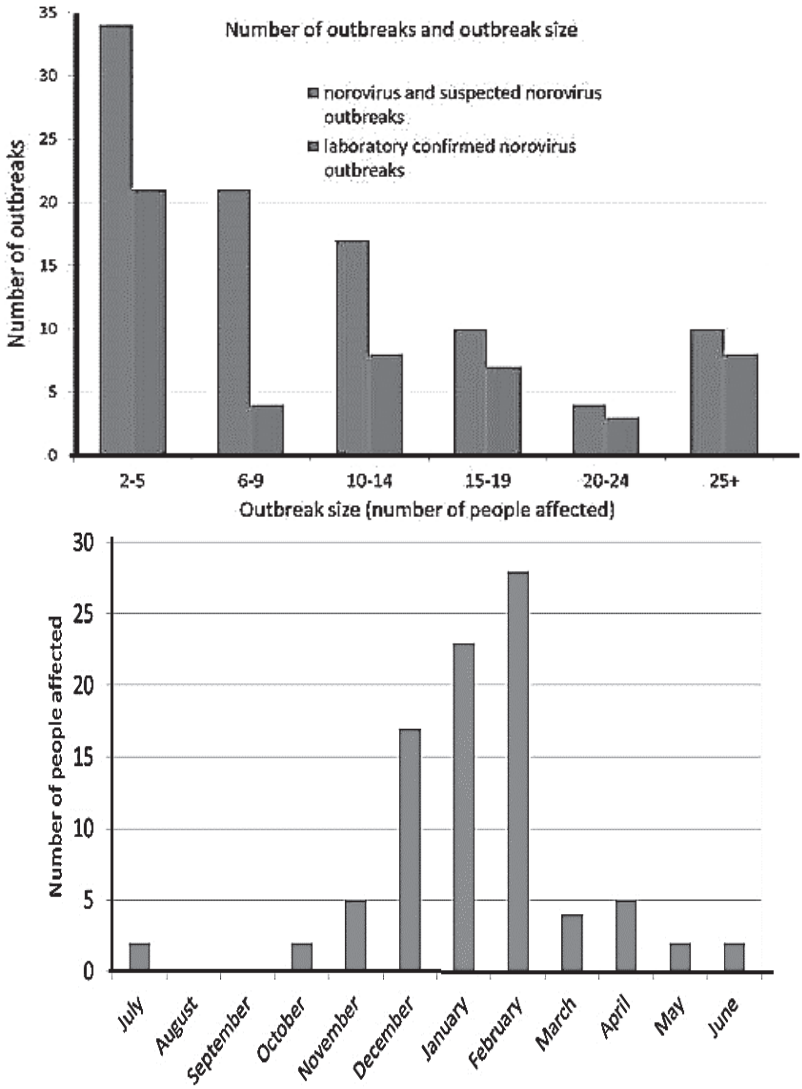

Fig. 2.1a Critical Review on the Public Health Impact of Norovirus Contamination in Shellfish and the Environment: A UK Perspective (Hassard and Sharp 2017, 2).

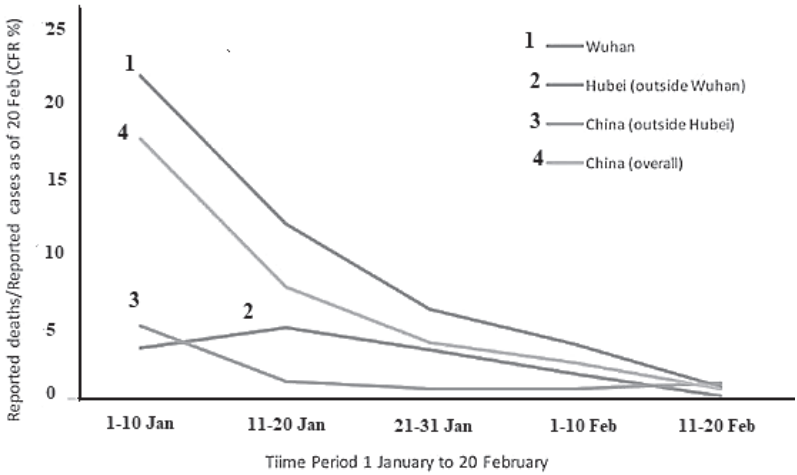

Fig. 2.1b Case fatality ratio (reported deaths among total cases) for COVID-19 in China over time and by location, as of 20 February 2020 (https://www.who.int/docs/default-source/coronaviruse/who-china-joint-mission-on-covid-19-final-report.pdf).

Adenoviruses (Ad) are a group of highly resistant viruses found in the environment, that are well able to endure low temperatures and the impact of virtually all organic solvents including chloroform and ether. The main source of infection is via sick individuals who exude a small amount of the virus during relapse, lasting two to four weeks from the manifestation of symptoms. Transmission occurs through airborne droplets with inhaled air infecting individuals during conversation, deep breathing, and sneezing. Adenoviruses thus fall into the categories of airborne and intestinal infection. The bacterium *Staphylococcus aureus* is the leading agent of nosocomial infection, including postoperative infection, due to its acquisition of resistance to most antibiotics and disinfectants.

Recently, the important problem of environmental biosafety in relation to adenoviruses and bacteria has arisen. Heterogeneous photocatalysis is a promising method for addressing this problem because of its efficiency and the ease of manufacturing the necessary material compared to other methods.

As such, the development of innovative photocatalysts for the effective disinfection of viruses and opportunistic pathogens without the substantial formation of toxic byproducts is absolutely necessary. According to data compiled by researchers at Johns Hopkins University,

Baltimore, Maryland, as of the number of reported COVID-19 cases worldwide has passed two million; the United States alone has seen more than 600,000. The death toll from the disease has also surged past 128,000 worldwide with some 24,000 people having died in the US, while more than 20,000 people have died in Italy. The pandemic has spread to every corner of the globe, with only about a dozen of the World Health Organization's member states not yet reporting cases. Most of these are small island-nations in the Pacific Ocean, such as Vanuatu, Tuvalu, and Palau.

Confined environments, especially public facilities, hospitals, and public transport, as a rule, see elevated concentrations of microorganisms, viruses, and volatile organic compounds in the air. The concentration of indoor pollutants is related to the low air exchange rates at which air-conditioning systems operate. Among microorganisms transported by air are those that can increase allergies or cause infection (fig. 2.1b).

Individuals at the highest risk for severe disease and death include people over 60 and those with underlying conditions, such as hypertension, diabetes, cardiovascular disease, chronic respiratory disease, and cancer. Symptomatic disease in children appears to be relatively rare and mild with approximately 2.4 % of the total reported cases in individuals under 19 years of age. Only an insignificant proportion of those aged under 19 have developed severe (2.5 %) or critical disease (0.2 %).

Numerous methods have been proposed to decontaminate indoor atmospheres. In the past, the most commonly used method has been the use of filters, mainly because of their low cost and ease of operation. The main disadvantage of this method is that it is non-destructive and demands frequent technical maintenance. To improve efficiency in air conditioning systems, ultraviolet (UV) lamps are also used. Some authors have reported that bacteria regenerate and start to regrow after removal of the UV source (Teixeira and Miranda 2012, 1). UV-C treatment can also be harmful to human health. Thus, alternative methods for air cleaning and elimination of microorganisms and viruses are necessary that do not pose a danger to human health (Michałkiewicz 2018, 11).

Photocatalysis is a promising method for the disinfection of indoor air, which allows the decomposition of a substantial portion of bacterial cell mass due to membrane damage in the presence of water or humid air, as well as the mineralizing of most volatile organic compounds, leaving carbon dioxide, water, and mineral acids as end-products (Gumy and Morais 2006, 1-2).

In recent years, TiO_2 nanopowder has been shown to be an effective agent for the treatment of organic and inorganic substances and various pathogens in the environment (Nakano and Ishiguro 2012, 8). The process of microorganism inactivation using photocatalyst TiO_2 lasts for 6 h (Dong and Xu 2017; Rodrigues-Silva 2016, 1-10).

TiO_2 can reduce the duration of disinfection to 10 min by using 2 M iron sulfate, which promotes the generation of hydroxyl radicals in an aqueous medium (Teixeira and Miranda 2012, 1). The dose of UV radiation in the presence of TiO_2 is 10 mW/cm^2 (Li and Liu 2014, 1-37; Bogdan and Zarzynska 2015, 10; Hayashi and Nozaki 2019, 1). The presence of bromide and chloride in photocatalyst TiO_2 was found to increase adenovirus inactivation by 10 times (Li and Liu 2014, 1-37).

Analysis of TiO_2 and ZnO photocatalytic nanopowder activity and the inactivation of gram-negative (*E. coli* Koch) and gram-positive (*Staphylococcus aureus*) bacteria was performed (Bogdan and Zarzynska 2015, 10). A powder concentration of 0.125 mg/L for photocatalyst TiO_2 (P25) was shown to increase the inactivation capacity to 90 % when compared to ZnO. This inactivation of gram-negative bacteria is due to their biochemical structure. The authors explain that gram-negative bacteria have a thin cell wall (2–10 nm) consisting of two phospholipid bilayers (an outer membrane and plasma membrane) separated by the periplasm, with two or three layers of peptidoglycans. Gram-positive bacteria have a thick cell wall (20–80 nm) and a similar plasma membrane to gram-negative bacteria. Mostly, the outer membrane of gram-negative bacteria consists of lipopolysaccharide backbones, which are attached to lipoproteins that are responsible for covalent linkage with peptidoglycan within the periplasmic space.

This lipopolysaccharide backbone provides a negative charge on the membrane surface, which imparts resistance to hydrophobic compounds, such as detergents and similar compounds, as well as ensuring structural integrity and cell viability. The structural integrity of cell walls also determines the tolerance or susceptibility of bacteria to foreign bodies like NPs. The outer membrane also includes porins and lipopolysaccharide molecules. Bacteria have no membrane-bound organelles and show a wide diversity of morphologies. Normally, gram-negative bacteria are more susceptible than gram-positive bacteria to NPs, because exposure to NPs reduces peptidoglycans (Mandal 2016).

Doping of TiO_2 with certain oxides can significantly reduce the bandgap of the photocatalyst. TiO_2 doped with Ag and Fe has shown enhanced photocatalytic and bactericidal activity (Liga and Bryant 2011, 2; Sagadevan 2015, 3). With increasing concentrations of Ag in TiO_2,

from 2.46 to 6.0 wt%, the inactivation rate for a bacteriophage virus was increased by up to 7 times and the duration of the disinfection process was reduced from 5 min to 0.75 min. The authors (Xiang and Ma 2011, 5) injected Ag nanoparticles into mesoporous TiO_2 with the aimed cleaning water. It was stated that UV irradiation of silver of 0.25 wt% destroys the Rhodamine B dye and an Ag concentration of 2.0 wt% provided rapid Koch inactivation of *E. coli*.

The synthesis of the composite photocatalyst TiO_2-Ag-SiO_2 by the sol-gel method and its bactericidal effect on intestinal *E. coli* ATSS25922 was examined (Hoang and Tran 2016, 2). It was established that the synthesized composite was characterized by a higher specific surface area of 164 m^2/g compared to P25. Thus, the composite photocatalyst's inactivation ability occurs over a wide spectral range of UV irradiation with an intensity of 2.5 mW/cm^2.

Recently, considerable attention has been attracted to the application of TiO_2 nanoparticles in polymer matrices (carriers) of different chemical structures to form films with enhanced antibacterial properties (Othman and Abd Salam 2014, 1-6). Methyl ethyl ketone suspensions containing 0.05–1 wt% TiO_2 were used to form polyethene films. A suspension with 1 wt% TiO_2 was found to inactivate *E. coli* Koch significantly faster under short wavelength irradiation of $\lambda = 365$ nm compared to $\lambda = 425$ nm.

A polymer matrix of polypropylene and polyethene was mixed with TiO_2 and ZnO in the presence of silane (1 wt%) and composite photocatalysts with antibacterial properties were obtained (Altan and Yildirim 2014, 2). The nanoparticle concentrations varied in the range 1–5 wt%. IR spectroscopy showed that the addition of silane-TiO_2 nanoparticles strongly connects the bond between the particles and the polymer (polypropylene) composite compared to ZnO. The increased nanoparticle concentration, from 3 to 5 wt%, promotes complete *E. coli* Koch inactivation after 2 h of disinfection with UV radiation.

TiO_2 oxide nanoparticles in aqueous media were injected into biopolymers (Shaili and Abdorreza 2015, 134) with a TiO_2-N concentration of 1–5 wt%. The inactivation zone (inhibition) for *Staphylococcus aureus* increased from 25 to 70 mm^2 with increasing concentrations of TiO_2-N up to 5 wt%. The current trend in antimicrobial and antibacterial techniques is focused on the development of strategies that operate faster and have higher yields. The problem lies in expanding the multifunctional application of composite photocatalysts with an optical irradiation spectrum.

There is no description in the research of the optimal morphological structure of doped TiO_2 that sees high photocatalytic activity and oxidative

degradation of toxic organic substances. The mechanism of adenovirus inactivation is of great importance in the study of TiO_2. It is necessary to understand the chemical structure of active receptors attacked by hydroxyl radicals during exposure and this understanding will enable us to find the optimal dose and duration to damage capsid proteins in the disinfection of air and water pollution.

2.2.1 The following problems were found in a review of the literature

First, we do not know how an adenovirus responds to photocatalytic inactivation using composite photocatalysts. Second, we do not know (for any virus) whether damage to its proteins or genetic material is primarily responsible for viral inactivation. Third, we know that HO• is primarily responsible for MS_2 (bacteriophage) inactivation. However, studies have demonstrated the inactivation of MS_2 by singlet oxygen. As such, a better model is needed to account for the effects of catalyst fouling and competitive adsorption with inactivated viruses.

2.2.2 Experimental results and antiadenovirus activity of TiO_2 nanoparticles

The creation of materials with new properties and characteristics is the focus of nanoparticle development. New industries and fields have emerged, including nanoscience, nanoengineering, nanoelectronics, and nanochemistry. These developments are being applied in a number of areas, including electronics, information technology, medicine, pharmacology, agriculture, medical technology, and molecular biology, etc. This phenomenon has developed along with several new methods that allow the synthesis of structures with properties that are regulated at the atomic-molecular level (Kavoosi and Modaresi 2018, 10).

Nanopowders of metals and their oxides are playing an important role in the development of compounds with antiviral properties. Metal oxides, such as ZnO, TiO_2, SiO_2, and ZrO_2, are all promising, as well as those containing Ag and Au. Many studies have shown their pronounced bactericidal, fungicidal, and virucidal activity (Toledano-Osorio and Babu 2018, 6). In particular, the antiviral activity of titanium dioxide nanoparticles against hepatitis B virus, norovirus, and influenza has been demonstrated under UV irradiation (Park and Shahbaz 2016, 238).

Under the influence of UV radiation, TiO_2 produces active oxygen-containing radicals that can damage biological molecules in pathogens,

such as proteins, lipids, and nucleic acids. As such, the search for substances safe for humans and the environment is an important one. In the case of UV irradiation, the charge can be released onto the catalyst's surface. The depth of penetration of ultraviolet light into TiO_2 particles is limited (~100 nm), so that only its outer surface is active. In TiO_2 nanoparticles, the electron exit time to the surface does not exceed 10 pcs, whereas micron-sized semiconductor powders, including titanium dioxide, are characterized by a value of approximately 100 ns, so that the separation of photogenerated charges in nano-TiO_2 occurs quite effectively; these then reach the surface and are further consumed in processes encouraged by UV irradiation. Reducing the particle size to the nanoscale contributes to the absorption of light, which increases TiO_2 antiviral activity (Krukov and Stroyuk 2013).

The Human Adenovirus Working Group reports the presence of 90 types of human adenoviruses that are divided into seven groups (A-G) (Khanal and Ghimire 2018, 1). Diseases caused by adenovirus infections have shown a steady rise. Adenoviruses affect human populations through direct contact with water. They have been detected in reservoirs, wastewater, rivers, drinking water, oceans, and pools. With the absence of a specific drug for the treatment of adenoviral infections, the search for new therapeutic alternatives is of great importance.

The kinetics of UV irradiation in the TiO_2 system play an important role. It is necessary to understand the chemical structure of the active receptors attacked by hydroxyl radicals during the irradiation of the TiO_2 system. Disclosure of the TiO_2 antiviral action mechanism and determination of the UV optimal dose to activate photocatalysis encourage their use in developing virus purification agents in the air and environment.

2.2.3 Materials and methods. Transplanted cell cultures used in the research

MDBK (Madin-Darby bovine kidney) cells and HEp-2-human laryngeal squamous cell carcinoma cells were obtained from the Cell Bank of the RE Kavetsky Institute of Experimental Pathology, Oncology and Radiobiology at the National Academy of Sciences of Ukraine (Kyiv, Ukraine). For cell cultivation, a growth medium was used consisting of 45 % DMEM (Sigma, USA), 45 % RPMI 1640 (Sigma, USA), and 10 % inactivated bovine embryo serum (Sigma, USA). The antibiotics used were penicillin (100 μg/ml) and streptomycin (100 μg/ml). Cell cultivation was conducted using a standard technique (http://dx.doi.org/10.18524/2307-4663.2016.4(36).86796).

The virus was accumulated and titrated on the HEp-2 cell culture and stored at -20 °C. The virus titre was determined at the endpoint of virus dilution with a cytopathic effect of 50 %.

Test compounds. The nanopowders used were: TiO_2-I and TiO_2-II with particle sizes and specific surface areas of 8–15 nm and 57.3 m^2/g and 20–30 nm and 50 m^2/g, respectively; and a commercial sample of titanium dioxide TiO_2-P25 produced by Evonik Industries AG (Germany) with a specific surface area of 52 m^2/g. We used 0.1 % aqueous suspensions of TiO_2 nanoparticles, which were prepared using a ULAB 2200 homogenizer (Germany).

The structure of the samples was determined using the JEM-1400 electron microscope (JEOL, Japan) with an instrumental magnification of 2000 to 100000 and an accelerating voltage of 80 kV. In studying the effect of UV radiation on the virucidal activity of titanium dioxide, a bactericidal lamp MEDICOR Q-139 with an irradiation level of 22.3±0.2 W/m^2 was used.

The cytotoxicity of the nanoparticles was determined in the MDBK cell culture using the MTT test according to the standard method (Mosmann 1983, 1-2). The optical density of the samples was recorded spectrophotometrically on a Multiscan FC instrument (Thermo Fisher Scientific, USA) with a wavelength of 540 nm.

The virucidal action of the oxide nanoparticles on the bull kidney cells was analyzed. A mixture containing equal volumes of adenovirus and a TiO_2 suspension was kept for 5, 15, and 30 min. in a thermostat at 37 °C and then used to infect the MDBK cells.

Nanopowders have mesoporous structures, but the volume and area of the mesopores vary. The characteristics of the porous structure of the synthesized and commercial TiO_2 samples were shown to correlate with each other using BET and BJH pore calculation methods. The TiO_2-II was characterized by decreasing parameters, V and D, which may be related to the structure of the particles and the presence of agglomerates.

The effect of titanium dioxide nanoparticles on the extracellular virus (its virucidal action) is presented in fig. 2.2. The results show that, as the time of incubation of the TiO_2-I and TiO_2-II samples (suspension 10 μg/ml) increased, the virucidal activity of the nanoparticles decreased. High activity was detected at lower concentrations (0.1–0.01 μg/ml) and we saw significant inhibition of virus reproduction (49 %) after 5 min. of incubation (0.1 μg/ml nanoparticles) with the TiO_2-I sample. However, the greatest virucidal effect (63 %) was seen for TiO_2-II nanoparticles at a concentration of 0.01 μg/ml after 15 min. of incubation with the adenovirus.

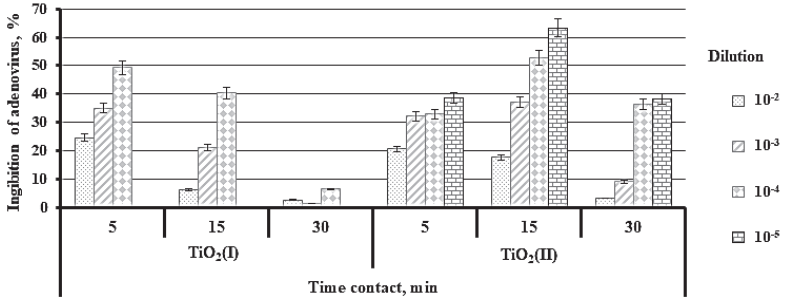

Fig. 2.2 Virucidal action of TiO_2 (I) and (II) nanoparticles against human adenovirus 5 serotype.

2.2.4 Influence of UV action with dose intensity on bacterial inactivation

Today, the incidence rate of microbiological contamination of the indoor air environment remains at a high level due to pathogens transmitted through air and airborne droplets. This problem is especially acute in places that see large crowds crammed together indoors in poorly ventilated rooms, as well as in rooms with air recirculation. Preventing the spread of diseases is the main task of air disinfection.

The inactivation of microorganisms sees the loss of their ability to reproduce after sterilization or disinfection. Ultraviolet radiation covers the wavelength range 100 to 400 nm of the optical spectrum of electromagnetic vibrations, i.e. lying between visible and X-ray radiation. Types of ultraviolet radiation are presented in table 2.1.

Table 2.1 Types of ultraviolet radiation

Name	Abbreviation	λ, nm	Photon energy, eV
Average	NUV	400–300	3.10–4.13
Long range	MUV	300–200	4.13–6.20
Extreme	FUV	200–122	6.20–10.2
Vacuum	EUV, XUV	121–10	10.2–12.4
UV A,	VUV	200–10	6.20–12.4
UV B (medium range)	UVA	400–315	3.10–3.94
	UVB	315–280	3.94–4.43

Changes in the DNA of microorganisms accumulate, leading to slower rates of reproduction and possibly even extinction. It has been noted that energy in the UV-C spectrum at 254 nm is most effective from a bactericidal perspective.

Raab O. discovered the optical methods for bacterial inactivation in 1900. The essence of this discovery was that, when the light intensity in the microscope field was sufficiently large and the cells were stained by acridine or other fluorescent dyes such as quinine, methyl phosphine, and eosin, they stopped moving and died.

This discovery suggested the possibility of photoinactivation of infectious agents in the visible spectrum of light (Bogdan and Zarzynska 2015, 10). This phenomenon is called 'photodynamic action'. Photodynamic reactions are reactions that see the oxidation of substrates with oxygen and cannot happen in the dark. All biological objects have varying sensitivity to this photodynamic action, including: vertebrates and invertebrates, protozoa; higher and lower plants; microorganisms; plant and microbial viruses; intracellular organelles; biopolymers; and biological molecules of various sizes. Bacteria, being simple structure prokaryotic cells, are very sensitive to photodynamic action.

Recently, a study found that bacteria can be inactivated using radiation in the visible region. According to the patent RU 2164427, Russian scientists used indocyanine green as a photosensitizer with an intensity of 40–50 mW/cm^2 for 20–30 min. Most of biological objects have endogenous (inside) photosensitizers, including porphyrins and flavins, which are the most ancient elements of living matter. Porphyrins absorb light in the violet region of the spectrum (400–420 nm), while flavins absorb in the blue region (440–480 nm).

We have observed the antibacterial effect of UV or blue light in the process of bacterial inactivation of infected areas and that it is possible to obtain an antibacterial effect without additional preliminary surface treatment with an exogenous photosensitizer.

In addition, the types of photobiological effect of radiation (for example, the death of bacteria) are strictly subject to the Bunsen-Roscoe law, which states: "... the number of products of a photochemical reaction is determined only by the dose of light, low radiation power densities are compensated by long exposure time and vice versa...".

Over the past 2–3 years, the authors have used a low-power irradiation flux of 2–6 mW/cm^2 in the wavelength range 200–300 nm.

2.2.5 The influence of irradiation intensity on bacterial inactivation

The inactivation of bacteria in the presence of TiO_2 irradiated with fluorescent light is a first-order reaction. The degree of inactivation increases with increased exposure to fluorescent light for all bacteria. However, the change in the rate of inactivation constant with increasing TiO_2 content is different for different bacteria types. *Escherichia coli* K-12 was selected to study the efficiency of inactivation by fluorescent light emitted by a TiO_2 catalyst. Figure 2.3 shows the inactivation of *E. coli* K-12 for 0, 15, 30, 45, 60, and 120 min. with six doses of UV-A (0, 11.7, 23.4, 35.1, 46.8 and 93.6 mJ/cm^2).

An increase in TiO_2 content from 234 to 1666 mg/m^2 accelerated the process of *E. coli* K-12 inactivation (fig. 2.3). With a TiO_2 load of 234 mg/m^2, more than 98 % of *E. coli* K-12 was inactivated after 60 min. with a dose of 46.8 mJ/cm^2 under fluorescent radiation. More than 96 % of bacteria were inactivated with a TiO_2 concentration of 1666 mg/m^2. This shows that the intensity of a fluorescent lamp of 0.013 mW/cm^2 is sufficient for inactivation, which is comparable to results of Prof. Huang, who reported damage to the cell walls of *E. coli* within 20 min after exposure to a UV light dose of 0.8 mW/cm^2 in the presence of TiO_2.

Note that nonporous titanium dioxide (TiO_2, P25, Degussa AG, Frankfurt, Germany) was used as a photocatalyst for these studies with a particle diameter of 21 nm and a specific surface area of 50 ± 15 m^2/g. TiO_2 suspensions in deionized water in nine concentrations ranging from 234 to 8662 mg/m^2 were prepared and autoclaved. Another TiO_2 catalyst, known as Hombikat UV-100, with a surface area of more than 250 m^2/g and a crystal distribution of 100 % anatase, was also used for a limited batch of experiments.

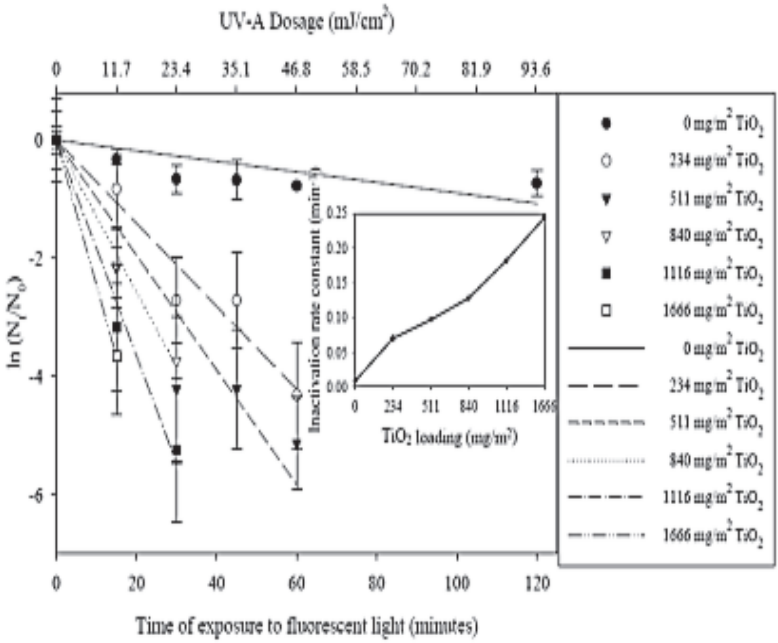

Fig. 2.3 Koch bacillus inactivation with different TiO_2 concentrations for 120 min (Madhumita B. Ray, University of Western Ontario).

The photoexcitation of TiO_2 particles leads to the generation of free electrons and holes and breaks the surface bridge bond of the Ti^{4+}–OH–Ti^{4+} type with the formation of adsorption centres of water molecules, or the breaking of both bonds of the surface bridge oxygen, and oxygen vacancies (Fujishima and Rao 2000, 1). The process is reversible in "dark" mode. Materials with surface TiO_2 particles are characterized by the phenomenon of super-hydrophilicity under the action of UV irradiation. The mechanism of action can be explained using the following scheme (Pitchel and Vivar 2018; Alrousan and Polo-López 2012).

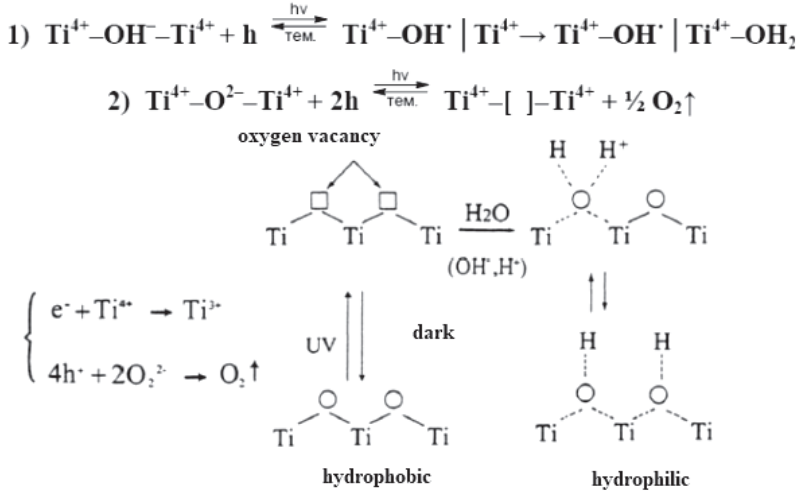

Fig. 2.4 The mechanism of TiO_2 action with UV radiation.

TiO_2 is a photocatalytic semiconductor (Bogdan and Zarzynska 2015, 10). When photons are irradiated using a beam of less than 385 nm, an electron in the TiO_2 passes from the valence band (VB) to the conduction band (CB). An electron-hole pair is involved in the chemical reaction, forming hydroxyl radicals and superoxide ions. These highly active particles oxidize organic compounds are adsorbed onto the surface of the catalyst. TiO_2 activation by the action of UV light can be written out as:

$$H_2O + h^+ \rightarrow \bullet OH + H^+ \quad (\mathbf{2.1})$$

$$O_2 + e^- \rightarrow O_2^-\bullet \quad (\mathbf{2.2})$$

$$O_2^-\bullet + H^+ \rightarrow HO_2\bullet \quad (\mathbf{2.3})$$

$$2HO_2\bullet \rightarrow O_2 + H_2O_2 \quad (\mathbf{2.4})$$

$$H_2O_2 + O_2^-\bullet \rightarrow \bullet OH + OH^- + O_2\bullet \quad (\mathbf{2.5})$$

Equation (2.1) is an oxidation reaction, while equations (2.2)–(2.5) are reductive reactions (Pitchel and Vivar 2018; Alrousan and Polo-López 2012).

In 1970, Fujishima and Honda discovered the process of water photolysis using titanium dioxide electrodes. The concept of photochemical sterilization of microbial cells with semiconductor particles was also

reported (Matsunaga and Tomada 1985, 1-2). Platinum black with a TiO_2 layer (Aerosil P25, 99.99 % anatase) at a ratio of 10:1 and suspended in water was used as a catalyst for a metal halide lamp with irradiation of 60–120 min for the photoelectrochemical oxidation of coenzyme-A. The bacteria *Lactobacillus acidophilus*, *Saccharomyces cerevisiae*, *E. coli* inhibit respiration and can lead to cell death. In this experiment, the survival rate of *E. coli* decreased to 20 % after 60 min. and disappeared after 120 min. Huang et al. used o-nitrophenol-D-galactopyranoside (ONPG) as a probe and *E. coli* as a cell model to illustrate how TiO_2 causes initial oxidative damage to the cell wall, although the cells remained alive. The photocatalytic effect gradually increased cell permeability as cell wall protection was removed and oxidative damage occurred in the cytoplasmic membrane. Also, in the presence of free particles, TiO_2 entered the membranes of damaged cells, accelerating cell death.

Ibanez tested bactericidal heterogeneous photocatalysis and microorganism resistance to UV light. Sublethal UV-A light caused mortality of *E. coli* K-12 with the presence of TiO_2 nanoparticles after irradiation for 40 min.

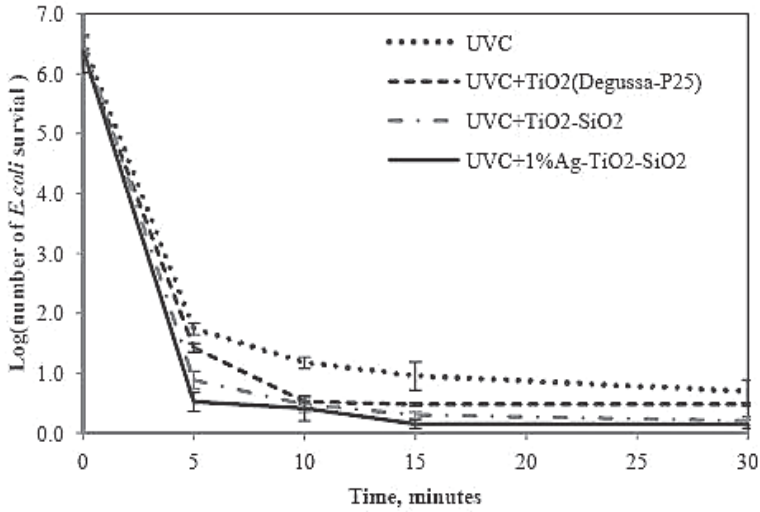

Fig. 2.5 Inactivation of *E. coli* using system TiO_2-SiO_2/Ag (1 %) during UV illumination (Hoang and Tran 2016, 2).

Figure 2.5 shows the inactivation of *E. coli* under UV-C irradiation using the photocatalysts TiO_2 (Degussa-P25), TiO_2-SiO_2, or 1 % TiO_2-SiO_2-Ag for 30 min. Ag with TiO_2 saw improved antibacterial activity against *E. coli* in terms of inactivation efficiency. Of the three types of catalyst (commercial TiO_2 (P25), TiO_2-SiO_2, and 1 % TiO_2-SiO_2-Ag), the disinfection efficiency of 1 % TiO_2-SiO_2-Ag was the highest. Additionally, the antibacterial effect of 1 % TiO_2-SiO_2-Ag was significantly higher than UV-C alone at 5, 10, and 15 min.

2.3 The Application of TiO_2 in Photocatalysis

2.3.1 Spectral analysis of TiO_2 nanoparticles

Raman studies (fig. 2.6) have confirmed the pure single-phase anatase modification of our TiO_2-I nanopowder. For the red spectrum, an intense scattering peak was observed in the region of 170–200 cm^{-1} (535 nm laser beam).

Study of the structure of the powders showed a more developed mesoporous surface in our sample (I). In photoelectrocatalysis, as in catalysis, the optimal pore size distribution plays a decisive role in providing charge transfer and mass transfer. The intensive signal of Ti^{3+} (blue colour spectrum) in the anatase lattice (sample-I) was present. The effect of defective Ti^{3+} positions on the surface state was based on the particle dimension of this sample of 10 nm (fig. 2.7).

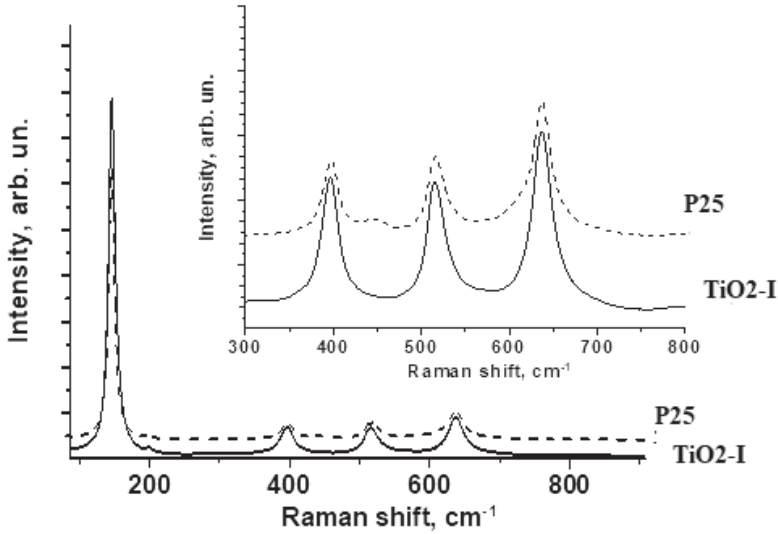

Fig. 2.6 Raman absorption spectra for TiO_2 samples.

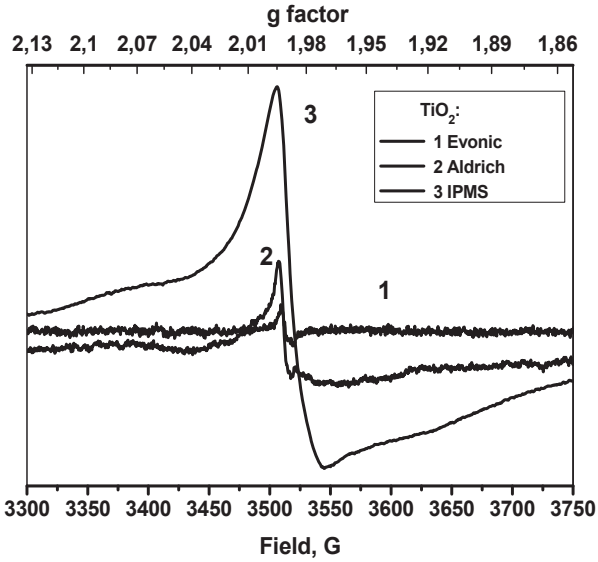

Fig. 2.7 EPR spectra of TiO_2 samples.

Using TiO_2, the EPR study in fig. 2.8 presents the molecular structure of C_3N_4 doped by oxygen, which is typical for the graphite form. EPR spectra confirmed the presence of carbon nitrides (0–15 wt% of O). These semiconductors consist of carbon atoms and nitrogen, enabling their functionalization within wide limits to control the reactivity of the material. Graphite carbon nitride is the most stable modification of carbon nitride and has attracted the interest of researchers due to its unique electronic properties and catalytic activity, including photocatalytic activity. The ideal carbon nitride form contains only C–N bonds and is a π-conjugated polymer "poly(tri-triazine)" (Bondarenko and Silenko 2018, 4). Given the aromatic nature of the component blocks (s-triazine rings), the corresponding 2D polymer is capable of forming π-conjugated flat layers, similar to graphite.

The presence of hydrogen (fig. 2.9) in the structure of carbon nitride testifies to its incomplete condensation and the existence of surface defects. It gives catalytic properties to carbon nitride in the reactions of hydrogenation, oxidation, and transesterification, etc. (Caputo and Gross 2014, 43).

The surface structural defects of carbon nitride, TiO_2 (EPR), and $C_3N_4O_x$ can provide active centres, with the possibility of additional chemical modification of the surface material for purposeful regulation of the structure of catalytically active systems and the performance of heterogeneous catalytic reactions. The high nitrogen content of carbon nitride means that it can be used as a major non-metal catalyst. Additionally, in the deposition of nanoparticles of metal oxides, particularly noble metals, on graphitic carbon nitride, TiO_2 increases the Schottky barrier, which, in turn, contributes to a better separation of charges at the boundary of the metal-semiconductor heterojunction. Therefore, conducting oxide nanoparticles can work as "active" carriers of metal nanoparticles, contributing to an increase in catalytic activity and the selectivity of the catalysts.

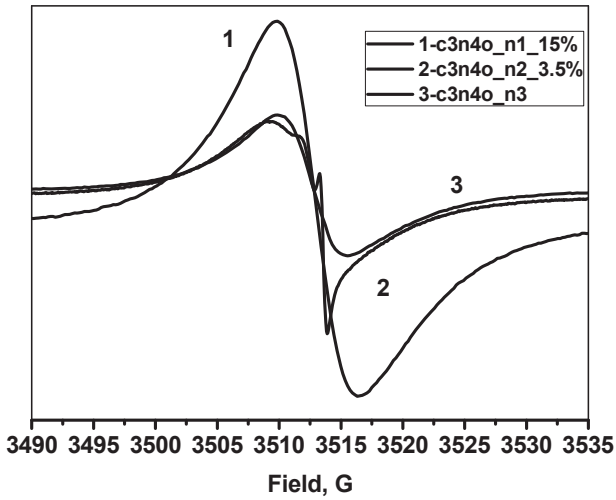

Fig. 2.8 EPR spectra of $C_3N_4O_x$ samples.

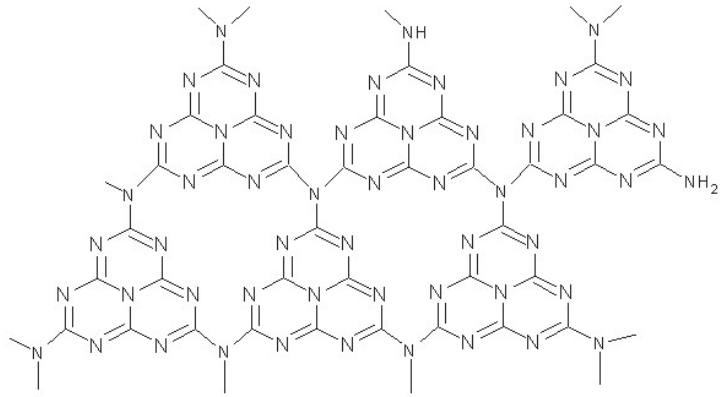

Fig. 2.9 Graphic formula fragment of the structure of carbon nitride containing surface functional groups.

Data analysis allows us to devise the basic requirements for a photocatalyst; it must be chemically and biologically inert, photocatalytically stable, cheap to manufacture, and active under the influence of sunlight. Titanium dioxide and C_3N_4 are close to ideal photocatalysts; their only drawback is a lack of activity in the visible range of solar radiation. In this regard, improving their light absorption capacity and the

photocatalytic activity of oxide materials in the near UV and visible regions of the solar spectrum is an important task.

2.3.2 Oxidative destruction of dyes with TiO_2

The photocatalytic activity of synthesized TiO_2 anatase was tested as follows:

1. The concentration of the powders was 0.160 g in 50 mL of an aqueous dye solution (0.32 %). The dye concentration in the system was 20 mg/L. The working volume was 50 ml. The glass diameter was 55 mm. The system was mixed in a magnetic stirrer in the dark to determine its capacity for adsorption.
2. The duration of powder contact with the dye was 30 min. The distance from the UV source to the working surface of the suspensions was 18 cm. The OBB15 brand lamp provided the irradiation source with a power of 15 W (UV-C 4 W). Before use in the experiments, the UV lamp was heated for 10 min.
3. We determined the photocatalytic activity of the powder according to decreasing dye concentrations in the solution.

Figure 2.10 shows changes in the optical density (D) of the initial MB solutions depending on the concentration. The maximum value of 1.32 was typical for 40 mg/L, a minimum value of 0.315 was typical for 10 mg/L, and an intermediate value of 0.670 was found for 20 mg/L. Subsequently, upon contact with TiO_2 anatase powder, MB concentrations of 20 and 40 mg/L were used.

Figure 2.11 shows the destruction of the dye (C_0 = 40 mg/L) after UV exposure for 30 and 60 min. The photoactivity of the powder increased, especially when the concentration of the powder was doubled. Within 60 min, the residual concentration of the dye decreased from 40 to 5.2 mg/L (pH 6.98; the aqueous medium was not alkaline).

With a decrease in the initial dye concentration to 20 mg/L, followed by contact with a powder weighing 0.160 g under UV irradiation (fig. 2.12), the residual dye concentration sharply decreased at 60 min. of exposure with a concentration of 1.7 mg/L.

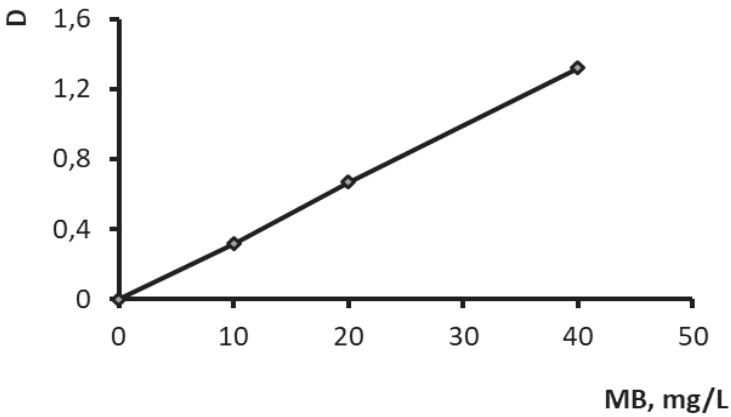

Fig. 2.10 Calibration line for MB of various concentrations.

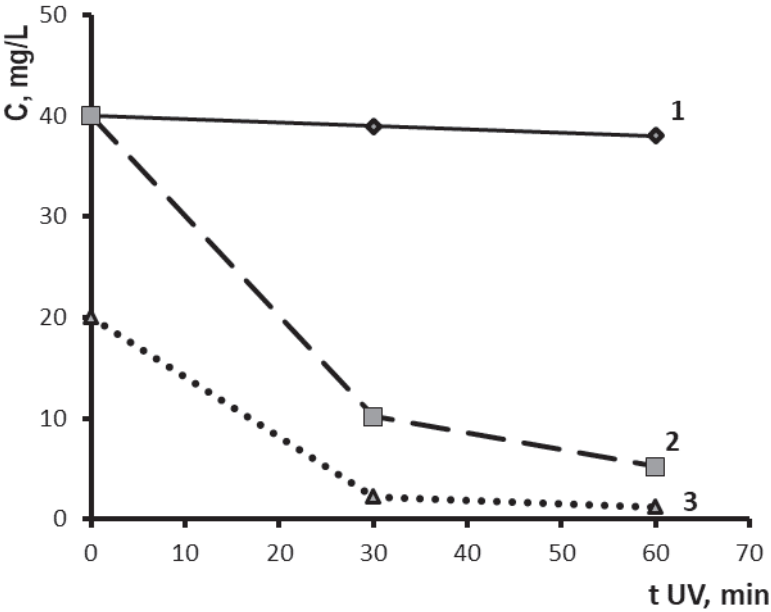

Fig. 2.11 Kinetics of MB irradiation with anatase (IPMS): 1) MB, 2)TiO_2-MB (40 mg/L), and 3) TiO_2-MB (20 mg/L).

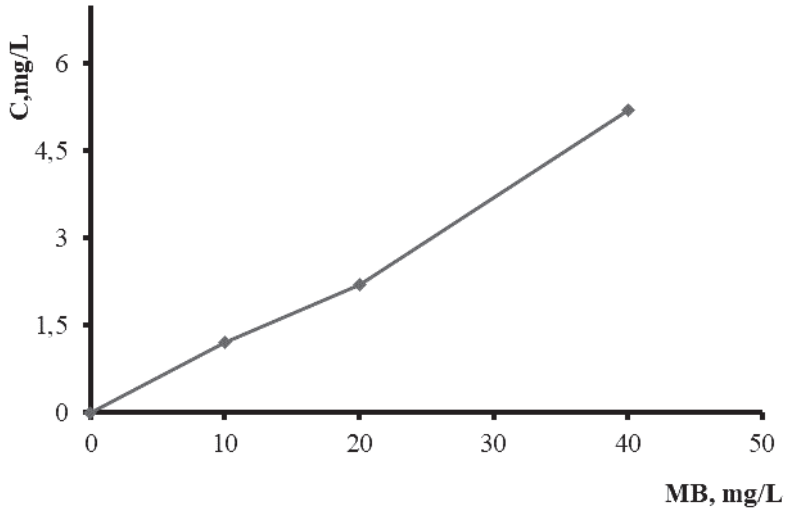

Fig. 2.12 The residual concentration of MB dye in contact with anatase nanopowder (IPMS) for 60 min. with different concentrations of the initial dye.

Figure 2.12 shows the maximum decrease of residual dye concentration after UV exposure for 60 min in the powder at maximum concentration. The process of MB destruction occurs using TiO_2 and initial MB (10–20 mg/L). The activity of TiO_2 nanodispersed anatase (IPMS) in aqueous solutions of the dye substantially depends on the surface properties of the TiO_2.

2.3.3 Nanophotocatalysis involving semiconductors of different natures

The use of nanosized TiO_2 particles leads to a significant increase in its photocatalytic activity. The advantage of nanoparticles over microparticles is the higher probability of charge release on the catalyst's surface. The separation of photogenerated charges in nano-TiO_2 proceeds quite effectively and they reach surface traps and are consumed in the UV irradiation processes (Zahornyi 2017, 56).

The number of publications on the photocatalytic activity of both pure ZnO and ZnO doped with various chemical elements (C, N, S, Co, Fe Cu, Mn, and Ag) is increasing. In particular, ZnO doped with nitrogen

exhibits 3.8 times greater photocatalytic activity than TiO_2. Carbon-doped ZnO demonstrates a water-splitting reaction and can be used to produce hydrogen as an alternative to clean solar fuel. Some publications have suggested that ZnO with a particle size of 20–25 nm and morphology of spheres and plates in the decomposition reactions of phenol, 4-aminobenzoic acid, and methylene blue exhibits the highest photoactivity. The thermal annealing of ZnO at a temperature of 650 ºC increases its photoactivity. However, the photocatalytic properties of nanosized ZnO are virtually undefined and there are no data on the photocatalytic oxidation of volatile organic compounds in air purification.

In recent years, the study of heterogeneous photocatalysis has shifted towards compounds with carbon (graphene, carbon nanotubes, and carbon nitride). A 2D-structure C_3N_4 graphene analogue was synthesized (Devthade and Kulhari 2018, 3). The authors investigated the effect of the precursor on the surface structure and photocatalytic activity of g-C_3N_4. Nanosheets synthesized by urea decomposition were found to be porous with a maximum surface area of 55 m^2/g. The rate of the degradation of the dye was 0.257 min^{-1} with irradiation in the region of 400–500 nm.

Due to its optical, conductive, and thermostable properties, C_3N_4 is a very promising material for photocatalysts. The bandgap for C_3N_4 varies depending on the conditions of synthesis and the precursors, within 2.50–2.80 eV. Its powders and films are synthesized by electrochemical methods (decomposition of acetonitrile in high electric field strengths) and chemical methods (thermal decomposition of organic compound urea, cyanuric acid). The authors used carbon nitride in the production of hydrogen from water or aqueous dye solutions under the action of visible irradiation. The use of ultra-thin non-metallic C_3N_4 nanosheets achieved a hydrogen removal rate of 189.3 μmol/h. The efficiency of hydrogen synthesis under visible-light conditions increases with the use of composites of type $W_{18}O_{49}$/ C_3N_4, $Mn_{0,8}CdO0_{,2}$/ C_3N_4. Publications and patents are being promulgated in which C_3N_4-Ag and C_3N_4-TiO_2-Ag composites are involved in photocatalysis for water purification.

It is interesting that oxide semiconductors in photocatalytic processes can act as activating additives to strengthen silicon nitride materials. For example, TiO_2 in dielectrics prevents the growth of material grains in the Si_3N_4 sintering process (Ragulya and Kryachek 2017).

The major disadvantage of pure ZnO based catalysts is the rapid recombination of charge carriers. Therefore, the usage of alloying impurities is likely to increase ZnO optical activity (Ievtushenko and Karpyna 2018).

Dopant cations can serve as traps for photogenerated charges, thereby partially suppressing unwanted recombination processes during UV irradiation. In many cases, dopant cations interfere with oxide semiconductors in the process of synthesis and stabilize low-temperature modifications of oxides (anatase).

Photocatalysis is widely used to clean the air of harmful organic pollutants. Photolysis of water and carbon dioxide recovery is another promising area of scientific and applied research. These methods only allow us to obtain fine powders and the use of powdered material in photocatalytic processes is difficult. As such, it is necessary to apply inert materials as substrates.

Nowadays, the development of advanced technology for drinking water and wastewater treatment systems is in great demand. Adenoviruses are ubiquitous in the environment and are resistant to many disinfection techniques; as a result they have emerged as a pathogen of concern. Photocatalysts produce highly oxidizing ROS that damage proteins; however, there are no published reports on the susceptibility of adenoviruses to this disinfection method. Catalyst modification increases ROS production, substrate adsorption, and solubility/dispersion stability. The mechanism of virus inactivation is useful for designing treatment systems with improved efficiency. According to the Global Antimicrobial Composite Materials Market Report, the value of this field for TiO_2, ZnO, and C was estimated to be $ 7.51 billion in 2016 and to reach $ 27.38 billion by 2022.

Analysis of the literature and our results shows that the use of TiO_2 and ZnO composites in sensor structures, solar panels, and lithium batteries is efficient due to the polymer surface area. For C_3N_4 materials, the presence of the amorphous carbon phase decreases their thermal stability and photocatalytic activity. Innovative materials based on C_3N_4 see the production of reactive oxygen species in the process of photogeneration. We propose that the physicochemical bonding of rare-earth metal oxides with C_3N_4 enhances its antimicrobial characteristics. In our opinion, doping of C_3N_4 with metals and creating nanocomposites with zinc oxide will lead to the harnessing of these materials for cancer treatment.

The HO• action generated by photocatalyst nanoparticles is efficient and effective in the inactivation of biological microorganisms. The development of an active composite photogenerator based on TiO_2 nanoparticles is thus an urgent task.

.

CHAPTER 3

PREPARATION, PHYSICOCHEMICAL PROPERTIES, AND APPLICATION OF POLYMER NANOCOMPOSITES FILLED BY OXIDE NANOPARTICLES

This chapter demonstrates the use and production of polymer composites based on polymer matrixes, oxides, and metal NPs. The methods for their preparation are generalized and the properties of the obtained materials and their possible applications described. Methods for the surface modification of nanoparticles are also presented.

Significant attention has been paid in the works of Ukrainian and foreign authors (A.V. Ragulya, V.O. Vilensky, Ya.I. Kurys, O.A. Pud, A.D. Pomogailo, L. Nicolais, Y. Chen, J.C Tang, Y. Safaei-Naeini, S. Thomas and many others) to the problems of NP synthesis and their stabilization in polymers. TiO_2, under the influence of UV radiation (in the presence of oxygen), can generate hydroxyl radicals, which can participate in the synthesis of polymeric material under photoinitiated polymerization (C. Dong, J. Wang). Under UV irradiation of thermoplastics, such as polyethylene, polystyrene, and polyvinyl chloride with TiO_2, accelerated photodestruction occurs. Wang and Fujishima described the phenomenon of super hydrophilicity of titanium dioxide nanoparticles. As such, oxide semiconductors are promising agents in polymer photochemistry that can influence the synthesis of high molecular weight products and impart several useful properties to materials. However, nanosized metal particles (Ag, Pd, and Pt) are also relevant as they can increase electrochemical activity and composite materials are promising for ampere metric sensors.

3.1 Synthesis, Molecular Structure, and Properties of C_3N_4

Carbon nitride is one of several allotropes in the carbon nitride family. This polyconjugated semiconductor, consisting of carbon and nitrogen atoms, is characterized by a layered graphite-like structure. The

fully polymerized form, having a carbon to nitrogen ratio of 0.75, is unobtainable in practise. The material contains about 1–2 % hydrogen—the amount varies depending on the method of synthesis. A number of works report that carbon nitride consists of graphite-like layers, but their relative location cannot be clearly seen (Doi: 10.14529/chem180104). Carbon nitride can be synthesized using solid-phase synthesis from cheap materials such as melamine (Devthade and Kulhari 2018). It is insoluble in most solvents and shows stability between pH 0 and pH 14. Carbon nitride has long attracted attention as a catalyst, in particular for the photocatalytic decomposition of water. Materials based on g-C_3N_4 have high activity and stability in the conversion of solar energy (Liu 2015, 6225). Graphite-like carbon nitride can be used in optoelectronics; however, its basic electronic and optical properties have not been fully explained yet and its precise crystal structure is not clear (Tay and Kanhere 2015, 14).

The history of carbon nitride dates back to 1834 when the scientist Berzelius and his staff synthesized the product and named it “melon”. It consists of C_3N_3 fragment moieties. The surface structure of g-C_3N_4, according to some works, shows that the carbon atoms are in the sp^2 hybrid state. Varied organic precursors with nitrogen content, such as melamine, urea, and dicyandiamide, are present in g-C_3N_4 synthesis.

X-ray phase analysis and solid-state NMR have confirmed the structure of two-dimensional g-C_3N_4 synthesized by the thermal condensation of organic polymers (Wang and Maeda 2009, 8). Due to the lack of long-range order in the material, it is impossible to obtain a refinement of the three-dimensional structure using the method of single-crystal X-ray diffraction. Tyborski and Mershjann (2012, 16) used the X-ray diffraction model and the entire body of data, including short-range diffuse scattering and neutron scattering, which is sensitive to hydrogen isotopes, to identify its structure. After numerous studies, they concluded that a structure consisting of heptazine rings linked through secondary amino groups is the most stable. In this chapter, the results of Shcherban N.D., Khalyavka T.A., Bondarenko M.E., Silenko P.M, and others are discussed and analyzed.

3.1.1 The nature of the precursor influences C_3N_4 surface structure and properties: Molecular structure of C_3N_4

The substitution of carbon atoms with nitrogen in the graphite structure to maintain its regularity can occur in several ways and leads to the existence of a family of similar carbon nitride compounds with different stoichiometry, in particular C_3N_4, C_3N_2, C_3N, C_5N, and $C_{10}N_3$ (Wang and

Wang 2010, 4). Carbon nitrides with different structures and compositions display high chemical and thermal stability, hardness, and semiconductor properties (Wang and Maeda 2009, 1). These characteristics determine the prospect of using carbon nitride in photocatalysis (Cao and Low 2015, 27); catalysis (Zhu and Xiao 2014); as elements of solar cells (Moto and Negro 2010); in sensors (for gases and moisture) (Lee 2008); and in water purification (Hu and Wong 2015**)**.

The presence of hydrogen in the structure of carbon nitride testifies to its incomplete condensation and the existence of surface defects (Caputo and Gross 2014, 43). It gives carbon nitride its catalytic properties, allowing it to be used in nanocomposites and in various reactions, including hydrogenation, oxidation, transesterification, Knevenagel condensation, acylation by Friedel-Crafts, Suzuki-Miyaura coupling, and Sonogashira coupling, etc.

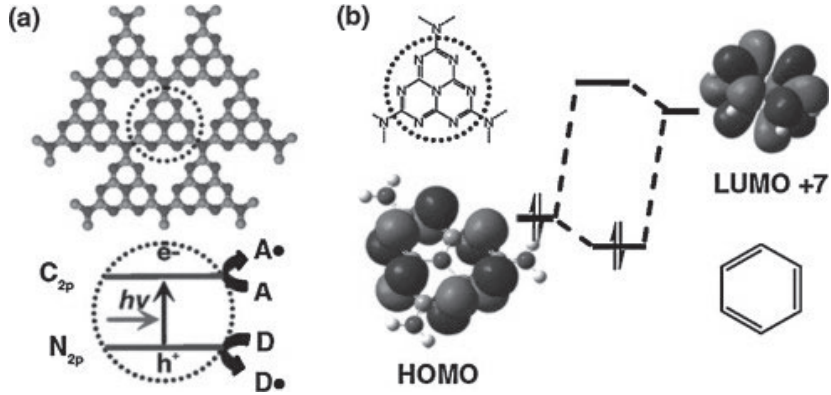

Fig. 3.1 Graphitic carbon nitride (g-C_3N_4) material-electronic structure (https://doi.org/10.1016/j.jphotochemrev.2014.04.002).

Obtaining graphitic carbon nitride involves the pyrolysis of nitrogen-rich organic compounds, during which the C–N bonds form two-dimensional three-s-triazine layers connected via tertiary nitrogen atoms (Lotsch and Schnick 2006, 18). Cyanamide is the simplest and most well-known g-C_3N_4 precursor (Zheng and Liu 2012, 5; Takanabe and Kamata 2010). Urea, thiourea, dicyandiamide, and melamine are also used to produce carbon nitride (Devthade and Kulhari 2018; Liu and Zhang 2012, 48; Zhang and Zhang 2012).

The CN precursor significantly affects the properties of the resultant g-C_3N_4, including its morphology, specific surface area, and porosity, as well as its photocatalytic and catalytic activity, due to the varying degree of material condensation obtained (Zhang and Zhang 2012). The presence of porosity in carbon nitride causes its photocatalytic activity (Dong and Zhang 2012, 22). Methods of synthesis with "soft" or "hard" templates are used in obtaining nanoporous carbon nitride from carbon materials (fig. 3.2). Hard template (exo-template or matrix) synthesis involves the use of "rigid" templates, which are stable porous structures (based on silica or zeolites, for example) (fig. 3.2b). The porous space limits the assembly of guest molecules and mesoporous materials are found in the form of rods after template removal (Yang and Zhao 2005). Thermal treatment of thiourea at 550 °C in air leads to the formation of a g-C_3N_4 layered nanostructure with curved, thin, and smooth layers (Devthade and Kulhari 2018; Dong and Sung 2012).

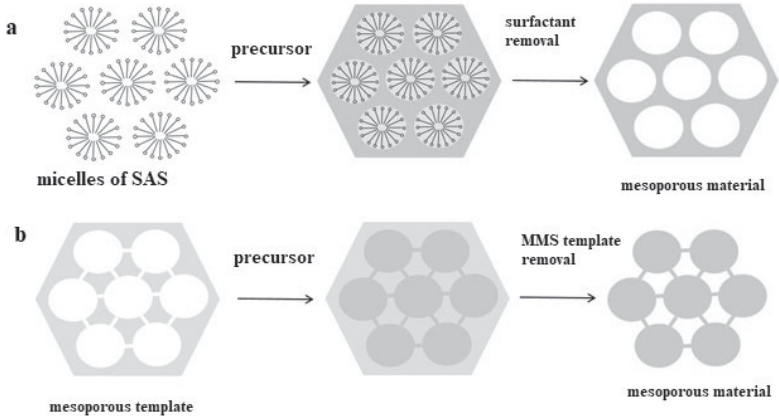

Fig. 3.2 Template synthesis schemes using "soft" (a) and "hard" (b) templates.

The materials obtained show photocatalytic activity in the decomposition reaction of the organic dye RhB under the action of visible light; this can be caused by a number of factors. Light in the visible spectrum causes excess nitrogen content (higher than that in C_3N_4) and improved charge separation due to the two-dimensional layered nanostructure.

3.1.2 The temperature of precursor decomposition

Variation in temperature of 450–650 °C for thiourea conversion in air allows the regulation of its textural characteristics (S_{BET} 10–97 m^2/g), the C/N ratio (0.66–0.78), bandgap, and the photocatalytic activity of the obtained samples of graphite carbon nitride in the reaction of hydrogen evolution (3–157 μmol/h) from water under the action of visible light (Zhang and Zhang 2012). In the obtained data, the sample with the highest values for porosity and photocatalytic activity was formed at a temperature of 650 °C. According to the authors, this may have been caused by the partial decomposition of *in situ* material accompanied by the generation of a porous structure in the bulk substance of C_3N_4. Note that the synthesized samples did not contain sulfur atoms in their composition and, according to the authors, sulfur-containing particles play a role in accelerating the polymerization/condensation processes.

g-C_3N_4 can be obtained from urea polymerization in air without using templates. Due to its better developed surface (~70 m^2/g), the synthesized material exhibits higher activity in the photocatalytic reaction of hydrogen release from water (~47 μmol H_2/h •g) in the presence of triethanolamine. Carbon nitride is then obtained from thiourea (15 μmol H_2/h•g; S_{BET} 11 m^2/g) and dicyanamide (21 μmol H_2/h•g; S_{BET} 12 m^2/g). The high photocatalytic activity of carbon nitride synthesized from urea (C/N = 0.72) is due to the higher C–O bond energy (358 kJ/mol) compared to C–S (272 kJ/mol) (Zhang and Liu 2012, 17).

Variation in urea pyrolysis (without templates) was used to adjust crystallinity, the parameters of the porous structure (S_{BET} from 31 to 288 m^2/g), and the bandgap (2.68–2.78 eV) of graphite-formed carbon nitride (Dong and Wang 2013). The obtained g-C_3N_4 showed high activity in photocatalytic reactions with nitrogen monoxide removal (conversion to 32 %) under the action of visible light. This was due to a slightly increased bandgap (2.78 eV) and the most developed surface (288 m^2/g), formed by the reduction of the layer thickness.

Nanoporous g-C_3N_4 (V_{por} up to 0.26 cm^3/g, S_{BET} up to 300 m^2/g, D_{por} from 3.1 to 5.6 nm) was also obtained with a soft template and using dicyanamide as an organic precursor, non-ionic and amphiphilic block copolymers (P123, F127, Triton X-100, Brij30, Brij58, and Brij76), as well as ionic liquids and structural directing agents (Wang and Wang 2010, 4). To suppress the processes of sublimation of volatile intermediates formed by the addition of a surfactant in the reaction mixture, stepwise pyrolysis was performed withholding the initial mixtures at intermediate temperatures (350–400 °C). The molar ratio of C/N in the obtained samples (in particular, 0.82–2.06 when using P123)

deviated from the theoretical value for graphite-like C_3N_4 (0.75) due to the inclusion of carbon fragments of organic templates in the synthesis process.

Carbon nitride with a bimodal mesoporous structure (D_{por} 3.8 and 10–40 nm) was obtained using the polymerization method and subsequent carbonization of reaction mixtures containing melamine and glutaraldehyde as reagents, as well as Triton X-100 as a soft template (Zhou and Hua 2011, 4).

The presence of a weak van der Waals interaction between g-C_3N_4 layers allowed the obtaining of graphene-like carbon nitride nanosheets due to thermal oxidation (500 °C, in air) of the bulk substance previously synthesized from dicyanamide (Niu and Zhang 2012, 22). The formed material had a large specific surface area (306 m^2/g), a small thickness of the layer (approximately 2 nm), and an increased bandgap (by 0.2 eV) with an increased value of the life of the charge carriers due to the quantum size effect.

Yang and Gong (2013, 17) describe carbon nitride synthesis. The obtained material exhibited high activity in the photocatalytic hydrogen reaction (93 μmol/ h•g vs. 10 μmol /h•g for the initial bulk sample) from water under the action of visible irradiation due to its small monolayer thickness (~2 nm). The developed surface (384 m^2/g), stoichiometric ratio N/C, and optimum bandgap (2.65 eV) of the material led to charge transfer intensification.

Relatively mild heat treatment (100 °C) of graphite-like volumetric carbon nitride in aqueous tetraethylammonium hydroxide solutions allows the obtaining of stable colloids containing g-C_3N_4 particles of medium size, 30–50 nm, and a thickness of 0.3–0.4 nm (Panasiuk and Raevskaya 2015).

Colloids of g-C_3N_4 are characterized by intense photoluminescence with a maximum at 460–470 nm and a quantum yield of 45–50 %. The bandgap E_g of colloidal particles of carbon nitride significantly exceeds the bulk material (3.45 and 2.82 eV) due to the spatial limitation of the charge carriers (Panasyuk and Raevskaya 2014, 5). Increasing the temperature during synthesis of g-C_3N_4 decreases the intensity of photoluminescence until it disappeared completely for samples obtained at temperatures above 675 °C. In the case of stratified carbon nitride, the intensity of photoluminescence increases sharply with an increase in the reaction temperature, which may be caused by a reduction in the size of g-C_3N_4 colloidal particles, as well as the removal of peroxide groups from the surface of the bulk material during exfoliation (Panasyuk and Raevskaya 2015).

Graphite C_3N_4 can also be obtained in the process of thermal condensation of ammonium thiocyanate, which is accompanied by the release of ammonia and hydrogen sulfide and contributes to the formation of a structure with optimal composition (C/N (at.) = 0.76) (Cui and Zhang 2011, 34). Performing NH_4SCN polymerization under matrix synthesis conditions (with hard templates: Ludox HS40 and SBA-15 nanosized silica) leads to the formation of spatially ordered carbon nitride, characterized by a developed surface (S_{BET} up to ~190 m^2/g) and large volume (up to 0.8 cm^3/g) with mesopores (D_{por} from 5 to 14 nm). Compared to the bulk material, the obtained porous carbon nitride is characterized by increased photocatalytic activity and stability of the reaction in the evolution of hydrogen from water under the action of visible irradiation (~220 versus 58 μmol H_2 /h•g).

Urea polymerization in the melamine sponge pores leads to the formation of three-dimensional macroscopic porous monoliths consisting of 2D porous nanowires of graphite carbon nitride (Liang and Li 2015, 31). Due to the more advanced porosity (S_{BET} 78 m^2/g, V_{por} 0.76 cm^3/g), increased light absorption in the visible region, and improved charge separation, the obtained materials exhibit high photocatalytic activity in the reaction of hydrogen evolution from water (up to 29 μmol H_2 /h•g) compared to bulk samples.

Thermal condensation of cyanamide in the channels of anodic aluminium oxide allows us to obtain oriented carbon nanotubes, which are characterized by an increased degree of crystallinity compared to the bulk sample, as well as increased photocatalytic activity in the decomposition of water under visible light (Li and Zhang 2011, 19).

Highly ordered mesoporous carbon nitride (V_{por} 0.67 cm^3/g, D_{mezo} 3.8 nm, S_{BET} 645 m^2/g) with a high nitrogen content (C_4N_2) was obtained using the matrix method with ethylenediamine and CCl_4 as organic precursors and a silica matrix (Jin and Balasubramanian 2009, 42). The carbon nitride formed had monodispersed particles (smaller than 150 nm) and indicated the replication of the original matrix, which consists of ultrafine mesoporous silica nanoparticles. The resulting carbon nitride has demonstrated the promise of using a metal-free base catalyst in the trans-esterification reaction of β-ketoesters with various alcohols (butanol, hexanol, octanol, cyclohexanol, benzyl, and furfuryl alcohols) with 100 % conversion with alcohol.

Hierarchical mesoporous spheres of carbon nitride obtained by the matrix method were found in MCF mesoporous silica (Jin and Yang 2010, 3). The obtained materials were characterized by spherical morphology (particle size of 4 μm), hierarchical mesostructure (pores of size 4 and 43

nm), and high specific surface areas (550 m^2/g) and volume of pores (0.9 cm^3/g). The synthesized materials showed an adsorption capacity for carbon dioxide of 2.9 mmol/g at 25 °C and 0.97 mmol/g at 75 °C.

To produce a partially oxidized product, Bondarenko M., Gubareni N., Silenko P., Zahornyi M. et al. (IPMS depart. 58, 48) carried out the pyrolysis of melamine in the presence of a fixed volume of air (http://dx.doi.org/10.1016/j.diamond.2015.11.006). Melamine was place in a ceramic crucible during experiments on the preparation of a formulaic (g-C_3N_4) composition carbon nitride from melamine. The obtained product was tested using SEM (MIRA3 TESCAN).

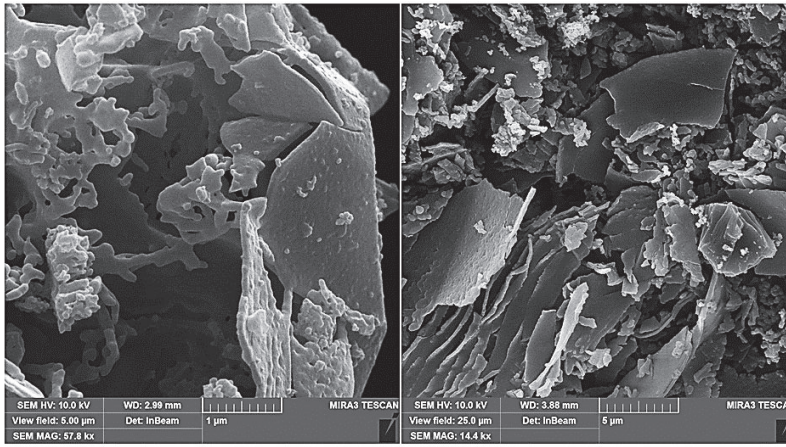

Fig. 3.3 Morphology of synthesized $C_3N_4O_x$.

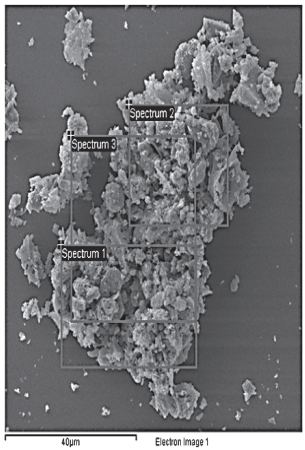

Processing option : All elements analysed EDAX (Normalised)

Spectrum	In stats.	C	N	O
Spectrum 1	Yes	39.21	50.37	10.42
Spectrum 2	Yes	40.49	53.15	6.36
Spectrum 3	Yes	40.62	52.56	6.82
Mean		40.11	52.03	7.87
Std. deviation		0.78	1.47	2.22
Max.		40.62	53.15	10.42
Min.		39.21	50.37	6.36

All results in mass.%

Electron micrographs of the samples were recorded on a MIRA3 TESCAN scanning electron microscope. Powders of 10 mg were applied with polished Si plates (5 × 5 mm), followed by spraying 15 minutes with thickness gold 30 nm.

Fig. 3.4 Analysis of synthesized $C_3N_4O_x$.

The results in fig. 3.3 and 3.4 show pore particles with oxygen content of 6–7 wt%. A new way of g-C_3N_4 sample preparation with oxygen-containing carbon nitride was performed. A new substance (g-C_3N_4)-O and carbon nitride O-g-C_3N_4 doped by oxygen were obtained through melamine pyrolysis in the presence of oxygen. The resultant (g-C_3N_4)-O is the analog structure of both carbon nitride and graphite oxide.

The composite photocatalytic materials (C_3N_4/TiO_2) have high photocatalytic activity (Zhong and Zhang 2019, 1; Lei and Chen 2019). Fe_2O_3/g-C_3N_4 composites with different iron oxide (III) content (2.8–11.6 wt%) were obtained by heating a mixture of melamine and ferric chloride hexahydrate at 500–520 °C (Zhang and Guo 2013). The synthesized materials exhibited high activity in photocatalytic rhodamine B decomposition. This was due to the synergistic effect of the nanostructure components. Fe_2O_3 particles act as electron traps and improve the separation of photogenerated electron-hole pairs under UV action.

The deposition of an O-g-C_3N_4 layer on the surface of anatase and rutile nanoparticles was performed using the method developed in IPMS (Bondarenko and Silenko 2019). O-g-C_3N_4/TiO_2 (anatase phase) samples of pale yellow color were obtained by melamine heat treatment at 540–580 °C for 0.5–1.5 h. We studied the morphology of the obtained O-g-C_3N_4/TiO_2. SEM micrographs of the O-g-C_3N_4/TiO_2 (anatase) composite nanoparticles (fig. 3.5) show the arrangement of TiO_2 in the form of

separated nanoparticles and clusters between the plates and in the channels of the O-g-C_3N_4 scaly plates.

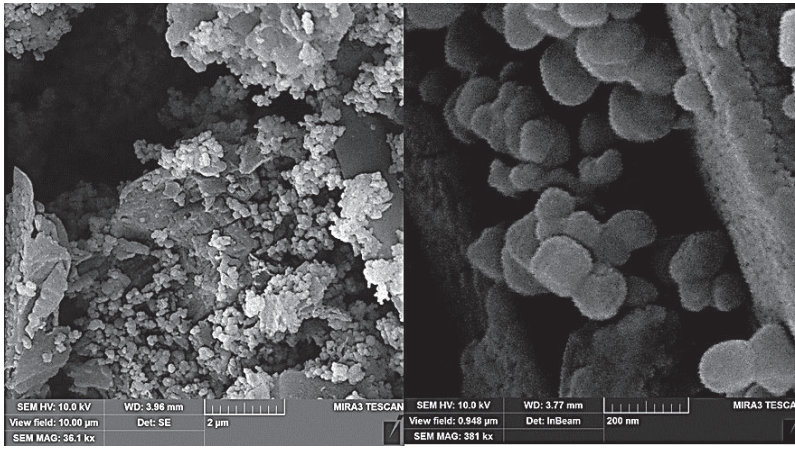

Fig. 3.5 Morphology of synthesized $C_3N_4O_x/TiO_2$.

Photochemical CO_2 recovery is a promising method for the conversion of solar energy. Once put into production, this process will simultaneously produce organic compounds and reduce CO_2 in the atmosphere. The synthesis of organic compounds from carbon dioxide in the presence of semiconductor materials and composites has been intensively studied (Park and Choi 2012, 22; Mori and Yamashita 2012, 2). In this respect, C_3N_4 is a promising photocatalyst and has attracted considerable attention (Zhao and Sun 2015, 7).

The decomposition of water in the presence of g-C_3N_4 during irradiation of the reaction mixture with visible light is a possible method for hydrogen production. The structure of the energy levels of carbon nitride, characterized by the potentials of the conduction band and the valence band at -1.3 eV and +1.4 eV respectively (Niu and Yang 2014, 74), makes it possible to achieve carbon dioxide recovery ($CO_2 + 2H^+ + 2e^- \rightarrow CO + H_2O$, $E^0 = -0.53$ V; $CO_2 + 6H^+ + 6e^- \rightarrow CH_3OH + H_2O$, $E^0 = -0.38$ V; $CO_2 + 8H^+ + 8e^- \rightarrow CH_4 + 2H_2O$, $E^0 = -0.24$ V), and the oxidation of water ($2H_2O + 4h^+ \rightarrow O_2 + 4H^+$, $E^0 = +0.82$ V).

As such, some studies (table 3.1) have shown the possibility of reducing carbon dioxide by irradiation in the presence of carbon nitride and various reducing agents to CO, CH_4, acetaldehyde, methanol, ethanol, and formic acid. However, the activity of C_3N_4 in the photoreduction of

CO_2 to organic products is low. Intensive studies have been undertaken to improve the efficiency of the transformation of carbon dioxide under the action of light by creating composites based on carbon nitride, such as metal-semiconductor structures, hybrid systems with metal-organic complexes, and organic acids.

The efficiency of many photocatalytic processes involving C_3N_4 nanoparticles is low due to their specific surface areas (Zhang and Liu 2012, 5). Therefore, the development of template synthesis methods of porous carbon nitride with developed surfaces is an urgent task.

Table 3.1 Scientists currently working on the synthesis of photocatalyticaly active systems of C_3N_4

Year	Journal	Lead Author	Cod Doi
2016	Theoretical and Experimental Chemistry	**Khalyavka T. A.**	10.1007/s11237-016-9472-8
2016	J. Ind. Eng. Chem ChemistrySelect	**Shcherban N. D.**	10.1002/slct.201601283
2018	*Him. Fiz. Tehnol. Poverhni*	**Bondarenko M.E.**	10.15407/hftp09.04.393
2016	*Solid State Chemistry*		10.1016/j.jssc.2016.06.003
2019		**Yuanzhi Hong**	10.1016/j.ijhydene.2019.01.274
2019	Advanced Powder Technology	**Mitra Mousavi**	10.1016/j.apt.2018.12.003

3.1.3 Catalysis of C_3N_4 systems

The surface structural defects of carbon nitride can act as active centres, and provide the possibility of additional chemical modification of the material surface for the structure regulation of catalytically active systems, as well as for performing heterogeneous catalytic reactions. Furthermore, the deposition of metal nanoparticles, in particular noble ones, on graphitic carbon nitride increases the Schottky barrier, which in turn contributes to a better separation of charges at the boundary of the

metal-semiconductor heterojunction (Zhao and Dai 2014, 10). Therefore, g-C_3N_4 acts as an "active" carrier of metal nanoparticles, contributing to an increase in catalytic activity and catalyst selectivity.

Mesostructured carbon nitride, obtained by the matrix method using urea and formaldehyde as carbon and nitrogen sources, as well as mesoporous silica (INC-2) with hexagonal symmetry as a hard template, exhibits high catalytic activity in cyclic reactions) with hydrogen peroxide; in particular, the conversion of cyclic olefins is 65–80 % and the epoxy selectivity is 40–90 % (Min and Ansari 2013, 204). The catalytic properties of the obtained samples are explained by the presence of surface oxygen-containing groups involved in the formation of intermediate peroxy radicals, which are subsequently converted into cyclic olefin peroxides.

Microporous carbon nitride is a catalyst for the Knevenagel condensation reaction between aldehydes and nitriles of different products. The catalytic activity of the obtained materials is due to the presence of nitrogen-containing groups, which act as Lewis centres. According to the proposed reaction mechanism, the N-containing base centre attaches a proton of the active methylene group of the original nitrile to form a protonated centre and a corresponding anion. The carbonyl atom of the starting aldehyde is then subjected to a nucleophilic attack by a pre-generated anion to form an oxyanion (Ansari and Min 2011, 13). The catalytic activity of obtained non-stoichiometric carbon nitride materials correlates well with the N/C ratio on the surface (calculated based on the RFES profiles) and not with the overall N/C ratio, including the corresponding groups in the bulk of the substance. The catalytic activity of the synthesized carbon nitride samples in the Knevenagel reaction exceeds that of other materials, in particular organometallic scaffolds, nitrogen-containing MSM-48, and graphite-like carbon nitride.

In work presented by Gang and Meng, the photocatalytic activity of g-C_3N_4 was examined in a Pyrex glass cylindrical reactor with a diameter of 50 mm and an effective volume of 100 mL. Phe MB photodegradation was performed using a 300 Xe lamp. After an interval of an hour, 2mL of suspension was removed and the concentration of MB was analysed using a UV-visible spectrophotometer at 648 nm (http://dx.doi.org/10.1155/2013/187912).

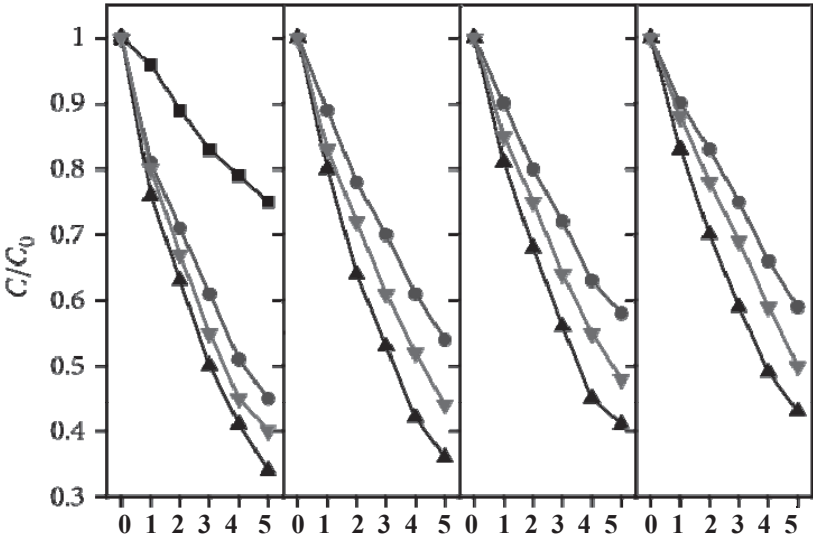

Fig. 3.6 Photodegradation of MB over the g-C_3N_4.

The photocatalytic activities of the samples for MB photodegradation were evaluated under visible light irradiation, as shown in fig. 3.6. A blank experiment (dark points, without catalyst) was used for comparison. The results showed photodegradation of 25, 55, 66, and 60 % of MB after 5 h irradiation for the blank, C_3N_4/C, C_3N_4/D, and C_3N_4/M. The average values of the C/N molar ratio were 0.671, 0.685, and 0.676 for all cases, which is lower than the theoretical value of 0.75, and the surface termination was affected by uncondensed amino functions due to defects.

The possible photodegradation mechanism of dye over the g-C_3N_4 semiconductor is discussed further. With UV spectra, the bandgap of the graphitic carbon nitride is estimated to be 2.6 eV. The optical gap is attributed to the transactions between weakly localized states of π-π^* states that come from the sp^2 configuration atoms in the network. Indeed, according to Wang, the wave function of the valence band is a combination of HOMO levels of the melem monomer, which are derived from nitrogen p_z orbitals. As such, the conduction band can be similarly connected to the LUMO of the melem monomer, which predominantly consists of carbon orbitals. Photoexcitation leads to spatial charge separation between the electron in the conductive band and the hole in the valence band. Thus, nitrogen atoms are the preferred oxidation states, whereas carbon atoms provide the reduction sites.

Under light irradiation, some active species, such as (•OH), superoxide (O_2• or HOO•), and holes, are formed during the reaction of photodegradation. In aqueous solutions, •OH, as the primary oxidant, is generated via direct hole oxidation or the photogenerated electron-induced multistep reduction of O_2 (O_2+e−=O_2•, O_2• + e− + 2H+= H_2O_2, H_2O_2+ e−= •OH + OH−).

In addition, a photogenerated hole can directly react with organic compounds if the semiconductor photocatalyst has moderate redox potential. For C_3N_4, the photogenerated holes are not an effective active species during degradation of MO over g-C_3N_4. The oxidation level for water splitting is located slightly above the valence band of C_3N_4, which would permit hole transfer, but with a low driving force. The authors suggest that this low driving force is not beneficial for hole reactions in aqueous solution systems.

In the other case, hydroxyl radical reactions are non-selective and will virtually react with almost all organic compounds by H-atom abstraction, direct electron transfer, or insertion. •OH is a reactive oxidant that can promote the complete mineralization of MB. Furthermore, the oxidation potential of holes generated in C_3N_4 is insufficiently high to directly oxidize OH to hydroxyl radicals generated by the multiple electron (in the conduction band) transfer process in the oxygen reduction reaction (ORR).

The C/N molar ratio and the degree of condensation are consistent with photocatalytic activity. This low photocatalytic activity is due to weak localized states of C_3N_4 that come from incomplete condensation. According to Alibart et al., the optical gap is attributable to the transitions between weakly localized states of π-$\pi*$ that come from the sp^2 configuration of atoms in the network. The states form valence and conduction band edges and control the width of the optical gap; π-bonding at Csp^2 sites favours the clustering of aromatic rings into graphitic sheets. This clustering dominates the π-component of the valence band edge, in optical absorption, and the filled states are excited to empty antibonding states.

Devthade, Kulhari, and Umare are currently studying the synthesis of graphitic carbon nitride (g-C_3N_4) photocatalysts through the thermal condensation of various nitrogen-rich precursors and their photocatalytic performance in relation to visible light-induced degradation of Acid Violet 7 dye (AV 7). To understand the effect of precursors on the degree of tri-s-triazine ring condensation and its electronic properties, we used different N-rich monomers (e.g. melamine (m), urea (u) and thiourea (t)), and their combinations. The structural, morphological, and optical properties of the prepared samples were characterized by powder XRD, SEM, and UV-

DRS. The photocatalytic degradation of AV 7 (20 mg/L) under visible light irradiation over various g-C_3N_4 samples saw substantial differences in photocatalytic activity, which can be attributed to altered electronic structures and increased surface area. The photocatalytic activity for the degradation of AV 7 follows the order: ug-C_3N_4 > tug-C_3N_4 > mug-C_3N_4 > mtug-C_3N_4 > mg-C_3N_4 > mtg-C_3N_4 > tg-C_3N_4 (https://doi.org/10.1016/j.matpr.2017.10.045).

Degradation experiments have been performed in previous research. In brief, a lab-made photo-irradiator was fitted with compact fluorescent lamps (12 lamps of 100 watts each, Oreva) vertically and equidistantly on the base of a rectangular galvanized iron chamber with air circulation to minimize the heating effect. The radiation of these lamps is primarily visible light along with a very small amount of UV light (~3 %). For each photocatalytic experiment, 100 mL of aqueous AV 7 (20 mg L-1) solution was placed in a beaker containing 0.1 g of the catalyst under ambient conditions. Before irradiation, the reaction mixture was magnetically stirred in the dark for 30 min. to ensure uniform dispersion and an adsorption-desorption equilibrium between the dye molecules and the surface of the catalyst. The photocatalytic activity was measured by taking a small volume of clear supernatant liquid from the reaction mixture at regular intervals of time, which was centrifuged and analysed using a UV-visible spectrophotometer (Shimadzu, UV-1800) at λ_{max} = 523 nm. The concentration of the solution remained unchanged when it was irradiated without the catalyst and in a dark control experiment.

The graphitic structure of g-C_3N_4 was confirmed by powder X-ray diffraction (XRD) analysis. The XRD patterns of all the samples derived from different precursors and their combinations displayed a characteristic diffraction peak at $2\theta = 27.4°$, corresponding to hkl (002) reflection of a tri-s-triazine ring of g-C_3N_4. Except for the melamine-derived g-C_3N_4, all the other samples showed a deviation in (002) peak position, suggesting variation in their crystal structures. The absence of (001) lattice reflection at $2\theta = 13.2°$ in all the prepared samples indicated the long-range ordering of atomic arrangements. The crystallite size of g-C_3N_4 was calculated using the Scherrer formula $D = K\lambda/\beta\cos\theta$, where D is the crystallite size (nm), K is the Scherrer constant (approximately 0.9), λ is the wavelength of Cu-K_α radiation (0.15418 nm), and β is the full width of (002) the crystallite peak at half maximum. The calculated crystallite size of g-C_3N_4 samples derived from different precursors is given in table 3.2.

Table 3.2 The crystallite sizes of different g-C_3N_4 samples computed by the Scherrer formula

Entry	Composition	Peak of crystallite	Peak Position(2θ°)	FWHM (β)	Crystallite size (nm)
1	mg-C_3N_4	(002)	27.56	0.892	9.18
2	ug-C_3N_4	(002)	26.92	0.975	8.39
3	tg-C_3N_4	(002)	26.73	0.928	8.81
4	mug-C_3N_4	(002)	27.03	0.816	10.02
5	tug-C_3N_4	(002)	27.03	0.846	9.67
6	mtg-C_3N_4	(002)	27.07	0.874	9.36
7	mtug-C_3N_4	(002)	27.16	0.851	9.61

The photocatalytic performance of g-C_3N_4 samples were tested for the degradation of AV 7 dye (20 mg/L) under visible light irradiation. The photodegradation ability of consecutive g-C_3N_4 samples obtained from the pyrolysis of various combinations of precursors exhibited differences in AV 7 degradation performance. The g-C_3N_4 derived from thiourea, melamine, melamine-thiourea, and melamine-urea thiourea mixtures showed poor photoactivity due to the rapid recombination of charge carriers, low light-harvesting capacity, low surface, and reduced surface sulfate as an adsorption-rendering site. However, g-C_3N_4 obtained from melamine, urea, and thiourea showed moderate degradation efficiencies. To our delight, urea-derived g-C_3N_4 displayed excellent degradation kinetics with 100 % degradation of AV 7 within 30 min. of visible-light exposure. The high photocatalytic performance of *u*g-C_3N_4 is due to its high surface area (55 $m^2 g^{-1}$) and high aspect ratio. The control experiment of AV 7 photolysis under light/dark irradiation with and without photocatalyst showed negligible photolysis of dye and hence confirmed the photodegradation process with the g-C_3N_4 photocatalyst; *u*g-C_3N_4 showed a much higher rate than all other samples (fig. 3.7b). Moreover, *u*g-C_3N_4 has a high surface area and moderate porosity even without the use of external templating agents such as SiO_2. These results suggest that urea should be preferred as a precursor for the synthesis of a highly efficient metal-free g-C_3N_4 base material with a wide variety of photocatalytic applications.

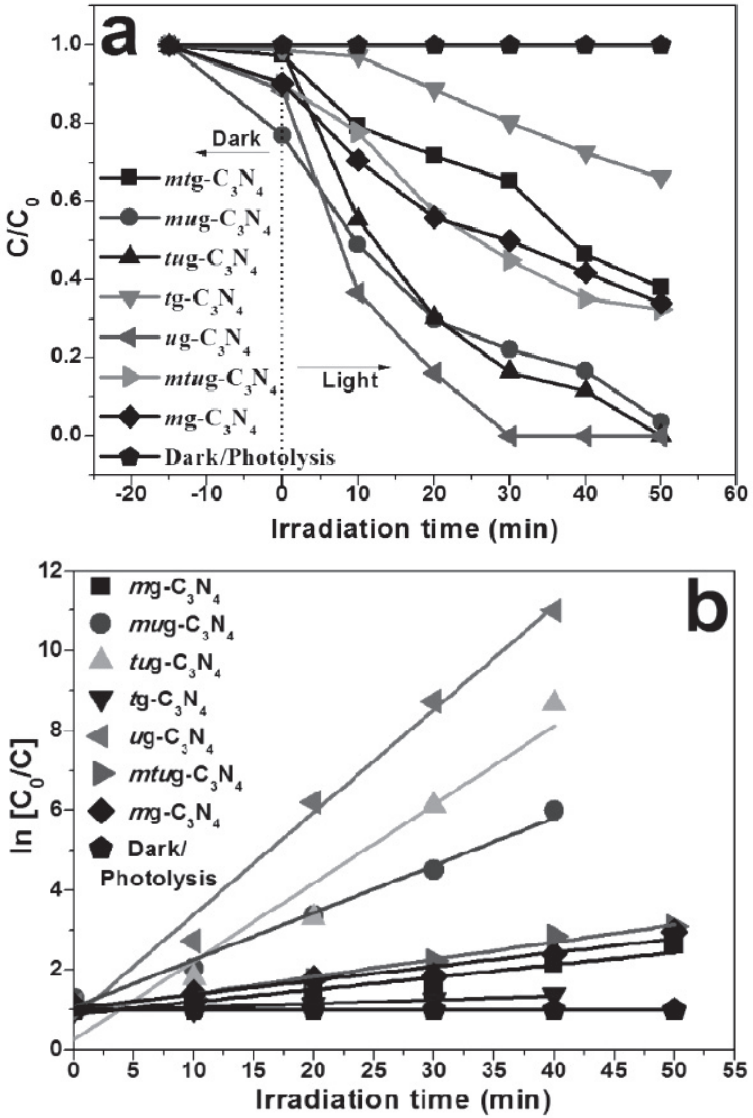

Fig. 3.7. (a) Photocatalytic degradation of AV 7 under visible light irradiation and (b) rate kinetics over g-C_3N_4 samples derived from different precursors.

In summary, different combinations of g-C_3N_4 samples were prepared by facile condensation of various nitrogen-rich precursors and their corresponding mixtures. All the obtained samples had a graphitic carbon structure, which was confirmed by characterization techniques. The photoactivity of the samples was assessed in terms of the photodegradation of AV 7. Differences in the rate of photodegradation were due to structural defects, low surface areas, and the rapid recombination of charge carriers. The *u*g-C_3N_4 samples exhibited better photodegradation performance than all the others due to its high specific surface area and carbon to nitrogen aspect ratio. Furthermore, g-C_3N_4 obtained from pyrolysis of thiourea and its complex mixture has negative photocatalytic performance, suggesting thiourea is unsuitable for the synthesis of bulk g-C_3N_4. Current study into the role of precursors reveals that an eco-friendly urea precursor is most suitable for efficiently obtaining bulk g-C_3N_4 photocatalyst.

C_3N_4 material has an amorphous carbon phase, which reduces its thermal stability and photocatalytic activity. Innovative materials based on $C_3N_4O_x$ during irradiation give reactive oxygen species in the process of photogeneration, increasing the concentration of hydroxyl radicals and enhancing their antimicrobial properties. We propose that the physicochemical bonding of rare-earth metal oxides with $C_3N_4O_x$ also enhances their antimicrobial characteristics. In our opinion, doping with $C_3N_4O_x$ metals and creating nanocomposites with zinc oxide will allow the use of these materials for the treatment of cancer.

The use of strong •OH from oxide nanoparticles causes mechanical damage and inactivation of biological microorganisms in aqueous and aerial media. The development of an active composite photogenerator based on TiO_2, ZnO, and $C_3N_4O_x$ nanoparticles is thus an urgent task.

3.2 Progress in the Preparation and Application of Polyaniline

This chapter considers the extensive class of nanostructured polymers in the form of polyaniline (PANI), methods of obtaining it and its numerous applications. Attention is devoted to the most stable form, emeraldine, which exists in both conducting and non-conducting states. The research describes the obtaining of self-organized PANI nanoparticles, PANI prepared by the chemical oxidation method, and the effect of different dopants and oxidizers. PANI is a sensitizer, depending on the nature of the dopant, and a strong oxidizer. We show that PANI synthesized in an acid medium is a photocatalyst for the oxidative destruction of dyes at

pH >7. This chapter has been written using the results of the authors' research and also summarizes the results of numerous foreign researchers.

The chemistry and physics of polymers, with a recent combined term of "the science of polymers", have now become an independent and high level branch of science. The chemistry of conductive polymers (CP) is now a rapidly developing direction and Nobel Prizes have been awarded for scientific developments in this direction. Paul De Gene received the award for the theory of liquid molecular crystals in 1999, while Allen Higher, Alan McDiarmid, and Hideki Shirakawa were awared the prize for their work on polyacetylene, polypyrrole, and polyaniline (Bhadra and Khastgir 2009, 8).

These polymers have a unique combination of properties: their conductivity in the process of doping varies between $10^{-9} \div 1000$ S/cm; they have inherent paramagnetism (the presence of unpaired electrons in the polymer chain), electrochromism, and other valuable properties (Stejskal and Gilbert 2002, 5; Stejskal and Sapurina 2010, 12). Today, research is opening up broad perspectives for the creation of various devices and technologies using CP. At Linkoping University (Sweden), scientists have managed to create a microrobot, with dimensions of 670 × 170 × 240 μm. Its small size allows it and its analogues to function in electrically conductive body fluids, such as blood. Such robots can replace the laboratory and perform tests directly in the liquid media of the human body (Nikolaeva 2002, 12; Tomczhykova and Plonska-Brzezinska 2019, 2).

This means that scientists have entered the stage of creating model devices. The chemistry of CP and its compounds will give the world fundamentally new industrial catalytic and optoelectronic systems—nanocomposites (Li and Zhao 2013, 1). Among the conducting polymers, polyaniline (PANI) is distinguished because of its wide range of properties, allowing it to be used in numerous applications and in a variety of materials and devices. Furthermore, the monomer is cheap, readily available and its methods of synthesis are simple and varied (Ko and Do 2014, 4). Interest has also grown in studying the properties of PANI with other components of different natures. It can be obtained directly through the oxidative polymerization of aniline in an acidic medium (Masters and Sun 1991, 1-2). The conductivity of the emeraldine salt obtained through the polymerization of aniline under the influence of ammonium persulfate in hydrochloric acid, the procedure recommended by IUPAC, is 5 S/cm (Stejskal and Gilbert 2002, 5). The deprotonation of an emeraldine salt in an ammonia solution, for example, leads to the formation of a non-conducting emeraldine base. The deprotonation process is reversible and

treating the emeraldine base with protic acids leads to the formation of an emeraldine salt. The protonation of amine groups is possible in strongly acidic media. As such, at pH 0, PANI contains 14 % protonated amine groups and 32 % imine groups (Ray and Richter 1989, 1). An early paper described the process of treating a solution of the emeraldine base in formic acid with strong oxidizing agents (Green and Woodhead 1910). The authors of that paper did not manage to separate the substance into its individual form due to its instability during drying. One of the first successful attempts to obtain a base of pernigraniline in the form of a powder or film is described in MacDiarmid and Manohar (1991, 1-2) where the emeraldine base was oxidized with m-chloroperbenzoic acid in a mixture of N-methyl pyrrolidone and glacial acetic acid. When the base of emeraldine reacts with reducing agents, for example with phenylhydrazine or ascorbic acid, a leucoemeraldine base is formed, which is unstable in air due to oxidation (Green and Woodhead 1910).

The influence of the component concentration on the kinetics of polyaniline synthesis and its structure and properties, is the purpose of the study. A promising direction is the creation of sensors based on PANI for the determination of ascorbic acid in solution.

3.2.1 Molecular structure of polyaniline

PANI is representative of the class of organic high-molecular-weight polymers. The polymer is used in shielding electromagnetic radiation and protecting metals from corrosion, as well as in medicine and for catalysis. Various electronic devices have been developed using PANI, including sensors, actuators, fuel and energy-saving elements, solar batteries, and electrochromic compounds (Khan and Ravi Kant 2016, 33). In these devices, the PANI is used as a thin layer on a carrier. The thickness of the layers is submicron and nanosized. Depending on the type of device, the layer of organic semiconductors is combined with different materials and have different morphologies (Asaka and Qkuzaki 2019). As such, layers in sensors and catalyst carriers should have developed a highly permeable structure with a large specific surface area. For application in electrochromic devices or light-emitting diodes, it is necessary to obtain dense and uniform layers of strictly regulated thickness (Patni and Jain 2017).

The development of technologies for depositing polymer layers with controlled thickness and predetermined morphology on various types of media is currently underway. PANI, like other conductive polymers, belongs to the category of non-processing materials. The polymer is non-

melting and the traditional technology of applying layers from solution is not applicable. Currently, polymer films are produced from colloidal forms of PANI. The creation of new electronic devices and their miniaturization requires new nanostructured materials. We need new materials for the creation of electronic devices characterized by low density, flexibility, low cost, and no toxicity. Electronic devices based on these materials can be used for identification markers in supermarkets and can be "embedded" in clothing or applied to the skin. At the heart of such devices lies a new class of semiconductor materials, called molecular or organic semiconductors, including both low-molecular weight organic compounds and polymers.

Electronic conductivity in organic materials occurs due to the presence of conjugated π-electron bonds in the molecule and the regular organization of such molecules in a macroscopic sample. As inorganic semiconductors, organic materials change their properties under the effects of heat and light and the action of weak electric fields. As such, they can play the role of a trigger—the main functional element of electronics (Krinichnyi and Konkin 2012, 13-14). PANI macromolecules form a polyconjugation system as a result of the alternation of benzene rings and nitrogen atoms in the main polymer chain. The delocalization of charge carriers and an increase in conductivity occur as a result of the stabilization of the polaron by strong acids. Depending on the state of oxidation and the degree of doping by acids, PANI can exist in different forms, connected by reverse transitions.

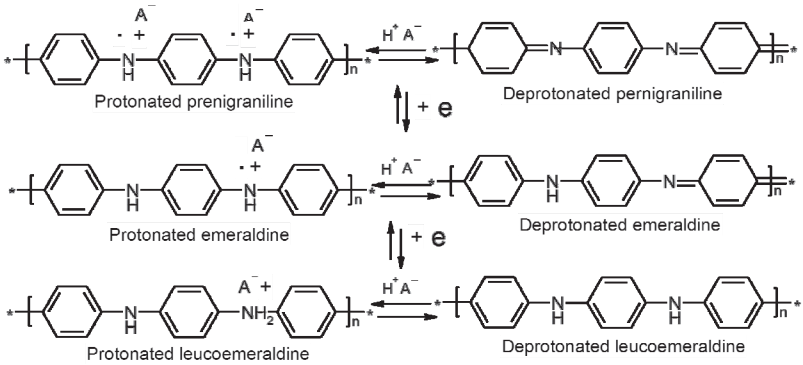

Fig. 3.8 Polyaniline with the different oxidizing conditions (H^+ A^- acid molecule) (Stejskal and Sapurina 2010, 12).

In the synthesis of PANI from the aniline salt (aniline hydrochloride), acid-base doping/dedoping reactions (fig. 3.9) are possible in stages, depending on the oxidizer, the pH of the medium, and other factors. The bandgap width of PANI varies from 0.7 eV to 4.0 eV (Ko and Do 2014, 4). Simultaneously, the conductivity of the polymer changes its optical, magnetic, and surface properties (table 3.3).

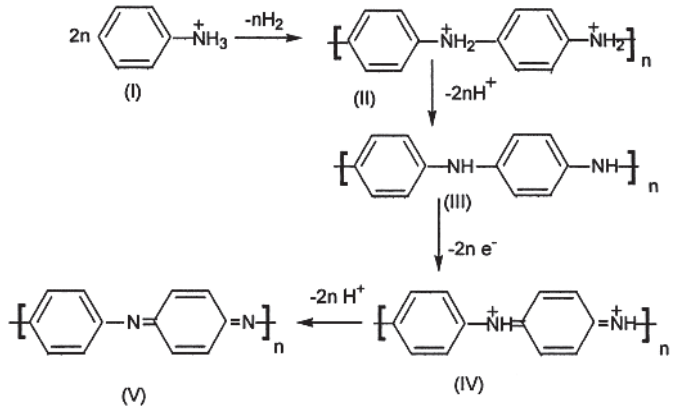

Fig. 3.9 Chain transformations of PANI: I - aniline salt; II - salt form; III - the base of PANI; IV - PANI in a charged state; V - PANI in an uncharged state (Zagorny 2008, 1).

Table 3.3 Characteristics of polymers

Properties	Doped emeraldine	Undoped emeraldine	Leuco-emeraldine
Conductiviy (S/cm)	$10^0 – 10^2$	$10^{-8} – 10^{-10}$	$< 10^{-8}$
Polaron concentration (spin/g)	$10^{19} – 10^{20}$	10^{16}	10^{16}
Absorption (λ_{max} nm)	400; > 800	380; 600	380

Due to the combination of its unique complex of properties, including high stability, lack of toxicity, and low cost, conductive polymers are used in electromagnetic radiation shielding, to protect metals from corrosion, and in medicine and photocatalysis (Zahornyi 2017). Various electronic devices have been developed using PANI: sensors, actuators, fuel, and energy-saving elements, solar batteries, electrode materials, and electrochromic compounds (Gedela and Srikanth 2014, 115; Chandrasekhar 1999).

PANI is used in the form of thin layers on different types of carriers in these devices. The thickness of the layers, as a rule, is in the submicron and nanosize range. Depending on the type of device, the organic semiconductor layer is in contact, and the thickness of the layers of, for example, 80÷100 nm for electrochromic devices ensure optimal absorption of solar energy by different devices. PANI layers should be combined with various carriers—insulating or conductive—and have various chemical and surface properties. These examples show that it is necessary to develop technologies for applying polymer layers of set thickness with diverse morphologies for different types of carriers (Nalwa 1997).

3.2.2 The kinetics of oxidative polymerization and morphology of reaction products

The potential of the *in situ* polymerization method is great, but the reasons for the formation of thin polymer layers during synthesis are not fully understood. Currently, there is no possibility of controlling the process to obtain layers of a given morphology and thickness. The total process of *in situ* polymerization is presented in the following equation (fig. 3.10):

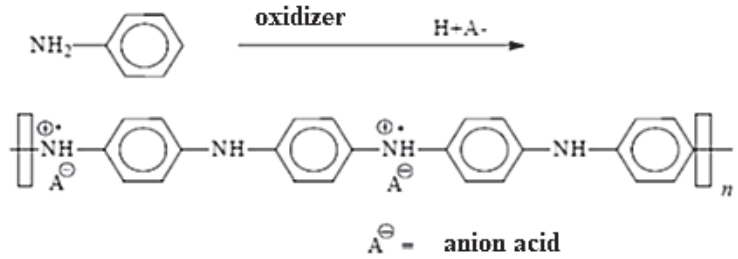

Fig. 3.10 Polymerization of aniline.

The thickness of the polymer layer on an optically transparent carrier was determined by the spectral method (from the absorbance at 400 nm) using a calibration curve (Sapurina and Riede 2001, 3). Study under different conditions showed the strength of the oxidizing agent, the pH of the reaction medium, and the concentration of the reagents (oxidizer [Ox] and aniline [An]). The reagent concentration ratio [Ox]/[An] = 2.5 and the initial synthesis temperature of 20 °C remained constant. Data on the conditions of *in situ* polymerization is summarized in table 3.4.

Table 3.4 Starting conditions for polymerization

Method	Oxidizer	Initial pH	Input concentration of aniline, $mol \cdot l^{-1}$
1	$AgNO_3$	>7	0.2
2	$(NH_4)_2S_2O_8$	<2	0.2
3	$AgNO_3$	<2	0.2
4	$(NH_4)_2S_2O_8$	<2	0.001
5	$(NH_4)_2S_2O_8$	4-7	0.2

Note: Oxidizing potential of $AgNO_3$ (0.8 V), $(NH_4)_2S_2O_8$ (2.01 V)

Method 1. Oxidation of aniline at pH >7 under the action of both strong and weak oxidants proceeds as a monotonic one-stage process. The reaction begins instantaneously and the rate decreases exponentially following the consumption of reagents (fig. 3.4). Products obtained at different stages of synthesis are identical in their properties. Optical product spectra (fig. 3.11-insert) represent a set of overlapping wide bands in the range 350–550 nm. Products have either amorphous morphology or form particles with dendroid structures. The layers formed during synthesis are non-homogeneous in thickness and have low conductivity ($<10^{-8}$ S/cm) and weak adhesion to the surface of the support.

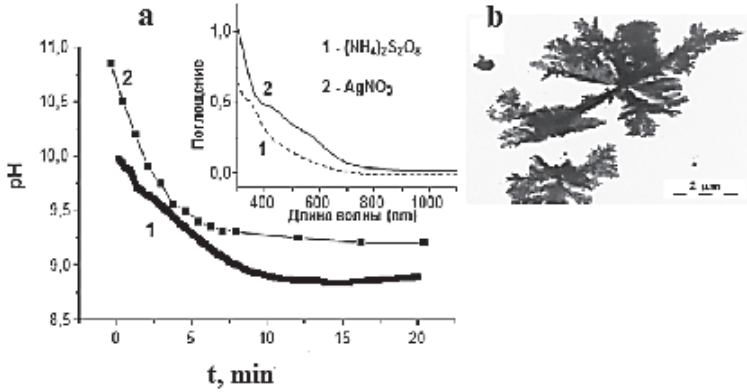

Fig. 3.11 a) pH curves of aniline oxidation under the action of persulfate and silver nitrate in a solution of ammonia; b) transmission microscopy of synthesis products (Shishov 2013).

Methods 2-5. The rate of aniline polymerization changes sharply when the pH medium comes close to 2.0. Products of the first and second stages differ. The spectra of the layers of the initial stage have a weak single peak with a maximum of 420 nm (fig. 3.11b). The conductivity of the layer is $10^{-8} \div 10^{-10}$ S/cm. An absorption band at 300–400 nm, caused by the π-π * transition of benzene rings and a wide intense band at λ_{max} ~800 nm is associated with the absorption of charge carrier-positive polarons (Krinichnyi and Konkin 2012, 13-14).

The specific conductivity of the layers is $10^{-2} \div 10^{1}$ S/cm, which also indicates that the layers are formed by PANI. The adhesion of the layers to the carriers is high, accordingly the scale of the cutting method corresponds to one. During the second stage, the thickness of the PANI layer on the support increases. As such, the thickness of the layers obtained from method 2 increases from 20 to 230 nm in the second stage. The resistance of the layer decreases from 10^{10} ohm·cm to 10^{-1} ohm·cm at the transition from the first to the second stage and then remains almost unchanged (fig. 3.12).

The morphology of the layers obtained from methods 2-5 is fundamentally different. The layers obtained from method 2 are formed by particles of a spherical 3D shape, while all the other films are formed by one-dimensional particles (1D). The electron microscopy data (fig. 3.13) demonstrate the stages of formation of the 3D morphology layer (method 2).

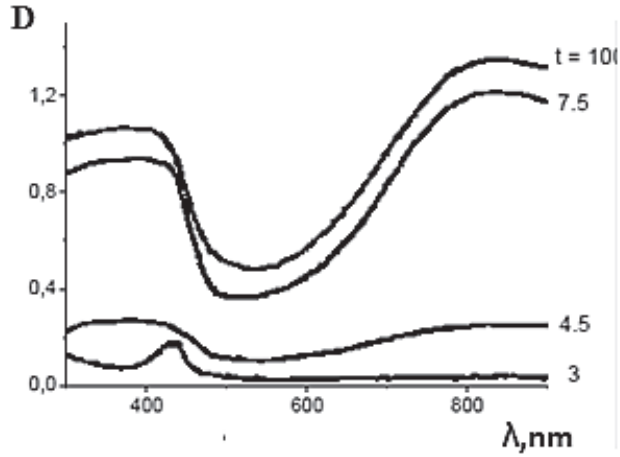

Fig. 3.12 Optical spectra absorbance of the layers obtained on glass with time *t* (indicated by arrows). Method 2 (Shishov, 2013).

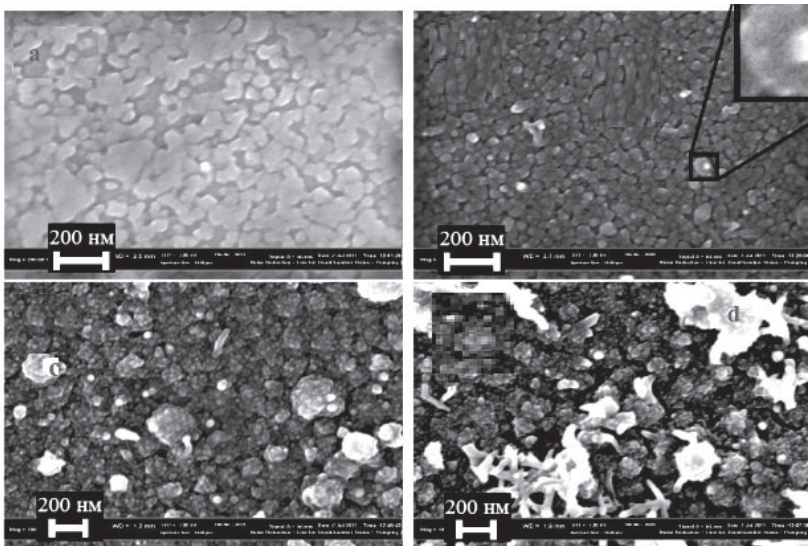

Fig. 3.13 Morphology of PANI layers obtained by method 2 at various stages of synthesis: a) 3 min.; b) 4.5 min.; c) 7.5 min.; d) 10 min. (Shishov and Moshnikov 2013, 8).

Today, a number of alternative technologies are being developed for the production of conductive polymer layers. Using the *in situ* polymerization method, it is possible to "grow" a polymer film directly on the surface of a support during polymer synthesis. The growth of PANI thin layers begins when the carrier is immersed in the polymerization medium, or when a polymerization composition is applied to the carrier surface. *In situ* polymerization has two processes—chemical and physical (with the self-assembly of chains growing into complex supramolecular structures). As a result, an ordered layer of conductive polymer is formed firmly on the surface of the support. Interest currently lies in how to control the polymer layer formation processes by changing the parameters of *in situ* polymerization.

3.2.3 Managed self-assembly and self-organization of polymer layers on the carrier

Aniline oligomers form at the initial stage of the polymerization process. Polymers are insoluble in the polymerization medium and are also prone to adsorption and the formation of various types of aggregates, both in the volume of the polymerization phase and on the surfaces with which they come into contact. This process leads to the transformation of a homogeneous reaction into a heterophase process and the self-organization of polymer chains into supramolecular structures occurs (Ding and Sanchez 2010, 32).

The self-assembly agglomeration of PANI oligomers fixes hydrogen bonds formed between growing near chains. The result of *in situ* polymerization is a polymer assembled from particles the morphology of which it is impossible to reconstruct. The form of the assembly of polymer chains is important (Sapurina and Stejskal 2012, 2). The time of the initial stage of monomer in situ polymerization allows us to control the morphology of the polymer (Sapurina, and Shishov 2012).

The self-assembly process depends on the conditions of *in situ* polymerization radically changing the structure of the polymer particles. The germination of blanks by polymer chains leads to the formation of a spherical polymer particle. Under the condition of a short initial stage, the sediment of the PANI layer on the carrier surface is collected from particles with three-dimensional spherical morphology (fig. 3.14a). SEM images show that polymeric spheres have a narrow size distribution and can aggregate into large particles of a quasispherical shape (granules).

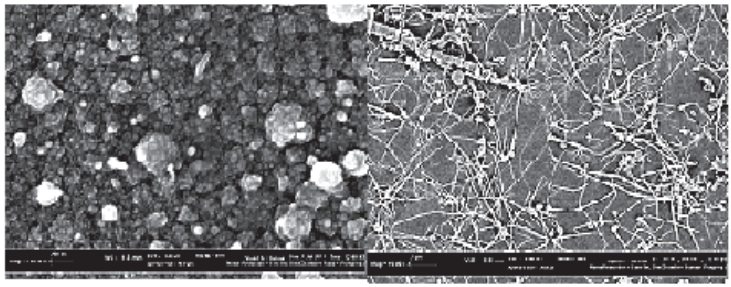

a b

Fig. 3.14 PANI layers with particles of 3D spherical structure a) and fibrous morphology b) (Shishov 2011).

The spherical morphology of particles becomes one dimensional and the polymer grows in the form of nanofibres and nanotubes. We can explain this phenomenon in terms of the polymer chain length, as these preforms lead to the growth of 1D PANI particles. The growth of 1D particles depends on several parameters of synthesis, such as the concentration of the reagents, the strength of the oxidizer, and the pH of the reaction medium. These effects are variable and increase in the initial stage of *in situ* polymerization and the production of films collected from one-dimensional particles. However, these films can have different structures and the layers of polymer form on the carrier when the reagent concentrations in the reaction mixture decrease. The fibres are oriented chaotically, leaving a significant part of the surface of the carrier without coverage. The use of a weak oxidizer at high reagent concentrations allows the production of continuous coatings organized from nanofibres. Here, 1D particles with a diameter of less than 100 nm are oriented, as a rule, along the normal of the carrier surface plane and the film displays a grass lawn-like structure (fig. 3.15b).

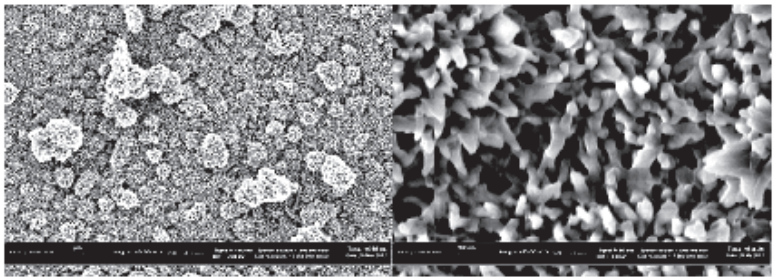

a b

Fig. 3.15 PANI film of fibrous structure on a glass surface obtained by in situ polymerization using a weak oxidizer. SEM images at various magnifications (Shishov 2011).

Depending on the reaction conditions, insoluble oligomers can form amorphous aggregates or particles with a complex hierarchical structure (fig. 3.16 a, b).

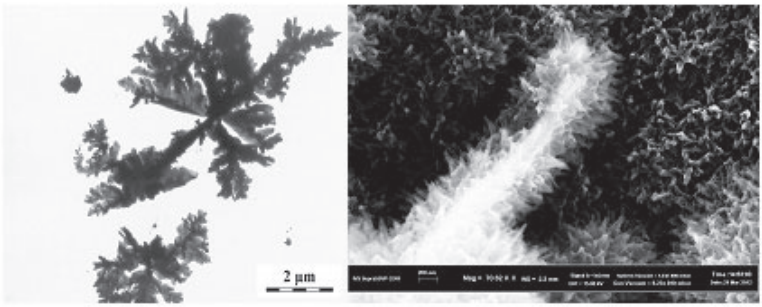

a b

Fig. 3.16 Dendrimer particle morphology: a) TEM; b) SEM (Shishov 2011).

The dendritic formation of particles indicates that the self-assembly process is carried out according to the principles of diffusion-limiting aggregation. Dense and homogeneous PANI films form with particles of spherical structure. The polymer spheres on the carrier surface assemble into large aggregates and the PANI film is a monolayer of close-packed granules. The size of the granules and the thickness of the polymer coating

is changed by regulation of the concentration and temperature conditions of the *in situ* polymerization and its duration. It is possible to obtain continuous polymer coatings with thicknesses of 30 to 350 nm. Figure 3.17 shows a continuous granular layer of PANI on glass with a thickness of 40 nm. By varying the concentrations of reagents and the temperature, it is possible to form "island" granular coatings with different "island" sizes and the presence or absence of percolation paths between them. Additionally, anomalously thick uniform PANI films can be grown using the *in situ* polymerization method. On some media, the film thickness is one and a half microns.

The temperature of synthesis has a strong effect on the thickness of the emergant layer. The thickness of the film coating decreases to 30 nm with a decrease in the temperature dimension by 10 degrees. However, this statement may be controversial in terms of polymer films or coatings.

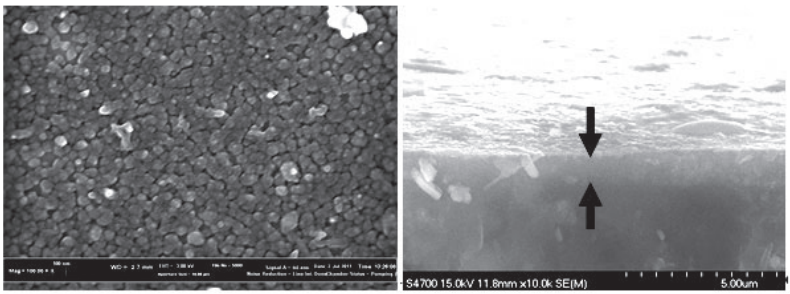

a b

Fig. 3.17 Solid polymer layers of PANI with thickness of 40 nm: a) the end of the polymeric sandwich break—a 1.5 μm thick PANI layer on a polymeric carrier; b) SEM image (Shishov 2011).

Nakata studied the effect of temperature, in the range of 10 to -5 °C, in the synthesis of polypyrrole films and using ferric chloride as an oxidizing agent. With the transition to low temperatures, film thickness decreased from 200 to 30 μm and conductivity increased from 2 to 10 S/cm. The authors explain that the diffusion of the monomer from the organic to the aqueous phase slows down, leading to the formation of films with maximum density and minimum thickness, as well as with increasing conductivity.

3.2.4 Mechanism of polymerization

Oxidative polymerization involves polycondensation with chain growth and the formation of low molecular weight products (Wei 2001; Sapurina and Tenkovtsev 2015, 4). However, chain formation can occur in two ways: through the recombination of radical cations and through electrophilic substitution (fig. 3.18). The oxidized nitrogen-containing structure attacks the phenyl ring of another aniline molecule and replaces one proton of the ring, according to the following scheme:

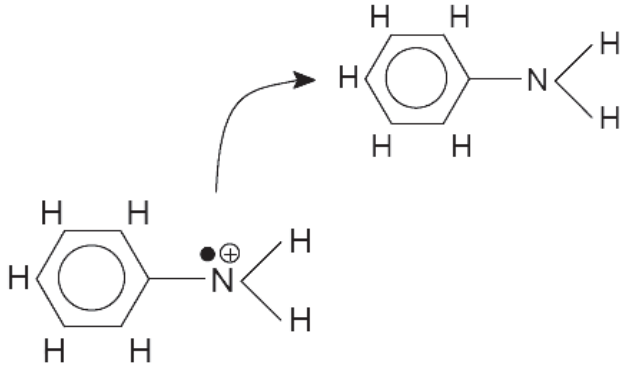

Fig. 3.18 Reaction of electrophilic substitution.

Both options, polycondensation and chain-growth, are possible. During polycondensation, fragments of any molecular mass react with each other and the monomer is converted to a low molecular oligomer, although high molecular fractions coexist. Different molecular weight distributions can be observed in the processes of chain growth. Research has distinguished the polymerization of aniline into the active chain process (fig. 3.19) and chain growth includes repeated activation/ deactivation of the polymer structure:

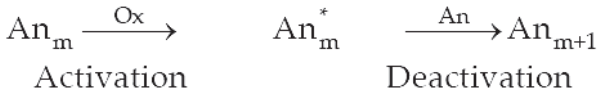

Fig. 3.19 The chain growth mechanism of the polymer.

The polymer chain is activated by *n* oxidizer (to form A_{nm}*), with the addition of the aniline molecule, and a new chain with a higher molecular weight (A_{nm} + 1) develops. In contrast to other types of polymerization with chain growth, oxidative polymerization requires a large amount of oxidizer. Here, at each stage the oxidizer attaches to monomers and the molar concentration of the oxidizer is comparable to the monomer concentration. The oxidizer works during polymerization and does not participate in redox interactions until the monomer molecule enters the polymer chain.

3.2.5 The influence of pH on monomer polymerization

Experiments dealing with aniline kinetic oxidation and the acidity of the reaction medium are discussed in this chapter (Sapurina and Shishov 2012). The oxidation of aniline is an exothermic process and is easily changed under the influence of temperature (Stejskal and Sapurina 2010, 12). Analysis carried out using potentiometry is presented in fig. 3.20.

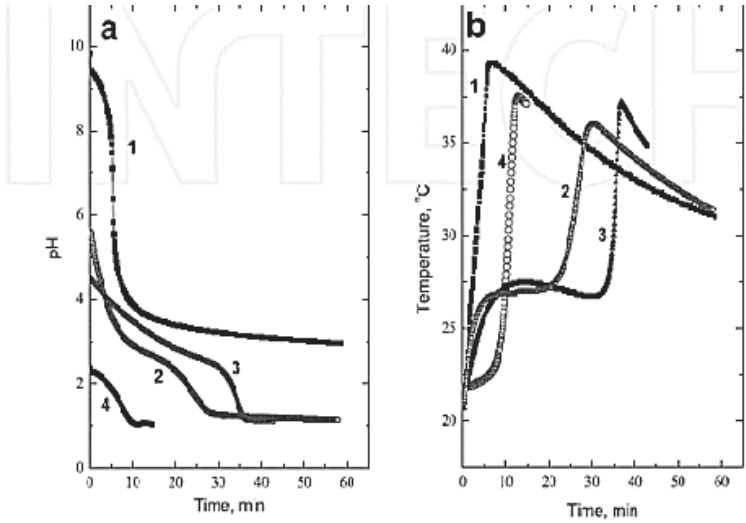

Fig. 3.20 Temperature change (a) and pH (b) profiles during the process of oxidative polymerization of aniline with APS at different acidities of the medium: (1) ammonia; (2) water; (3) acetic acid; (4) sulfuric acid (Stejskal, and Kratochvíl 1996, 2).

First, oxidative aniline polymerization (0.2 mol/L) is carried out using a stoichiometric amount of ammonium persulfate (0.25 mol/L) and varied acidity, such as 0.2 M ammonia solution (pH 0), water (pH 6,0), 0.4 M acetic acid (pH 4.5), and 0.2 M sulfuric (pH 2). The pH and temperature parameters are changed synchronously. The exothermic stage promotes a decrease in the pH medium and thus the initial oxidation rate of aniline increases with an increase in the initial pH of the medium. With increasing acidity, the initial rate of polymerization decreases. In the presence of sulfuric acid (pH 2) or pH 0, the stage is described as the oxidation induction period. Processes of oxidation at pH ~2.5 are characterized by a single temperature oxidation wave. These processes include oxidation to ammonia, which starts at pH 10 and ends at pH >3, and the reaction medium of sulfuric acid at pH <2.2. In oxidative processes that occur in this pH range, including pH ~2.5, there are two temperature waves. These processes involve a reaction in water and acetic acid beginning at pH 6 and pH 4.5, respectively, and ending at pH 1. However, to achieve pH 2.5, the exothermic reaction recovers its energy and the temperature of polymerization lies in the second wave. The change in pH in the second wave is identical, which is typical for polymerization in sulfuric acid. The decrease in pH in water occurs much faster than in acetic acid because this weak acid serves as a buffer and binds protons released during polymerization.

For oxidation at low [Ox]:[An] ratios (0.025, 0.5, 0.25), acidity below pH 3 is not observed. For high ratios of [Ox]:[An] (0.75, 1.0, 1.25), the final pH of the medium is less than 2.5. In the first series, in the range 2.5 <pH <3, the reaction proceeds extremely slowly. The second exothermic wave begins after the reaction medium reaches pH 2.5. As follows from the presented data, regardless of which parameter changes (initial pH of the medium or the ratio [Ox]:[An]), the processes have a similar character and operate in the same region. In the first series of experiments, the synthesis resulted in a 100 % conversion rate of monomer to polymer. Aniline oligomers with M_w and M_w/M_n parameters were present in the acid medium (table 3.5). The electron spectrum of oligomers does not show the polaron transfer typical of the emeraldine polymer form. The morphology of the oxidating products is primarily that of spherical particles with diameters ranging from 500 nm to 2 μm. PANI synthesized in the presence of sulfuric acid (1 <pH <2.2) with M_w ~ 40000 and M_w/M_n = 13.1 and the polymer has a spherical structure, typical of PANI with globules, measuring 100 to 200 nm (table 3.5).

Table 3.5 Properties of polymers synthesized in acetic acid at pH 4.5 with various molar ratios

[Ox:An]	0.25	0.5	0.75	1.0	1.25
End pH	4.0	3.3	2.5	1.2	1.1
б, S/cm (doped form)	$< 10^{-10}$	$2.4 \cdot 10^{-10}$	-	0.036	0.095
Molecular mass M_w	3600	2100	23600	17600	44600
Polydispersity M_w/M_n	3.8	16.4	11.1	9.4	10.6
Morphology	amorphous	2D	nanotubes		

A number of authors describe the optimum method for the synthesis of PANI with a developed mesoporous structure in the presence of an inorganic dopant and the absence of surfactants (Tomczhykova and Plonska-Brzezinska 2019, 2; Sapurina and Tenkovtsev 2015, 4). The conditions for the synthesis of mesoporous polyaniline have already been described. We synthesized polyaniline in several ways. The first method of synthesis was carried out in a dopant acid media at 0 and 15 °C followed by stirring of the reaction mixture with a magnetic stirrer and with exposure and filtration of the system. The second method saw synthesis in a Teflon drum on a roller table followed by stirring of the reaction system with zirconia spheres at 15 °C. The third method involves the mixing of the organic and aqueous phases—emulsion polymerization in the absence of mixing followed by exposure (table 3.6). Scanning and transmission high-resolution microscopy were used to investigate the features of the PANI structure synthesized at 0 °C with a yield of 98 %. Plate-shaped PANI (1.25:1) particles with sizes of 50÷80 nm were shown to be formed. The resulting polymer is preferably amorphous with a pore size of 10÷15 nm. Another typical situation for PANI is synthesis in the granular apparatus. PANI is an inhomogeneous and aggregated polymer (fig. 3.21–3.23).

Table 3.6 Yield of polyanilines synthesized from the monomers GHAn and An in the presence of an oxidizer $(NH_4)_2S_2O_8$ for 2 hours

Sample of polyaniline	Monomer	Medium of synthesis	Yield, %
PANI-1	An	1N HCl	82
PANI-2	GHAn	1N HCl	83
PANI-3	GHAn	NH_4OH	78
PANI-4	GHAn	1N HCl (roll)	80
PANI-5	An	CCl_4, KCK	40

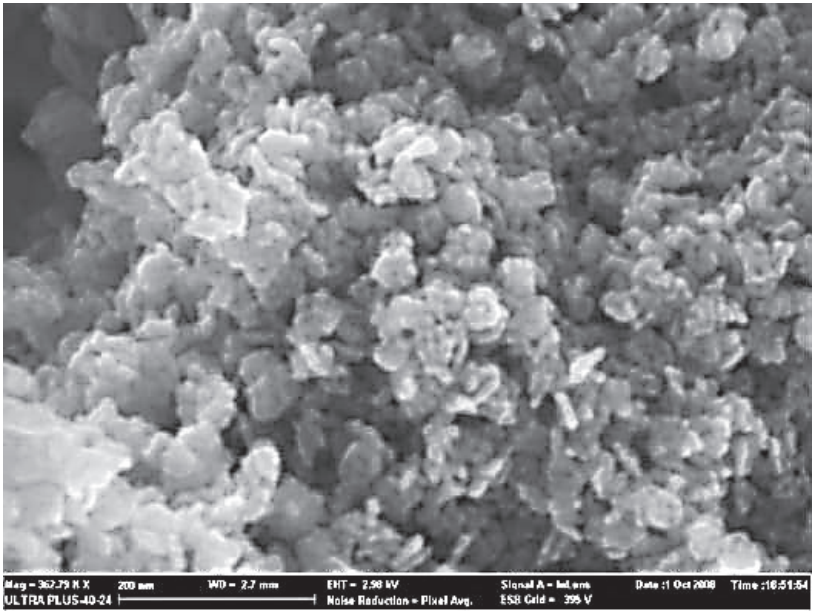

Fig. 3.21 SEM image of the PANI structure (authors).

As such, adding a strong oxidizer to a medium of varying pH leads to changes in the polymer molecular structures. A high molecular PANI with high conductivity is formed when aniline is oxidized at pH <2.5, in contrast to oligomers obtained in a medium at high pH. In different pH ranges, the morphology of the products varies; however, there is no direct correlation between conductivity, molecular weight, and the

type of supramolecular structure. Additionally, oligomers can exist in the form of microspheres or two-dimensional formations, and high molecular weight PANIs can form 1D (nanofibres and nanotubes) or 3D structures (granules).

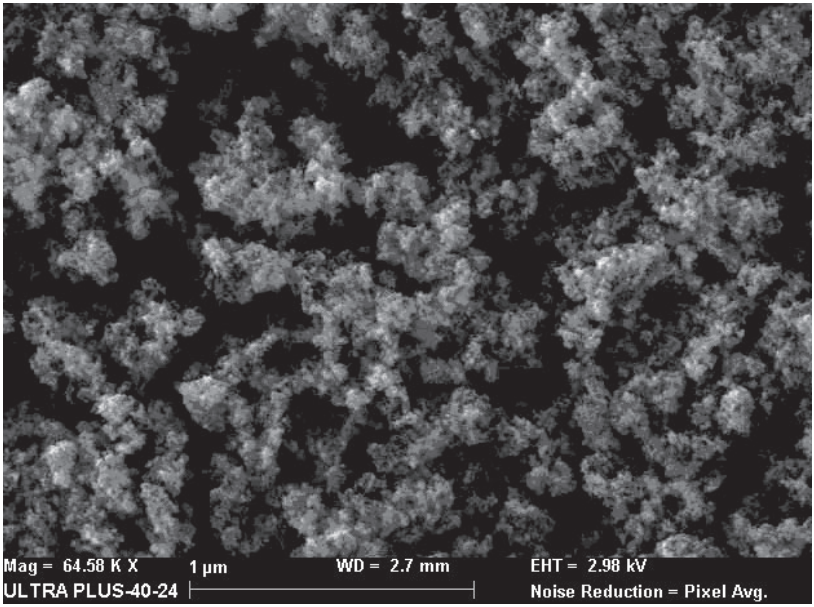

Fig. 3.22 SEM image of the PANI structure (drum).

The oxidation of aniline with $AgNO_3$ (Sapurina 2012) gives amorphous products. Silver is present in the form of particles with sizes in the range of 50–200 nm. Aniline oxidation was studied in acid solutions at higher pH values and, for example, in a solution of acetic acid (0.4 M) with monomer 0.2 mol/L and 0.25 mol/L APS (0.5 mol/L $AgNO_3$); the initial pH values were 4.5 and 5.7, respectively.

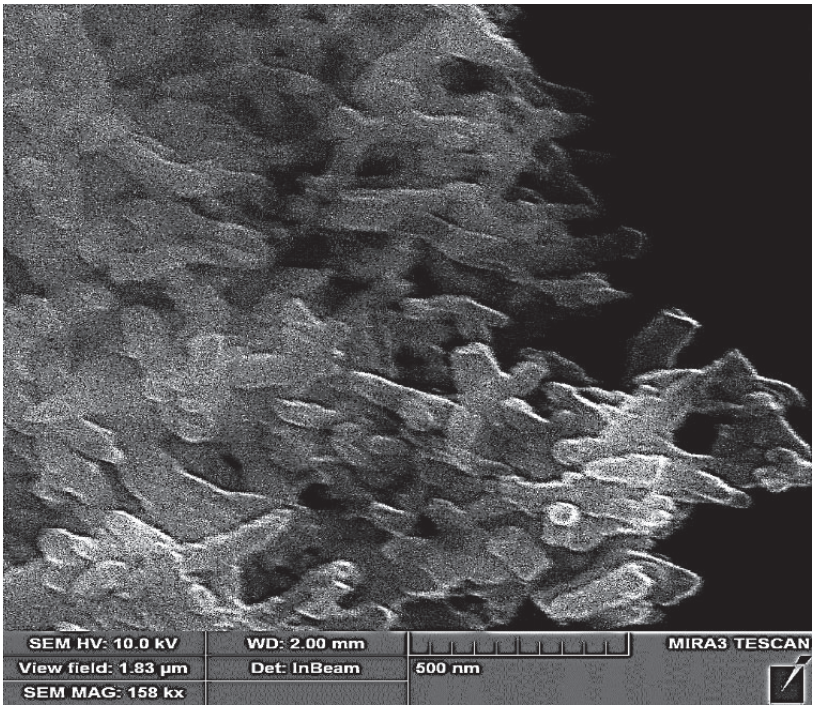

Fig. 3.23 SEM image of PANI in H_2SO_4 (authors).

Aniline polymerization follows the concepts of organic chemistry at pH >3.5. Other methods of substitution are possible, for example, the polymerization process leading to a head-to-head structure. A focus on the oxidized polymer fragment directs it towards the ortho and para-positions due to the presence of an amino group (an electron donor substituent) in the aniline. The benzene ring contains two vacant ortho-positions and monomer blocks with ortho-structures must prevail. The monomer units of the ortho-structures have low oxidation potential and undergo further oxidation leading to the formation of phenazine rings (fig. 3.24). Thus, in addition to the linear ortho and para-monomer units, the polymer chains contain phenazine fragments.

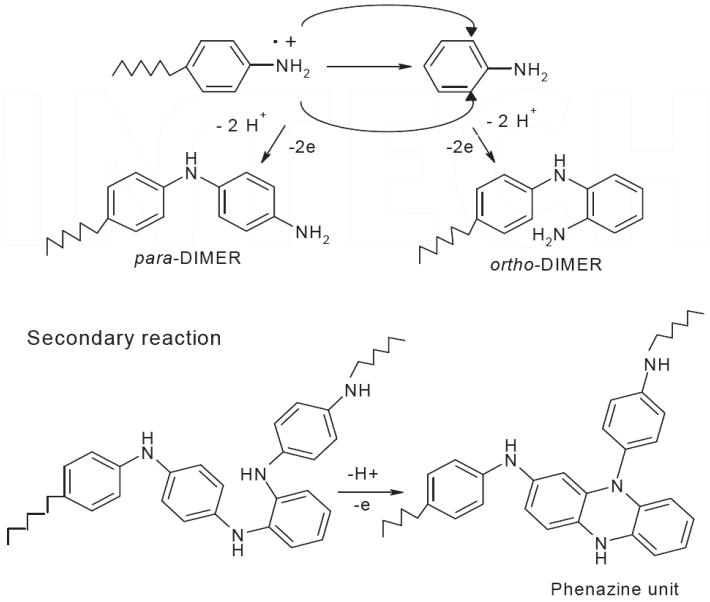

Fig. 3.24 The formation of intermediate products after aniline oxidation (Stejskal, and Kratochvíl 1996, 2).

Additionally, hydrolysis and the formation of quinones can occur in products in the presence of an oxidant. Thus, at medium and high pH values, aniline oxidation gives a chain with a heterogeneous structure and predominantly linear or cyclic ortho-units—this has been proved using spectral methods (Stejskal 2012). Oxidation of the deprotonated form of the reagents occurs at low potentials (0.3–0.5 V) under the influence of weak oxidizing agents. The reaction rate in cases of strong and weak oxidizers is comparable. The growth of polymer chains of regular structure becomes possible at pH <2.5. The protonation of the amino group of monomers leads to oligomers and their oxidation potential increases. This process restores the balance of the oxidation-reducing interaction between reagents. The chain is again capable of oxidizing and adding a monomer, albeit in a protonated form that dominates this pH range. The growth of the chain leads to the formation of conjugated polymers in a conductive form.

This book has shown, the chain reaction of aniline oxidation in alkaline, weakly acidic, and acidic mediums, proceeding by various molecular mechanisms. As a result, products with different molecular structures,

morphologies, and properties form. The presence of a monomer in a growing chain of doped and undoped forms presents different oxidation potentials. Aniline oxidation at pH >2.5 occurs with the participation of a deprotonated monomer and this process proceeds under the influence of weak oxidants. The products of this reaction are oligomers with a low degree of polyconjugation and low conductivity. At pH <2.5, the reaction proceeds through a stepwise change in the oxidation potential. In the induction period, oxidation proceeds with a low energy level at a potential of 0.5 V and gives cyclic dimers having the structure of phenazine. The limiting step is the "germination" of the phenazine rings (with the birth of future polymer chains). Phenazine has an oxidation potential of 1.05 V and the oxidative addition of the monomer to this fragment can only take place in the presence of a strong oxidant. The oxidizer has a potential lower than +1 V and the process is inhibited at the stage of phenazine unit formation. However, the addition of 1 mol% of a strong oxidant is sufficient to overcome this barrier. After chain growth, the oxidation potential falls again to 0.7 V and the reaction proceeds later under the influence of a weak oxidizer.

The polymerization process can be divided into three ranges. A polymer with irregular chains has a molecular weight of 4000–5000 at pH <2.5. A feature of PANI synthesis is heterophase polymerization. In the region of 3.5> pH >2.5, the oxidative-reduction processes see the slow formation of a cyclic dimer with a phenazine structure. At pH <2.5, the monomer is protonated, leading to the formation of ordinary conjugated chains with high molecular weight. As a rule, synthesis begins with homogeneous conditions and aniline is easily soluble in an acidic medium. However, the oxidation reaction of the monomer becomes heterophase. The process of the "polymerization of precipitates" gives insoluble polymers. Thus, we proceed to describe the mechanism of PANI self-organization.

Here, the use of PANI in various electronic devices and the role of the polymer layer structure for operational optimization are discussed. We describe the methods of obtaining PANI films on structural supports. The method of applying films from colloidal polymer forms, in addition to an alternative method of *in situ* polymerization, is currently used. Moreover, this is the only way to obtain polymer layers on porous and powdery nanoscale carriers. The *in situ* polymerization method also depends on the nature of the chemical carrier and its stability in acidic aqueous media.

We wish to mention here a book written by Marija Gizdavic-Nikolaidis, Graham Bowmaker, and Zoran Zujovic, published in 2018: "Synthesis, Physical Properties, Bioactivity and Potential Applications of

Polyanilines" (ISBN 978-1-5275-1114-9). A detailed analysis of the synthesis, morphology, and properties of conjugated polymers is given. We pay attention to that part dealing with the semiconducting polymer in obtaining a photosensitizer. The use of experimental polymerization conditions allows the obtaining of optical composites with nanoparticles of TiO_2, $C_3N_4O_x$ (see Chapter 4).

3.2.6 Spectral analysis of synthesized PANI

Let us consider the IR spectrum of the initial GHAn monomer (fig. 3.25a). The IR spectrum of the initial monomer displays a wide absorption band with characteristic vibrations of OH bonds in the frequency range of ~3433–3259 cm^{-1}. Oscillations in the frequency range of ~3100–3200 cm^{-1} are attributed to NH stretching vibrations and the frequency range of 1560–1630 cm^{-1} sees characteristic deformation vibrations of δNH. The presence of absorption bands in the frequency range of ~2560–2930 cm^{-1} is characteristic of CH stretching vibrations, as well as of deformational CH at frequencies ~476 and 522 cm^{-1}. Two strong narrow bands are found at ~682 and 742 cm^{-1}, corresponding to a monosubstituted benzene ring. Absorption bands in the frequency range ~1494–1520 cm^{-1} characterize C–C stretching vibrations of the benzene ring. Absorption bands at the frequencies ~1192, 1290, and 1325 cm^{-1} are characteristic of stretching vibrations of C–N bonds. The absorption bands in the frequency range ~1000–1146 cm^{-1} are characteristic of in-plane oscillations of CH, while the absorption bands in the frequency range ~800–900 cm^{-1} are out-of-plane oscillations. Weak absorption bands in the frequency range 1740–1800 cm^{-1} are characteristic of stretching C=O vibrations. The band in the frequency range 2500–2650 cm^{-1} characterizes the GHAn in the form of an ionically bound salt.

During the polymerization of the monomer at 0 °C for 2 h, an intermediate product was analyzed, which was obtained by adding an oxidizing agent to a solution of GHAn in acid for 15 min. The product was filtered, washed, and dried to achieve a constant weight.

Let us consider the spectrum of the obtained product (fig. 3.25b). The presence of feeble absorption bands in the frequency range of ~2750–2930 cm^{-1} characterized the CH stretching vibrations, as well as deformational CH at the frequencies ~471, 507, 604, and 640 cm^{-1}. The presence of very weak absorption bands in the frequency range ~750–900 cm^{-1} (750, 824 cm^{-1}) corresponds to out-of-plane vibrations of CH. Wide absorption bands in the frequency range ~960–1162 cm^{-1} characterize the in-plane oscillations of CH. The strong absorption band at ~1304 cm^{-1} and

the absorption band at ~1376 cm^{-1} characterized stretching vibrations of C–N bonds. We propose that there was a disordering of the structure through the conjugation of benzene rings with quinoid rings. This fact explains the strong absorption bands at 1500 and 1586 cm^{-1}, corresponding to the stretching vibrations of C=C and C=N bonds of the benzene and quinoid rings. A weak absorption band at 1750–1800 cm^{-1} characterized the C=O vibrations. Based on the results of IR spectroscopy, we assume that the product is in a partial state of oxidation (due to the presence of monomer fragments in its chain).

The IR spectrum of PANI at a molar ratio of 1:1 is shown in fig. 3.26a. The IR spectrum of the polymer contains weak absorption bands at ~2560–2930 cm^{-1}, characterized by CH stretching vibrations, as well as of CH deformation at frequencies ~507 and 594 cm^{-1}. The absence of absorption bands in the frequency range ~682–742 cm^{-1} and the presence of absorption bands in the frequency range ~800–900 cm^{-1} (798, 814, and 880 cm^{-1}) are characterized by the para-disubstituted benzene ring and off-plane vibrations of CH.

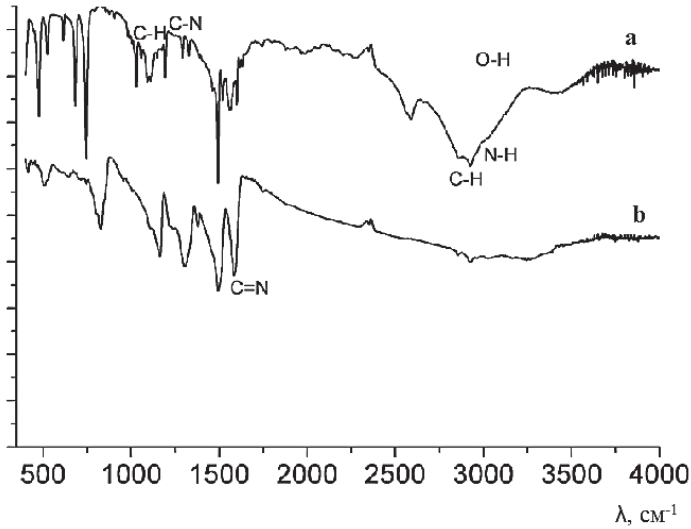

Fig. 3.25 IR spectra absorbance of the monomer GHAn: (a) intermediate product; (b) (partially oxidized state).

The absorption band in the frequency range of ~600–700 cm^{-1} corresponds to N-Cl– vibrations. Wide absorption bands in the frequency range ~1000–1146 cm^{-1} are characteristic of in-plane oscillations of CH.

The absorption band around the frequency ~1300 cm^{-1} is characteristic of stretching vibrations of C–N bonds in the benzene ring. The appearance of a strong absorption band in the frequency range ~1240–1250 cm^{-1} is characteristic of C-N+• (charge redistribution in the polymer chain) and indicates polarons; a strong absorption band around the frequency ~1571 cm^{-1} is due to the vibration of the quinoid ring and indicates that conjugation of the benzene rings occurs, while the ordering of the polymer structure is violated. In addition, the absorption band is broadened in the frequency range of 1480–1490 cm^{-1}, which is characteristic of stretching vibrations of C=C in the benzene ring.

The IR spectrum of PANI, obtained at a molar ratio of 1.25:1, is presented in fig. 3.26b. The IR spectrum presents weak absorption bands at ~2560–2930 cm^{-1} with CH stretching vibrations and CH deformation at ~507 and 594 cm^{-1}. The presence of weak absorption bands in the frequency range of ~800–900 cm^{-1} (706, 798, 814, and 880 cm^{-1}) characterizes the disubstituted benzene ring—off-plane vibrations of CH, respectively. The appearance of a weak absorption band in the frequency range ~1240–1250 cm^{-1} is C–N+•. An absorption band at ~1561 cm^{-1} is due to the vibration of the quinoid ring. Additionally, the absorption band weakens in the frequency range of 1470–1480 cm^{-1}, which is characterised by stretching vibrations C=C of the benzene ring. Thus, there is a frequency shift, especially for C=C. A bond of the –HN=C type forms with the quinoid ring conjugated with the benzene ring (and the formation of paramagnetic centres –N+H=). It occurs due to an increase in the probability of polaron transition to neighbouring polymer chains (Stejskal 2010, 12).

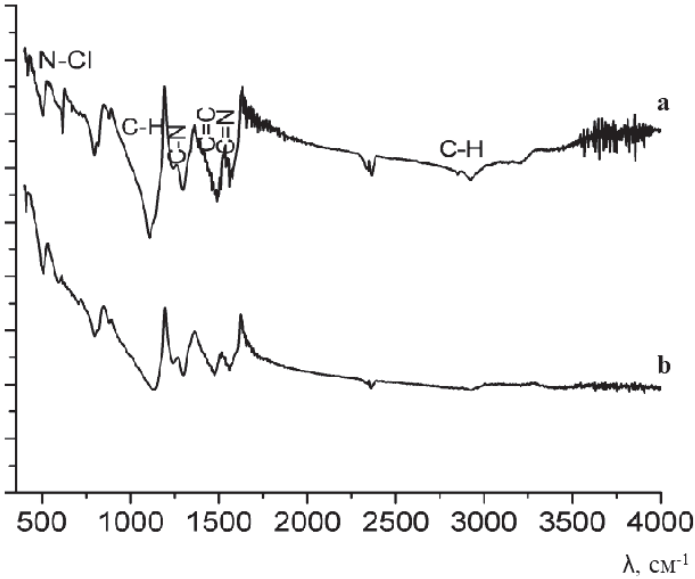

Fig. 3.26 IR spectra absorbance of polymers with different ratio Ox/monomer: a) PANI (1:1); b) PANI (1.25:1).

Thus, the process of adding an oxidizing agent gives a polymer in a doped state. The oxidizer/monomer molar ratio of 1.25:1 and the synthesis temperature of 0 °C are optimal for the formation of polyaniline and composites based on it.

3.2.7 Conductivity and photocatalytic activity of polyaniline

Polyaniline deposition on the metal electrodes occured in an organic medium. The kinetics of polymer particle deposition in the ethanol (isopropanol) solvent were studied with different U voltage fields. The presence of the electric field voltage was shown to influence the behaviour of PANI systems (fig. 3.27). The dependences of I=f (U) for the polymer samples were linear. The dependence I=f (U) for a polyaniline sample doped to 44 % (1.25:1) indicates that the deposition process begins at a voltage of 10 V. The maximum current is 13.6 mA at a field voltage of 200 V.

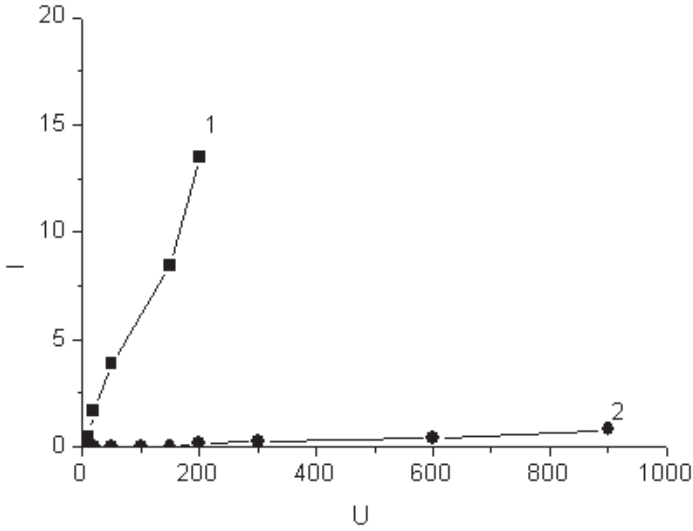

Fig. 3.27 The current (mA) dependence of the electric field voltage for polyaniline samples with a distance between the electrodes of 10 mm and a duration of electrophoresis of 60 seconds: 1 - PANI•HCl (44 %); 2 - PANI•NH_4OH (4 %).

The coating weight was ~2 mg at a field voltage of 200 V. These results show that a field voltage of 200 V allows the obtaining of maximum deposition of PANI particles (44 %); however, the current does not pass through a sample of PANI doped to 4 % at a field voltage of 600 V. The kinetic I=f(t) curves are presented in fig. 3.28. At a voltage of 150 V, the current value stabilizes after 1.5 minutes. At a voltage of 200 V, the current reaches its maximum value. The rate of movement of polymer particles to the cathode increases with the field voltage up to 200 V.

These results show that the PANI polymer obtained with doping of 44 % conducts current even in a liquid medium and so the deposition of polymer particles is carried out on the Ni– cathode, not on the anode. Electrons transferred to the nitrogen atom of the polyaniline chains and holes h^+ start moving from left to right. The scientists, MacDiarmid, Heeger, and Stejskal, have suggested the possibility of a potential barrier to the migration of the electrons in the PANI chain.

A number of scientific works have paid attention to the oriented structure of PANI (nanofibres and nanotubes). We present the results of our studies into the adsorption and photocatalytic activity of the polymer in a medium pH range of >7 in this book chapter.

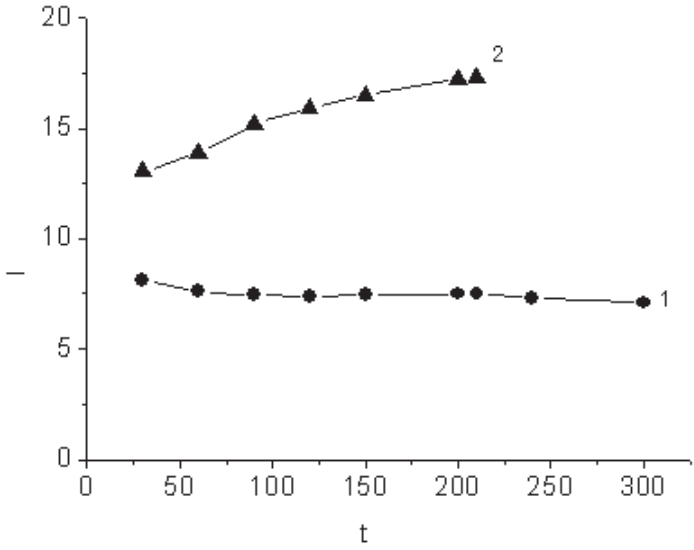

Fig. 3.28. Dependence of current I (mA) of electrochemical deposition of PANI particles (44 %) on the nickel surface as a function of time (s) for a given voltage and interelectrode distance of 10 mm: 1 - 150 V; 2 - 200 V.

Table 3.7 Conductivity (1 kHz) of synthesized PANI samples

Sample N	Oxidizer:monomer	Porosity, %	Density, g/cm^3	σ, S/cm
1	1:1	10	1.25	7.0×10^{-2}
2	1.25:1	5	1.32	1.3
3	1.4:1	12	1.24	3.2×10^{-2}
4	0.75:0.25	13	1.19	2.1×10^{-3}
5*	1.25:1	12	1.22	1.0×10^{-9}

Note: Polymer PANI (5) was synthesized in a 0.1 M NH_4OH solution

UV irradiation of PANI slurries containing MB (sample 2) were accompanied by destruction (with a decreasing concentration of MB); the rate of the process reached its maximum during the first 5–10 min (fig. 3.29). The maximum degree of destruction of MB was observed for the suspension containing particles PANI doped with HCl acid (An/Ox=0.8). Under UV irradiation at 200–400 nm excitation we find a PANI molecule and the formation of traps (NO; OH) in the polymer. As conductivity increases, the PANI trap concentration increases too.

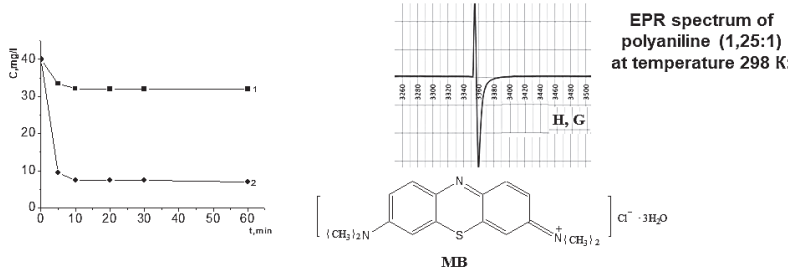

Fig. 3.29 Kinetics of the process of MB destruction under UV irradiation with a medium of pH 9.2 and PANI powders: 1 - PANI (NH_4OH); 2 - PANI (1.25:1).

The process proceeds in an oxidizing medium at pH 9.2 and the contact surface of these dye traps contributes to its oxidative degradation. MB dye adsorption on the surface of PANI is the primary instrument of the photocatalytic oxidation process since it occurs in an oxidizing environment with an aqueous solution, oxygen, and ozone generated by the passage of UV irradiation through the air. The adsorption process without UV has been studied in an earlier book (Zahornyi 2018, ISBN 978-613-8-27486-5).

3.2.8 MXene functionalized polyaniline systems

These MXene systems were first synthesized at Drexel University in 2011 and have rightfully grabbed the spotlight of the research world due to their chemical and mechanical properties. MXenes consitute an emergent class of 2D transition metal carbides. Density functional theory is used to predict newer ordered MXenes, which are derived from the MAX phase with the chemical configuration of $M_{n+1}AX_n$, where M represents a transition metal. Any element from Cd, Al, Si, P, S, Ga, Ge, As, In, Tl), S (groups 12-16), and X refers to C or N (in some cases, a combination of C and N), while *n* equals 1, 2, or 3[2]. MAX phases can be exfoliated into 2D layered transition-metal carbides and nitrides through selective etching using hydrofluoric acid (HF). Although the applications of the predecessor are limited, when exfoliated into a 2D MXene, some exceptional properties can be achieved from these carbon nitrides, which are of great scientific interest. Among the applications for which MXenes are currently being used, researchers are investigating their extraordinary

electronic, magnetic, optical, electrochemical, and water barrier properties (https://doi.org/10.1016/j.eurpolymj.2019.109367).

Polyaniline is a polymer belonging to the family of semi-flexible rod polymers; it has received attention due to its high conductivity. These days, PANI is being utilized in conductive coatings for making intelligent and multifunctional yarns. Easily prepared by changing the pH value, the polymerization mechanism and nature of oxidation of PANIs is intricate. In their study, the authors fabricated a composite of $Ti_3C_2T_x$ MXene/polyaniline (PANI) with a sandwich-intercalated structure, as shown in fig. 3.30, to investigate its microwave absorption properties (0.1016/j.compscitech. 2018.10.016).

Multiple MXene/PANI composites were created from mixing a suspension of MXene and aniline monomers. The mixture was then agitated in an ice-water bath for several hours with one addition of APS. Then, the precipitate was washed by HCl and distilled water to obtain composites with different mass ratios. Tiny particles were dispersed across the surface post-polymerization. Thus, the morphology and particle size of the sample changed with the control of the amount of aniline.

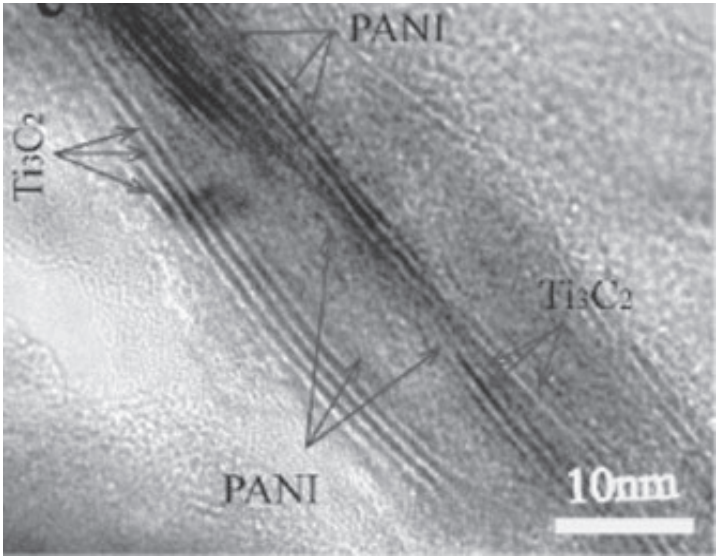

Fig. 3.30 Composite structure $Ti_3C_2T_x$ MXene/polyaniline (PANI).

The aniline control on the surface of the composite shows a relationship to its dielectric properties. Amongst the various mass ratios of 2:1, 1:1, 1:2, and 1:3, the loss of maximum reflection observed in the range of 2–18 GHz were -9.13 dB, -6.30 dB, -17.56 dB, -9.30 dB, and -8.57 dB at 14.4 GHz, 13.80 GHz, 13.74 GHz, 18 GHz, and 16.02 GHz, respectively. The multiple layers in the composite acted as a reflective surface, causing internal reflections. Like the model of the resistor-capacitor circuit, the MXene/PANI presented a similar model with electromagnetic attenuation at each reflection site and an uneven charge distribution. With increments in the conductive paths of the MXene, the sample with a 1:3 mass ratio displayed good microwave absorption, reaching an Rl of -56.3 dB at 13.80 GHz and with an absorption efficiency of 99.9999 %. The high absorption efficiency of this composite suggests that it has the potential to become state of the art.

The novel capacitance performance of PANI with branch-like chains was first investigated at the molecular level. PANI with branch-like molecular chains was synthesized using a simple template-free polymerization method. The results indicate that the branch-like chains disintegrate into small linear fragments during galvanostatic charge-discharge cyclings, with a concomitant increase in conductivity and a decrease in the internal resistance (IR); this is consistent with a stronger π-π molecule conjugation inside the small linear PANI fragments. As such, branch-like PANI exhibits a novel capacitance property and the specific capacitance rises 73-fold (from 4 to 294 $F \bullet g^{-1}$) after 107 charge-discharge cycles. This work offers a new pathway in the design and preparation of high-quality PANI-based supercapacitors with novel molecular chain structures
(https://doi.org/10.1016/j.reactfunctpolym.2019.02.011).

The *in situ* polymerization parameters of aniline, affecting the thickness and morphology of the polymeric layer, have been determined. Methods for obtaining powders and porous films formed by particles of a one-dimensional structure (1D) lying parallel to the carrier plane (1D∥), or arranged perpendicular to the carrier plane (1D⊥), as well as methods for obtaining continuous, homogeneous films, have been developed and formed from densely packed particles of spherical shape (3D). The thickness of solid layers can be a controlled variable in the range of 30±10 nm to 300±30 nm. The self-assembly of growing chains into complex supramolecular structures is revealed when using the *in situ* method. The polymer layer is formed simultaneously with the growth of polymer chains at the points of contact of the carrier and the polymerization medium. Scientific and practical interest lies in the development of ideas about

controlling the formation of a polymeric layer by deliberately selecting the parameters of *in situ* polymerization.

Although there is progress in its commercialization, there are also obstacles that hinder the practical use of PANI. The first problem is the synthesis of a polymer with reproducible properties. PANI is obtained by the method of oxidative polymerization of aniline (An); however, the quality of the products is critically dependent on the conditions of synthesis and products differ in their spectral, magnetic, and redox characteristics, as well as their morphologies. The electrical conductivity of some samples is tens or even hundreds of S/cm, while others do not exceed 10 S/cm.

The difference in properties is determined by the nature of intrachain and interchain electron transport, which depends on the structure of the polymer chains and their supramolecular organization (Sapurina 2015). The chains of PANI consist of parasubstituted monomer units connected by the head-tail type. Only in this case does the polyconjugation necessary for the transport of charge carriers appear in the circuit.

The second problem relates to the difficulties of processing PANI. During synthesis, simultaneously with the growth of polymer chains, it self-organizes into supramolecular aggregates and the final product is a non-melting and insoluble powder. The manufacture of commercial products is based on the use of PANI dispersions (according to Heeger, Sapurina, and Stejskal). Both tasks—improving the performance of PANI and solving the problems of its processing—are associated with its synthesis, which emphasizes the role of the conditions of synthesis in obtaining ready-to-use polymer materials. However, despite the decisive role of synthesis, ideas concerning it are not fully developed. For example, there is no explanation of the complex nature of aniline oxidation and the critical dependence of product properties on synthesis conditions; the mechanism of growth of regular polyconjugated chains is unclear—they are assembled from para-links connected by the head-tail type in the presence of an alternative variant of the assembly of chains with a heterogeneous structure of units based on the seven types of monomer that aniline can form (“head-head”, “tail-tail”, and “head-tail”, including ortho, meta, and para-isomers). Solutions to these issues are important, since they are necessary for developing controlled methods of synthesis of polymer materials, including dispersions and composites of PANI, with selected morphologies and properties, and for various applications.

3.3. Functional Composites with Different Types of Polymer Matrix

3.3.1. Polyaniline composites filled with metallic and oxide nanoparticles

Cutting edge applications need new hybrid material properties. A large amount of research has been carried out to discover various potential nanomaterials with particular functionalities. Conducting polymer/metal nanocomposites is one such class of hybrid material. The optical, electrical, and dielectric properties of the obtained polymer matrices are reinforced in different ratios with nanoscale fillers. Moreover, these polymers have a number of potential applications in the electronics industry.

Conducting polymers are also known as "fourth-generation polymeric materials" (Heeger). Among the conducting polymers, PANI has received significant interest due to its distinct physical and chemical properties: redox properties; a variable range of conductivity upon doping; ease of synthesis; and environmental stability (http://www.azom.com/article.aspx?ArticleID=1267). Due to these properties, PANI has seen a wide variety of technological applications, for example, in static charge dissipation, LED displays, electromagnetic shielding, gas sensors, pressure sensors, biosensors, transistors, and lightweight batteries. PANI also has limitations due to its low solubility, processability, and mechanical strength (Cardoso and Bhadra). To overcome these disadvantages, the blending of PANI with other higher molecular weight polymers, such as polyvinyl alcohol (PVA), has been extensively studied (http://www.4spepro.org/view.php?article=006131-2015-11-10). The good mechanical and promising electronic properties of these materials indicate their wide potential for usage in various devices.

Silver (Ag) and gold (Au) metal nanoparticles have gained considerable attention recently because of their promising technological applications and properties. These properties mean that Ag is suitable for numerous applications, such as catalysis, conductive inks, thick film pastes, and in adhesives for electronic components in photonics and photography. Several approaches have been employed to prepare polymer-metal nanocomposites. One of these is the deposition of metal nanoparticles on a polymer layer using various oxidants, as presented in a number of papers (Stejskal, Sapurina). The photo-reduction process of metal is a novel and hassle-free method for the preparation of Ag nanoparticles with the polymerization of aniline.

Recently, PANI (1D) has been of interest because of its promising optoelectronic and chemoelectronic properties. These properties are due to a higher effective surface-to-volume ratio and shorter penetration depth for target molecules compared to their bulk counterparts. They are efficient materials for application in light-emitting diodes, electrical nanodevices, solar cells, and chemosensors. Most of the methods adopted for the preparation of 1D polymer nanostructures use hard or soft templates (http://www.azom.com/article.aspx?ArticleID=5969). However, this technique also produces unaligned 1D nanostructures, but the complete removal of the templates might be a challenge. As a result, the authors have had to compromise the purity of the samples. Despite numerous attempts in the successful fabrication of PANI nanofibres, there are a limited numbers of reports for chemical synthesis of PANI-aligned nanofibres.

A novel and hassle-free approach has been proposed for the synthesis of aligned 1D PANI nanofibres using a photo-reduced Ag-PVA matrix as a reaction medium. Four molar concentrations of $AgNO_3$ were used to investigate their effect on the morphological and electrical properties of useful polymer nanocomposites for electronic microchip applications (Bhadra and Al-Thani 2016). The long tail surfactant (DBSA) assisted in the formation of circular micelles, which further elongated to form aligned fibres. However, for the next higher concentration of Ag, the fibres started to agglomerate, while in the highest concentration, some non-uniform particles were formed. This may be due to an inadequate quantity of surfactant (DBSA) to disperse all the Ag nanoparticles and keep them separate (in the case of 1.5 and 2.0 M of Ag). DBSA concentrations were kept constant while Ag concentrations were increased. The elemental composition showed Ag in the nanocomposite. The presence of O signals is believed to be due to the PVA matrix.

The UV-vis absorption spectra of PANI-Ag nanocomposites are provided in fig. 3.31; the inset shows the spectra of Ag nanoparticles dispersed in the PVA matrix with a characteristic absorption peak of Ag-PVA at 380–450 nm. This peak is attributed to the surface plasmon resonance absorption of electrons in conducting silver (Vorga and Prokes 2012). Pure PVA only exhibits a single absorption peak at 294 nm. For the composite samples, the absorption peaks were seen at 220–226 nm and at 396–420 nm, corresponding to the $\pi \rightarrow \pi^*$ of benzenoid rings and localized polarons (quinoid, Q), respectively. The band at 396–420 nm is broadened due to the Ag content in the interaction between PANI and Ag. Another broad absorption peak is observed at 800 nm and describes an exciton located in the quinoid ring. Another phenomenon is observed

when a conducting polymer-metal nanocomposite is excited by light photons, coupled at the interface of the polymer and metal (Abbasi and Yu 2015).

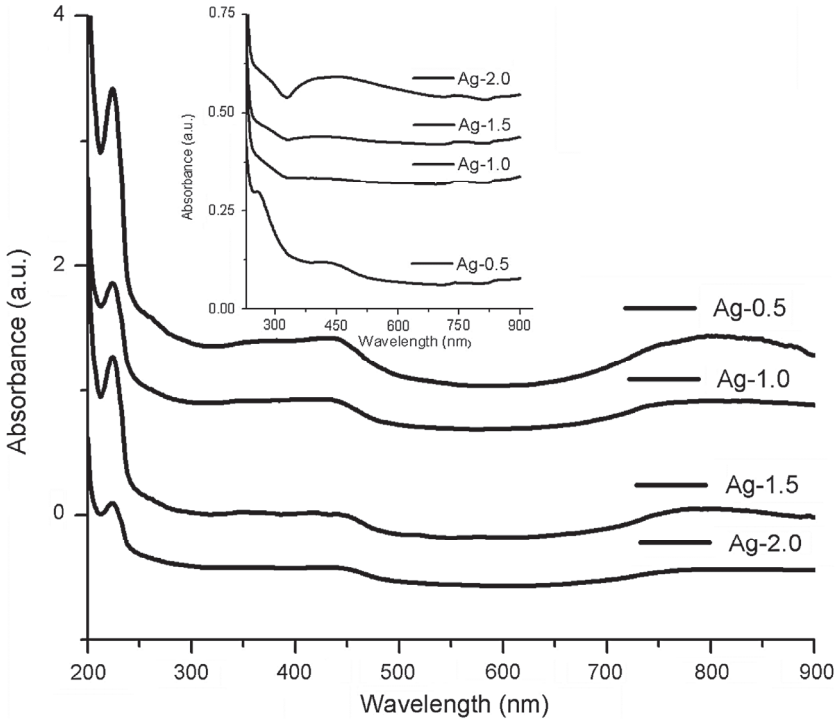

Fig. 3.31 UV-vis spectra of PANI-Ag nanocomposites and PANI (https://doi.org/10.1016/j.arabjc.2016.10.001).

The preparation and performance of four silver (Ag) concentrations in a polyaniline (PANI) and polyvinyl alcohol (PVA) nanocomposite blend was investigated by Bhadra et al. Morphological analysis using SEM and TEM revealed the formation of nanoparticles with diameters of 30–70 nm. Nanocomposites with lower Ag concentrations had highly aligned PANI-Ag nanofibres of diameters 50–80 nm and with agglomeration in higher concentrations. In addition, FTIR spectra showed a systematic change in the characteristic peaks with an increase in Ag contents. The study of crystallinity found the tetragonal crystal structure of metallic nanocomposites showed the same particle sizes as obtained in

SEM and TEM. To explore the possible applications of these nanocomposites in the electronics industry, their electrical properties were investigated. The in-plane *I-V* characteristics indicated a transition of polymer nanocomposites from non-ohmic to ohmic material with an increase in Ag content. Conductivities were found in the range of $4.74 \cdot 10^{-4}$ to $3.96 \cdot 10^{-2}$ S/m with no major difference in the activation energy for all the nanocomposites.

Table 3.8 The crystal lattice parameters, particle size from both XRD, SEM, and PANI-Ag nanofibre diameters (Bhadra and Al-Thani 2016)

Sample. Code No.	Calculated lattice parameter (Å)	Corrected lattice parameter (Å)	Av. Particle size by XRD nm	Particle size by SEM	Nanofibre diameter nm
Ag-0.5	a=b=7.54(3) c=9.93(1)	a=b=7.53(3) c=9.94(2)	42	35	50
Ag-1.0	a=b=9.70(1) c=7.54(4)	a=b=9.69(1) c=7.52(5)	47	50	65
Ag-1.5	a=b=4.94(3) c=7.54(1)	a=b=4.93(2) c=7.53(1)	64	60	-
Ag-2.0	a=b=9.87(2) c=12.34(2)	a=b=9.89(3) c=12.34(4)	68	70	-

The conditions of the oxidative polymerization of aniline, the effect of the ratio, the pH of the reaction medium, and the filler concentration on the yield product were studied. The oxidation of one gram of aniline with a stoichiometric amount of $AgNO_3$ theoretically yields 1.31 g of PANI and 2.9 g of metallic silver. Therefore, according to the stoichiometry of the reaction, the content of reduced silver in the metal/polymer composite

should be 68.9 wt%. The oxidation of aniline oligomers took place in the composite with 74 wt% silver content.

TGA analysis established the silver-containing product's composition. The weight fraction of metal was determined as the weight of incombustible residue left after heating of the sample in airflow to more than 600 °C. According to the TGA data, the silver content in all the composites corresponded to the stoichiometry of the redox process; in alkaline media this was 75 wt% while in acidic media it was 70 wt%. These data prove that it is $AgNO_3$ that acts as the oxidizing agent. Aniline polymerization with strong and weak oxidizers was studied in an article by Shishov (2013).

The result of $AgNO_3$ usage is the formation of metallic silver. During the reaction, at any initial value of pH, silver is reduced in stoichiometric amounts for oxidized aniline. This proves that silver cations serve as an oxidizing agent. Depending on the conditions of synthesis, we get reduced silver precipitation in the form of various nanodimensional structures (spheres, sticks, or bands covering oligomer particles). The presence of silver provides high conductivity in the obtained materials and these composites have a wide application in polymer electronics. It is interesting to note that, depending on the conditions of synthesis and in spite of equal silver content, the conductivity of PANI/Ag composites changes over a wide range (from 10^{-2} to 10^{3} S/cm). The morphology and properties of PANI/Ag composites, as well as reasons for this difference in conductivity, are discussed in Sapurina and Stejskal (2012).

PANI-Ag composites obtained through emulsifying polymerization of aniline with Ag (0–50 wt%) were examined. The composite's conductivity typically has a percolation character with access to a portion of the "plateau" at silver content of >24 wt%, which corresponds to the highest electrical conductivity of the composite (Root and Koren 2011; Kovalchukand Koren 2012). It is due to the dual system of π-electron bonds that the polymeric matrix is able to act as a one-dimensional (1D) transport carrier and have chain transitions (3D). The morphologies of composites with low silver content (2.5 wt%) were not uniform and show pyramidal formations, like polymer crystals as small as 150 nm. The maximum degree of order was achieved for silver at 30 wt% in the composite. This resulted in the ordering of polymer chains into long bundles, maximizing the deployment of macro chains. AFM 3 D surface images of composites showed silver particles covered with polymer. The authors believe that the particles act as a skeleton for the soft polymer molecules. The polymer matrix surrounds the metal surface particles helping prevent spontaneous aggregation.

The authors obtained PANI-Au, PANI-Pt, and PANI-Pd composites through oxidative polymerization of aniline in $HauCl_4$, H_2PtCl_6, and K_2PdCl_4, as shown in table 3.9. The table shows increased yield of composites compared to pure PANI. Metal (Au, Pt) content in the polymer matrix has electrical conductivity when compared to Pd (Ag)-polymer systems. XRD analysis of composite PANI-Au showed a uniform distribution of metal in the polymer grains with dimensions of 12.6±3.4 nm; however, the chemical interaction between the components was weak. For composite PANI-Ag, there was a negligible quantity of metal on the polymer surface, but its average particle size saw 30.5±6 nm included in the polymeric matrix.

Table 3.9 Characteristics of composite polyaniline-metal (metal content in the reaction mixture 15 wt%)

Type sample	Yield, %	$\sigma \times 10^3$, S/cm	Optical absorption*, λ, nm
PANI	55	35	340, 640
PANI-Au	80	61	340, 450, 650
PANI-Pt	64	75	340, 640
PANI-Pd	67	13	340, 640
PANI-Ag	59	13	350, 660

Note*: Spectra were obtained for polymer solutions in N-methylpyrollidone.

The authors investigated the synthesis of hybrid composites based on polyaniline. The surface morphology of PANI-Ag composite films varies with increasing metal content in the transition from amorphous to crystalline ordering through the formation of hybrid structures. Part of the metal included in the composite nanoparticle (Au, Ag) is evenly distributed in a polymer matrix; at the same time, the metal component (Pt, Pd) can be incorporated into the polymer chain by coordinating ligands of the polymer to form new chemical compounds.

Metal oxides (TiO_2, ZnO, SnO_2, and MoO_3, etc.) have been utilized as gas sensors for several decades. However, they have some drawbacks, including the inoperability of the sensors under room-temperature conditions (most are operational above 200 °C) and long-term instability. Among these metal oxides, nanocrystalline TiO_2 has shown good results in the detection of hydrogen, ammonia, and nitrogen dioxide. Polymers, such as polyaniline, polypyrrole, and polythiophene, have been investigated for

their unique electrical properties and the combination of these components allows composite materials with the appropriate optical, sensorial, and antimicrobial properties to be obtained (Han and Parveen 2018, 19; Li and Wu 2015, 3) has also been realized. To ensure good electrode performance of these MFCs, a graphene additive was used during the *in situ* polymerization of aniline on TiO_2 particles (Han and Parveen 2018, 19).

3.3.2 Preparation methods and properties of organic composites with TiO_2 nanoparticles

The unique properties of TiO_2, especially at the nanoscale, give it great potential to address important energy and environmental issues and have led it to become the subject of a large number of scientific works into its synthesis and studies into its antiviral properties and practical applications (Zahornyi 2017, 3-4**)**. The antiviral activity of TiO_2 anatase nanoparticles against human adenovirus 5 serotypes was found to be between 45 and 95 %, depending on the nanoparticle concentration (Pankivska and Biliavska 2019, 5).

The production of crystalline TiO_2 with maximum photocatalytic activity and stability in corrosive media (organic substances) is a priority for many researchers in the field of photocatalysis (Li and Wu 2015, 3; Ghosh and Kouame 2015, 5). The authors have made a number of attempts to dope sulfur, nitrogen, carbon, Ce, and MnO_2 with titanium dioxide, so as to shift the absorption range of the photocatalyst into the visible light and near-IR region (Khalyavka and Shcherbakov 2019; Sokolsky and Zahornyi 2019, 2). For example, mixing the levels of p (nitrogen) with 2p (oxygen) makes it possible to narrow the width of the trapped zone of the oxide semiconductor. Doping with nitrogen was undertaken through the treatment of a powder with nitrogen, ammonia, or ammonium chloride, and other nitrogen-containing compounds.

Doping with metals sees good results because the Schottky barrier is created through contact between the metal with the surface of the TiO_2, which acts as an electron trap. As a consequence, the recombination of electron-hole pairs is suppressed during photocatalysis (Ghazzal and Kebaili 2012, 115-116; Brooms and Otieno 2017, 2).

Many authors have noted that doping with metals (rare-earth) elements allows the shifting of photocatalytic activity into the visible region; however, this activity decreases, especially in the UV range. In terms of electronic interaction, nitrogen sees electrons pass from the orbitals 2p or 3p to the 3d orbital Ti, and the width of the forbidden band decreases. The problem of doped oxide TiO_2 powders is that their

photocatalytic activity in a polluted environment can sharply decrease, especially in the visible region.

Conducting polymeric materials are now playing an important role in the development of this area. Only a few basic chemical functions are performed by TiO_2 polymers and other NPs (Heshmatpour and Zarrin 2017). A number of works have been devoted to research in the use of TiO_2 and polymers. However, there are practically no studies on the kinetics of the synthesis of polymers in the presence of oxide NPs, particularly TiO_2 (Gnanaprakasam and Sivakumar 2015).

Nevertheless, there are several publications on the synthesis, structure, and properties of polymer composites based on nanosized TiO_2 carried on acrylate polymers. These polymers have valuable practical properties and offer the possibility of widespread use as optical displays, sensors, and switches, etc. (Adriana 2018, 350; Burunkova and Denisyuk 2013, 3). The main task in the manufacture of nanocomposite materials is to obtain the necessary level of controlled dispersion of components and to prevent the aggregation of nanoparticles. This requirement can be met through the design of chemical methods for forming composites, where one of the components previously synthesized is used to obtain another component. Sol-gel synthesis is carried out using TiO_2 precursors with a polyacrylate solution/dispersion, or a polymer film. In both cases, to regulate and stabilize the dispersibility of the resulting composite requires the formation of strong physical and chemical bonds between components. The choice of method is down to the requirements of the final material.

Polymer-composites are not limited to having metal fillings (Ren and Koshy 2017, 325). The physicochemical properties of polymeric composites are improved when the content of inorganic filler >10 wt%. In the case of nanoscale particles, these effects can be achieved with a small filler content (Arora and Srivastav 2012, 2). Polymer-oxide nanocomposite PANI-TiO_2 has been obtained using: the sol-gel method (Liu and Zhow 2006, 9-10); *in situ* polymerization (Li and Zhang 2010, 3); polymerization using micelles (Jumat and Wai 2017, 7); and emulsion polymerization (Phang and Tadokoro 2008, 6). The electrical, optical, and chemical properties of the colloidal particles of the oxide phase (TiO_2) significantly affect the kinetics and mechanism of polymerization of the monomer, providing a triggering or inhibiting effect by promoting the ion-radical deactivation of the overall process when passing through oxidation and polymerization. A number of factors, including the components in the reaction system, the proportion of oxidizer/monomer/oxide filler/monomer, the dopant, the temperature, and the time of synthesis, have a significant influence on the course of these processes (Rajakani and Vedhi 2015, 4).

The authors investigated the photocatalytic activity of composite powder PANI/ TiO_2 with a particle size of 100 nm for 90 min using MB dye solutions at 10 and 100 mg/L and pH 6.8. It was found that in the presence of PANI/TiO_2 the dye was decolourized by 84 %, compared to results with pure anatase TiO_2 (80 nm) of 34 %. Adsorption in the first 20 min. was only 10 % and saw no further changes. The authors believe that under such conditions of irradiation, the charge transfer from the PANI to the TiO_2, which leads to effective separation of electron-hole pairs in the interfacial layers of PANI and TiO_2, makes PANI/TiO_2 act as a photocatalyst **(**Chaturmukha and Naveen 2016**)**.

Chemical synthesis of nanocomposite polyaniline/nano-TiO_2 and its properties were investigated using SEM analysis (Yatsishin 2011). The results showed that a polyaniline nanolayer forms on the surface of the dispersed particles of titanium dioxide and the spatial nanonet. It was found that crystalline TiO_2 promotes the formation of a highly dispersed phase of polyaniline on the surface. The polyaniline forms a three-dimensional network of the incorporated nanoparticles (~20 nm) and agglomerates of TiO_2 particles (60−20 nm). Thus, the effect of the oxide phase concentration on the structure and the electrical properties of PANI composites using various synthetic methods were determined. In this regard, the EPR method allows us to obtain information about the structure of the polymer and composites; the nature and properties of the paramagnetic centres (PC); and the relaxation of electron mobility in TiO_2 nanoparticles.

Investigation of the surface area and morphology of the PANI/TiO_2 nanocomposite as a photocatalyst remains vital (Zagorny and Bykov 2014, 8). Composite PANI-TiO_2-II (S_{BET} = 108 $m^2 \cdot g^{-1}$) saw a slight decrease in the adsorption characteristics of a volume filling of 51.6 %. The pronounced effect of titanium dioxide particle size determined the sorption activity of TiO_2 nanocomposites at a concentration of 95 wt%. Here, the probability of transition increased the more PANI formed *in situ* in the state of thin films, despite an increase in the TiO_2 particle aggregation process. Naturally, this effect occurs to a lesser extent with composite powders with TiO_2-III.

Conducting polyaniline-titanium dioxide (PANI-TiO_2) composites have been synthesized by *in situ* polymerization. PANI/TiO_2 nanocomposites of different compositions were prepared with varying weight percentages of TiO_2 nanoparticles, e.g. 10 wt%, 20 wt%, 30 wt%, 40 wt%, and 50 wt%, in a fixed quantity of aniline monomers. The prepared powder samples were examined using XRD and SEM. The intensity of the diffraction peaks for the PANI/TiO_2 composites was lower than for TiO_2

and the SEM images showed the nanocomposite in the form of long PANI chains decorated with TiO_2 nanoparticles. Their dielectric loss and conductivitywere studied in the frequency range 1 kHz–10 MHz. At higher frequencies, the composites exhibited zero dielectric loss and the maximum value of σ_{ac} was found for a concentration of 20 wt% TiO_2 in polyaniline (Zhang and Wan 2005).

O_2 and doped PANI nanoclusters have a strong connection to the generation rate of oxide radicals in determining the rate and complete reactions of organic substance decomposition (Song and Yan 2013). The effect of the rutile phase at 0–50 wt% on the structure and electrochemical properties of PANI-TiO_2 composite films was studied (Moghaddam and Nusirian 2014). The results of SEM showed that a composite sample of 15 wt% TiO_2 had a uniform porous cylindrical shape. The sample composite of 25 wt% TiO_2 was found to have uneven pore structure and the absence of cylindrical pores. TiO_2 nanofibres at a concentration of 40 wt% displayed porous cylindrical morphology with a three-dimensional surface; this pattern is suitable for gas adsorption. 40 wt% TiO_2 in the rutile modification shell of PANI oxide encapsulated particles of spherical shape and the electron transfer mechanism at PL were also examined. Thus, the scientific and technical information we currently have about NP/PANI nanocomposites indicates that they have great potential in the synthesis of nanocomposites, especially PANI (Harada and Onoda 2016, 25).

The porous structure of the photocatalyst, in turn, determines the structure and properties of its interfacial layers, as well as the availability of exposure to the active surface of the catalyst and substances, which are subject to degradation. The efficient transmission of electronic processes between oxide NPs and the polymer requires a strong interaction. This will, to a large extent, depend on the rate of generation of hydroxyl radicals, which determines the speed and completeness of decomposition reactions of toxic organic substances.

The introduction of PANI to TiO_2 nanoparticles has been shown to enhance its photoactivity under visible light. It is well known that the overall photocatalytic activity of photocatalysts is primarily governed by three properties: light harvest efficiency; the separation efficiency of photogenerated charges; and the interfacial reaction process. A high separation efficiency of photogenerated charges is achieved at the heterojunction built between TiO_2 and PANI (Harada and Onoda 2016, 25).

The energy levels of PANI are well matched to the wide bandgap semiconductor of TiO_2. Both PANI and TiO_2 nanoparticles absorb photons

at their interface under irradiation. Since the CB of TiO_2 and the lowest unoccupied molecular orbital (LUMO) of PANI is well matched for charge transfer, the electrons generated by the PANI $\pi \rightarrow \pi^*$ transition under visible light illumination can be injected into the CB of TiO_2 and the electrons in the VB of TiO_2 are delivered to the PANI layer (Choquette-Labbé and Sheva 2014, 6). The enhancement of charge separation in the PANI/TiO_2 nanocomposite is achieved because PANI is an efficient electron donor and a good hole-transporter. These features of PANI ensure the effective separation of photogenerated electron-holes at the interface of PANI and TiO_2 in the nanocomposite (Moghaddam and Nusirian 2014).

Thus, the introduction of modified oxide nanoparticles into the system of organic compounds can substantially affect aniline polymerization because of the competition between the adsorption of components on a solid surface and their change in chemical activity. By varying the dispersed solid phase surface area and its quantity in the reaction system, we can influence the polymerization process.

The dopant is a necessary component in the reaction system for cationic oxidizing polymerization during PANI synthesis. The charge injected into the polymer system forms cations and anions in each repeating fragment of a polymer with the addition of a dopant.

We used a number of dopants, including HCl, H_2SO_4, H_3PO4, CSA, and DBSA, with the p-doping process. The dopants with hydrocarbon radicals were found to be suitable for both increasing solubility and the dispersion of nanocomposites, which are defined by the dopant concentration. We can obtain the core-shell particles, where the core is made up of TiO_2 and the shell is a semiconductor-to-dielectric single layer.

The presence of conducting particles contributes to field enhancement in the TiO_2 phase and leads to lower breakdown strengths. The conducting polymer contributes to dielectric losses making devices less useful for many applications. As such, the trade-offs between these parameters have been investigated to assess the usefulness of these materials in terms of their application.

3.3.3 Polyacrylate composites with oxide nanoparticles

The unique properties of TiO_2 and its use in the energy and environmental fields have led to a growth in the quantity of scientific work on its synthesis and practical applications. TiO_2, with its high photocatalytic activity and stability, has been studied by many researchers in the field of photocatalysis (Rajender S. Varma et al. Patent No.: US 8,791,044 B2, 2014). Doping with metals gives good results because the

Schottky barrier is created in the contact between the metal and the surface of TiO_2 during the photocatalytic process. Alkoxysilane can be introduced in small quantities to stabilize the TiO_2 nanoparticles and ensure better dispersion in the acrylate matrix used (Zhang and Luo 1997, 32; Whang and Xu 2006). The polysiloxane formed on the surface of TiO_2 particles protects the polymer matrix from degradation.

It is known that optical quality PMMA material has a small refractive index in the visible range at n=1.49; whereas TiO_2 has n=2.45 (anatase) and n=2.70 (rutile). Using these data, Chen and colleagues obtained a hybrid composite using a sol-gel process and MSMA to form interfacial chemical bonds. The resulting composite films had refractive indices in the range 1.202–1.867 (Sun and Chen 2010; Chen and Lee 1999, 9; Whang and Zhang 2008, 2-3).

Due to their unique properties, ZnO nanoparticles can be used in ultraviolet (UV) emitters, photocatalysis, piezoelectric devices, and chemical sensors. To change the chemical surface and physical properties of the ZnO, we use chemical adsorption methods, grafting, and various precursors, as well as varying the parameters of technological processes. Thus, homogeneous polymer composites containing up to 14 wt% of ZnO nanoparticles have been developed and investigated. It was found that physical properties, such as light scattering and Brinell hardness water absorption, vary monotonically with increasing concentrations of nanoparticles, by modifying the internal structure of the nanocomposite.

The structure of the nanocomposite was investigated using infrared spectroscopy and atomic force microscopy. Compared to an unmodified polymer matrix, it did not show reduced hardness and decreased moisture absorption and light scattering. Due to the interactions of the active groups in the monomer (carboxyl groups) with the surface of the nanoparticles, these were distributed uniformly throughout the volume of the material forming an optically homogeneous nanocomposite medium. It has been proved that the ZnO nanoparticles are photocatalysts and centres of the polymerization process. Synthesized composites are transparent in the visible and UV regions of the spectrum with high concentrations of ZnO nanoparticles (up to 14 wt%). With the introduction of NPs at 14 wt%, the refractive index increases to 0.045 and the introduction of 10 wt% ZnO reduces the water absorption of the material by five times (Burunkova and Denisyuk 2013).

The same authors investigated uniform nanocomposites containing SiO_2 nanoparticles (12 wt%) (Burunkova and Denisyuk 2012). The method for obtaining nanocomposites was based on self-organization processes in the formation of thin polymer membranes around each nanoparticle, which

is the main way of obtaining an optical quasi-homogeneous material. Using IR spectroscopy, the determination of the adsorption capability and hardness of the composites confirmed the presence of self-organization processes in the formation of the material. The types of nanoparticle-polymer chemical bonds were identified and investigated. The composites were transparent in the visible region of the spectrum with high concentrations of SiO_2 nanoparticles. When 12 wt% SiO_2 was administered, the refractive index decreased to 0.02.

A TiO_2/polymer was prepared with anatase and dispersed in a poly(methyl methacrylate/butyl acrylate/methacrylic acid) [(PMMA/BA/MAA)] matrix using the emulsion polymerization process (https://doi.org/10.1016/j.porgcoat.2016.10.007). TiO_2 nanoparticles of 5–8 nm in diameter were synthesized using a non-aqueous process and then modified with γ-methacryloxypropyltrimethoxysilane (A174) to improve compatibility with the polymer. FTIR, TGA, and dispersity tests in monomers/water were used to verify that the A174 was chemically bonded onto the surface of the TiO_2 nanoparticles. TEM, SEM, and EDS analyses indicated that the TiO_2 nanoparticles were homogeneously dispersed in the polymer matrix. TGA and DSC studies confirmed that the thermal properties of the resultant nanocomposites were significantly enhanced for neat polymer. UV–Vis transmission spectrum results revealed that films with TiO_2 nanoparticles have excellent UV-shielding properties. Even at a loading of 1.5 wt%, TiO_2 nanoparticles can almost completely block UV light below 350 nm while still having high visible transparency. Therefore, the resultant nanocomposite films can be used as transparent UV-shielding materials.

In a research paper (https://doi.org/10.1080/01694243.2015.1050758), the authors report a facile method for the preparation of a TiO_2/polyacrylate/TiO_2 multilayer core-shell hybrid emulsion through the polymerization process. The chemical composition of the copolymer was studied using Fourier transform infrared spectroscopy. TEM images revealed that the nanocomposites had different core-shell structures with TiO_2. As the weight percentage of TiO_2 was only 2 wt% (based on the monomer and as below), there were no TiO_2 cores in some nanocomposites. When TiO_2 was increased to 3 wt%, TiO_2/polymer/TiO_2 multilayer core-shell composite particles appeared; however, TiO_2 shells disappeared when the TiO_2 content continued to increase. TGA showed that TiO_2 dispersed in latex films uniformly and thermal stabilization improved with an increase in TiO_2 content. The effects of parameters, such as the polymerization temperature and concentrations of polymerizable emulsifier, initiator, and monomer, on kinetic behaviors were investigated and the

interaction mechanism between components of the TiO_2/polymer/TiO_2 multilayer core-shell structure were inferred.

Photocathode protective coatings have been applied in a number of areas such as ship and building protection, as well as in the chemical industry. In this work, a composite of titanium dioxide was loaded with reduced graphene oxide (RGO/TiO_2) and used as filler on a waterborne polyacrylate (PA) coating to reinforce metal protection against corrosion. The RGO/TiO_2-PA coating shows photocathode protection under visible light illumination compared to the currently used zinc phosphate filler.

GO/TiO_2 with dispersity and a micropore-blocking ability has been used in metal protection. The RGO/TiO_2-PA coating showed that graphene provides an extra barrier layer and photocathode protection under the action of light **(**https://doi.org/10.1002/app.48733).

Rutile (TiO_2)/poly(methyl methacrylate-acrylic acid-butyl acrylate) nanocomposites were synthesized by emulsion polymerization. The nanocomposites were characterized by dynamic light scattering, XRD, (UV-vis) spectroscopy, SEM, TEM, and TGA analysis to study their UV-shielding properties. The effects of the surfactant concentrations and monomer amounts on the morphologies of the resulting nanocomposites were investigated. Optimized results were obtained for the addition of 2 wt% TiO_2 nanoparticles and the effectiveness of UV shielding increased with the use of the synthesized rutile nano-TiO_2/polyacrylates. This nanocomposite coating with a thickness of 200 μm blocked up to 99.99 % of UV light (≤350 nm), as confirmed by UV-vis spectrometry (https://doi.org/10.1002/pc.22903).

3.3.4 Synthesis and properties of polypyrrole nanostructures: optimization and applications

The advantageous properties of polythiophene, polyaniline, and polypyrrole (PPy) were studied, such as electrochemical reversibility, relative environmental stability, high conductivity, good mechanical performance, and ease of preparation by chemical and electrochemical methods. They have applications in chemistry, physics, electronics, optics, biomedicine, and bioelectronics (Zohreh Deljoo Kojabad, Seyed Abbas Shojaosadat, doi: 10.1016/j.matdes.2016.02.04). The conversion of the closed-shell system to a corresponding cation or anion radical and the stability of the product are the most important features of monomer molecules in the formation of conducting polymers. The preferred methods of polymer preparation are either the chemical or electrochemical oxidation of monomers in an aqueous medium. The synthesis of a polymer

by either of these methods depends on the intended application of the polymer (Federica De Riccards and Martina 2014). Traditionally, electrochemically initiated polymerization reactions have taken place in bulk solutions and not near the electrode surfaces (Genies and Bidan 1983).

3.3.5 Some aspects of the oxidative polymerization of pyrrole by APS

To determine the influence of the molar ratio of ammonium persulfate (APS)/ pyrrole in the initial reaction mixture, the authors devised the corresponding experimental dependences (fig. 3.32). The maximum yield of PPy was reached with a half-fold excess of the oxidant in the reaction system. The PPy yield depends on the pH solution, especially in the region of high molar concentrations of the oxidant. The PPy yield also depends on the temperature of the oxidative polymerization of pyrrole at 35 °C (Piskareva 2012, 2).

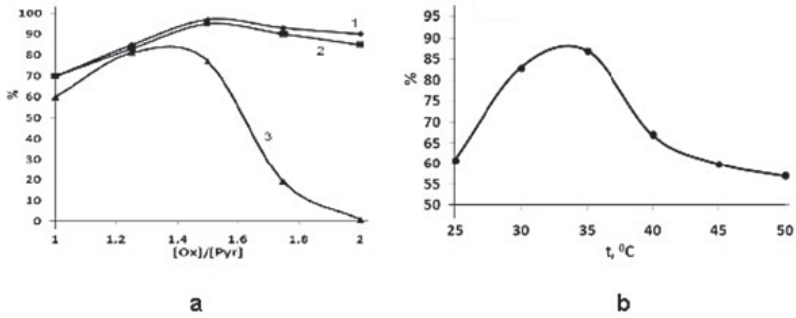

Fig. 3.32 The PPy yield (%) dependences of the oxidizer/pyrrole ratio at 25 ° C: a) after washing 100 ml: 1 - distilled water; 2 - 5 % aqueous solution of sodium carbonate; 3 - 10 % aqueous solution of KOH (duration of polymerization 24 h); b) the PPy yield dependences on temperature for a molar excess of ammonium persulfate relative to pyrrole were equal to 1.5 (polymerization time of 1 h).

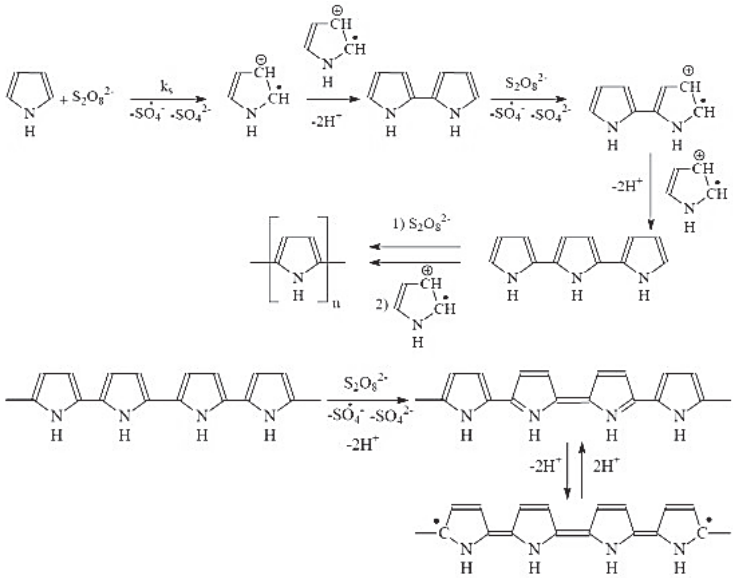

Fig. 3.33 Diaz mechanism of pyrrole polymerization.

The low PPy yield in the region of small molar ratios of oxidizer/pyrrole was associated with a shortage of APS to form higher pyrrole and PPy oligomers. An excess of oxidizer leads to a significant reduction in PPy yield, especially after washing the polymer product with a 10 % aqueous solution of KOH. Additionally, a decreasing pyrrole concentration in the reaction system can increase polymer yield. With a synthesis duration of 24 h and a temperature of 25 °C, the PPy yield was 97 %, 85 %, and 71 %. A pyrrole concentration in the reaction system was equal to 0.01, 0.03, and 0.05 mol/l, respectively. To achieve a greater PPy yield under conditions of oxidative polymerization of the pyrrole, ammonium persulfate in an aqueous medium requires a temperature of 30–35 °C and a 1.5 times molar excess of the oxidizer with a monomer whose concentration should be as low as possible. The oxidative polymerization of pyrrole under the action of ferric chloride is a bimolecular process, the mechanism of which has been proposed by Diaz (fig. 3.33). Partial oxidation with the formation of bipolarons is present in the PPy chain.

The literature presents data on the oxidative polymerization of pyrrole by sodium persulfate, which indicates auto-acceleration with a

mechanism that Diaz does not explain. Simultaneously, there are no systematic studies of oxidative polymerization of pyrrole under the action of persulfate. The authors have proposed a complex formation with charge transfer between the monomer and electron-deficient PPy in the works (fig. 3.34).

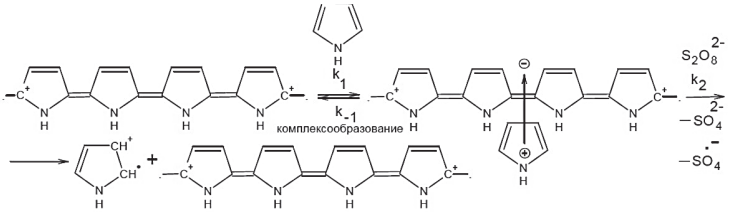

Fig. 3.34 Formation of a complex with charge transfer during the oxidative polymerization of pyrrole.

Recently, PPy has attracted attention as a conductive polymer. Methods used to prepare PPy include chemical polymerization in solution (Brezoi 2010, 1); chemical vapour deposition (CVD) (Walker and Naran 1988); and electrochemical polymerization (Ourari and Aggoun 2014). A number of investigators have shown interested in the third method and there are more than 300 reports concerning electrochemical polymerization of pyrrole (Wang and Ting 2014, 137).

The chemical polymerization method, which can be traced back to 1916, is used less often. The selection of the polymerization solvent in the process was only by chance. We have recently found that PPy obtained from chemical polymerization can exhibit high conductivities. The preparation of conductive composites using the chemical polymerization method has been developed and this method is more effective. The pyrrole monomer is polymerized by oxidizers, such as APS and $FeCl_3$, for the PPy composite.

In this method, there is a good distribution of PPy and the host polymer and thus electrical conductivity and mechanical properties increase; however, the two phases are immiscible. Many papers have discussed the electrolysis of pyrrole and the properties of the obtained PPy films (Wang and Ting 2014, 137).

Chemical polymerization occurs in the presence of various oxidizing agents, such as $FeCl_3$ and $K_2S_2O_8$ (Brezoi 2010, 1). The films were synthesized by the chemical oxidation of pyrrole with the addition of $FeCl_3$; a pyrrole solution of 0.043 M (2.881 g) was mixed with an

oxidizing solution of $FeCl_3$ (0.1 M). The synthesis was carried out at 5–7 ° C and the pyrrole was kept in a bath before adding the $FeCl_3$ (16.25 g). The synthesis was carried out without stirring and in a nitrogen atmosphere. PPy precipitate was collected with filtration, washed with distilled water, and dried at 25–35 °C. IR spectroscopic studies of pyrrole in water showed intense narrow bands of plane deformation vibrations δ (CH-) at 1015, 1045, and 1075 cm^{-1}. Immediately after the addition of $FeCl_3$ to the pyrrole solution, new weak bands at 1100, 1125, and 1150 cm^{-1} appeared against the background of pyrrole bands. The intensity of the new bands increased with time, while the pyrrole vibrations simultaneously decreased. The half-widths of the relative positions of these bands show that they relate to deformation vibrations of the pyrrole ring in the pyrrole complex.

According to this scheme, the formation of a PPy film through reactive intermediates is possible. The proposed mechanism explains the inhibition of the PPy synthesis caused by mixing of the polymer solution. SEM image showed the porous structure of the film with cavities fig. 3.35).

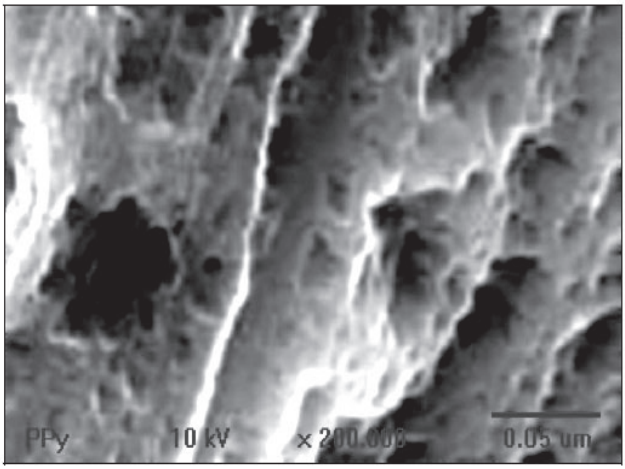

Fig. 3.35 PPy film structure.

The disadvantage of this method of synthesis is the low conductivity of polymer at 10^{-2} S/cm. PPy nanostructures (nanowires or nanotubes) were synthesized inside an alumina template and the response surface methodology (RSM), based on the central composite design

(CCD), was used to determine the relationship between the morphology of the nanostructures (nanowires or nanotubes) and the conditions of synthesis. The concentrations of pyrrole, oxidizer, time, and temperature of the experiments were all independent parameters selected to achieve the desired morphology of the PPy nanostructures. Monomer concentrations in the range of 0.13 to 0.4 M and 0.47 to 0.78 M resulted in the formation of nanotube and nanowire structures, respectively. The formation of nanotube and nanowire morphology was confirmed by SEM analysis of template cross-sections. The crystallographic and chemical structures of the PPy nanowires were studied using XRD, UV-vis, Raman, and FTIR spectroscopy. Electrochemical impedance spectroscopy (EIS) results showed a decrease of four orders of magnitude in the impedance of PPy nanostructure arrays rather than bare stainless steel sheet, which makes PPy nanostructures suitable for use in neural microelectrode surface modification (doi: 10.1016/j.matdes.2016.02.04).

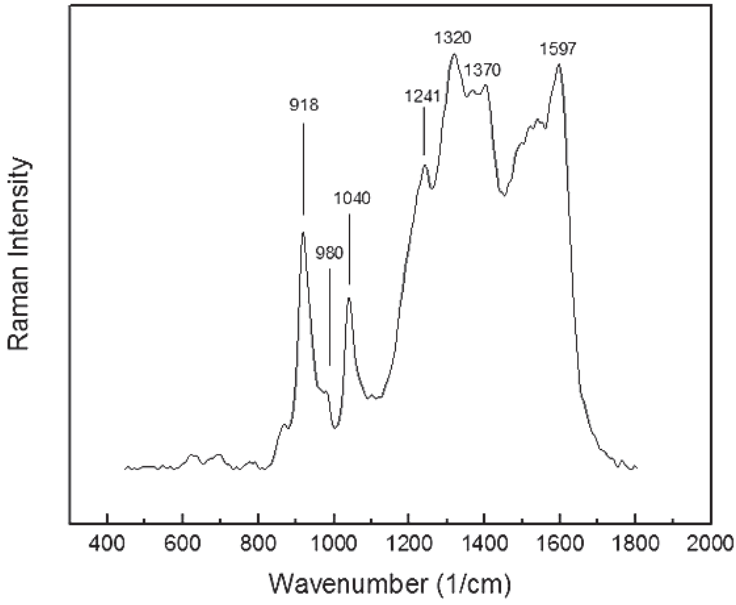

Fig. 3.36 Raman spectrum of chemical synthesized PPy nanowires.

As shown in fig. 3.36, which presents the Raman spectrum of PPy nanowires, the bands at 1241 and 1040 cm^{-1} are assigned to the C–H in-plane and show ring stretching, while the peak at 1597 cm^{-1} represents

C=C symmetry stretching. The two peaks located at 1370 cm^{-1} can be attributed to the inter-ring C–C stretching. The peak at 1320 cm^{-1} is due to the antisymmetrical C–N stretching of PPy. The peak at 918 cm^{-1} is associated with the bipolaron and at 980 cm^{-1} to the polaron structure. Raman results agreed well with the PPy chemical structure. Thus, a unique set of physicochemical properties, including the presence of electrical conductivity, characteristic of polyconjugated systems, has attracted considerable interest in the comprehensive study of the laws of synthesis. A special place among polyconjugated systems is occupied by PPy with its high electrical conductivity in a doped state. PPy is a promising material for coatings with antistatic properties (Mostatizur and Ali 2018, 10).

Note that PPy is applied to a substrate by chemical or electrochemical polymerization. Moreover, electropolymerization requires strict control of the process conditions to obtain durable and thin coatings or PPy films. However, as the authors have shown, the formation of stable aqueous dispersions of polypyrrole-polyvinylpyrrolidone allows them to be applied to various surfaces from aqueous media. The PPy matrix itself provides increased adhesion to metals and uniform application to surfaces. Additionally, the authors showed that the use of surfactant micelles (containing sulfur groups) can increase the conductivity of PPy by several orders of magnitude
(ubs.rsc.org/en/content/articlelanding/2017/ra/c7ra09725e#!divAbstract).

3.3.6 Morphology and properties of polypyrrole nanocomposites

As noted above, due to its unique properties, the PPy matrix (PANI) is also widely used to produce hybrid composites with particles of oxide semiconductors (ZnO, TiO_2, etc.) for use in electronics, gas sensors, galvanostats, electrodes, and batteries (Yuang and Yang 2014, 271). For example, PPy-TiO_2 (Arenas and Rodriguez-Nunez 2013, 2) composites were obtained by the oxidative polymerization of pyrrole with a solution of iron (III) chloride in an organic medium of isopropyl alcohol and the addition of a titanium compound ((Ti (OCH $(CH_3)_2)_4$) followed by ultrasonic treatment on a disperser with a power of 100 W. The SEM results are presented in fig. 3.37. Composites obtained before hydrothermal treatment mainly contained agglomerates of composite particles in the range 110±25 nm (fig. 4.7a). After processing at a temperature of 130 °C for 3 h, clusters of irregular shape formed with a particle size of 113±26 nm (fig. 3.37c). After processing the ultrasound data (fig. 3.37b), the cluster size was 121±26 nm. Homogeneous particles

of the correct shape and size of 175±42 nm (diameter) were obtained after combinations of ultrasound + hydrothermal treatment of the composite (fig. 3.37d). As such, the authors stated the dependence of the particle size of the PPy composites on the processing conditions.

The authors obtained a PP-TiO_2 composite by pyrrole monomer polymerization with ammonium persulfate and anatase particles (Sundaram and Sangareswari 2014). As a result, particles of PPy and titanium dioxide were formed in the form of balls. To determine their photocatalytic activity, an acid violet dye was used. The maximum dye photodestruction was achieved after irradiation for an hour.

Recently, researchers have shown considerable interest in ZnO semiconductors, due to their refractive index, thermal stability, good transportation, and high electron mobility. The authors performed oxidative polymerization of pyrrole on the surface of zinc oxide particles with a content of 0–20 wt% to obtain thermally stable and electrically conductive PP-ZnO films (fig. 3.38).

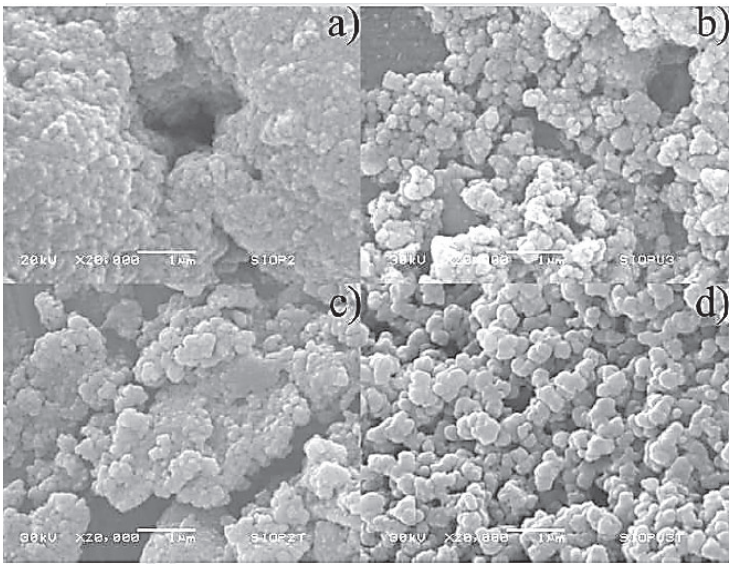

Fig. 3.37 Particle morphology of PPy composite dependence on the synthesis conditions (Batool and Kanwal 2012, 23-24).

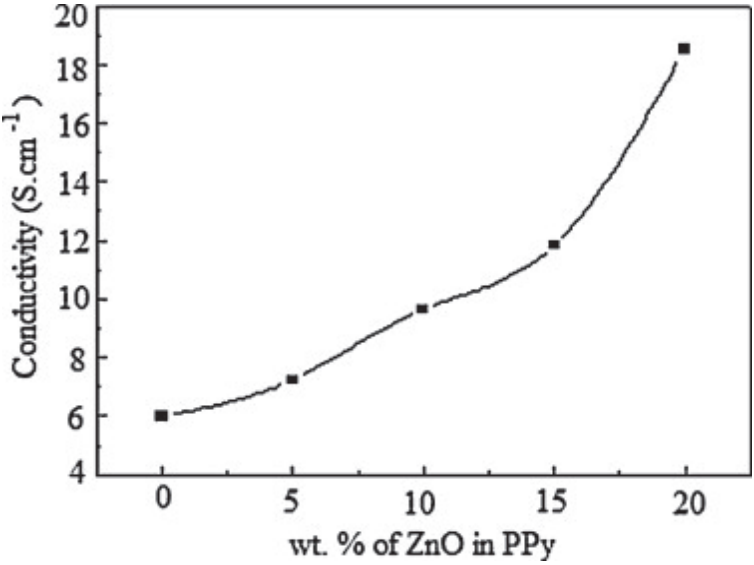

Fig. 3.38 PPy composite conductivity dependence on the concentration of ZnO.

The conductivity of pure PPy was 6 S/cm. When the ZnO content increased from 5 to 20 wt%, the conductivity of PPy-ZnO sharply increased from 7.24 to 18.52 S/cm. The authors believe that an increasing concentration of zinc oxide promotes efficient electronic transitions, followed by a decrease in the PPy bandgap (fig. 3.39). PVA is used for nanocomposites synthesis due to its solubility in water. The OH groups form hydrogen bonds with water molecules or amine/imine groups of the polymer chain. PVA can control the stereochemistry of the polymer molecule and, ultimately, the size and morphology of the polymer particles (PPy, PAn). PVA can act as a soft template.

Hybrid PPy/PVA-TiO_2 composite films were obtained on a glass substrate using oxidative polymerization in an aqueous PVA solution on the surface of TiO_2 particles. The photocatalytic activity of the composites increased compared to TiO_2. RhB is a blue dye used in the process—before irradiation, the dye concentration was 10 mg/L and after it was 2 mg/L (Cao and Zhang 2015, 342). Levels of PPy (unfilled HOMO orbital) were located above the conduction band of titanium dioxide. Under UV irradiation, both PPy and TiO_2 absorb energy, followed by transiting electrons from the valence band to the conduction band of TiO_2. The

electrons transit to the low molecular orbital of PPy and the photogeneration of electron-hole pairs with subsequent separation occur (fig. 3.39). Additionally, in the conduction band, an electron interacts with oxygen, giving O_2 particles with the formation of radicals. Abandoned holes react with a water molecule to generate OH• radicals, which are the source of photodegradation in the organic dye. The resulting composite films showed good optical absorption in the range of 200–800 nm.

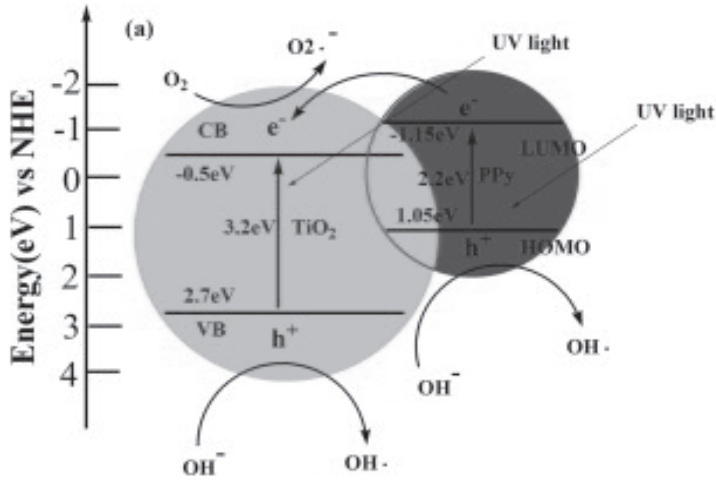

Fig. 3.39 The mechanism of electron transition in a PPy composite under UV irradiation (Cao and Zhang 2015, 342).

Today, the development of colloidal and physical chemistry, physics, and materials science is contributing to the accumulation of a considerable amount of research devoted to the study of nanoscale structures of different natures. Such objects have shown significant differences in terms of the chemical, thermal, optical, electrical, and magnetic characteristics of nanometer-sized particles compared to macroscopic analogues and the possibility of their innovative use in the fields of science and technology. Among such materials, the most in-demand are currently individual particles of metallic iron and precious metal gold, silver, bimetallic composites of Ag-Au, Fe-Au, Au-Pd, Au-Pt, and ferric oxide particles coated with a layer of precious metals.

The polypyrrole-silver (PPy-Ag) nanocomposite has been successfully synthesized by the chemical oxidative polymerization of

pyrrole with iron (III) chloride as an oxidant in the presence of a colloidal suspension of silver nanoparticles (https://www.researchgate.net/publication/333004299). The Turkevich method (the citrate reduction method) was used for the synthesis of silver nanoparticles. The Ag nanoparticles were characterized by UV-visible spectroscopy, which showed an absorption band at 423 nm, confirming the formation of nanoparticles. The morphological and structural confirmations of the PPy-Ag nanocomposite were characterized using the TEM, SEM, Fourier transform infrared spectroscopy (FTIR), and XRD techniques.

TEM and SEM images revealed that the silver nanoparticles were well dispersed in the PPy matrix. The XRD pattern showed that PPy is amorphous, but the presence of peaks at 2θ values of 38.24°, 44.57°, 64.51°, and 78.45°, corresponding to a cubic phase of silver, revealing the incorporation of silver nanoparticles in the PPy matrix. A possible formation mechanism of the PPy-Ag nanocomposite was also proposed. The conductivity of the PPy-Ag nanocomposite was studied using the two probe method and was found to be 4.657×10^{-2} S/cm, whereas that of pure PPy was found to be 9.85×10^{-3} S/cm at room temperature (303 K). The activation energy (E_a) for pure PPy was 0.045 eV, decreasing to 0.034 eV for PPy-Ag nanocomposite.

The synthesized nanocomposite powder is a potential material for the fabrication of gas sensors operating at room temperature. In this work, the PPy-Ag nanocomposite was successfully synthesized via the *in situ* chemical oxidative polymerization of pyrrole in the presence of a colloidal suspension of Ag NPs. The results of TEM, SEM, FTIR, and XRD measurement indicated that preparation of the PPy-Ag nanocomposite was successful. As such, Ag nanoparticles with an average size of ~40 nm were embedded in the PPy matrix. The conductivity of PPy-Ag nanocomposite was studied using the two probe method and was observed to be 5 times higher than that of pure PPy. It was also observed that the E_a decreased from 0.045 eV to 0.034 eV for the PPy-Ag nanocomposite, compared to that of pure PPy. The obtained nanocomposite has potential for the fabrication of gas sensors operating at room temperature.

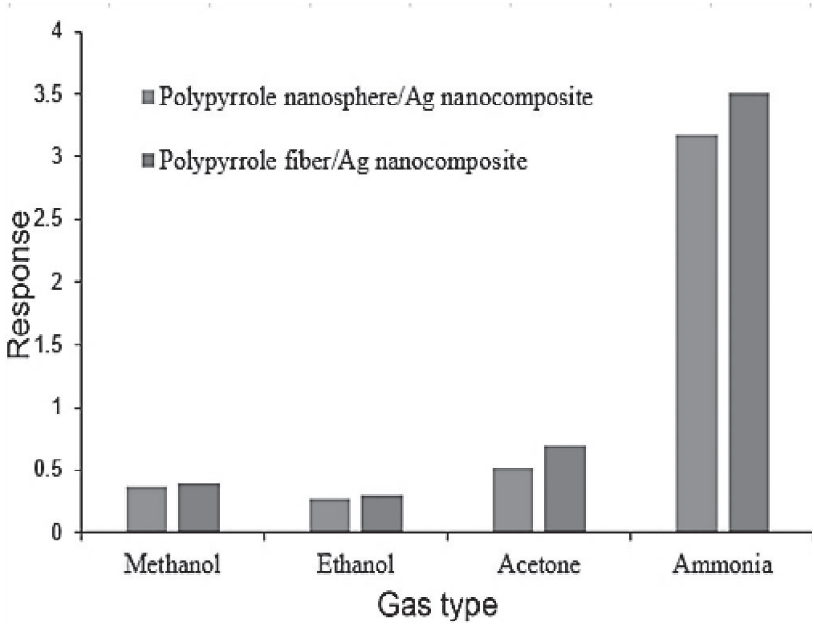

Fig. 3.40 Selectivity investigation of two types of ammonia gas sensors in the presence of different gases with a concentration of 50 ppm.

PPy-Ag nanocomposites were obtained by pyrrole monomer polymerization with silver nitrate, ammonium persulfate, and $LiClO_4$ additives (DOI 10.1007/s12221-018-8097-z). The materials were characterized using SEM imaging and EDS analysis. Thin nanocomposite films obtained from the spin-coating method were used to study their ammonia gas sensing properties. Their ammonia gas sensing performance was better than that of the polypyrrole nanosphere/Ag nanocomposite sensor. The polypyrrole fibre/Ag nanocomposite sensor did not have saturation in the presence of 250 ppm ammonia gas and the polypyrrole nanosphere/Ag nanocomposite saw saturation with a 100 ppm ammonia gas concentration (fig. 3.40).

3.3.7 Pyrolysed metal-nitrogen-carbon (Me-N-C) catalyst reduction of oxygen based on polypyrrole

PANI, PPy, and polythiophene composites have applications in molecular electronics, photovoltaic systems, supercapacitors, and biosensors (MacDiarmid 2001, 14). In particular, such materials can act as electrocatalysts for the oxygen reduction reaction (ORR) (Khomenko and Barsukov 2005, 718) and the materials show electrocatalytic properties in ORR (Qi and Pickup 1998, 21; Posudievsky and Kurys 2004, 2; Hajik and Pron 1993, 55). However, such electrocatalysts currently lack efficiency and have low stability in acidic cathode environments, or high cost (for platinum-containing composites), impeding their commercial use (Kashyam and Zelevay 2006, 443).

Recently, metal-polymer electrocatalysts in the ORR based on nitrogen-containing polymers (primarily PPy and PANI), transition metals (Co, Ni), and carbon substrates (AC, carbon nanotubes) have been proposed as mimetics of cobalt-containing porphyrins. Having substantially inferior activity to the latest generation of electrocatalysts in terms of the ORR, they are much more stable when functioning in an acidic electrolyte. The main feature of such electrocatalysts is high activity in the ORR, even in the absence of heat treatment (Malinauskas and Malinauskiene 2005).

The activity of metal-polymer electrocatalysts in the ORR is related to the existence of the Me-Nx centres in them, although the structure of such centres is not yet fully proven. The authors propose a cobalt-polypyrrole nanocomposite cathode catalyst for fuel cells with high ORR activity and stability during operation. This PPy-Co/C catalyst provided a specific power of ~0.15 W/cm^2 in an H_2-O_2 fuel cell without losing performance for more than 100 h (Yuasa and Yamaguchi 2005, 17).

Using a similar approach, metal-polymer composites based on various metals (Co, Ni) and polymers (PA, PPy, poly-3-methylthiophene) were obtained and their electrocatalytic properties in ORR were compared. The PPy-Co/C electrocatalyst was more active in this process, while PANI-Co/C provided a higher current density, but a much lower open circuit potential. In the absence of d-metal, the polymer/C electrocatalysts in all cases have lower ORR activity (Reddy and Rajalakshmi 2008, 46).

As mentioned above, other nanoscale carbon materials can be used as a carbon substrate to obtain metal-polymeric ORR catalysts along with Ac. In particular, Dodelet (2006) used multi-walled carbon nanotubes to synthesize PPy-Co/C composites, making it possible to increase the activity of the catalyst in ORR compared to analogues based on Ac.

Additonally, the resulting electrocatalyst was characterized by considerable stability during operation in a fuel cell (at least 50 h).

N-CP polymers, as sources of nitrogen and carbon, have an advantage for obtaining Me-N-C RIC catalysts. Their macromolecular structure ensures a uniform distribution of nitrogen atoms in a partially graphitized carbon matrix. The use of N-CP in the formation of Me-N-C electrocatalysts is preferably limited to PANI and PPy, with a mixture of aniline or pyrrole with an oxidizer (Lefevre and Proietti 2009) being used as a nitrogen source alongside the PANI or PPy (Bezerre and Zhang 2008, 53).

The polymerization of the corresponding monomer begins during preparation of the reaction mixture and under moderate temperatures in the initial stages of heat treatment (Altand and Binder 1973, 28). The properties of the ORR of the non-pyrolyzed and highly heat-treated metal-polymer cobalt-containing composite PPy-Co/C were compared. Although both composites showed activity in ORR, in the case of the pyrolyzed catalyst (Co-N-C) this was significantly higher. Considering also that pyrolysis leads to a positive change in the mechanism of the ORR flow (the number of electrons involved in the electrochemical process increases), the authors conclude that heat treatment is a necessary prerequisite for improving the activity of such catalysts. The authors attribute this improvement to the formation by pyrolysis of catalytically active pyrrole and quaternary nitrogen configurations of composites.

The authors found that the use of PANI as a nitrogen donor in the preparation of Me-N-C catalysts during pyrolysis provides high content in the final nitrogen-doped graphene structures, which is related to the similarity between the aromatic structures of PANI and graphene. However, this effect occurs only when there is a transition metal salt in the reaction mixture, with a greater percentage of graphene sheets observed when using Co compared to Fe (MacDiarmid 2001, 14; Millan and Thompson 2009, 34).

The preparation of Fe-N-C, Co-N-C, and Fe-Co-N-C electrocatalysts in ORR, using high-temperature treatment of a mixture of Fe and Co salts, PANI, and reduced OG, was considered by Fu and Liu (2013). According to the authors, the high efficiency of such composites in the specified process in both acidic and alkaline environments provided catalytically active Me-Nx centres (where Me = Fe and Co, x = 2 or 4) embedded in graphene sheets. The most active in ORR was the Fe-Co-N-C composite, which simultaneously contained both metals in its composition. Zhu and Zhang (2016) showed that the presence of iron in Fe-N-C catalysts plays a crucial role in their high activity in the ORR (the absence of metal in the

composite leads to a cathodic shift of Eonset by ~400 mV). In addition, it was shown that nitrogen in Fe-NC catalysts coordinates with Fe, forming active centers in RIC and thereby stabilizing iron in acidic solutions, with the number of active centres controlled by different types of nitrogen—a higher content of pyridine nitrogen led to the formation of more Fe-Nx centres and higher composite activity in the ORR.

Accelerating the rate-limiting oxygen reduction reaction (ORR) at the cathode remains the foremost issue for the commercialization of fuel cells. Transition metal-nitrogen-carbon (M–N/C, M = Fe, Co, etc.) nanostructures are the most promising class of non-precious metal catalysts (NPMCs) with satisfactory activities and stability in practical fuel cell applications. However, the long-debated nature of the active sites and the elusive correlation between structure and performance impede further developments of M–N/C materials. Recent endeavours have sought to elucidate the actual structures of the active sites by adopting various physicochemical techniques to provide a profound mechanistic understanding of M–N/C catalysts with conducting polymers (Shen and Wei 2017, 10). The recognition of the right active centres and site-specific engineering of these nanostructures will provide future directions for designing advantageous M–N/C catalysts.

A new facile template-free method is presented to synthesize Fe-treated N-doped carbon (Fe/N–C) catalysts for the oxygen reduction reaction (ORR) by employing a synthesis protocol of a pyrolysis-leaching-stabilization (PLS) sequence of polypyrrole in the presence of a ferric source, which serves the dual purpose of an oxidant for pyrrole polymerization and a source of iron (Tran and Song 2016, 22).

Each step of the PLS sequence has been assessed in detail in terms of the related structural properties of the resulting carbon catalysts and their effects on ORR activities. These have been elaborated to confirm the validity of the current synthesis protocol. It was found that the prepared carbon catalyst exhibited outstanding high catalytic activity in both alkaline and acidic conditions. The carbon catalyst prepared at a pyrolysis temperature of 900 °C (FePPyC-900) showed a remarkably high ORR activity with an onset potential of 0.96 V (*vs.* RHE), which is similar to that of Pt/C. In contrast, the half-wave potential ($E1/2$) of FePPyC-900 is 0.877 V, which is more positive than Pt/C with the same catalyst loading amount under alkaline conditions. Furthermore, the FePPyC-900 catalyst also illustrates exceptionally high activity under acidic conditions with onset and half-wave potentials of 0.814 and 0.740 V, respectively. These are comparable to those (0.817 and 0.709 V) of the state-of-the-art Pt/C catalyst, which is rarely observed for non-Pt-based carbon catalysts. In

addition, the FePPyC-900 catalyst displays much better stability and methanol tolerance than the Pt/C catalyst and exhibits a four-electron transfer pathway under both alkaline and acidic conditions. Such extraordinarily high ORR activity and stability of the FePPyC-samples can be attributed to the implementation of an extra stabilization step in addition to the conventional sample preparation steps of pyrolysis, subsequent leaching in the current PLS synthesis protocol, and the use of highly conducting PPy as a single precursor of carbon and nitrogen in the presence of Fe.

The main objective of composite science is to fabricate new materials with specific properties, giving high chemical, mechanical, or biological performance. In this research, new conductive nanocomposites of copper metal-organic frameworks (Cu) and polypyrrole (PPy) were fabricated with the aim of exploiting the electrical conductivity of PPy in the final products. The prepared compounds (PPy/*x*%Cu, x = 20, 50, and 80) were investigated using FTIR, PXRD, SEM, TEM, DLS, BET, EDS mapping, cyclic voltammetry (CV), and zeta potential (ξ) measurement. The spherical morphology was confirmed by SEM and TEM analysis.

The PPy/80%Cu-MOF nanocomposite showed the highest ξ potential (-40 mV), demonstrating the stability of the dispersed particles. The results revealed that the nanocomposites have a higher capacitance compared to the pure materials. *In vitro* degradation of the prepared compounds in simulated body fluid (SBF) was studied by EIS (electrochemical impedance spectroscopy) and Tafel polarization tests. Furthermore, *in vitro* biocompatibility of the PPy/*x*%Cu-MOF composite was evaluated on a group of cells, including 3T3 fibroblasts, MCF-7 breast cancer cells, J774.A1 macrophages, and red blood cells (RBCs). The viability of 3T3 fibroblasts, MCF-7, and J774.A1 cells, by the methyl thiazolyl diphenyl-tetrazolium bromide (MTT) method, depended on the Cu-MOF percent and amount of composites.

A hemolytic assay for RBCs exposed to different amounts of the PPy/*x*%Cu-MOF composites showed haematological toxicity of less than 5 % in most concentrations. In addition, to investigate pro-inflammatory activity, J774.A1 macrophages were exposed to non-toxic concentrations of the PPy/*x*%Cu-MOF; no significant change in the expression of two inflammatory genes for COX-2 was observed. Injection of the PPy/*x*%Cu-MOF (5 mg kg^{-1}) into the bloodstream of mice did not increase the level of the liver damage marker enzymes alanine transaminase (ALT) and aspartate transaminase (AST) in serum for the week post-injection. Moreover, we observed a slight but not significant increase in serum copper levels in mice 1 week after injection. According to the results, the

PPy/*x*%Cu-MOF nanocomposites exhibited good *in vitro* and *in vivo* biocompatibility without inducing pro-inflammatory responses in macrophages and show promising potential for different biomedical applications, such as biosensors and drug delivery. The release of curcumin from curcumin-loaded PPy/*x*%Cu-MOF nanocomposites was detectable in the plasma of mice 4 days after administration (Neisi and Ansari-Asl 2019, 178).

Pyrolyzed carbon-supported cobalt polypyrrole (Co-PPy/C) catalysts were prepared with and without three selected dopants—sodium dodecylbenzene sulfonate (DBSNa), sodium para-toluene sulfonate (TSNa), and sodium benzene sulfonate (BSNa)—through chemical oxidation with ferric chloride as an oxidant.

The structures, surfaces, and electrochemical properties of the obtained catalysts were investigated using X-ray diffraction, X-ray photoelectron spectroscopy, Brunauer-Emmitt-Teller (BET) analysis, cyclic voltammetry, the rotating disc electrode technique, and Raman spectroscopy. The introduction of dopants increased the surface concentrations of nitrogen and cobalt, providing more active sites for the oxygen reduction reaction (ORR), and enhanced the degree of graphitization of the carbon support, improving electron conductivity. The electron numbers for the ORR for non-doped and doped Co-PPy/C were evaluated to 2.7–3.1, respectively. The pyrolyzed BSNa-doped Co-PPy/C exhibited the best electrocatalytic activity in relation to the ORR due to its high surface area, larg number of micropores, and relatively high nitrogen and cobalt contents (Feng and Lee 2012, 8).

N-CPs are thus promising compounds for the creation of hybrid ORR catalysts that do not contain precious metals in their composition. Such polymers can be used to produce both pyrolyzed and non-pyrolyzed catalytically active composite materials (Shao and Chang 2016, 116; Wu and More 2011, 332; Tetteh and Lee, 2020). Although metal-polymer electrocatalysts show inferior activity to RICs compared to carbonized Me-N-C catalysts, their study has provided a basis for the fundamental understanding of the nature of ORR active centers and the mechanisms and processes of carbon-deposited metal-nitrogen complexes. Further study will be aimed at the synthesis of inexpensive, stable, and highly active electrocatalysts.

As noted above, in most of the polymeric and Me-N-C electrocatalysts of ORRs described in the literature, PPy or PANI are used as the polymer component or nitrogen source. At the same time, N-CP is promising for creating such catalysts, with its high nitrogen atom content, as well as the different environment in the macromolecule. This contributes to the

formation of more and diverse active centers in the ORR, which, in turn, can improve the efficiency of such metal-polymer and Me-N-C electrocatalysts.

The largest share of the currently proposed Me-N-C systems is covered by Fe-N-C catalysts; this can be explained by their high activity in the ORR (in acidic electrolytes) compared to, for example, cobalt-based analogues. At the same time, the problem of stability of Fe-N-C catalysts during operation in real PE is acute. In the case of Fe-N-C catalysts, dissolved Fe^{2+} ions can interact with H_2O_2 by the Fenton reaction and generate active radical groups. These can further lead to the degradation of catalysts, ionomers, and membranes in PE. Thus, attention in the scientific literature has focused on the urgency of developing new Co-N-C and Mn-N-C electrocatalysts.

The photocatalytic porous structure determining the properties of the interfacial layers and irradiation of the active surface catalyst for substance decomposition have been studied. In the efficient passage of electronic processes between oxide NPs and PANI (PPy), they must have a strong bond, because of the rate of hydroxyl radical generation and completeness of the decomposition of organic and inorganic substances. Thus, analysis of the current literature in this chapter makes it possible to single out the polymers and nanocomposites that are the most promising for the development of new technologies.

The summarised results show that the photocatalysis of composites with TiO_2, C_3N_4, ZnO, noble metals, and MXenes used for water purification, offers the possibility of using sunlight as a sustainable and renewable source of energy. This technology is based on the presence of a semiconductor that is excited by light with an energy higher than its bandgap, inducing the formation of energy-rich electron-hole pairs that can be involved in the ORR. Recent progress has explored the chemical nature of nanoscale semiconductors with the object of improving their electronic and optical properties, and enhancing their photoresponse to visible-light. In addition, nanomaterials have large specific surface areas and size-dependent properties, etc. They also have applications in water purification.

In Chapter 2, the authors discussed the application of various nanomaterials, such as metal nanoparticles, metal oxides, carbon compounds, and filtration membranes in the field of wastewater treatment. Over the last few years, most photocatalysts have been devised for applications in sunlight, but a number of researchers have focused their attention on UV-active systems. As such, here, we will differentiate

between UV and visible light or sunlight-active nanoscale semiconductors (https://doi.org/10.1016/B978-0-12-813926-4.00028-8).

Stable electrode materials based on PANI and PPy have been used for capacitors, batteries, and other electrochemical devices. The functional characteristics of such composites can be significantly higher than those of their constituent components. The researchers studied the interfacial interaction, the electron transfer mechanism, the nature of the appearance of the quasiparticles, and the diffusion characteristics of polymer nanocomposites. Obtaining nanocomposites involves a compromise between the improvement of some characteristics of the material and the deterioration of others. Properly prepared nanomaterials can avoid this degradation, although, at the same time, they must not be expensive. In the future, nanotechnology will see many applications in areas where the unique functional properties of a material are more important than its cost. However, we should not forget that new technologies are usually more complicated than old ones and their development will require a certain leap in the preparation of a new generation of technologists and engineers.

CHAPTER 4

THE PREPARATION AND OPTICAL ABSORPTION OF POLYANILINE-TiO_2 ($C_3N_4O_X$) NANOCOMPOSITES FOR PHOTOCATALYSIS

In this chapter, the authors present some of their results on active nanocomposites with TiO_2, $C_3N_4O_x$, and Ag nanoparticles.

Recently, hazardous and toxic wastes from the textile and dye industry have caused environmental problems. Many of the organic substance used are non-biodegradable and toxic. Azo dyes are chemicals with a double bond between two nitrogen atoms (-N=N-); they are used in the textile, printing, and food industries (Gilia and Novakovic 2017, 12). The dyes RB5 (Reactive Black 5) and Rhodamine B, with N-substituted aromatic biotransformation products, are toxic, mutagenic, and carcinogenic (Jumat and Wei 2017, 7).

Some disinfecting chemical solutions contain substances, such as aldehydes, phenols, and cresols, which are destructive for microorganisms, as well as peroxide compounds (for microorganism cell penetration). In a study of abattoir wastewater in Quebec and Ontario, Canada, typical concentrations of chemical oxygen demand (COD) and suspended solids (TSS) were found to range from 2,333 to 8,627 mg L^{-1} and from 736 to 2,099 mg L^{-1}, respectively (Heinz and Hautzinger 2007). Analysis found that residual blood was a principal source of organic matter found in wastewater. To achieve compliance with state and central environment regulations, effective treatment of this wastewater and the removal of such pollutants is essential before discharge into the environment. The treatment of this wastewater necessarily reduces its critical effects on environmental and human health. Photocatalytic degradation is an efficient and economical method that is attracting increasing attention (Thabo and Maurice 2014). It is particularly useful for cleaning biologically toxic or nondegradable materials, such as aromatics, pesticides, petroleum constituents, and volatile organic compounds, in wastewater. Through this process, contaminating materials are, to a large extent, converted into

stable inorganic compounds, such as water, carbon dioxide, and salts, i.e. they undergo mineralization (Ghazzal and Kebaili 2012).

TiO_2 is an excellent photocatalyst due to its high chemical stability and photocatalytic activity (Luna and Dragoe 2017, 26). However, TiO_2 has a wide bandgap, restricting its use to UV light activation; UV light only accounts for 3–5 % of solar energy utilization (Zahornyi 2017). As such, the goal is to modify the optical response of TiO_2 from UV to the visible light range by shortening its bandgap.

Recently, conducting polymers have shown potential as photosensitizers under UV irradiation due to their low bandgap and π-π* transition. Electron excitation occurs from the highest occupied molecular orbital (HMO) to the lowest unoccupied molecular orbital (LUMO) (Olad and Behboudi 2012, 35; Li and Wu 2015, 3; Ghosh and Kouame 2015, 5).

Zhu and Hu reported the photocatalytic degradation of methyl orange using polythiophene-titanium dioxide composites (Zhu and Xu 2010). Gu and Wang observed the photocatalytic degradation of Rhodamine B using a novel TiO_2-polyaniline composite (Gu and Wang 2012, 5). The prepared composite turned out to be an efficient photocatalyst under visible light irradiation. The degradation of recalcitrant aromatic compounds including phenol and p-cresol in abattoir wastewater using a TiO_2-ZnO composite doped by PANI was evaluated. Detergents used for cleaning and residual blood were found to be sources of organic matter in the wastewater. The *in situ* chemical oxidative polymerization of aniline was used to prepare the composite, which was tested on an annular reactor fitted with a 25W UV-C lamp (Thabo and Maurice 2014). The photocatalytic activity of hierarchical rutile TiO_2 nanorod spheres was found to be higher than that of the commercial photocatalyst P25 (Xu and Jia 2007, 7).

A new PANI-TiO_2 nanocomposite with a bionic structure synthesized by a facile hydrothermal method was investigated and the photocatalytic activity of TiO_2 under visible light (>400 nm) was increased by doping. Numerous groups utilize transition metal ions, such as Fe, Au, Ag, V, Cr, and Ni, to hinder the recombination process (Luna and Dragoe 2017, 26). The recombination process in TiO_2 can also be suppressed by preparing PANI-TiO_2 composites—this is a promising, though poorly investigated, approach. The advantage of PANI is that it is a conductive, non-toxic, and thermally stable polymer, with a high absorption coefficient in the visible spectrum (Gopalakrishnan and Elango 2012, 4).

PANI-TiO_2 composites can be prepared through chemical oxidation of aniline in the presence of TiO_2 particles (Heshmatpour 2017). Aniline

oxidation can yield different products as oligomers and oxidation products with an amino group in the ortho-position (Zaleska-Medynska 2018), presenting imperfections that influence aggregate size (Radoičić 2017).

Conducting polymers are finding increasing use in various electronic devices, such as chemical sensors, light-emitting diodes, and electrochromic displays. Among these polymers, polyaniline occupies a special place, due its availability, ease of synthesis, and resistance to oxidation in air. It exhibits a number of other properties, including multicolour electrochromism and chemical sensitivity.

The titanium oxide and polyaniline complex has become a hot research topic. TiO_2 nanomaterials have high catalytic activity, good stability, a high yield of hydroxyl radicals, and limited corrosion, etc.; they are used in anticorrosion coatings, water purification, and sterilization, as well as exhibiting antibacterial properties. Polyaniline has good environmental stability; in the visible region, it sees strong absorption, acts as an electron donor, and has excellent hole transport. Patents CN102432876A and CN102866181A disclose a process for preparing a polyaniline-titanium dioxide nanocomposite. Patent CN104084241A discloses a 3D flower structure titanium dioxide-polyaniline photocatalyst and preparation method.

The technical solution provided in patent CN 105542456 A is devoted to a Si-TiO_2-PANI (silicon-titanium dioxide-polyaniline) composite material assembled with a ternary hierarchical structure, as well as its application. PANI with a particle size of 10–60 nm (p-type semiconductor) has been grown in TiO_2 rutile nanorods with diameters of 40–250 nm. A photocatalytic activity test was carried out using methylene blue as a simple model pollutant. The concentration of methylene blue changed over time; the methylene blue dye was degraded for 7 h and the degradation was found to be more efficient with this composite than with pure TiO_2 and pure PANI nanorods. Thus, it remains an important task to create a composite photogenerator based on TiO_2 that can control the distribution of h^+ (generation) and be applied for the effective destruction of phenol with a high concentration of oxide radicals. Polyaniline (PANI) can be used as a photosensitizer to prepare the polyaniline-TiO_2 (PANI-TiO_2) nanocomposite for use as a photocatalyst.

4.1 Synthesis and Morphology of TiO_2 Nanocomposites

Doped polyaniline was synthesized with PANI-TiO_2 using the “in situ” polymerization method (Zahornyi 2018). First, TiO_2 nanoparticles were modified in a water solution of GHAn (SAn) using the homogenizer

ULAB2200 (Germany) at a speed of 300 min^{-1} for 1 h. Then, the APS solution was added dropwise at a temperature of 0 °C. Polymerization on the surface of the anatase was carried out in a medium of pH 2–4, depending on the GHAn content of the mixture (table 4.1). The polymerization process gave a dark green product. The nanocomposites obtained were washed with deionized water, acetone, and ethanol. Then, the PANI-TiO_2 nanocomposites were dried at 50 °C for 24 h.

Table 4.1 The composition of the reaction mixture and parameters of the polymerization process (authors)

Sample N	Quantity monomer, g	Ratio monomer-TiO_2, g/g	pH	t, min. (green colour)	Weight product
1	0.025	0.005	2.40	80	4.98
2	0.05	0.01	2.37	25	5.00
3	0.1	0.02	2.45	30	4.70
4	0.150	0.03	2.6	35	4.90

Note: Serial composites 1-4 with TiO_2 (anatase, IPMS).

The polymerization process with TiO_2 particles was slowed down at with a smaller concentration of the monomer. When the monomer concentration was increased by 2–2.5 times, the polymerization process speeded up. With a monomer concentration of 0.05–0.1g/60ml in the volume reaction mixture, the polymerization time did not vary practically. The pH value decreased to 2.50 when an oxidizer was added to the reaction mixture for 10 min (oligomers appeared). The mixture was mixed for 15 min. and became green in colour (pH 2.40) with the formation of a polymer layer on the TiO_2 surface particles.

4.1.1 TiO_2 surface structure systems

The results of high resolution SEM presented in fig. 4.1 show that increasing concentrations of polymer PANI influence the form and orientation of the TiO_2 particles. For example, with a small concentration of polymer in sample №1 (25 mg GHAn in the reaction mixture) the compacting TiO_2 particles were not all surrounded by the fibre threads in comparison to sample №3.

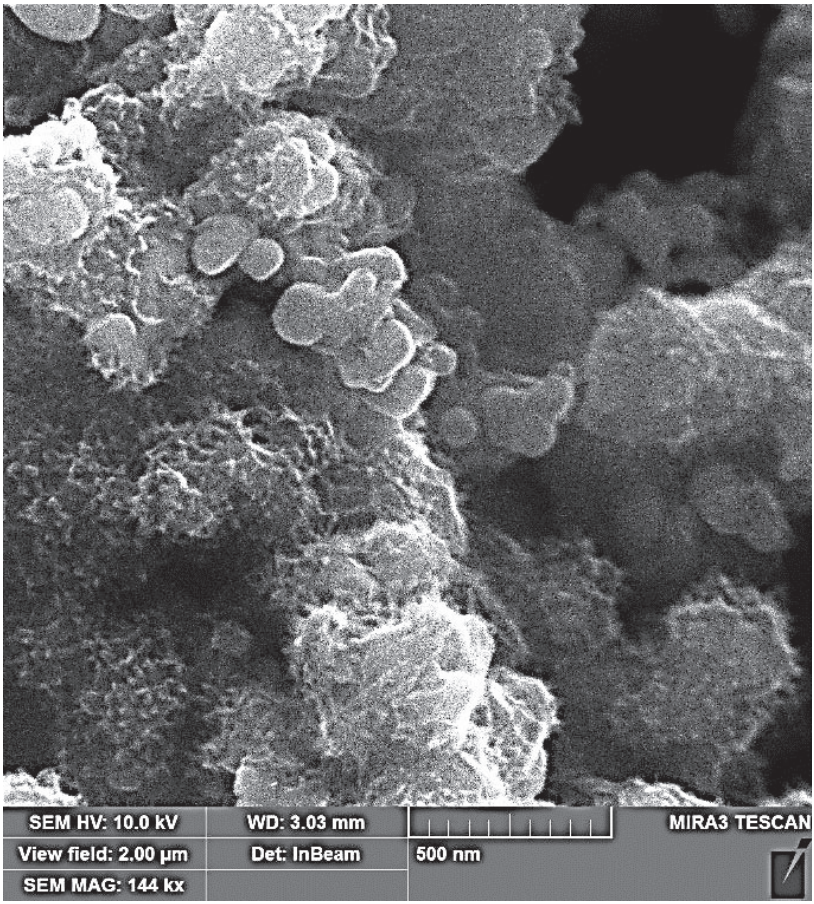

(**a**)

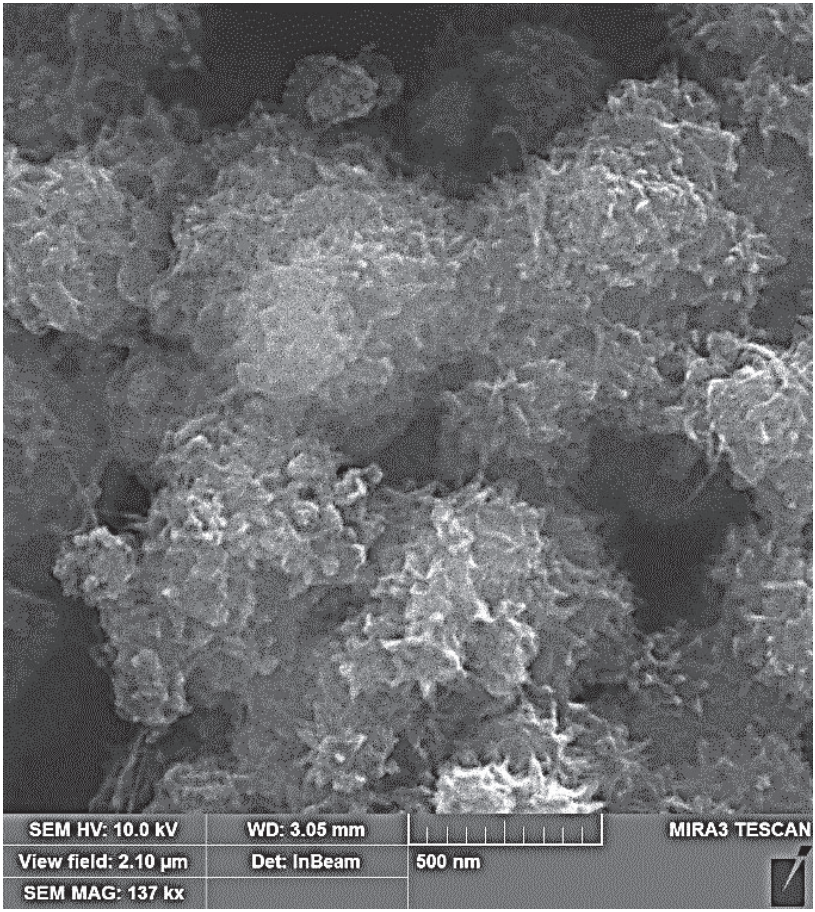

(**b**)

Fig.4.1 SEM images of samples of polymer-TiO_2: (a) №1; (b) №3.

4.2 Spectral Characterization of TiO_2 Nanocomposites

XRD patterns for PANI-modified TiO_2 (50 and 60 wt%) are presented in fig. 4.2. A diffraction peak is found at 25.3° in the PANI-TiO_2 composite samples. Anatase peaks appeared at 37.8° and 48.0° with the 101, 004, and 200 reflections, respectively. The anatase phase was indexed from the patterns and the rutile and brookite phases of TiO_2 were absent.

Moreover, the TiO_2 content in the polyaniline nanocomposites does not practically change the peak positions; this content was slightly lower than 50 % TiO_2, which may be due to the lower degree of doping of PANI. We suggest that the polymer is in an amorphous state in the composite (fig. 4.2b). Broad peaks at 20 and 25°, suggesting the high crystallinity of the PANI, were found to be absent in the composites.

PANI encapsulated the titanium dioxide nanoparticles via the polymerization of aniline on the surface of TiO_2 nanoparticles. The IR, SEM, and EPR techniques were used to study the mechanism of electron interaction in the PANI-TiO_2 nanocomposite. The resulting PANI-modified TiO_2 composites exhibited significantly higher photocatalytic activity than neat PANI in the degradation of methylene blue (MB) in aqueous solution under UV irradiation.

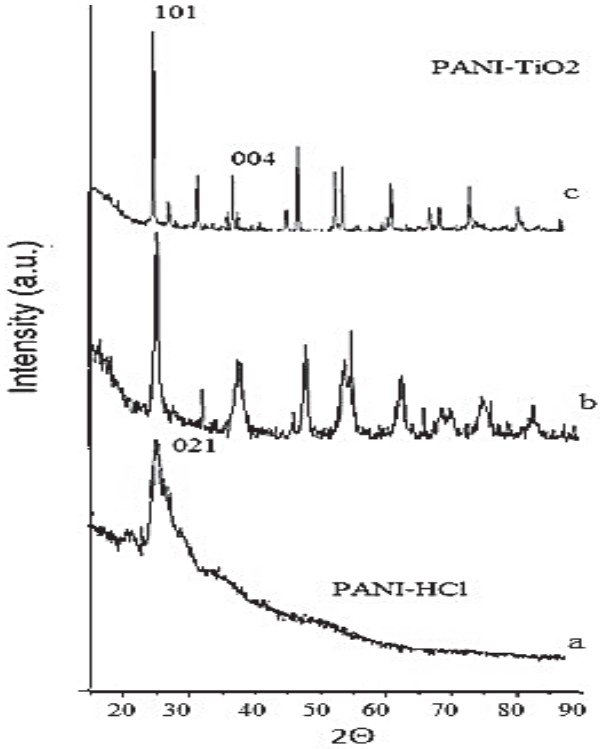

Fig. 4.2 XRD patterns: (a) doped PANI; (b) PANI with 50 % TiO_2; (c) PANI with 60 % TiO_2.

Study of the surface structure of doped polymer-TiO_2 powders shows the dominant influence of TiO_2 dispersion as a process for their formation and sorption activity. The maximum adsorption activity of the polymer-TiO_2 was shown at 95 wt% of TiO_2 (5 nm) content (sample №1). The results of EPR analysis of TiO_2 (5nm), doped polymer, and nanocomposites with TiO_2 concentrations of 25–95 wt% at 77–300 K are presented in fig 4.3. In pure TiO_2, an intense signal was observed with a line width of 3.2 G and g = 2.0033. This signal was attributed to the surface centres. The centres are associated with defects in O_2^- or OH.

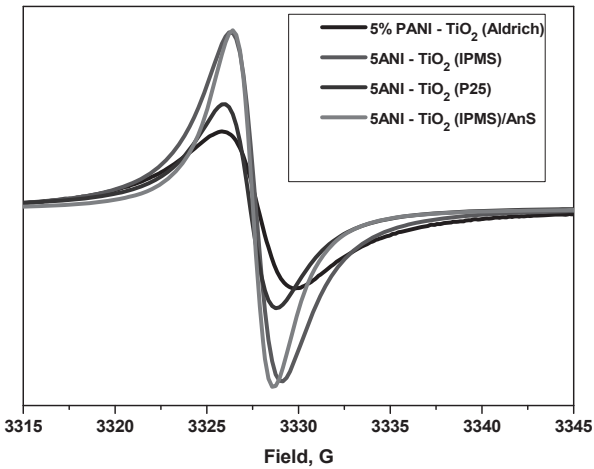

Fig. 4.3 EPR line widths in the investigated polymer-TiO_2 samples.

The non-linear nature of dH dependence of TiO_2 (5nm) content can be explained by the electronic interaction between the polymer and TiO_2 because of the decreasing degree of polymer doping in the TiO_2 systems.

4.3 Photocatalytic Activity Test

Photocatalytic activity in the removal of phenol (initial concentration of 50 mg/L) in a 4 ml reactor with oxygen gas was evaluated according to the method of the Laboratoire de Chimie-Physique CNRS UMR 8000. The temperature was kept at 20 °C and the weight of the

photocatalysts used for each experiment was 3.6 mg. A 300 W lamp of Xe with a cut-off filter (λ = 420 nm) served as a UV and visible light source. The photocatalytic activity of PANI-TiO_2 was evaluated for the degradation of phenol. The photocatalytic degradation of phenol was measured at ambient pressure and room temperature in a photoreactor. A phenol aqueous solution with an initial concentration of 50 mg• L^{-1} was prepared with the nanocomposite powder. Before irradiation, the suspension was left in the dark for 30 min. to achieve adsorption-desorption equilibrium between the photocatalyst and the phenol. The photocatalytic reaction was started through irradiation of the suspension with a lamp. Air with oxygen was supplied for the adsorption-desorption process under light irradiation. Then, 0.5 ml of the phenol suspension was withdrawn at regular time intervals and it was centrifuged at 10 rpm for 15 min. The concentration of the remaining phenol was analyzed using a UV-visible spectrometer and chromatography and the percentage of degradation was calculated (UV-vis absorption spectra Cary 300 Scan, UV-vis-NIR spectrophotometer, Australia, chromatography 1260 Infinity of S/N DEACN 25033).

The photocatalytic activity of synthesized systems (k1-k3) with different concentrations of the polymer were tested over 10–60 min. First, the experiments were performed in darkness for 30 min. with the absence of UV irradiation. Results showed adsorption of the polymer on the TiO_2 surface in the region of 200–275 nm. When the polymer concentration increased, the intensity of the phenol peak area decreased, especially after 40 min. under UV contact. A more rapid process of phenol degradation occurred after the first 10 min. with the use of system №1 with a monomer content of 25 mg (fig. 4.4a).

In comparison to systems using a GHAn monomer (№1 and №4), a new absorption band (fig. 4.5) can be seen in the region of 400–450 nm, which may be connected to the strong vibrations between the benzoic ring and sulfur oxide group in the polymer (sample N).

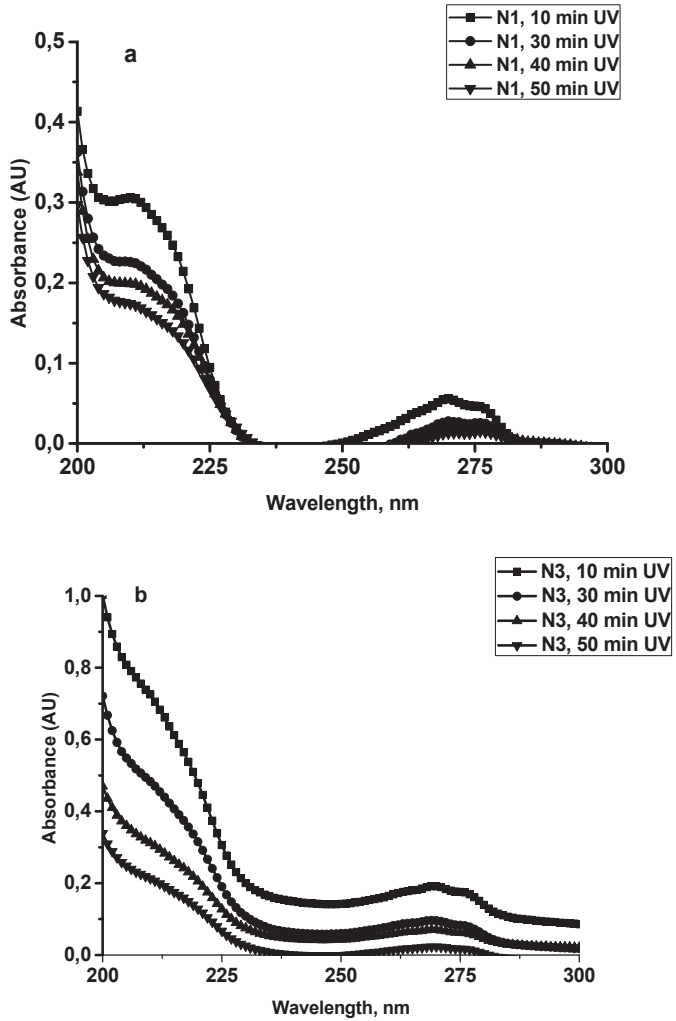

Fig. 4.4 UV spectra of phenol degradation with polymer-TiO_2 contact under UV irradiation over 10-50 min.: (a) №1; (b) №3.

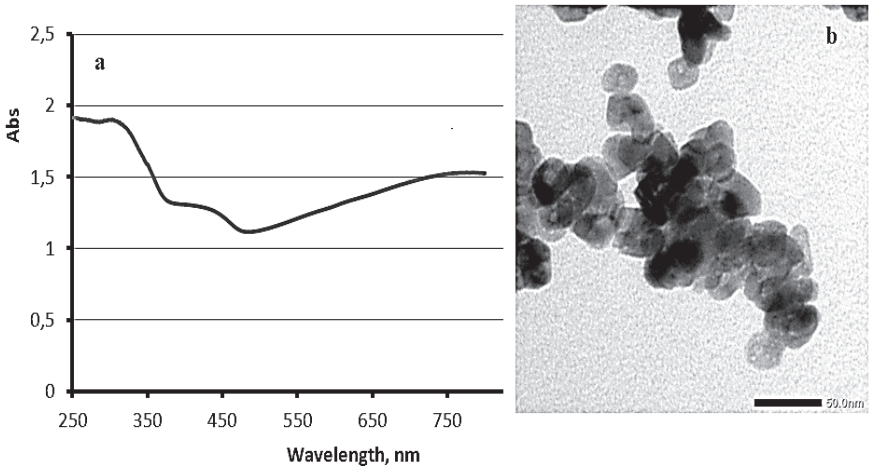

Fig. 4.5 Characteristics of system N (monomer sulfate aniline SAn): (a) UV-vis spectrum of system N; (b) TEM image particles of system N.

4.3.1 Mechanism of irradiation of PANI-TiO_2 nanocomposites

In polyaniline formed in a doped state, the redistribution of electron density occurs between the atomic orbitals of nitrogen and carbon. As a result, the formation of (N-H)-bonds between nitrogen and protons increase N-C polarity ionic bonds. There is a partial loss of the density of π-electrons of nitrogen, increasing the positive charge on the nitrogen atom of polyaniline. In addition, the polymer chain becomes flexible because of the transformation of the double bonds of N=C to single bond N-C. In polarons formed on the nitrogen atoms, the transport of electrons along the polymer chain are followed by a jump to a neighbouring chain. When the electrons of the nitrogen atom pass to the neighbouring nitrogen atoms in the polyaniline chain, for example, to the left, holes are formed h^+, starting from left to right (fig. 4.6). The authors noted the possibility of a potential barrier in the migration of electrons in PANI (MacDiarmid 2001), therefore, with control of the thickness and molecular weight, polymer crystallinity was observed.

In the case of titanium dioxide, there may also be a potential barrier in the grain region. According to the authors, this is due to chemisorbed negative oxygen ions on the surface of TiO_2 grains. Electrons overcome the barrier in the grain region and the width and height of the barrier

depends on the shape and size of the grain, the number of borders, and the particle size, etc. Thus, by doping TiO_2 with PANI, we can obtain a strong electrostatic interaction with a decrease in the potential barrier.

The authors noted that when PANI-TiO_2 composites were illuminated with UV light, both TiO_2 and PANI absorbed photons to generate electron-hole pairs. The relative energy levels of PANI (HOMO, p-orbital, and LUMO, π*-orbital) and TiO_2 (conduction band (CB) and valence band (VB)) create a synergistic effect. Photogenerated holes in the TiO_2 VB directly are transferred to the HOMO of PANI. Simultaneously, the photogenerated electrons are transferred to the CB of TiO_2 and charge separation with stabilization occurs. As a result, electron-hole pairs were effectively separated and photocatalytic capability improved remarkably. Electrons in an excited-state were injected into a TiO_2 conducting band with a synergistic effect. A positively charged hole was formed by electron migration from the TiO_2 VB to the π-orbital of PANI. Subsequently, excited-state electrons and holes may transfer to the surface to react with water and oxygen (phenol), yielding hydroxyl and superoxide radicals, which oxidize organic pollutants. As a result, rapid charge separation and slow charge recombination occur, resulting in higher the photocatalytic activity of TiO_2 composites.

4.3.2 Nanostructured optical composites of $C_3N_4O_x$-polyaniline and $C_3N_4O_x$-TiO_2

This section is devoted to the synthesis of TiO_2 ($C_3N_4O_x$)-PANI composites with optical properties. The bandgap decreased from 3.2 to 2.3 eV in the nanocomposites and one-step synthesis was used to realize their synergistic effect and enhance photocatalytic activity.

The combination of g-C_3N_4 and TiO_2 (anatase) enhanced photocatalytic activity for the inactivation of bacteria in water; however, g-C_3N_4-TiO_2 and g-C_3N_4 could only make limited use of solar energy because they exhibit photoactivity in the near-blue visible region only (at wavelengths of less than 460 nm).

$C_3N_4O_x$ samples synthesized in IPMS are photosensitive in the visible spectrum. Combining $C_3N_4O_x$ with TiO_2 (polyaniline) allows us to obtain a new and effective semiconductor photocatalyst.

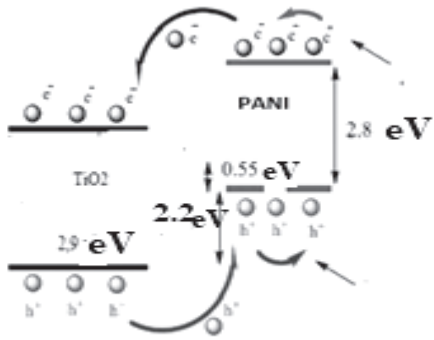

Fig. 4.6 Photocatalytic mechanism for PANI-TiO_2.

Functional components of synthesized nanocomposites:

1. TiO_2 nanoparticles have virucidal and antiviral properties (https://doi.org/10.15407/microbiolj81.05.073).
   These nanoparticles show good results in photoelectrocatalysis (https://DOI10.15421/081914).
2. The combination of PANI nanoparticles with TiO_2 and $C_3N_4O_x$ can create excited-state electron (e^-) and hole (h^+) pairs, with an O_2 and water vapour reaction in the atmosphere producing superoxide ions (O_2^-) and hydroxyl radicals (OH•) under irradiation. The O_2^- and OH• radicals act as agents for the destruction of toxic chemical compounds and bacterial cells, forming CO_2 and water. Mesoporous polyaniline produces h+ in the valence band due to its electronic structure and conductivity.
3. Defects in the structure of $C_3N_4O_x$ with good optical characteristics allow us to combine it with TiO_2 and PANI to increase optical and photocatalytic activity for use in optics and the disinfection of air.

We report on PANI-$C_3N_4O_x$ composite synthesis with g-C_3N_4 (O ~5 %) and anatase nanoparticles. The prepared hybrid material has the characteristics of PANI and $C_3N_4O_x$ with specific morphological and optical properties.

The spectra for polyaniline-$C_3N_4O_x$ samples have absorption bands in the region of 200–400 nm and 500–700 nm. Thus, the synthesized samples can absorb light at both UV and visible intervals. Due to the formation of a polymer layer and electronic transitions between PANI and $C_3N_4O_x$, a charge transfer complex is possible.

The new composite was obtained using a gas-phase method with $C_3N_4O_x$ deposition on anatase powder (~10 nm). The synthesized product was analyzed using X-ray analysis, scanning electron microscopy, X-ray photoelectron spectroscopy, and Fourier transform infrared spectroscopy. SEM images of $C_3N_4O_x$-TiO_2 (anatase) composite nanoparticles show the arrangement of TiO_2 in the form of separated nanoparticles and clusters between the plates and the channels of the porous scaled O-g-C_3N_4 plates (fig. 4.7b).

The bandgap energies of the materials were estimated using the Kubelky-Munch equation. The bandgap (E_g) of the obtained samples was evaluated at the point of intersection with the abscissa tangent to the long-wave edge of the band of fundamental absorption.

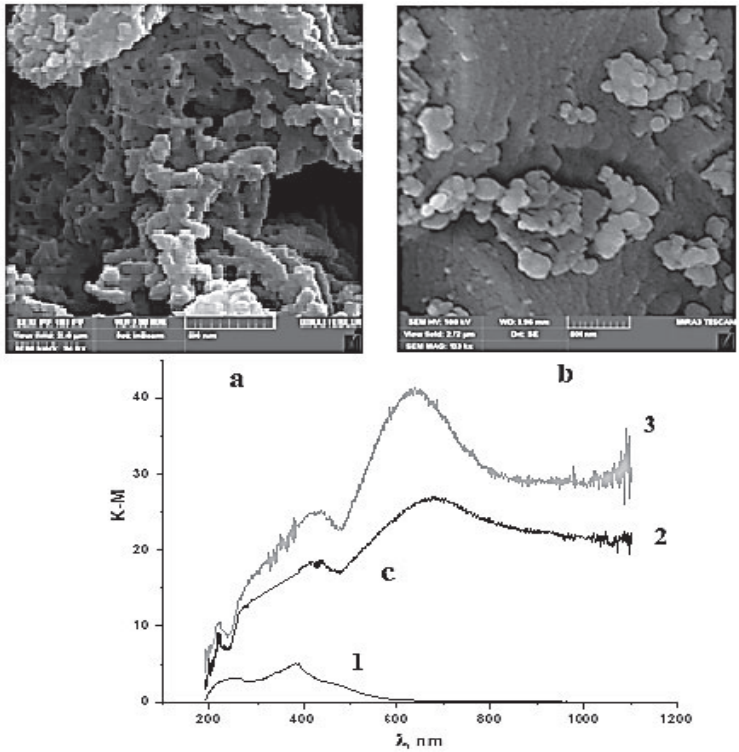

Fig. 4.7 SEM images: C_3N_4Ox-polyaniline (a); $C_3N_4O_x$-TiO_2 (b); (c) optical spectra absorbance of C_3N_4Ox (1), 5 % PANI+ C_3N_4Ox (2), 25 % PANI+ C_3N_4Ox (3).

Estimation of the values of E_g synthesized samples (fig. 4.8) shows that oxygen admission leads to the bandgap of the synthesized powders narrowing (from 2.6 eV for pure g-C_3N_4 to 2.35 eV, 2.3 eV, and 2.25 eV for Og-C_3N_4- TiO_2-1.5 h samples, Og-C_3N_4-TiO_2-0.5h, and Og-C_3N_4 respectively). Increasing light absorption and narrowing the bandgap of nitride-carbon materials during oxygen doping agrees well with the literature and is predicted to result in higher photocatalytic activity.

A bathochromic shift in the long-wavelength edge of the fundamental absorption band was observed in the spectra of the samples under UV and visible spectroscopy. The bandgap decreases from 2.6 eV to 2.3 eV due to doping by oxygen and the formation of active centres along the heterojunction between phases.

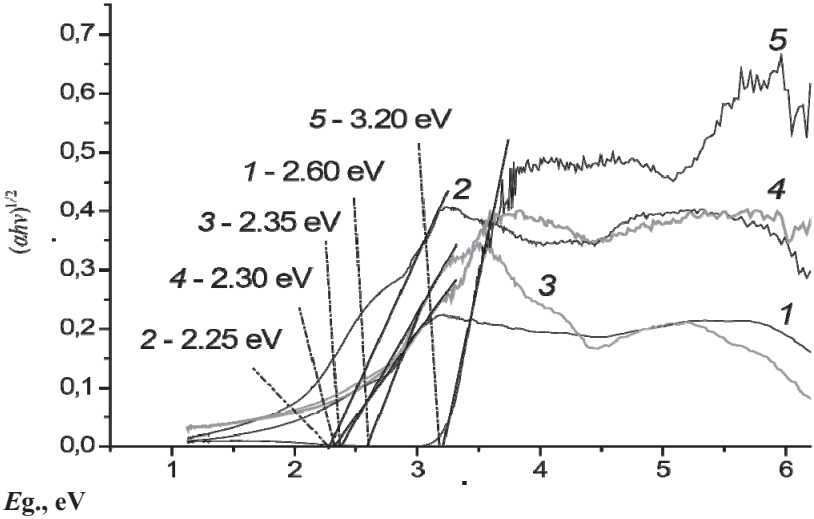

Fig. 4.8 Experimental estimation of bandgap energy E_g for samples: 1) g-C_3N_4; 2) O-gC_3N_4; 3) Og-C_3N_4-TiO_2-1.5h composite; 4) Og-C_3N_4-TiO_2-0.5h; 5) TiO_2 (anatase).

The conductivity of pure PANI and PANI-TiO_2 nanocomposites with different TiO_2 contents (10 wt%, 20 wt%, and 40 wt%) was measured and compared. The conductivity was found to be as follows: PANI-TiO_2 (10 wt%) > PANI > PANI-TiO_2 (20 wt%) > PANI-TiO_2 (40 wt%). It is interesting to note that PANI-TiO_2 (10 wt%) has higher conductivity than PANI. The p-type semiconductor (PANI) is in contact with an n-type semiconductor (TiO_2) and the electron from the valence band of TiO_2 will be extracted and added to the LUMO of PANI with an increase in its conductivity; however, PANI has higher conductivity than PANI-TiO_2 (20 wt%) and PANI-TiO_2 (40 wt%) (fig. 4.9).

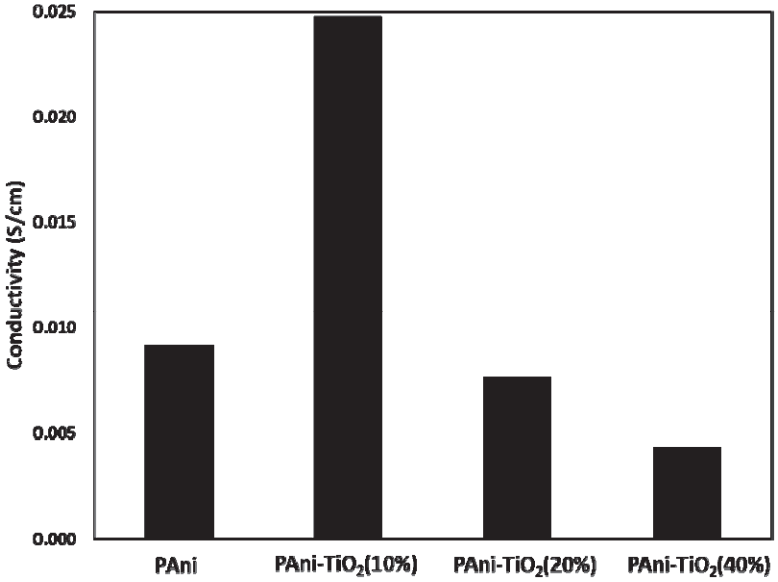

Fig. 4.9 Conductivity of PANI and PANI-TiO_2 nanocomposites with different TiO_2 contents.

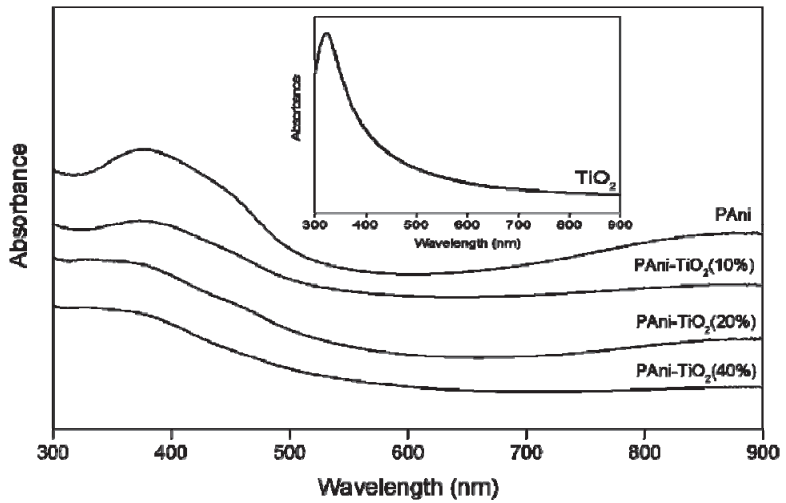

Fig. 4.10 UV-vis spectra of TiO_2, PANI and PANI-TiO_2 nanocomposites with different TiO_2 contents.

The conducting behaviour of PANI was investigated for the PANI and PANI-TiO_2 nanocomposites obtained. Spectra showed that all the nanocomposites used in this work have similar peaks in UV-vis spectra. The peak at 389 nm indicates a π-*π transition of the benzenoid ring and the shoulder peak of approximately 800 nm indicated the emeraldine salt phase of doped PANI. UV-vis spectra indicate the presence of conductive PANI in the synthesized nanocomposites. The absorption of TiO_2 has a peak at around 328 nm, as shown in fig. 4.10. The estimated bandgap energies of pure TiO_2 and PANI-TiO_2 (10 wt%) are approximately 3.22 eV and 2.10 eV. The presence of PANI in PANI-TiO_2 (10 wt%) nanocomposites successfully reduced the bandgap of TiO_2 from UV to visible light region.

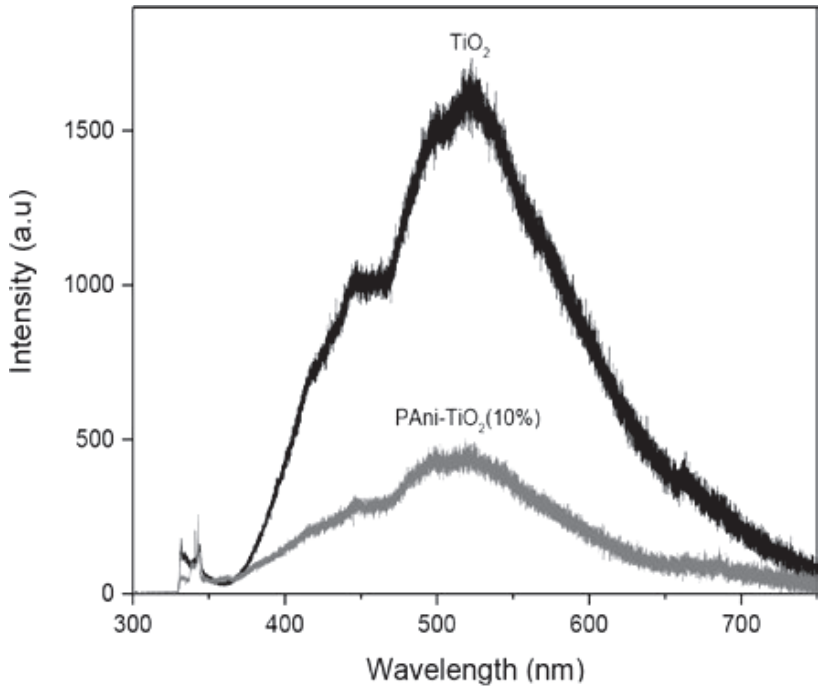

Fig. 4.11 Pl spectra of TiO_2 and PANI-TiO_2 (10 %).

Figure 4.11 shows photoluminescence analysis of pure TiO_2 and PANI-TiO_2 (10 wt%). PANI-TiO_2 (10 wt%) displays lower intensity than TiO_2, which indicates a lower electron-hole recombination rate and better

photocatalytic activity than TiO_2. PANI acts as an electron donor and efficient hole transporter under visible light illumination. As such, a low photogenerated electron-hole recombination rate was achieved with an increase in photocatalytic efficiency.

The bandgap of PANI-TiO_2 (10 wt%) is 2.10 eV, which is narrower than the 3.22 eV of TiO_2. When PANI absorbs energy that is equal to or larger than the bandgap, an electron is promoted from HOMO to LUMO. PANI acts as a photosensitizer, responding to visible light. Photogenerated electrons in LUMO transfer into the lower conduction band of TiO_2. This phenomenon increases the spatial separation of charge carriers, reduces the probability of recombination, and increases the production of OH• and superoxide ions. The synergistic interaction of conductive PANI and TiO_2 is well matched. The authors report that the position of the conduction band is perfectly doped below LUMO of PANI and causes electrons to be easily transferred from PANI to TiO_2. TiO_2 is triggered by PANI to produce O_2^-. The strong oxidation power of h^+ enables it to react with water to generate highly active OH•. Repeated attacks by O_2^- and OH• on organic pollutants will consequently degrade these organic compounds to CO_2 and H_2O. In addition, the FESEM image also reveals the nanorod/nanotube morphology of PANI-TiO_2 (10 wt%) and shows a better dispersion of TiO_2 compared to other samples. RB5 molecules are easily adsorbed to nanocomposites and further mineralized to CO_2 and H_2O.

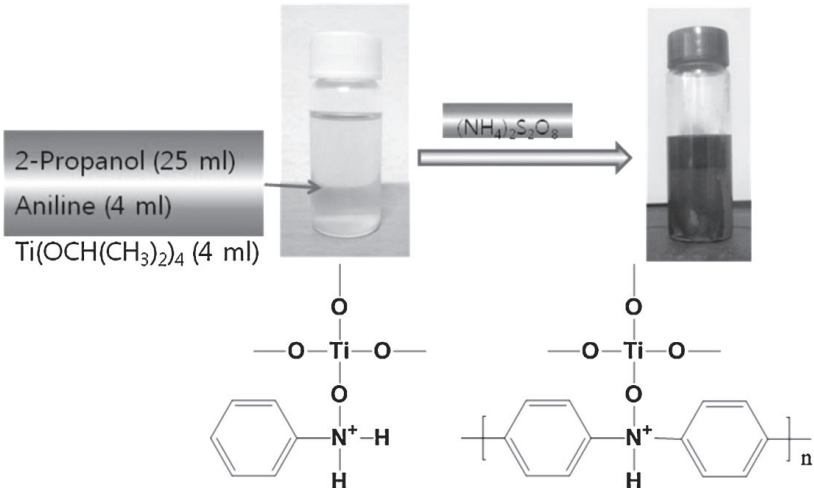

Fig. 4.12 Schematic representation of the synthetic process and possible chemical structures.

4.3.3 Synthesis of nanosized composites based on an oxide semiconductor and metal

Nanocomposites based on magnetite and anatase doped with noble metal cations have applications as new biocompatible materials with unique physicochemical properties. Coating of magnetite nanoparticles by noble metals leads to their stabilization in corrosive biological media and gives them particular electrical, magnetic, catalytic, and plasmonic properties as well. Nanoparticles of magnetite and core-shell type composites, Fe_3O_4-Ag^0 and Fe_3O_4-Au^0, were formed under rotation-corrosion dispersion conditions on a steel 3 (St3) surface in contact with distilled water and water solutions of argentum nitrate and free flowing oxygen into the reaction zone.

Our team synthesized bioactive magnetite and anatase doped cations of Ag, Pt, and Pd with a concentration in the interval of 0–5 wt%. The concentration of the noble metals influenced the surface structure and magnetic properties of the prepared UV irradiated nanocomposites doped with Ag, Pt, and Pd. EDAX analysis testifies to the composition of TiO_2-Ag (Ti-58.6 wt%, O-36.69 wt%, Ag-4.12 wt%) and Fe_3O_4-Ag (Fe-50.84 wt%, O-44.92 wt%, Ag-4.23 wt%).

Spectral methods of investigation (XRD, IR, and Raman) established the presence of silver in the concentration range 0–8 wt%. The presence of Ag on the surface and in the lattice of TiO_2 promotes efficient electronic transitions during the formation of the Schottky barrier. The formation of titanium-based nanostructures doped with Ag by chemical deposition are presented.

XRD analysis was carried out for the range $2\Theta = 20–80°$ as shown in fig. 4.13. All the diffraction peaks correspond to the anatase phase of TiO_2 (JCPD Card: 21-1272). No diffraction peaks were found in the impurity phases of Ag and AgO, even at a doping concentration of 4 wt%. The absence of an impurity phase revealed the successful incorporation of silver ions into the structure of the TiO_2 matrix. SEM images of doped TiO_2 confirm the deposition of silver on the oxide surface (fig. 4.14).

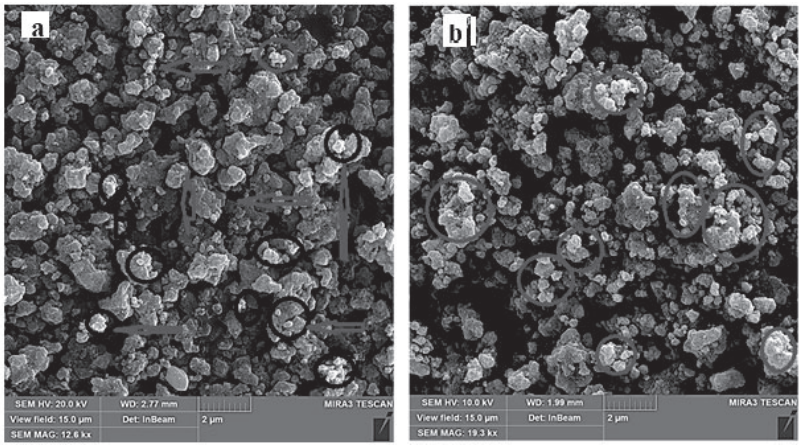

Fig. 4.14 SEM images of doped TiO_2 with Ag, wt%: (a) 4; (b) 8.

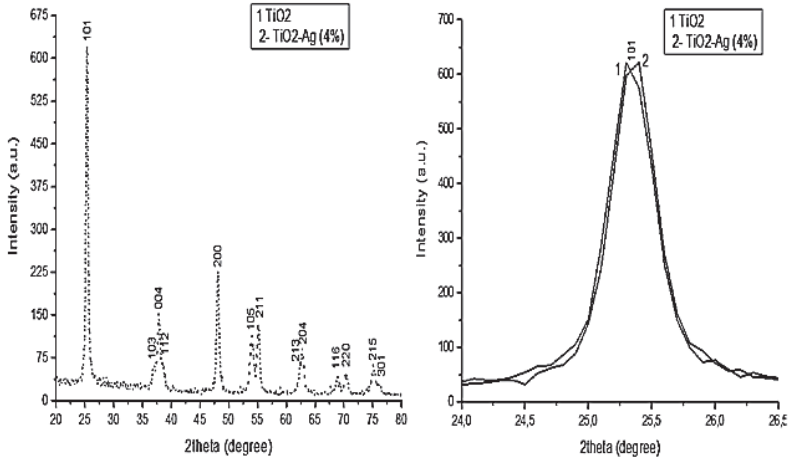

Fig. 4.13 XRD spectra of doped TiO_2.

Raman spectroscopy was performed for the surface investigation of pure TiO_2 and TiO_2-Ag phases and we note the region of 300–700 cm^{-1}. Raman bands were observed at 395, 514, and 637 cm^{-1} for pure TiO_2 and TiO_2-Ag (fig. 4.15). There were no peaks marking the presence of silver oxide, even in the highly doped sample; however, there were some slight shifts in Raman peaks with low intensity in comparison to TiO_2 when

silver ion content increased due to the size of the particles. There is a high-frequency shift and increase in the half-width of the E_g (1) band at 142 cm^{-1} and E_g (2) band at 196 cm^{-1}, while the B_{1g} band at 636 cm^{-1} and A_{1g}/B_{1g} at 513 cm^{-1} show low-frequency shifts and a significant increase in half-width in the Raman spectra of the silver-doped nanopowders. A wide complex band in the range of 220–300 cm^{-1} is due to the processes of multiphonon scattering. In the Raman spectra, because all the oscillations primarily move oxygen atoms, the introduction of silver atoms changes the local coordination of oxygen around Ti^{4+}.

As such, we can assume that the presence of structural defects on the surface of the anatase leads to the creation of acceptor and donor centres in the oxide conduction band and holes in the valence band. The surface defects create narrow donor zones of electronic energy states near the bottom of the conduction band belonging to small traps. Deep traps associated with disturbances in the structure of the crystalline phase of anatase TiO_2 are due to oxygen vacancies. It is possible to form several localized electronic states for anatase. Additionally, as EPR studies have shown, there are ionic Ti^{3+} centres in the TiO_2 samples. Their concentration depends on the method of anatase synthesis and the presence of free hydroxyl and O_2 anion radicals. The energy electron structure within the bandgap in nanocrystalline doped samples is complex. This contributes to the sensitization of semiconductor nanoparticles to visible light, improves the relaxation of electronic excitation, and creates conditions to reduce losses in photogenerated charge carriers. Doping with Ag is important for TiO_2 and electron transfer occurs from Ag to the conducting band of the oxide, achieving Fermi level equilibrium following by localized surface plasmon resonance. Step by step, we aim to discover all the components and deliver all the evidence of such a concept for the development of an effective antimicrobial guard.

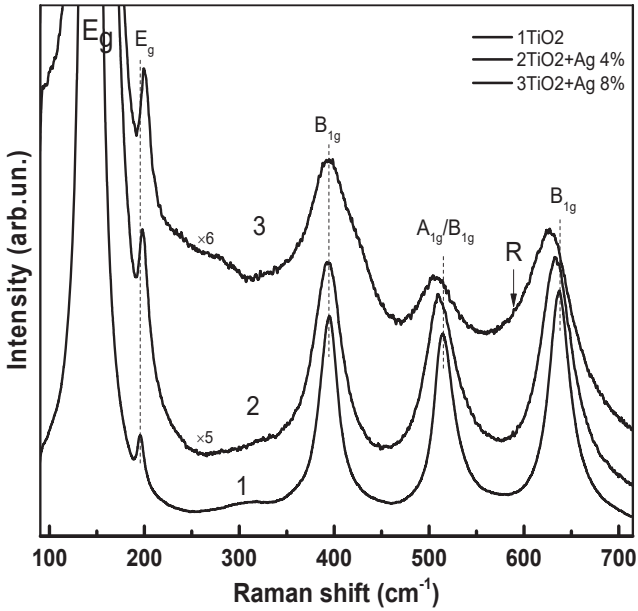

Fig. 4.15 Raman spectra of pure and Ag-doped TiO_2 NPs.

IR spectra analysis of the samples show that the first sample is characterized by the manifestation of absorption bands for Ti-O oscillations with frequencies at ~504 and 664 cm^{-1} (fig. 4.16, spectrum 1). For IR spectrum 2 of the sample, a shift in the absorption frequencies of Ti-O oscillations in the longwave direction are observed (fig. 4.16, spectrum 2). The shift in the characteristic oscillations of the Ti-O bond towards lower frequencies when modifying anatase with silver is caused by distortions in the symmetry of the coordinating environment of Ti^{4+} and is a sign of the presence of silver cations in the crystalline structure. A change in the shape of the absorption band Ti-O oscillations and the manifestation of the absorption band with a frequency of ~895 cm^{-1} characterizes the distortion of octahedron titanium-oxygen. The frequencies ~1110 and 1188 cm^{-1} characterise the surface oscillations of the functional groups (SO_4^{2-}, -OH), and are related to the doping method (fig. 4.16, spectrum 2). A further change is seen in the shape of the absorption bands for anatase after loading the sample with 8 wt % of Ag (fig. 4.16, spectrum 3).

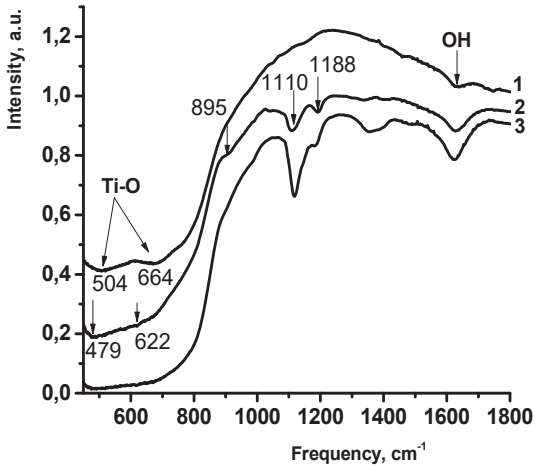

Fig. 4.16 IR spectra of TiO_2 (1), TiO_2 +4wt% Ag (2), TiO_2 +8wt% Ag (3) powders.

The development of complete methods for modifying oxide NPs are an important step in the preparation of hybrid composites based on polymer matrixes of different natures. The development of new, effective, and nanoporous nanocrystalline photocatalysts will lead to intense expansion in the field of fusion research. Research into the physicochemical properties and the surface structure of PANI-TiO_2 composites in the area of the dispersed phase concentration of 25–98 wt% has shown that, with increasing dispersion of TiO_2 particles of under 5 nm, a significant increase is seen in the efficiency of the process of forming *in situ* composite powders of PANI-TiO_2 with highly porous structures and specific surface areas of 50÷120 $m^2/g\cdot$. Composite powders of NP-PANI with developed mesoporous structures display increased photocatalytic activity with increasing particle dispersion.

The formation of nanocomposites of $C_3N_4O_x$-polyaniline was carried out by oxidative radical polymerization of aniline in the presence of $C_3N_4O_x$ (plates) nanoparticles. Absorption bands in the region of 200–400 nm and 500–800 nm were found and, thus, the synthesized samples absorb light in the UV and visible range. Due to the conductive polyaniline and electronic transitions between the polymer and $C_3N_4O_x$, a charge-transfer complex is possible.

The hydroxyl group content on the TiO_2 surface samples is important for its antimicrobial and photocatalytic properties because, in

the process of UV irradiation, OH groups on the defective surface of TiO_2 are active due to hole capture and subsequent formation of •OH radicals, which are active in the destructive of toxic organic substances and pathogens. Additionally, the presence of silver provides an efficient photogeneration process of electrons and their transfer from the conduction band Ag to the TiO_2 with the subsequent formation of the Schottky barrier, inhibiting the rate of recombination of photogenerated charges.

Ag and TiO_2 have different work functions (ΦTiO_2 = 4.2 eV, ΦAg = 4.6 eV) and therefore, when silver is in contact with TiO_2, electrons will transfer from the TiO_2 to the silver. These electrons transfer to silver and loads on the surface of silver will be scavenged by the electron acceptor, thus decreasing the recombination between electron and hole; as such, the silver atoms act as electron traps. Electron-hole recombination is the main reason for the low efficiency of TiO_2 photocatalysts. Therefore, the existence of the silver atom in Ag-TiO_2 facilitates the transport of more holes to the surface and enhances optical activity. The Ag particles on TiO_2 act as electron-hole separation centres and the transfer of photogenerated electrons from the TiO_2 conduction band to the metallic silver particles on TiO_2 are thermodynamically possible, because the Fermi level of TiO_2 is higher than that of the silver metal. The Schottky barrier is formed at the Ag-TiO_2 contact region, which improves charge separation and thus retards the recombination of the photogenerated electrons and holes. Photogenerated electrons that have accumulated on the surface of the Ag have good fluidity and can be transferred to oxygen molecules, which is absorbed on its surface.

CHAPTER 5

NANOSIZED TiO_2 COMPOSITES IN PHOTOELECTROCATALYSIS

5.1 General Aspects

The history of photoelectrocatalysis (PEC) dates back to the 19th century when H. Becquerel discovered the photovoltaic (PV) phenomena in electrochemical systems (Becquerel 1839, 9). As shown by A. Einstein in 1905, the quantum nature of light is the origin of the photoelectric effect and W. Brattain and C. Garret constructed a new theory explaining the properties of semiconductor-electrolyte interfaces in 1955 (Garret and Brattain 1955, 99).

A. Fujishima and K. Honda (1972, 238) reported the first photoelectrochemical application in 1972. These researchers from Tokyo University discovered the effect of photosensitization in TiO_2 electrodes under UV light irradiation for water electrolysis, i.e. the latter proceeded with a much lower bias voltage compared to normal electrolysis using a TiO_2 semiconductor anode and a Pt metal electrode as a cathode.

Important contributions to the photoelectrochemistry of semiconductors and the discovery of the wet PV solar cell were made by H. Gerischer (1972, 119; 1975, 58) and Yu. Pleskov (1984, 15). M. Gräztel (Hagfeldt and Grätzel 2000, 33; Grätzel 2003, 421; 2004, 164) was the first to propose the application of a wide bandgap semiconductor for chemical stability and an electron transfer sensitizer for absorption in the visible light spectrum to inject charge carriers across the semiconductor/electrolyte border.

The natural photochemical process of photosynthesis has existed in plants for billions of years and numerous attempts to realise photosynthesis artificially have been made. Recently, they have seen rapid progress (Najafpour and Madadkhani 2017, 7; Limburg and Bouwman 2016, 120; Limburg and Wermink 2016, 6). The combination of photo and electrochemistry with catalysis has many advantages and PEC mimics the

Z-scheme of natural photosynthesis (Mo et al. 2019, 241); however, unlike photosynthesis, PEC is mostly an interface phenomenon.

As a green technology, PEC has promising and effective uses for the degradation of various kinds of pollutants by utilizing abundant solar energy (Malato and Fernández-Ibanez 2009, 147). These technologies demonstrate rapid progress in anion reduction, CO_2 reduction and electrosynthesis, disinfection, and the generation of radicals through the PEC process, as well as having some particular issues (Bessegato and Guaraldo 2015, 6).

Despite many technical difficulties limiting its practical application, photoelectrocatalytic water splitting is one of the most promising artificial photosynthesis approaches for solar fuel production. Water splitting is also recognized as a means to developing a clean and abundant energy source through the production of hydrogen (Horiuchi and Toyao 2013, 15).

Photogenerated $h^+(e^-)$ migrate to the anode (cathode) surface and participate in the water oxidation (reduction) reaction. Since the reaction sites in PEC are spatially separated, there is no need to separate H_2 and O_2. The conversion of visible light into electric energy has become an important PEC application (Parkinson 2002, 6; Horiuchi and Toyao 2013, 15).

Above all, the technological-economic evaluation of PEC hydrogen generation shows its competitiveness with fossil-based technologies, provided that the technical barriers to implementing large scale PEC water splitting are overcome and solar-to-hydrogen (STH) efficiency reaches at least 10 % (Ding 2017, 7). STH efficiency is an important metric for benchmarking and performance evaluation. It can be expressed as a production of the light absorption efficiency (η_{abs}), the charge separation efficiency (η_{sep}), and the injection efficiency (η_{inj}) of photogenerated carriers to reactants. The following key criteria have to be met for efficient PEC water splitting (Dotan and Sivula 2011, 4):

(1) Broad light absorption range for efficient sunlight utilization;
(2) Efficient charge transfer from the bulk of the photoelectrode to the surface;
(3) Rapid consumption of photogenerated carriers for the surface reaction with minimal overpotential;
(4) Excellent durability for practical applications.

Recent progress in PEC has been closely related to advances in electrocatalysis, material science, and nanotechnology. The design of an

efficient photocatalyst at different levels of organisational structure is defining progress in the latter two fields

Electrocatalysis, as a phenomenon, promises a process of efficiency enhancement (current density increase at the given electrode potential value, etc.) via indifferent electrode material. In turn, a further improvement in efficiency occurs in PEC after the absorption of light quanta by the photoelectrocatalyst.

Noble metal nanoparticles display the best electrocatalytic performance, since they combine both catalytic activity and chemical inertness in an electrolyte medium (Wieckowski and Savinova 2003; El Guindy 2001). Many novel efficient electrocatalysts of non-metallic nature have been introduced during the past decades and these are proving important for PEC. Pioneering work in PEC water splitting includes the successful deposition of CoP_i as water oxidation cocatalysts (WOCs) on photoanodes, resulting in a great reduction of the overpotential and enhancement of the photocurrent (Ding 2017, 7). Among such cocatalysts, Mn-based oxide materials have shown an indisputable advantage (Zaharieva and González-Flores 2016, 9; Huynh and Bediako 2014, 136).

5.1.1 PEC phenomena at the semiconductor/electrolyte interface in TiO_2

PEC on the oxide semiconductor electrode | electrolyte border is a complex multistep process. It occurs in the conduction band of a semiconductor after excitation of light-induced electrons (e^-) when the former electron position becomes a hole (h^+). Multiple exciton generation (Werner and Kolodinski 1994, 72) and singlet fission (Singh and Jones 1965, 42) can also be seen with excitation energy transfer from the absorber to the catalyst due to a hopping mechanism and dispersive transport in less ordered semiconducting materials (Miller and Abrahams 1960, 120). A number of alternative processes have been identified in photosynthesis and organic devices, such as the Dexter electron transfer mechanism (Dexter 1953, 21). Among these processes, the hopping of light-generated excitons and the transmitter-antenna mechanism for energy transfer by coulombic interaction can also be mentioned.

The electronic excitation transfer between a donor, D, and an acceptor molecule, A, can be shown as follows (Lewerenz and Heine 2010, 3):

$$D^* + A \rightarrow D + A^*.$$

When light irradiation gives energy greater than the semiconductor bandgap, an electron/hole pair (e^-/h^+) is generated. The duration of the excitation state for commercially available TiO_2 particles is in the range of nanoseconds, although a range in seconds has been measured for decay reactions.

The gradient potential in PEC supports the separation of photogenerated e^-/h^+ pairs. Combining electrochemical and photocatalytic processes, electron/hole recombination shows a tendency towards minimization. The application of a bias potential is one way to control the Fermi level and improve charge separation, facilitating the reactions of charge carriers on the electrode's surface (Egerton 2011, 86; Pelaez and Nolan 2012, 125; Bessegato and Guaraldo 2014).

Enhanced electron/hole separation in the PEC system has been confirmed even in the case of an unbiased titania/FTO electrode. The azo dye Basic Blue 41 was subjected to photocatalytic and photoelectrocatalytic degradation using nanoparticulate titania films deposited on either glass slides or fluorine doped tin oxide (FTO) transparent electrodes. Degradation was faster when using FTO as a titania support even without bias and was further accelerated under forward electric bias (Papagiannis and Koutsikou 2018, 8).

Phenomena found at the oxide semiconductor | electrolyte interface require further study. A semiconductor forms a Schottky junction through contact with an electrolyte that changes the electrochemical potential (Fermi level) of the semiconductor to an equilibrium value at the interface. Thus, band bending within the semiconductor phase occurs depending on the difference in the semiconductor and electrolyte Fermi levels. The space charge layer or depletion layer is a region where bending occurs, characterized by the depletion of the majority of the carriers (electrons in an n-type semiconductor and holes in a p-type semiconductor) (Paramasivam and Jha 2012, 8).

Photoelectrocatalysis is an advanced oxidation process (AOP) based on the generation of hydroxyl radicals (•OH), which constitute a highly active oxidizing species that is able to mineralize organics. The hole (h^+) in the valence band produces •OH radicals through the oxidation of H_2O molecules or OH^- ions adsorbed on the semiconductor surface and can also oxidize organic molecules directly. The schematic representation of a PEC anode process on TiO_2 as a typical n-type semiconductor is shown in fig. 5.1. The anode and cathode PEC processes can be summarized as follows (Bessegato and Guaraldo 2015, 6):

Anode:

$$TiO_2 - h^+_{VB} + H_2O_{ads} \rightarrow TiO_2 - HO\bullet_{ads} + H^+$$
$$TiO_2 - h^+_{VB} + HO_{ads} \rightarrow TiO_2 - HO\bullet_{ads}$$
$$TiO_2 - h^+_{VB} + RX_{ads} \rightarrow TiO_2 - RX\bullet_{ads}$$

Cathode:

$$H_2O + e- \rightarrow H_2 + 2OH^-.$$

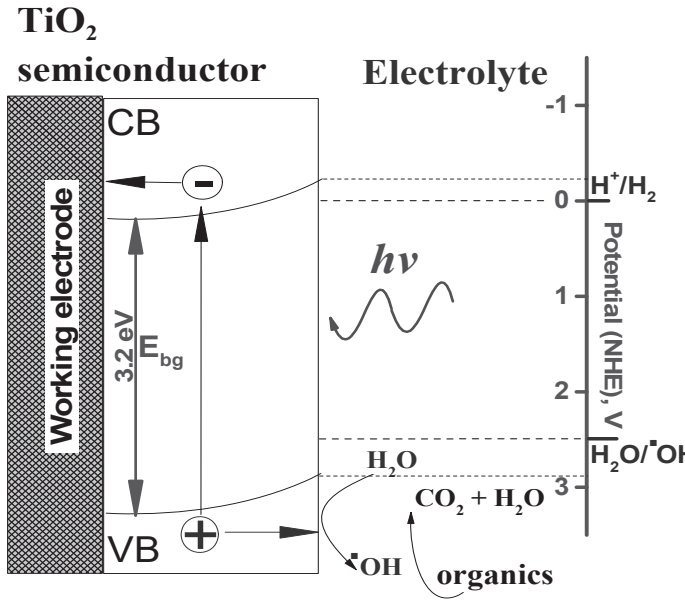

Fig. 5.1 PEC degradation of organics on TiO_2 as a n-type semiconductor (CB—conductivity band; VB—valence band). The scale of the potentials demonstrates the oxidizing properties of the OH radicals formed.

5.1.2 Advantages of nanostructured transition metal oxides in PEC

Unlike electrocatalysis, semiconductor electrodes based on TM oxides make good photoelectrocatalysts. The advantages of a 3D-series TM also include low price and abundance in nature. Among the disadvantages, their low conductivity and brittleness can be mentioned.

Titanium dioxide is one of the most intensively studied TMO PEC compounds. It is naturally abundant, commercially available, economically

viable, chemically stable, non-toxic, and environmentally friendly (Hashimoto, Irie and Fujishima 2005, 44). Annual production of titanium dioxide is significant reaching more than 5 million tonnes in 2011 (Fries and Simko 2012). It is used in the production of pigments, textiles, and plastics, as well as in cosmetics and the food industry (EFSA Panel on Food Additives and Nutrient Sources added to Food (ANS) 2016).

Nanomaterials based on TM oxides, including nanotubes, nanowires, nanofibres, nanorods, nanopores, and nanowalls, among others (Carbó 2009; Regonini and Bowen 2012, 20; Shen and Chen 2018, 98; Bessegato and Guaraldo 2015, 6), have become the focus of intensive research because of their:

- high surface area;
- quantum or size effects;
- excellent electronic transport capabilities;
- reduced electron-hole recombination.

Reduced electron-hole recombination implies improved interaction between the material and the medium. In TiO_2 nanotubes, the size effects have been demonstrated by the direct dependence of TiO_2 nanotube array length on PEC activity (Liu and Zhang 2008, 112). The capability for precise control of tube dimension in the preparation of TiO_2 NTs by electrochemical anodization is certainly an additional advantage (Grimes and Mor 2009). An important challenge in PEC today is the development of stable semiconductor nanomaterials activated by visible light irradiation.

Titanium dioxide nanoparticles have been assessed by European authorities for use as UV-filters in sunscreen formulations and they are one of a limited number of nanomaterials to have cosmetic applications (Weir and Westerhoff 2012, 46). The use of TiO_2 in sunscreen is an example of an exception in which PC (photocatalytic) activity limits safe consumption.

In TM oxides, the inner space can be involved in photoelectrochemical transformations. Molecular sieve (MS) structures are encountered among TM oxides, which are available for “guest” particles. MS structures, as microporous solids, have been used in the industrial processes of purification, separation, and petroleum refining, etc. for decades (Haw and Song 2003, 36). Although most MS structures, including microporous carbons and zeolites, are based on the arrangement of four-coordinated C, Al, and Si tetrahedral units, scarcer inorganic solids arise from the organization of MO_6 octahedra. These materials were named octahedral molecular sieves (OMS) by S.L. Suib (2008, 18). The manganese (IV)

oxide family of tunnelled OMS polymorphs can also be mentioned. OMS tunnel polymorphs of vanadium (Kanke and Takayama-Muromachi 1995, 115; Djerdj 2008, 130); tungsten (Besnardiere and Ma 2019, 10; Coucou and Figlarz 1988, 30; Gerand and Nowogrocki 1979, 29); titanium (Anderson and Klinowski 1990, 17); and niobium (Pless 2007, 19) are also encountered.

OMS polymorphs possess significant versatility in terms of redox (Kakazey and Ivanova 2003, 114) and substitution (Shen and Morey 2011, 115; Chen 2015, 54; Vasconcellos and Gonçalves 2015, 498) abilities, opening up new opportunities in catalysis (Ivanova and Ivanov 2002, 75; Jin 2010, 20; Suib 2008, 18; Chen 2015, 54; Vasconcellos and Gonçalves 2015, 498); energy storage (Kakazey and Ivanova 2003, 114); sensing (Suib 2008, 18); information technology and smart systems (Suib 2008, 18). The tunnels available for metal ions and small molecules of water, carbon monoxide, oxygen, and hydrocarbons, etc. explain the high catalytic and electrocatalytic activity of OMS compounds. Unfortunately, studies into OMS photoelectrocatalysis are limited in number (Said and El Maghrabi 2018, 6; Paramasivam and Jha 2012, 8).

5.1.3 Bandgap engineering in TiO_2

The strategy of bandgap-engineering can be applied in PEC as well. The bandgap in TiO_2 (3.0–3.2 eV) is large enough to be overcome with visible light energy and is suited to the more energetic UV spectrum; in turn, UV irradiation comprises about 5 % of sunlight. Meanwhile, the recombination of photogenerated electron-hole pairs on or near the TiO_2 surface takes place at high speed within 10^{-9} s (Pan 2015, 50). As such, efforts have been geared towards making TiO_2 responsive to visible light by using *bandgap engineering*. The main strategies include doping and coupling with other semiconductors with small bandgap energy, surface decoration with noble metals, and using conductive materials like polyaniline, graphite, and MXenes, etc.

The *coupling* of two semiconductors reduces e^-/h^+ pair recombination since both the UV and visible regions of the spectrum are involved and charge carriers transfer from one semiconductor to another. This can greatly promote photo-cacrrier separation and enhance photocatalytic quantum yields (Wang and Tan 2014, 321; Dai and Yang 2015, 349). Modified TiO_2 nanotube arrays with $CuInS_2$ have demonstrated a bandgap of 1.5 eV and the compound obtained showed enhanced UV and visible light absorption with a higher PEC oxidation rate of 2-chlorophenol. Similar effects are expected when coupling MnO_2, as a semiconductor

with a bandgap of 1.3 eV, and TiO_2 (Gao and Glerup 2008, 112). Both have isostructural polymorphs of rutile-type, opening up opportunities for cationic doping.

The coupling of WO_3 with TiO_2 has also demonstrated more active photocatalysis than the array of individual oxides, as well as efficiency in the visible spectrum (Georgieva and Valova 2012, 211; Georgieva and Sotiropoulos 2010, 41; Zhang and Yang 2014, 148). These bi-component oxides are semiconductors with bandgap energies in the range of 2.5–3.2 eV, although WO_3 presents values of 2.5–2.8 eV compared to TiO_2, which sees values of 3.0 to 3.2 eV. This behaviour of TiO_2/WO_3 composites can be explained by photoexcited electron transfer from the WO_3 particles to the TiO_2. Most likely, efficiency is improved with the growing number of holes on the surface of the TiO_2 and an increase in the flow of electrons to the counter electrode.

Decoration of the TiO_2 surface with Ag, Au, Pt, and Pd, with the semiconductor and metal particles coming into contact, forms a Schottky barrier in the new material due to the difference in the Fermi levels of the TiO_2 and the metal NPs. Pt NPs deposited on TiO_2-NTs have been found to decrease the bandgap energy of TiO_2-NTs from 3.21 eV (TiO_2NTs) to 2.87 eV (Pt-TiO_2NTs), dramatically increasing the kinetics of degradation of an acid dye (Almeida and Zanoni 2014, 25).

The application of nanocarbon materials with TiO_2 and other semiconductors as a conductive additive in electrocatalysis is necessary; otherwise, a thin film electrode should be used to facilitate the charge transfer. Nanocarbon materials have attracted much attention owing to their superior photocatalytic performance. For instance, couplings of TiO_2 and conductive carbon nanotubes (An and Chen 2012, 4; Chen and Luo 2014, 485; Dong and Tang 2014, 296; Yu and Yu 2005, 61); graphene (Wang and Wang 2013, 5; Wang and Wang 2013, 132-133; Tan and Chai 2012, 5); carbon black (Cong and Li 2015, 138; Yu and Chen 2004, 90); graphitic carbon (Wang and Lin 349: 13; Zhang and Fu 2008, 18); and C_{60} (Chai and Peng 2013, 42; Lian and Xu 2015, 7) have all been extensively fabricated to enhance photocatalytic activity in various applications.

5.1.4 TiO_2 doping strategies in PEC

Doping is an important strategy in tuning a semiconductor's functional properties, especially in the search for photoactive materials using nanostructured semiconductors capable of being more active under visible light irradiation. The carrier concentrations are equal ($n = p$) in extrinsic semiconductors. When donor impurities are added to a neutral

semiconductor, even additions at rates of parts per billion can have a profound electrical effect since the intrinsic carrier concentrations are low (sub-parts per trillion). In a *p*-doped semiconductor case, the Fermi level now lies close to the valence band (VB) edge and, vice versa, the Fermi level shifts towards the conductivity band (CB) edge for an *n*-doped semiconductor.

Different approaches to semiconductor oxide doping exist. To introduce additives, one can modify the preparation procedures. The framework TM cationic substitution is generally heterovalent. In the case of MeO_2 (Me = Ti, Cr, Mn, Ce, etc.), substitution by a low valence cation is the source of additional electrons in the material. Otherwise, there is an opportunity to introduce cations of higher valence (for instance, vanadium subgroup elements) to generate additional holes or they can be substituted by cations of the same valence. Impurities also have a general tendency to be concentrated in the layer near the interface as a common defect state in any material. They modify the position of the Fermi level. For instance, TiO_2 doped with a metal, such as W (Gong and Pu 2013, 36), Cr (Yang and Pu 2014, 27), Zr (Liu and Liu 2011, 82), or Fe (Tang and Chen 2014, 187) shows decreased bandgap energy due to new energy states either within or beyond the VB and CB. Such additives stimulate PEC activity in many ways. If an excess number of impurities exist as a minor phase, this means that the composite doped material is formed outside the limits of doping, which can have a positive influence on photoelectrocatalytic activity due to coupling phenomena (see above).

A more complex doping strategy is usually called *co-doping*. This involves the incorporation of more than one anion or cation into the structure. Dopant additives have different targets. For instance, there can be simultaneous substitution in cationic and anionic sublattices, like N-Zr-co-doped TiO_2 nanotube arrays, with increased photoelectrocatalytic activity under UV and visible light (Liu and Liu 2010, 363). Electrodeposition of manganese dioxide with M (M = alkali metal ions or NH_4^+) and TM ions simultaneously stimulates hollandite phase formation because of the presence of M^+; this is a particle template effect with TM substitution in the hollandite structural framework (Sokolsky and Zudina 2018, 133). The positive effect of *self-doping* is also mentioned in the literature in relation to Ti^{3+} into TiO_2 (Li and Huang 2017, 9; Liao and Yang 2014, 136), resulting in increased electrical conductivity and visible light absorption. The redshift of the absorption edge is linked to the formation of centres, including Ti^{3+} and oxygen vacancies (Serpone 2006, 110).

General difficulties encountered here include the limitations of crystal chemistry relating to framework substitution, such as the chemical

similarity or affinity of a dopant to a host structure and the narrow limits for additives able to be incorporated (Rao and Gopalakrishnan 1997).

5.2 Titanium Dioxide and other Titanium Compounds in PEC

Titanium dioxide has been one of the most intensively studied substances since the discovery of PEC water photolysis by Fujishima and Honda in 1972. TiO_2 has been widely applied in photocatalytic degradation of pollutants, water splitting, supercapacitors, dye-sensitized solar cells, sensors, biological materials, and self-cleaning (Litter 1999, 23; Ge and Cao 2016, 5). The photoelectrocatalytic activity of other titanium compounds has also been intensively studied (Murray and Wriedt 1987, 8).

5.2.1 Substoichiometric compounds of TiO_2

Conductive Magneli phase materials of sub-stoichiometric TiO_2, such as Ti_nO_{2n-1} ($4 < n < 10$), should also be mentioned (Kuylenstierna and Magneli 1956, 10). They have crystal structures derived by crystallographic shear from rutile-type structures. High purity rod-like Ti_4O_7 powders have been successfully fabricated by molten salt synthesis and their electrochemical behaviour was studied in Wang and Liu (2017, 704).

5.2.2 TiO_2 polymorphs

Titanium dioxide can form at least eight polymorphs, including some artificial ones. Four main crystalline polymorphs occur in nature. These are: tetragonal rutile; tetragonal anatase; orthorhombic brookite; and monoclinic B TiO_2 (Wang 2014, 70; Liu Chen 2014, 114). Rutile and anatase absorb UV irradiation. At temperatures above 915 ^oC, anatase transforms monotropically (only in one direction) into rutile.

Anatase and rutile are the most thermodynamically stable and photocatalytically active, while the brookite and other polymorphs currently have no particular practical significance. The commercially available TiO_2 photocatalyst P25 has an anatase-rutile (80:20) phase ratio. The synergistic effect of *coupling* between TiO_2 polymorphs exists as well. The distortion of uniformly-shaped TiO_6 octahedron units in the lattice structure of the four types of TiO_2 can cause different mass densities and bandgaps in the different polymorphs of TiO_2 (Wang 2014, 70).

Li and colleagues demonstrated that the formation of anatase-rutile phase coupling on the exposed surface is critical to achieving enhanced photocatalytic activity of TiO_2 nanoparticles owing to the efficient synergistic effects of the two phases (Wang, and Liu, 704 2017). Yu et al. demonstrated that the high brookite content in mesoporous TiO_2 with a crystalline (anatase and brookite) framework played an important role in enhancing its photocatalytic activity in the oxidation of *n*-pentane in air. The phase coupling between the most frequently studied TiO_2 phases (rutile and anatase) and less common TiO_2 phases (brookite and B phase) and charge-separation mechanisms deserves greater attention in the future (Liu Chen 2014, 114).

Nanomaterials have a number of different advantages in PEC, one of which is a reduced electron-hole recombination effect. TiO_2 nanomaterials of varied morphology and structure have been the subject of many recent studies, including: nanopores (Liu and Gan 2009, 171); nanowires (Cardoso and Boldrin Zanoni 2010, 45; Miao and Xu 2002, 2); nanorods (Li and Zhang 2013, 38; Wang and Zheng 2012, 71); and nanotubes (Grimes and Mor 2009; Mor and Varghese 2006, 90). However, of the several TiO_2 morphologies, titanium dioxide nanotube arrays (TiO_2NTs) have received the greatest interest. The most typical TiO_2 nanotube preparation method is Ti anodization by adjusting the voltage between 15 and 60 V. Uniform tubular structures are formed and the diameter and length increase with the voltage (Qiu and Wang 2018, 207; Ge and Cao 2016, 5). The 3D-arrays of TiO_2 nanotubes on Ti mesh obtained have been used as photoelectrodes for photoelectric conversion and photoelectrocatalytic removal of pollutants.

TiO_2 nanotube array (TiO_2 NTA) photoelectrodes were synthesized using an anode oxidation method (Cheng and Liu 2013, 661). Before anodization, fresh Ti plate (30×10×0.5 mm) was polished using a dilute acid with a volume ratio of 1:4:5 for HF: HNO_3: H_2O for 30 s. Then, the cleaned Ti plate was repeatedly washed with MQ water and dried for 2 h at 105 °C. The anodization process was conducted in a traditional two electrode configurations, in which Ti plate and Pt electrode served as the anode and cathode respectively. Additionally, the pre-treated Ti plate was anodized at 20 V for 2 h in a mixed electrolyte solution of 1 $mol \cdot L^{-1}$ Na_2SO_4 with 0.5 g NH_4F dissolved. After anodization, the sample was rinsed with MQ water several times and then dried for 24 h at 70 °C. Afterwards, the obtained electrode was calcined at 450 °C for 2 h in a muffle furnace with a heating rate of 3 $°C \cdot min^{-1}$.

5.3 PEC Degradation of Organics Using Titanium Dioxide

Electrochemical degradation of organics is a cost-effective technology in which direct and indirect oxidation takes place (Feng and Yang 2016, 2). Different types of electrodes have demonstrated appropriate activity, including boron-doped diamond (BDD) (Rocha and Gomes 2014, 140) and platinum, among others.

Ti_nO_{2n-1} Magneli phases ($4 < n < 10$) have been explored as electrode materials or conductive supports in electrochemical systems for more than a decade because of their high electrical conductivity and corrosion resistance. Their oxygen reduction activity was studied in Oturan and Ganiyu (2017, 217). Electrochemical degradation of organics has recently been realized by sub-stoichiometric Ti_4O_7 coating of TiO_2 obtained by plasma deposition (Oturan and Ganiyu 2017, 217). Along with the electro-Fenton process and electrochemically generated OH radicals, this was successfully applied in the electrocatalytic destruction of the antibiotic amoxicillin. Rapid oxidation of a 0.1 mM antibiotic solution in a short electrolysis time was achieved. The performance of this new anode material has been compared with boron-doped diamond (BDD) and other conventional anodes, such as Pt and dimensional stable anodes (DSA), in terms of degradation kinetics, mineralization current efficiency (MCE), and energy costs.

The results of current studies show that Ti_4O_7 provides a similar oxidation rate and MCE as BDD, while giving better results than DSA and Pt anodes. Solutions treated using the electro-Fenton process with a Ti_4O_7 anode have shown a low percentage of bioluminescence inhibition of *V. fischeri* bacteria, indicating excellent detoxification of the test solution.

There is relatively little research into water treatment with the electrochemical degradation of the azo dye MO by anodic oxidation on Ti_4O_7 electrodes (He and Liu 2018, 29).

Anatase TiO_2-NTs prepared with an anodization voltage of 30 V showed excellent solar photocurrent, photovoltage, interface impedance, and photoelectrocatalytic (PEC) efficiencies for the removal of dye molecules and Cr(VI) heavy metal ions (Qiu and Wang 2018, 207). A TiO_2-NT sample with an average diameter of 70 nm and thickness of 4.56 μm showed photocurrent density of 1.63 mA/cm^2, photovoltage of −0.36 V/cm^2, and removal efficiencies of 71.31 %, 51.39 %, 98.07 %, and 48.26 % for the PEC removal of methyl orange (MO), Rhodamine B (RhB), methyl blue (MB), and Cr(VI), respectively. The excellent photoelectrochemical property of TiO_2 NTs can be attributed to their

effective pollutant adsorption and carrier transportation. This flexible photoelectrode has drawn attention for its application in solar cells, pollutant degradation, photolysis of water, and gas sensors.

PEC oxidation of acid green 50 dye in aqueous solution using a Ti-TiO_2-NT electrode was investigated by Ensaldo-Rentería and Ramírez-Robledo (2018, 6). Highly ordered TiO_2 nanotube arrays wrapped with C_3N_4 nanoparticles were studied for their efficient charge separation and increased photoelectrocatalytic degradation of phenol (Wang and Liang 2018, 344).

5.3.1 PEC methyl orange degradation by TiO_2 of different origins

A strong dependence of the functional properties of non-stoichiometric oxides on the origin, dispersion, and particle shape of the material stimulated our interest in new preparation methods of active titanium dioxide PEC. This work studied the activity of conductive composite electrodes based on graphite of spectral purity and titanium dioxide of various origins, and phase composition during PEC degradation of MO under UV irradiation, to analyse the efficiency of a TiO_2 sample synthesized from domestic raw material (a suspension of hydrated titanium dioxide, metatitanic acid, or $TiO(OH)_2$) compared to commercial samples. The physicochemical properties of the corresponding materials were studied using chemical, X-ray diffraction phase analysis, electron microscopy, and UV spectroscopy.

Titanium dioxide (sample 1) was obtained from Frantsevich Institute for Problems of Materials Science at the National Academy of Sciences of Ukraine. The $TiO(OH)_2$ raw material was a product of the intermediate stage of titanium concentrate and slag processing at PJSC "Sumykhimprom". To obtain anatase TiO_2, the suspension was heated at 600 °C with a heating rate of 5 °C/min. Standard samples of titanium dioxide from various manufacturers were also studied: No. 2, reagent (Huntsman TR-92 rutile, (USA)); No. 3, with an anatase-rutile phase ratio of 80:20 (P25 Evonic (Germany)).

The phase composition of the powders was determined by X-ray phase analysis (XRD) using a DRON-3M diffractometer with Cu-Kα radiation (λ = 0.154187 nm). Electron microscopic studies were conducted with the JEOL JEM1400 transmission microscope. Thermogravimetric study of the TiO_2 powders was carried out on a Q-1000 derivatograph with a 10 °C/min heating rate. The porous structure of the powders was studied using the adsorption-structural static volumetric method on an ASAP

2000M instrument (Accelerated Surface Area and Porosimetry System) designed to determine nitrogen adsorption isotherms.

The absorption spectra of samples in the range 190–400 nm were studied on a Shimadzu UV-2401PC spectrophotometer. UV-transparent polymethyl methacrylate plates were used instead of the usual quartz cuvette. Plates of 3 mm thickness were cut on a laser machine with cuvette geometry. The loading of the attached suspension was 0.75 mg/cm^2. A petroleum jelly layer was first attached to a 3 mm thick polymethyl methacrylate plate. Titanium dioxide powder was added and the absorption spectrum of the suspension was registered in the UV range vs. petroleum jelly. The mass of the solid phase (TiO_2 samples) was 3.0 mg, while the mass of the liquid phase (petroleum jelly) was 15.0 mg.

The linear voltammetry method with a sweep potential scan (potentiodynamic method) is the main method for studying photoelectrocatalytic TiO_2 activity in the anodic oxidation of organic compounds. Cyclic voltammetry (CVA) and potentiostatic methods were used. Chronovoltamperograms were recorded on the universal potentiostat-galvanostat IPC-PRO (Russia), consisting of a measuring unit of a potentiostat and a PC running the programme IPC2000. The IPC2000 software package was designed to manage the measurement process on a potentiostat-galvanostat, receive data from a potentiostat-galvanostat, and then undertake further mathematical processing.

The electrode potential was measured and compared to a standard silver chloride reference electrode. Polarization measurements were performed starting with the stationary potential. The potential scan rate was in the range 0.001–0.5 $V \cdot s^{-1}$. The fabrication of a carbon paste electrode for PEC degradation has a number of steps. First, the oxide sample is individually ground in a mortar, then graphite of spectral purity is gradually added in the ratio of graphite:TiO_2 at 50:50 or 70:30, respectively, to improve electrical conductivity. A polytetrafluoroethylene (PTFE) emulsion (Merck, 60 wt%) was added to the obtained electrode material. The resulting electrode material was pressed with constant pressure onto the copper current collector with a diameter of 0.3 cm. The electrode active mass was 10 mg. A Luggin capillary was situated as close as possible to the working electrode's edge in the three-electrode cell. A glassy carbon plate with an area 10 times larger than that of the working electrode served as an auxiliary electrode. The measurements were carried out in 10^{-4} M MO solution with 0.1 M KCl electrolyte under dark conditions and with UV irradiation. The cell was placed in a closed container with a UV lamp (OSRAM, PURITEC HNS 6WT5 G5, 212 mm) at a distance of 5 cm.

Sample 1, obtained from a hydrated titanium dioxide $TiO(OH)_2$ suspension, had a phase composition of pure anatase. The porosity study showed a highly developed mesoporous surface, as well as the specific surface area. In photoelectrocatalysis and catalysis, the optimal pore size distribution plays a decisive role in providing charge and mass transfer. Another important difference between the samples studied was the presence of Ti^{3+}. An intense paramagnetic Ti^{3+} ion signal in the solid oxide lattice was detected by the EPR signal only in anatase sample 1. Defective Ti^{3+} positions influence surface states due to the small size of this sample's particles (approximately 10 nm).

It is worth mentioning that Ti^{3+} defects can result from the fixation of UV-generated electrons at cationic trap-positions in titanium dioxide. The reason for the formation of a significant concentration of Ti^{3+} paramagnetic centres in the oxide lattice of sample 1 is found in the conditions of the temperature-processing mode (with partial Ti^{4+} reduction and oxygen loss occurring up to 600 °C starting from the nanoparticle surface of the material). Multivalent states in the lattice of oxide catalysts are known to be active centres of catalysis. Stoichiometric TiO_2 differs significantly in its photocatalytic properties and the presence of surface Ti^{3+} defects reduce the bandgap of titanium dioxide, contributing to the photocatalytic process being initiated by photons closer to the edge of the visible range.

Based on the absorption spectra of the samples in the range 190–400 nm, the bandgap was estimated for direct and indirect transitions in the Taut coordinates $(\alpha hv)^2$–hv, $(\alpha hv)^{1/2}$/hv by extrapolating its linear section to the abscissa axis. It turned out that the bandgap was minimal for sample 1, making up for the indirect transition of 2.75, 3.0, and 3.5 eV for samples 1, 2, and 3, respectively.

Using the CVA method, we can study the ability of chemical compounds to undertake oxidative degradation, in particular, MO in anodic photoelectrocatalytic oxidation. The current-voltage dependencies were recorded first in dark mode and then sequentially with the UV source. The potentiostatic mode was selected based on the effects of the CVA curves. Various scanning rates were used to determine the range of potentials where oxidation occurs and to evaluate the kinetic parameters. The studied potential scanning window (–1.4 to +1.6 V) corresponds to the region of stability of the aqueous electrolyte used in this work.

Diagnostic criteria in the voltammetry method made it possible to analyse the reaction pathways in depth and the differences in the anode PEC process in samples 1-3. In the range –0.5 to +0.5 V, for all samples, the following dependences were studied:

$I_p / V^{0.5}$—V; I_p — $V^{0.5}$; E — lnV; lnI_p — lnV; and Semerano criterion $X_S = \left(\frac{\Delta lgI_p}{\Delta lgV}\right)_{c=const}$ where I_p is the peak current density of anodic oxidation under dark conditions or UV irradiation and V is the potential sweep rate.

Despite the low-power UV irradiation source (6 W), the photoelectrocatalytic effect manifested clearly at high potential scan rates (more than 0.05 $V \cdot s^{-1}$ in the electrode potential range –1.0 to +0.5 V) in comparison to dark conditions for sample 1 (fig. 5.2). The oxidation current increase was 100 % and higher in the absence of significant changes under the same conditions for standard samples 2 and 3. The observed photoelectrocatalytic oxidation process is comparable to a scan rate of 0.1 $V \cdot s^{-1}$ (since it manifests itself maximally at this potential scan rate) and is relatively fast. The increase in the current strength of anodic oxidation was about 5–10 % for the samples of TiO_2 (2 and 3).

MO is used as a model for the mineralization of organic anionic dyes and the consideration of possible degradation pathways. As shown in our previous publications, nanosized TiO_2 is an excellent photocatalyst due to its high chemical stability and photocatalytic activity (Zahornyi 2018).

The UV irradiation effect on the anode polarization curves of sample 1, corrected for effects in an electrolyte solution without MO, is shown in fig. 5.2. The distinctive features of the anode curves at a maximal scan rate for curve 1 under UV-light are shown (fig. 5.2a). Curve 2 (dotted) corresponds to the absence of UV irradiation The PEC fast proc/ess “starts” at low anode potentials for sample 1 and is relatively uniform.

The lower starting position of curve 1 (dotted), in our opinion, may be due to the reducing activity of surface Ti^{3+}, which plays a role in bandgap decrease under UV light as the photocurrent appears. It is also known that the standard redox potential of Ti^{3+}/Ti^{4+} is 0.1 V (against standard hydrogen electrode (SHE) or 0.3 V vs. Ag/AgCl/Sat. KCl reference electrode). The more realistic potential value in our case is:

$$2TiO_2(s) + 2H^+ + 2e^- \rightleftharpoons Ti_2O_3(s) + H_2O$$

with −0.56 V vs. SHE or −0.36 V vs. Ag/AgCl/Sat. KCl.

Nevertheless, this fast electrode process presents a broad shape and can be complex and heterogeneous under UV irradiation. It is worth

noting that curve 1 for samples 2 and 3 shows no distinct differences under the same experimental conditions.

Using the diagnostic criteria of the voltammetric method for evaluation, it was concluded that the PEC process is irreversible, the chemical stage of oxidation is present, and reagent adsorption impacts the PEC process mechanism both in the dark and under UV irradiation.

Fig. 5.2b sees CVA curves registered at the same rate in different electrolytes. It can be concluded that the KCl electrolyte solution has some advantages due to the higher currents of anodic oxidation seen.

In support of the features of sample behaviour indicated above, PEC processes were studied potentiostatically at CVA effect potentials (fig. 5.3). We chose the potentials of 0, 250, 500, and 1000 mV (against the Ag/AgCl/Sat. KCl reference electrode). The PEC process rate increased under UV irradiation and was different in this potential range. At 0 and 250 mV, the photocurrent was stable and maximal (50 % of the total value). At higher potentials (500, 1000 mV), the photocurrent increased significantly at first; however, over time, the process slowed down and the effect of the photocurrent decreased due to surface blocking by products of MO oxidation. This observation does not contradict the idea of maximal PEC activity with sample 1. The low power of the UV source is the main reason for this new rate-determining step compared to samples 2 and 3.

The complexity of this process has been confirmed by the relaxation of the current in the intervals between anodic oxidation pulses and some cathode photocurrent peaks appear after the current step at 250 mV (fig. 5.3). Their nature and intensity change regularly with potential growth—about four such maxima appear and disappear sequentially, which is consistent with the complex MO oxidation mechanism. As such, the change in the process mechanism was established during the transition from potential at 0 V to 1.0 V for anatase sample 1. No changes were seen for the standard samples 2 and 3 (Sokolsky and Zahornyi 2019, 27).

Study of the composite electrode material interface has constituted an important part of its characterization. We analysed the electrode based on the material in sample 1 containing TiO_2, a graphite conductive additive, and a PTFE binder (60 % emulsion) by the SEM method with gold vacuum deposition to improve contrast in the SEM images (fig. 5.4-5.12).

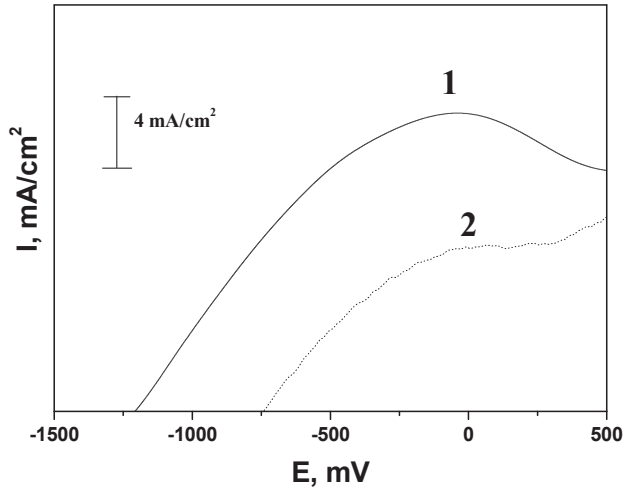

(a)

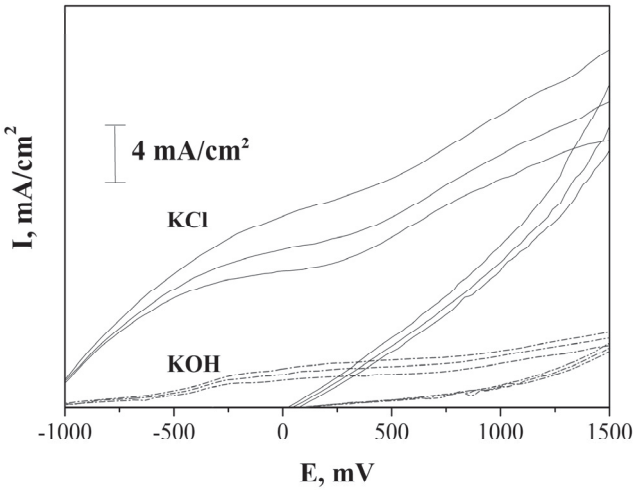

(b)

Fig. 5.2 Polarization CVA curves 1 and 2 registered on the working electrode with TiO_2 sample 1 and a 30:70 ratio with graphite under UV irradiation at potential scan rates 0.1 V/s (------- dashed line designates polarization curve without UV) with subtracted background current of 0.1 M KCl on the same electrode (a); CVA-curves of the same electrodes in 0.1M KOH and KCl at 0.1 V/s under UV irradiation.

As mentioned earlier, at least two factors favour PEC activity growth here: TiO_2-graphite coupling and the impact of Ti^{3+} on the bandgap decrease. From this viewpoint, it is of interest to reconstruct the mutual distribution of electrode material constituent parts and evaluate their influence on PEC.

Basic observations about the difference in appearance of the interface before and after photoelectrocatalysis were made. TiO_2 particles have a plate-like morphology with a crystallite dimension of less than 50–100 nm and, except for the coupling effect, they need graphite as a conductive additive due to their low conductivity. The PTFE binder makes electrode material more stable and durable against TiO_2 powder brittleness.

Figures 5.6 and 5.7 demonstrate, with a magnification of 2070 (36100) times, the random distribution of small white TiO_2 particles in a grey-black medium of conductive additive, which is consistent with 70 % by weight content of graphite powder. A lower ratio of graphite additive significantly decreases the current. The white colour on such images is typical for low conductive material reflecting electrons and vice versa for black material. The conductive additive predominates on the interface and the application efficiency of TiO_2 is improved by the increase in its conductivity.

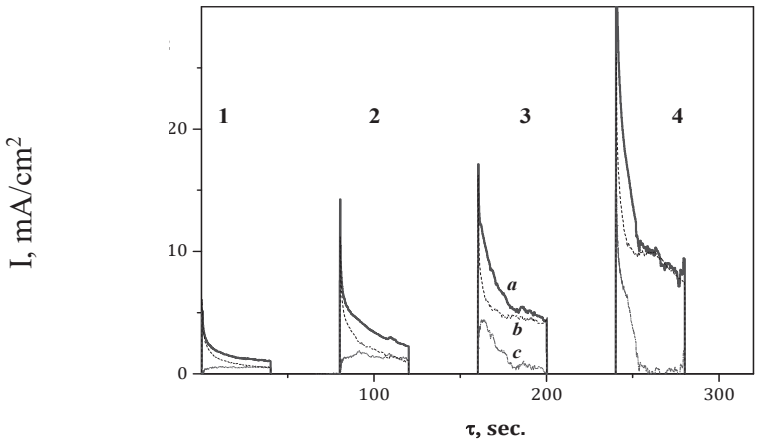

Fig. 5.3 Potentiostatic curves: a) under UV irradiation; b) darkness conditions c) difference (c= a – b), short dot line registered at 0 (1), 250 (2), 500 (3), and 900 (4) mV potential steps and -1200 mV between them on working electrode with TiO_2 sample 1 and 30:70 ratio with graphite.

Figures 5.8-5.12, with maximal magnification, demonstrate good contrast due to gold vacuum deposition. The long white filaments can be observed at the interface and are not abundant. We attributed them to PTFE-emulsion particles (fig. 5.8, 5.9, and 5.12). Brittle flakes of grey colour in figures 5.10 and 5.11 are consistent with graphite behaviour. Fig. 5.11 shows a white colour aggregate of nanoparticles with a size that is close to that previously evaluated for TiO_2 sample 1. It lies on nanoflakes of graphite and such a position is ideal for the PEC process. Similarly, less conductive TiO_2 aggregates can also be seen in fig. 5.8.

Analysing TiO_2 (10 nm) nanoparticle aggregates of approximately the same size (~1 μm in fig. 5.8 and 5.11), it is interesting to discuss the issue of the optimal size of these aggregates for PEC. On the one hand, their low conductivity is a disadvantage for application in PEC; on the other, smaller sized aggregates and a more uniform distribution in the conductive medium give further improvement. The next issue is how to control the size of the TiO_2 aggregates. Generally, Ti^{3+}-self-doping and other doping strategies significantly improve PEC characteristics. The other alternative involves increasing the mixing time or optimization of the PTFE content.

Thus, sample 1 is a promising PEC material for organic compound degradation according to its physicochemical properties. The higher photoelectrocatalytic activity of sample 1 can also be explained by the particle size being under 10 nm. Under UV irradiation, the electron migration time to the interface (τ_{migr}) does not exceed 10 ps, while the direct electron-hole recombination in crystals of some semiconductors, including titanium dioxide, has typical values of τ_{rec} of 100 ns. This large difference between τ_{migr} and τ_{rec} defines the primary separation of the photogenerated charges in the nanocrystal—they reach surface traps and are subsequently consumed in the irradiation processes.

Although the electrode area was very small compared to the cell volume (50 ml) and low power of the UV source, the solution became brown at the end of a short experiment, confirming an active process of degradation of MO amino dye in the electrolyte solution.

Previously, we successfully obtained PANI-TiO_2 composites using the method of *in situ* polymerization. The particles exhibited a photocatalytic effect on the decomposition of phenol under the influence of UV irradiation and visible light compared to nanoparticles of pure anatase. The excellent photocatalytic effect of PANI-TiO_2 can be explained by the synergistic effect of PANI and TiO_2, which contributes to the efficiency of photogenerated carrier migration at the PANI-TiO_2 interface. Polyaniline film has been shown to be a good sensitizer under

the influence of UV irradiation and is a promising candidate for photoelectrocatalysis.

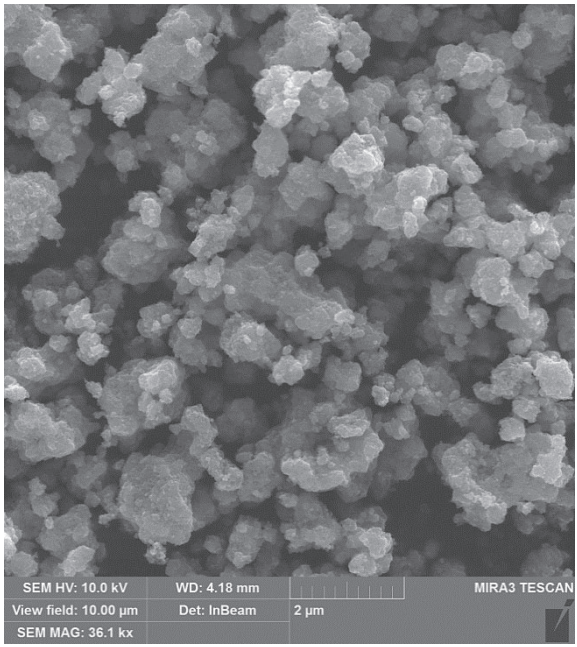

Fig. 5.4 SEM image of sample 1 based on electrode material with titanium dioxide produced in IPMS NASU (magnification by 36,100 times).

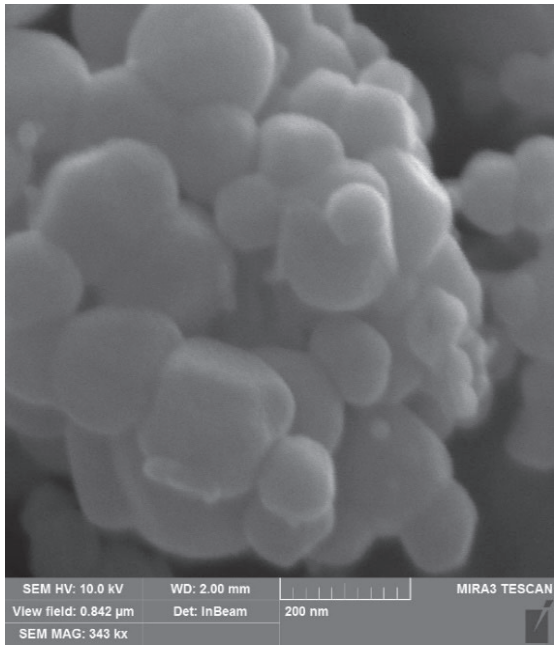

Fig. 5.5 SEM image of sample 1 based on electrode material with titanium dioxide produced in IPMS NASU (magnification by 343,000 times).

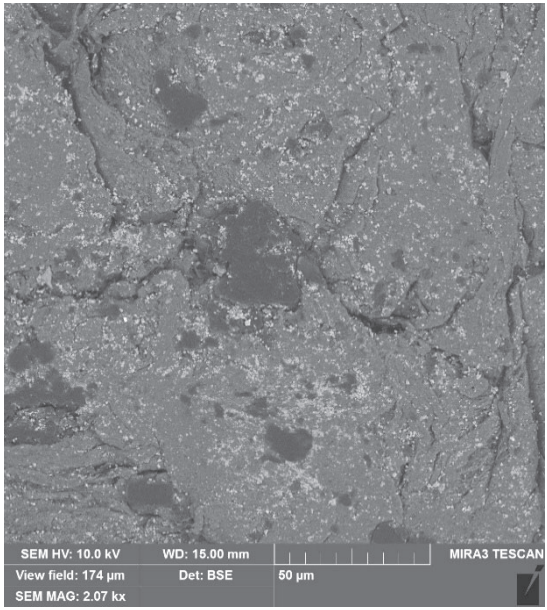

Fig. 5.6 SEM image of sample 1 based on electrode material with titanium dioxide produced in IPMS NASU (magnification by 2,070 times).

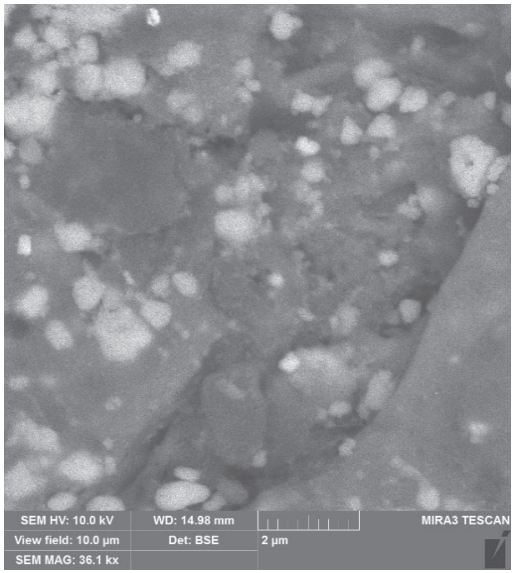

Fig. 5.7 SEM image of sample 1 based on electrode material with titanium dioxide produced in IPMS NASU (magnification by 36,100 times).

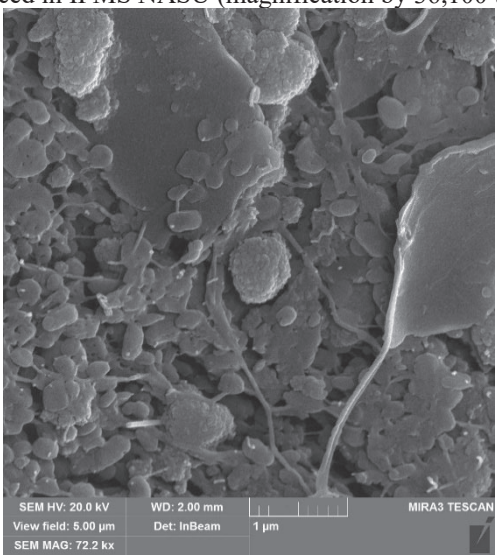

Fig. 5.8 SEM image of sample 1 based on electrode material with titanium dioxide produced in IPMS NASU (magnification by 72,000 times).

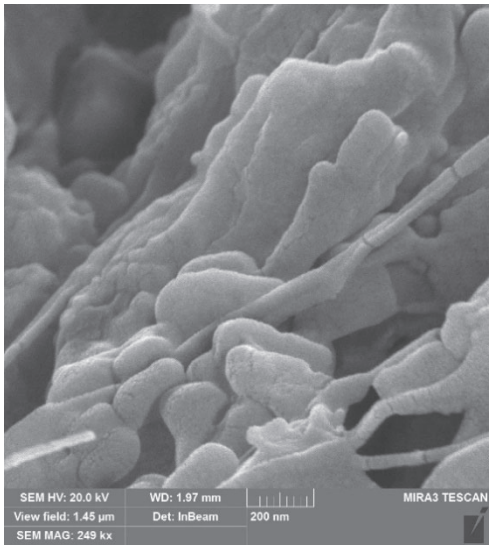

Fig. 5.9 SEM image of sample 1 based on electrode material with titanium dioxide produced in IPMS NASU (magnification by 249,000 times).

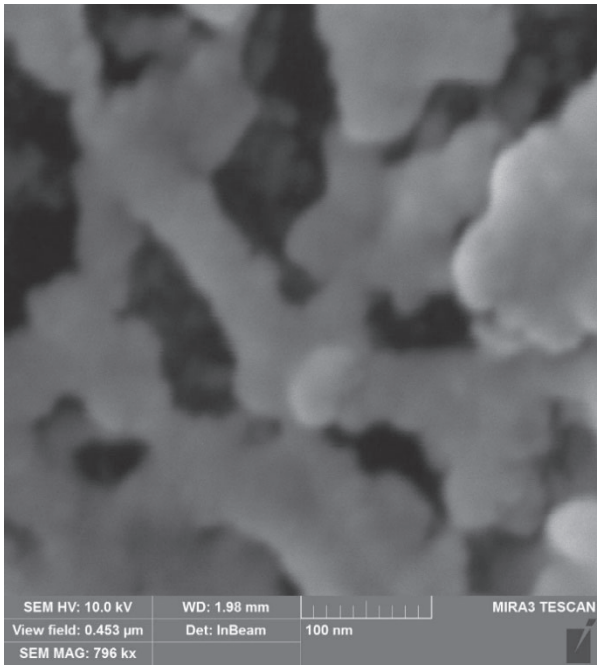

Fig. 5.10 SEM image of sample 1 based on electrode material with titanium dioxide produced in IPMS NASU (magnification by 796,000 times).

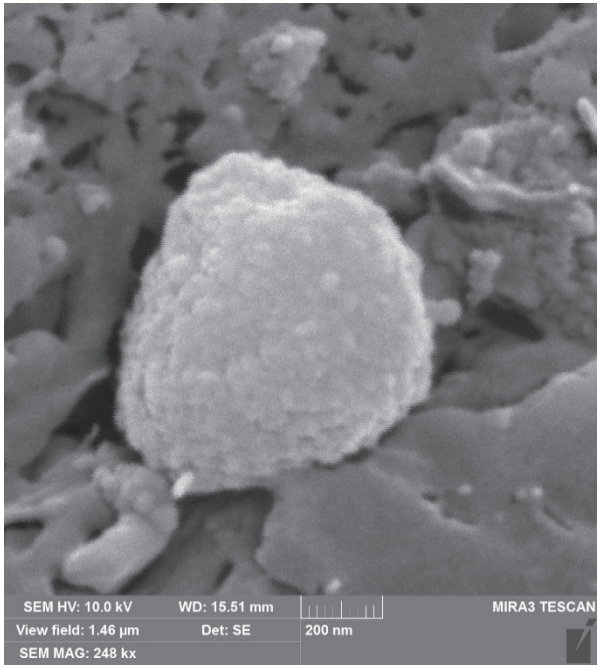

Fig. 5.11 SEM image of sample 1 based on electrode material with titanium dioxide produced in IPMS NASU (magnification by 248,000 times).

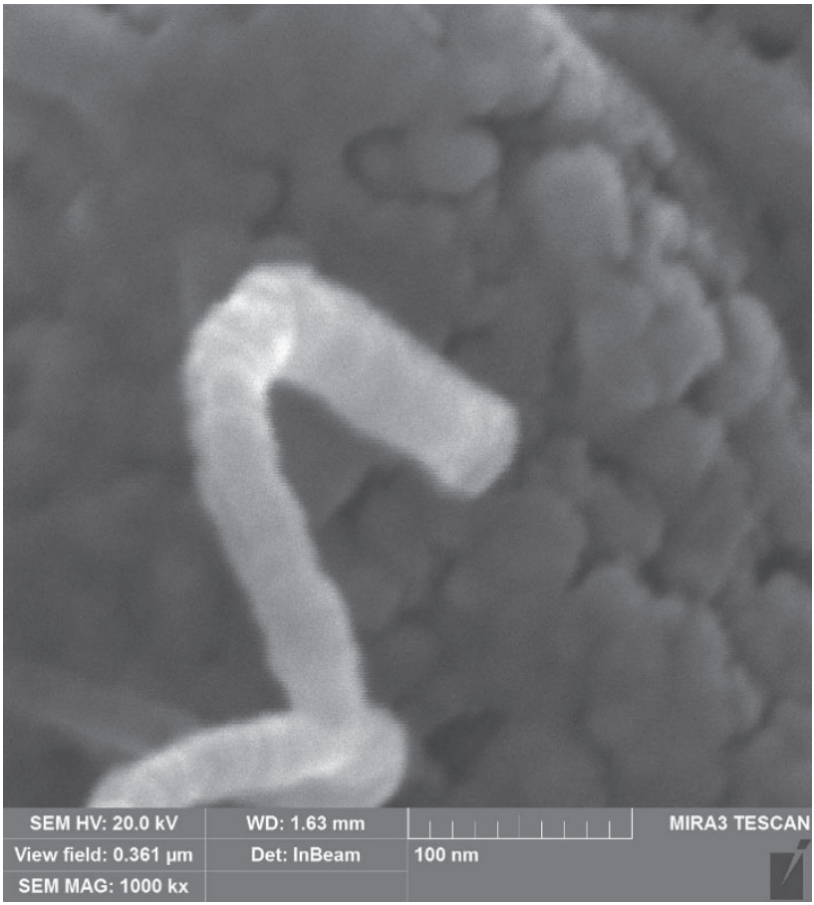

Fig. 5.12 SEM image of sample 1 based on electrode material with titanium dioxide produced in IPMS NASU (magnification by 1,000,000 times).

The process of photoelectrocatalytic amino-azo dye MO degradation was studied in a neutral medium under UV irradiation with a titanium dioxide photoelectrocatalyst of nanodispersed morphology and anatase structure synthesized by the authors from a metatitanic acid $TiO(OH)_2$ suspension. Its activity was also compared with that of standard samples (P25 with anatase-rutile phase ratio of 80:20, pure rutile). The samples were characterized by XRD, TG, DTG, TEM, EPR, and the adsorption-

structural static volumetric method. The phase composition, unit cell parameters, and dispersion of the samples were determined.

The results of thermogravimetric measurements and the porosity characteristics were also analysed. The presence of Ti^{3+} defects (EPR) was the reason for the semiconductor bandgap decrease in the synthesized sample. Using potentiodynamic and potentiostatic measurement of carbon-paste TiO_2-graphite electrodes, low-powered UV irradiation was shown to increase the oxidation current to 100 % and higher at scanning rates above 50 mV/s and potentials of up to 500 mV for the synthesized sample, as well as the absence of significant changes under the same conditions for the standard samples used. The photoelectrocatalytic activity of the samples was defined by their nanodispersity, crystallite morphology, and pore size distribution. This varies symbatically with the concentration of Ti^{3+} and surface hydroxide groups.

A promising option is the doping of titanium dioxide with other cations, primarily manganese. Composite materials based on TiO_2 and MnO_2 are used due to their complementary properties as oxidizing agent, electrocatalyst, and photoelectrocatalyst. Generally, both carbon paste electrodes with TiO_2 and conductive polymer composites of TiO_2 with PANI are promising methods for combating environmental pollution. Considering the synergy recorded for PANI-TiO_2 composites during the photocatalytic decomposition of phenol under the influence of UV-vis, polyaniline film is a good sensitizer under the influence of UV radiation and is also promising for use in photoelectrocatalysis. The synthesized TiO_2 sample 1 showed the highest efficiency for the photoelectrocatalytic process. This effect is associated with the influence of defective Ti^{3+} centres near the interface due to a bandgap decrease in the TiO_2 semiconductor.

5.4 TiO_2-MnO_2 System in PEC Processes

As mentioned earlier, coupling with other narrower bandgap semiconductors is an efficient strategy to develop highly-active TiO_2. Bandgap data for manganese dioxide varies significantly. The optical bandgap of α-MnO_2 nanofibres has been estimated at 1.32 eV (Gao et al. 2008, 112) and MnO_2 nanoparticles display E_g = 1.30 eV based on UV-visible absorption (Chan et al. 2013, 756). The bandgap of β-MnO_2, obtained from PL and UV-vis in Sherin and Thomas (2015, 4), was found to be in the range 3.185 eV–3.45 eV. The narrow bandgap of MnO_2 (0.26–2.7 eV) was reported in Chen and Zhang (2019).

Below, the focus is on manganese dioxide as a useful semiconductor. Its physicochemical properties, structure peculiarities, and electrochemical applications, i.e. properties that promote the use of manganese dioxide in PEC, are analysed.

5.4.1 Manganese dioxide: its occurrence, polymorphic structure, and chemical thermodynamics

Abundance in nature, minerals, and biological role. Manganese dioxide is one of the most thermodynamically stable compounds of manganese and is found in abundant deposits of various kinds in the Earth's crust. Crystal rocks contain, on average, about 0.1 % Mn and thirty manganese oxide/hydroxide minerals are known (Emsley 2001). Mn has a tendency to partition into minerals forming in the early stages of magmatic crystallization. Manganese is readily depleted from igneous and metamorphic rocks by interactions with surface water and groundwater; as Mn(II), it is highly mobile in acidic aqueous systems (Varentsov 1980). Near the Earth's surface, Mn is easily oxidized to Mn oxide minerals that are brown-black and typically occur as intimately intermixed, fine-grained, poorly crystalline masses or coatings.

The most important manganese ore is pyrolusite (β-MnO_2). The minerals *hausmannite* Mn_3O_4 and *brownite* Mn_2O_3 are also important. The most abundant manganese ores are *hollandite* ($BaMn_8O_{16}{\cdot}2H_2O$), *rhodochrosite* ($MnCO_3$), and *manganite* (MnOOH).

Land-based resources are large, but irregularly distributed. Approximately 80 % of the world's known manganese resources are found in South Africa. Other important manganese deposits are found in Ukraine, Australia, India, China, Gabon, and Brazil (Corathers 2009). Manganese forms chemical sedimentary deposits in shallow, near-shore environments. The most significant of these deposits formed to the north of the Black Sea about 35 million years ago during the Oligocene. Named Chiatura and Nikopol, after two cities in Georgia and Ukraine, they contain an estimated 70 % of the world's known resources of high-grade manganese (Skinner 2015).

Manganese nodules at the bottom of oceans, seas, and lakes (Vereshchagin 2019) are significant prospective sources of this element that are not yet available to industrial production. Nevertheless, recent developments are bringing the practical use of these valuable resources closer in terms of approaches and equipment (Lungemeister 2020). In-depth characterization of low-grade Mn ores also has the potential for future exploitation (Ali 2020). Lithiophorite, hollandite, and birnessite are

the major Mn minerals reported in soils (Taylor et al. 1964; Golden et al. 1993).

Manganese is available in three valence states (II, III, IV) whose stability boundary lies within the range of the natural environment (Glasby 1986; Morgan 2000). Manganese oxides also have high adsorption capacities.

The high redox potentials of Mn (III, IV) compounds in the aqueous environment explain their close relationship to other redox elemental cycles (oxygen, carbon, iron, sulfur, and arsenic). The biological significance of manganese lies in oxygen formation as a result of the photosynthesis II system and in disposing of superoxide radicals (superoxide dismutase). It has more than 20 biological roles in enzymes and proteins. Biological processes exert significant influence on the geochemical cycle of manganese through bacterial reduction and oxidation, and incorporation in biomass (Morgan 2000).

Manganese dioxide polymorphs and their structure. Manganese(IV) oxides form a large family of metastable structural polymorphs that are stable at ambient temperatures. The tunnel polymorphs of pyrolusite (β-MnO_2, rutile structure type), ramsdellite (diaspore structure type), and hollandite (α-MnO_2, hollandite structure type) see a sequential increase in MnO_6 octahedrons filling the tunnel walls: 1×1, 2×1, 2×2, etc. (fig. 5.13).

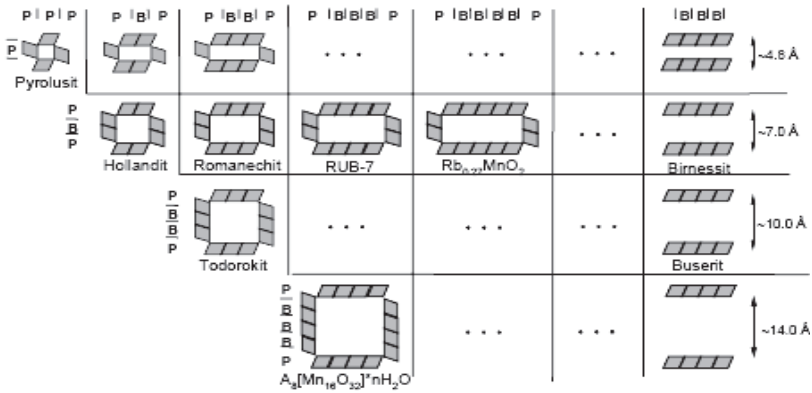

Fig. 5.13 Tunnel polymorphs and the limiting layered phases of the manganese dioxide family, as shown in Veblen (1991) and Rziha (1997).

Octahedrons of MnO_6 share edges and form double and triple or more chains. These chains share corners with neighbouring chains to form a framework structure containing large tunnels. Starting with hollandite, the tunnels are too large to be empty. Therefore, tunnel polymorphs of 2×2, 2×3, 3×3, and 3×4 channel size belong to "open structures" with some species inside tunnels stabilizing the structural framework. The spinel λ-MnO_2 polymorph is also known. The limiting cases are birnessite and buserite 2D-layered structures that can be described as 2×∞ and 3×∞, respectively (Wells 2012). The abovementioned structural peculiarities of manganese(IV) oxides explain their molecular sieve properties. The unit cell parameters of the most important manganese dioxide tunnel polymorphs are presented in table 5.1.

Pyrolusite or β-MnO_2 is the most stable and abundant manganese dioxide polymorph. It has a rutile (TiO_2) structure type, forming a framework of oxygen octahedrons and MnO_6 containing tunnels with square cross sections laid out one octahedron by one octahedron (1×1) a side (fig. 5.14). The tunnels in pyrolusite are too small to accommodate other chemical species and chemical analysis indicates that its composition deviates at most only slightly from pure MnO_2.

Ramsdellite has a structure consisting of a framework of tunnels with rectangular-shaped cross sections with 1×2 octahedrons on each side (Fig. 5.14). The tunnels are generally empty and its composition is very close to the stoichiometric one. Ramsdellite with a stoichiometric composition is a relatively rare isostructural mineral along with goethite (FeOOH) and gibbsite (AlOOH).

Hollandite or α-MnO_2 forms an isostructural series with the general formula $fA_{0.8–1.5}[Mn(IV), Mn(III)]_8O_{16}$, where A = Ba, Pb, K, or Na depending on the species of the A-cation (Ba^{2+}, K^+, Pb^{2+}, and Na^+). These are hollandite, cryptomelane, coronadite, and manjiroite, respectively. The tunnels are partially filled with large uni- or divalent cations and, in some cases, water molecules. The charges on the tunnel cations are balanced by the substitution of lower valence cations (e.g., Mn(III), Fe(III), Al(III), etc.) for some of the Mn(IV). Hollandite minerals commonly occur intermixed and, in some cases, grade from one to another along a single crystal (Post 1999).

Hollandite can be found in tetragonal or monoclinic crystal systems. The stability limits of the hollandite phases, depending on the physical Shannon ionic radii (Shannon 1976) for the coordination number 8 of tunnel cations and atomic number Z, are shown in Fig. 5.15.

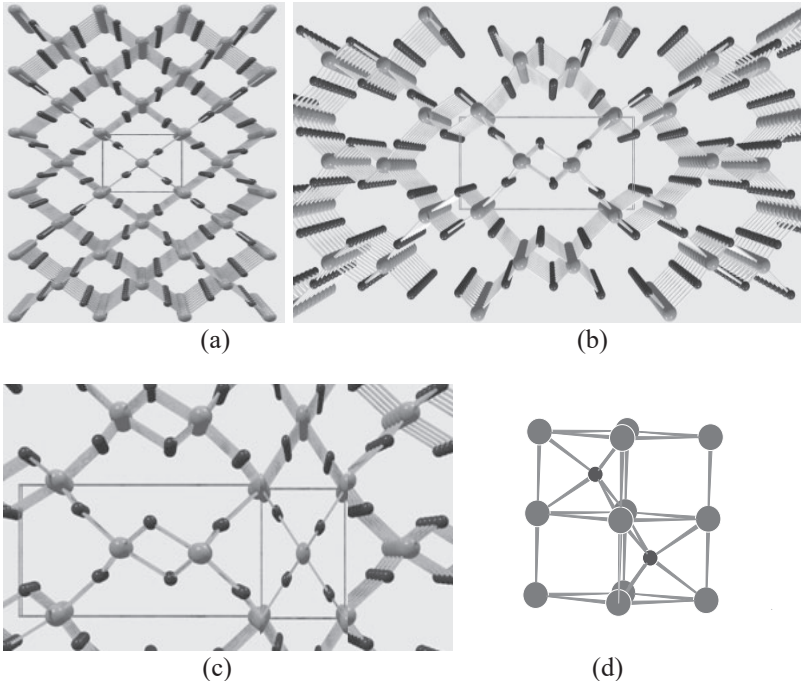

Fig. 5.14 Fragments of MnO_2 polymorph frameworks with their unit cells built in Powder Cells for Windows v. 2.3: pyrolusite (a); ramsdellite (b); a structure with ramsdellite/pyrolusite intergrowth defects that is usually called γ-MnO_2 (c); and the ε-MnO_2 unit cell with cation vacancies (d).

According to Zhang and Burnham (1994), inequality (5.1) demonstrates the conditions for hollandite tetragonal phase stability:

$$r_{\mathrm{Me}} > \sqrt{2}\,(r_O + r_{Mn^{4+}}) - r_O = 0.133\ nm \qquad (5.1)$$

where r_{Me}, r_{O}, and r_{Mn}^{4+} are the ionic radii of the metal cations in the tunnel cavity, oxygen, and manganese, respectively. They introduce additional inequality for the lowest limit of the tetragonal phase stability region (5.2):

$$r_{Me} > \sqrt{2}\,(r_O + r_{Mn^{4+}}) - r_O - 0.015 = 0.118\,nm \qquad (5.2).$$

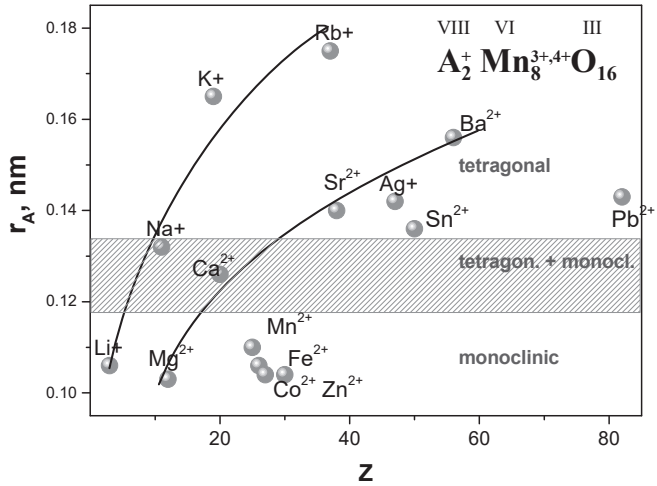

Fig. 5.15 Stability limits of hollandite $A^+_2Mn^{3+,4+}_8O_{16}$ phase depending on physical Shannon ionic radii (coordination number 8) of tunnel A cations and atomic number Z (high-spin Mn^{2+}-Zn^{2+} configurations were used).

Chemical thermodynamics. Detailed study of the thermodynamic properties of pure metastable phases of manganese(IV) oxides and MnOOH hydroxides was conducted by S. Fritsch (1997). Like zeolites, the polymorphism of the system insignificantly affects the thermodynamic parameters, as revealed by high-temperature calorimetric experiments (Petrovic 1993); the differences between experimentally determined values of enthalpy of 1×1 and 2×1 tunnel structures was shown to be insignificant (about 6 $kJ \cdot mol^{-1}$). The similarity of the thermodynamic parameters of different oxide structures of manganese(IV) indicates that the process of synthesis of such metastable microporous materials is not thermodynamically limited.

Gibbs energy calculations for the tunnel structures of manganese(IV) oxides of different stoichiometries were performed by Parc et al. (1989). The stability fields of each phase were evaluated in accordance with the behaviour of its natural analogues. The phases of pyrolusite and nsutite have identical values of free energy (−465 $kJ \cdot mol^{-1}$ and −470 $kJ \cdot mol^{-1}$, respectively). However, the presence of cations or water in the cavities, reduces the free energy significantly (−3800… −4100 $kJ \cdot mol^{-1}$, −4400 $kJ \cdot mol^{-1}$) for cryptomelane and birnessite, respectively.

Table 5.1. Unit cell parameters of (n×m) tunnel manganese dioxide polymorphs

1×	**1×1**	**1×2**	**1×3**	**1×4**	**…**	**1×∞**
Phase	*pyrolusite*	*ramsdellite*	*?*	*?*		*?*
Space group	P42/mnm	Pbnm (Pnam)				
crystal system	tetrag.	orthorhom.				
a, nm	0.434	0.451 (0.932)				
b, nm	0.434	0.926 (0.446)				
c, nm	0.287	0.286 (0.285)				
2×	**2×1**	**2×2**	**2×3**	**2×4**	**2×5**	**2×∞**
Phase	*ramsdellite*	*hollandite*	*romanechite*	*Rub-7*	*$Rub_{0.27}MnO_2$*	*birnessite*
Space group	Pbnm (Pnam)	I4/m (I12/m1)	C12/m1 (A12/m1)	C2/m	A 2/m	C2/m
crystal system	orthorhom.	tetrag. (monocl.)	monocl.	monocl.	monocl.	monocl.
a, nm	0.451 (0.932)	0.982 (1.001)	1.393 (0.956)	1.419	1.500	0.515
b, nm	0.926 (0.446)	0.982 (0.287)	0.286 (0.288)	0.285	0.289	0.284
c, nm	0.286 (0.285)	0.285 (0.975)	0.968 (1.385)	2.434	1.464	0.718
3×	**3×1**	**3×2**	**3×3**	**3×4**	**3×5**	**3×∞**
Phase	*?*	*romanechite*	*todorkite*	*woodruffite*	*?*	*buserite*
Space group		C12/m1 (A12/m1)	P2/m	C2/m		C2/m
crystal system		monocl.	monocl.	monocl.		monocl.
a, nm		1.393 (0.956)	0.979	2.481		0.223
b, nm		0.286 (0.288)	0.283	0.285		0.2854
c, nm		0.968 (1.385)	0.955	0.958		1.0265
4×	**4×1**	**4×2**	**4×3**	**4×4**	**4×5**	**4×∞**
Phase	*?*	*Rub-7*	*Woodruffite*	*?*	*?*	*?*

5.4.2. Manganese dioxide non-stoichiometry as a primary advantage for PEC

The influence of defects on catalytic and electrochemical activities. The electrochemical, catalytic, and electrocatalytic properties of manganese dioxides depend on their defects and their concentrations. The non-stoichiometry of manganese dioxide is defined by ions of manganese of mixed valence that occupy the same sites of the crystal lattice (Brenet 1979) and the cation vacancies (Ruetschi 1988). Oxygen vacancies are also incorporated into the Mn oxide framework with the highly efficient ozone decomposition or doping of γ-MnO_2 by transition and rare earth metals like Co^{2+} and Ce^{4+} (Li 2018**)**. MnO hexagonal sheets possessing abundant oxygen vacancy defects (MnO-Vo) were synthesized by pyrolyzing and reducing $MnCO_3$ in an atmosphere of Ar/H_2 (Zou 2019). The oxygen vacancies (Vos) were generated in the reduction process for ultra-long life lithium storage with high capacity. Oxygen vacancies were also introduced by special plasma and heat treatments.

Some polymorphs support intergrowth defects. For instance, the γ-MnO_2 polymorph represents a group of ramsdellite products with randomly distributed intergrowth microdomains of pyrolusite (De Wolff 1959). Reports on other intergrowth types were published in the HRTEM study (Busek 1983; Shao-Horn 1998). As shown by Sokolsky et al. (2012), semi-amorphous manganese dioxide products with only a γ-MnO_2-like phase in the XRD-pattern revealed hollandite tunnels through porometry. This means that the size of the hollandite structure domains is below the XRD phase determination limit (<2–5 nm).

The influence of defect types on the electrochemical activity of MnO_2 was studied in depth in France (Chabre and Pannetier 1995). The structural model developed enables the reproduction of details of the diffraction patterns of these materials and, conversely, quantitative determination of structural disorder. Comparison with experimental diffraction data shows micro-twinning and the De Wolff disorder in all γ-MnO_2 synthetic samples. The micro-twinning concentration is predetermined by the preparation method. Chemically synthesized MnO_2 (CMD) and electrochemically obtained MnO_2 (EMD) exhibit different amounts of De Wolff disorder. The main conclusion of this work is that γ- and ε-MnO_2 are similar materials due to their structure. Both forms are derived from the ramsdellite structure, differing only in terms of the concentration of structural defects. ε-MnO_2 samples exhibited more micro-twinning than γ-MnO_2 samples. Researchers have quantified the effects of intergrowth

(DW), the calculated pyrolusite fraction (Pr), and the introduced defects of twinning (Tw) for the first time (5.3–5.6):

$$Pr = 0.602\cdot(DW) - 0.198\cdot\delta^2(DW) + 0.026\cdot\delta^3(DW), \quad (5.3)$$

$$\delta\,(DW) = 2\theta\,(110) - (Tw) - 21.808, \quad (5.4)$$

$$\delta\,(Tw) = -0.0054 \cdot Tw - 8.9 \cdot 10^{-5} \cdot Tw^2, \quad (5.5)$$

At $Tw < 55\%$; $\delta\,(Tw) = -0.56$, when $Tw \geq 55\%$,

$$Tw = 100 - 68.17 \cdot \Delta 2\theta \quad (5.6)$$

where $\Delta 2\theta$ is the distance between peaks (221) and (240).

Numerous investigations into the electrochemical activity of manganese dioxide in batteries have been performed and the impact of defects, their type, and their concentrations have been defined (Brenet 1979; Ruetschi 1988). These defects can facilitate mass and charge transfer during a solid state electroreduction process that includes the incorporation of protons in the cathode material of alkaline batteries. The Zener effect is a "double exchange" effect detected in EPR analysis that accounts for improvements in charge transfer (Kakazey 2001, 2003). Here, an exchange with an electron occurs between a Mn^{4+} cation and the defect position of a Mn^{3+} cation separated by an O^{2-} anion (5.7):

$$Mn^{3+}—O^{2-}—Mn^{4+} \leftrightarrow Mn^{4+}—O^{2-}—Mn^{3+} \quad (5.7)$$

This transfer is the result of two processes: (a) the transfer of a p-electron from the Mn^{3+} cation to the Mn^{4+} cation and (b) a jump by the d-electron from the second cation to fill its place. Alternatively, this mechanism includes the facilitation of the proton transport process because points of Mn^{3+} defects in the bulk are fixed in the crystal lattice by OH-groups or Coleman protons (Ruetschi 1988). As a result, correlations between EPR signal broadening, ΔB, and OH^- and Mn^{3+} content and ionic conductivity values are observed (Kakazey 2001, 2003).

The challenges of manganese dioxide synthesis. The non-stoichiometric nature of manganese dioxide favours electrochemical (catalytic) activity and leads to the problem of how to reproduce its composition, structure, and properties. This has been such a problematic task that the industrial sector and scientific community sought to introduce a global classification of manganese dioxide for the practical purposes of companies and producers in the late 1970s. The table below presents the International Standard Samples (ISS) of manganese dioxide (Takahashi 1981; Table 5.2).

Even now, when the non-stoichiometry driving forces are better understood, the uncertainty surrounding reproducible manganese dioxide behaviour in catalytic, chemical, and electrochemical processes remains a challenge for researchers.

The method of electrodeposition has many advantages and is frequently used in industrial production—EMDs belong to the group of γ-MnO_2 products (Chabre and Pannetier 1995). The electrodeposition phase composition in this case is significantly defined by the admixtures present in the electrolyte and, particularly, by its cationic and anionic species. The influence of these parameters on EMDs is not yet sufficiently taken into account in the literature. Nevertheless, as shown by Sokolsky et al. (2015), the presence of low M^+ content, where the M^+ is in the form of alkali metal or ammonium ions, causes hollandite phase electrodeposition, but Cr^{3+} ion additives cause birnessite phase electrodeposition (Sokolsky 2018). The duration of electrolysis is the parameter that changes the structure of the product (fig. 5.16). The influence of electrolyte composition on the polymorphs formed is shown in fig. 5.17. It can be seen that, at the same M^{3+} and M^+ (0.1M) concentrations, the phase composition is defined by the nature of these ions. Hollandite crystallizes with needle-like shapes, as shown in fig. 5.18 (Sokolsky 2007). Their identity was established by electron diffraction.

The electrodeposition mechanism of manganese dioxide has been the subject of numerous publications (Paul 1986; Clarke 2006; Ivanova 1999; Sokolsky 2020). EMDs are most frequently obtained from the anodic electrodeposition of Mn(II) species. Sulfuric acid electrolytes are commercially used to obtain γ-MnO_2, while fluoride-containing electrolytes have the advantage of high rate electrodeposition (Ivanova 1999).

As shown earlier, a manganese (IV) oxide electrodeposition process includes the following charge transfer stages in dilute acid solutions (5.8–5.11). The chemical stages of anodic oxidation (disproportionation or hydrolysis) confirmed the diagnostic criteria of the voltammetry method:

$$[Mn(H_2O)_6]^{2+}ads \leftrightarrows [Mn(H_2O)_6]^{3+}ads + e- \text{ (fast)} \quad (5.8)$$

$$MnOOH \leftrightarrows MnO_2 + H^+ + e- \text{ (slow).} \quad (5.9)$$

$$2Mn^{3+} + 2H_2O \leftrightarrows MnO_2 + Mn^{2+} + 4H^+; \quad (5.10)$$

$$[Mn(H_2O)_6]^{3+}ads \leftrightarrows [Mn(H_2O)_5(OH)]^{2+}ads + H^+ \quad (5.11)$$

$$\downarrow$$

$$MnOOH$$

(fast).

Table 5.2. International Standard Samples of manganese dioxide (January, 1975)

№	*Sample type*	*Producer*	*Crystal structure*	*Composition*			*Density, g/cm³*	*Surface area, m²/g*
				Mn	*MnO_2*	*H_2O*		
1	**EMD** (Ti anode)	Japan	γ	60.6	91.2	1.2	4.46	58.5
2	**EMD** (Pb anode)	Japan	γ	60.1	91.8	2.2	4.47	50.1
3	**EMD** (C anode)	Japan	γ	60.0	90.8	1.7	4.41	53.5
4	**EMD**	France	γ	59.6	90.4	3.1	4.44	53.9
5	*CMD*	Japan "Japan Met. & Chemicals Corporation"	γ	61.1	92.7	1.5	4.76	82.5
6	β-**MnO_2**	Reagent	β	-	-	-	-	-
7	**MnO_2** *Natural*	Ghana	γ	53.4	81.2	0.6	4.25	22.0
8	*CMD*	Belgium *"Sedama"*	γ	60.9	90.6	1.0	4.7	70.5
9	**EMD** .	USA "Kerr-McGee Corp."	γ	60.3	91.7	3.5	4.5	74.1
10	**EMD**	USA "Kerr-McGee Corp."	γ	59.2	89.7	2.0	4.42	59.9
11	*CMD (chlorate method)*	USA "Kerr-McGee Corp."	γ	60.2	92.8	0.5	4.40	12.4
12	*CMD*	Belgium *"Sedama"*	γ, ρ	61.5	91.8	1.7	2.74	80.0

The foreign ions in an electrolyte solution broaden the scope of the electrodeposition method. As shown previously, these ions influence the polymorphic composition, structure, size, and morphology of crystallites of the product (Sokolsky 2020) and make possible the direct preparation of non-stoichiometric transition metal oxides based on thin-film cathodes for lithium rechargeable batteries by electrodeposition (Boldyrev 2013).

The electrolytic doping procedure modifies the manganese dioxide phase and chemical composition, and defect states have a strong influence on the functionality of the transition metal oxide. Further efforts are needed to combine the unique chemical, catalytic, and electrocatalytic activity of doped MnO_2 with state-of-the-art nanotechnologies. This could be done by bringing the accumulated experience in this area (Massaro and Colletti 2017, 5; Cavallaro and Lazzara 2017, 5; Cavallaro and Danilushkina 2017, 7) to bear on natural nanotubes of halloysite (HNT). Their eco-friendly behaviour opens the door to new green approaches in the removal of organic contaminants, as the activity of manganese dioxide on a contaminated interface is controlled by the HNT, making it safe for the environment.

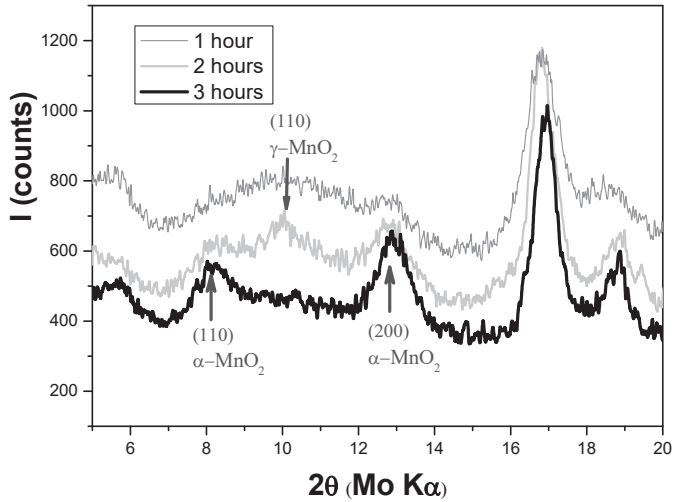

Fig. 5.16 XRD patterns of manganese dioxide samples obtained from anode electrodeposition on Pt electrode with electrolyte 1.5M $(NH_4)_2SO_4$ + 0.7M $MnSO_4$ + 0.1M HF in characteristic hollandite and ramsdellite peaks (1-1 h of electrolysis; 2 - 2 h of electrolysis; 3-3 h of electrolysis).

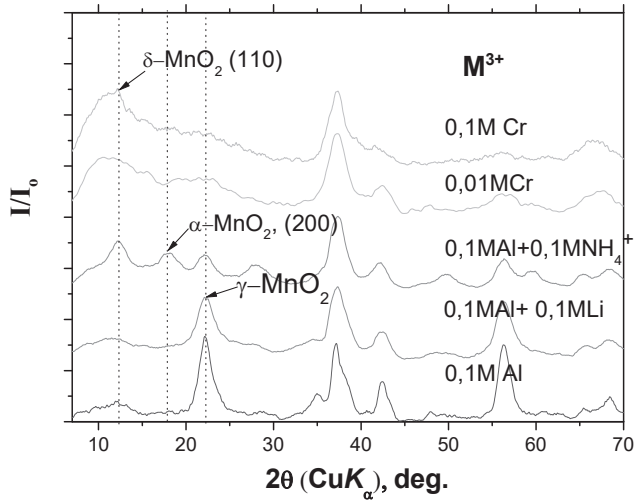

Fig. 5.17 XRD patterns of manganese dioxide samples obtained by anode electrodeposition on a Pt electrode in an electrolyte solution with 0.1M M^{3+} ions (M^{3+} = Al^{3+}, Cr^{3+}) and in combination with M^{+} ions (M^{+} = NH_4^{+}, Li^{+}).

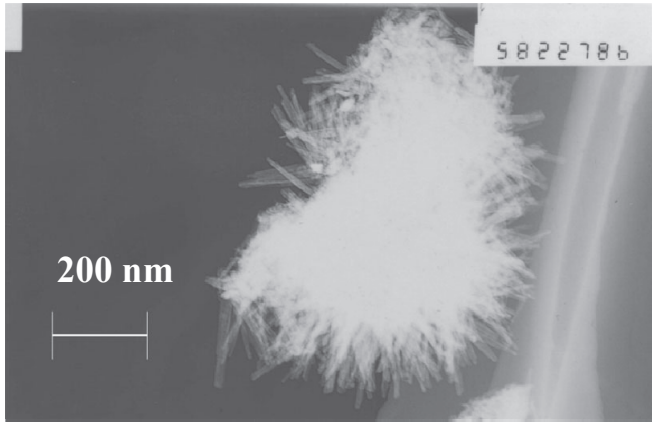

Fig. 5.18 Microphotographs of a manganese dioxide sample doped by Li^{+} ions and obtained by anode electrodeposition on a Pt electrode (Sokolsky 2007).

5.4.3. Manganese dioxide applications

The roots of natural manganese dioxide applications date back to Neanderthal times (Heyes 2016). In the last century, MnO_2 (primarily γ-MnO_2) was used as a cathode material in zinc-carbon dry-cell batteries. Alkaline batteries, using synthetic electrolytic Mn oxide, have increasingly come to dominate the market (Post 1999). Leclanché dry cells (invented and patented by Leclanché in 1866), alkaline, and air-MnO_2 primary batteries, can also be mentioned. Manganese (IV) oxide system compounds have also attracted attention as low-cost precursors of cathode material in the recently invented Li-ion battery technology.

Other examples of their practical use include the selective recovery of lithium from seawater (Yoshizuka 2002; Ryu 2019) and the immobilization of certain radioactive cations as part of a waste storage system (Xhaxhiu 2015). It has been shown that at high pressures feldspar minerals transform into a hollandite-like structure (Ringwood 1967), making this phase a potentially important structure type in the lower crust and upper mantle of the Earth.

The high selectivity and activity towards catalytic oxidation of CO (Ivanova 2002) and volatile organic compounds (Suib 2000) have also been mentioned in a series of studies. The electrocatalytic activity of manganese(IV) oxides in anode oxidation reactions has also been noted (Sokolsky 2012).

OER (ORR) electrocatalysis on MnO_2. The lower overvoltage and the higher current densities at the same electrode potential, the more promising an electrode material is for various applications, including oxygen reduction (ORR) and oxygen evolution (OER) reactions (Song 2008). The processes of oxygen evolution and reduction are important constituents of sustainable power generation and water splitting technologies. The ORR process has found wide application in many energy conversion devices, such as fuel cells, metal-air batteries, and regenerative fuel cells (Ng and Wei et al. 2013, 12).

Despite their excellent electrical performance, new findings and developments in lithium-air battery (LAB) technology are crucial. A recent strong interest in the oxygen reduction reaction (Débart 2008) has focused on nanowires of α-MnO_2 hollandite, as well as other doped manganese dioxide polymorphs (Sokolsky 2018) as highly active electrocatalysts. Recently, the α-MnO_2 polymorph with nanowire morphology demonstrated an exceptional capacity of 3000 $mA{\cdot}h{\cdot}g^{-1}$ for Li-air battery (LAB) technology (Débart 2008). The crystal structure of

this polymorph has the ability to accommodate both Li^+ and O^{2-}, or O^{2-}_2 in the case of aqueous and nonaqueous types of LAB. Synthesis of a material like α-MnO_2 with special designs may provide a successful strategy. A new 3D hollow α-MnO_2 framework (3D α-MnO_2) with porous walls assembled by hierarchical α-MnO_2 nanowires has been prepared by a template-induced hydrothermal reaction and subsequent annealing treatment. Such a distinctive structure offers some useful properties for Li-O_2 batteries, including the intrinsic high catalytic activity of α-MnO_2, more catalytic active sites of hierarchical α-MnO_2 nanowires on a 3D framework, a continuous hollow network, and rich porosity for the storage of discharged product aggregations and oxygen diffusion (Liu and Zeng 2019, 15).

The redox pairs of Mn(III)/Mn(IV) and the Jahn-Teller distorted Mn(III) ions of the surface layer of the crystal lattice are the most likely active sites of oxygen reduction and oxygen oxidation reactions (ORR (OER)). As described by many authors, the generation of oxygen vacancies in a material enhance its efficiency as an air electrode. This is the case with γ-MnO_2 nanorod-assembled hierarchical microspheres with abundant oxygen defects synthesized using a simple thermal treatment approach as oxygen reduction electrocatalysts for Al-air batteries (Ge et al. 2020). The γ-MnO_2 nanorod-assembled hierarchical microspheres calcined under 300 ºC in an Ar atmosphere showed the best ORR performance. A standard doping procedure has also been shown to improve the discharge characteristics of novel Ni and Al doped manganese oxide $Ni_xAl_yMn_zO_2$ (Cai et al. 2020, 10).

Oxygen reduction reaction (ORR) electrocatalysts do not show an active oxygen evolution reaction (OER) process and vice versa. Therefore, developing a bifunctional ORR and OER catalyst for LAB technology is quite a complicated and important task. An example of an effective strategy is to control the growth of a small amount of nanosized transition metal oxides on the surface of the carbon electrode. This approach combines the advantages of surface, interface, and nanoengineering. A MnO_2 content of 9 wt% was deposited on reduced graphene oxide ($MnO_2@r_{GO}$) and the MnO_2 particles grew uniformly on the r_{GO} surface with a particle size smaller than 20 nm. The r_{GO} framework possesses a porous multilayer structure. The nanosized MnO_2 possesses a highly exposed surface, which enhances surface transport of LiO_2 species and avoids the accumulation of discharge products on the electrode surface. Furthermore, a transition between lithiated and nonlithiated manganese oxide during the discharge and charge processes was observed. This transition promotes electron transfer between discharge products and the

catalyst, thereby reducing the overpotential of the oxygen evolution reaction (Lihua et al. 2019, 2).

Electrocatalysis of phenol oxidation. Thin film manganese dioxide coatings can maintain stability by the control of medium acidity and selection of the appropriate range of working potentials. As such, film electrodes based on manganese (IV) oxide, obtained by electrodeposition from fluoride electrolytes, were studied and compared to platinum electrodes in the anodic oxidation of ethanol using cyclic voltammetry. The results showed that Pt and MnO_2 displayed close values for electrochemical activity. The possibility of anode oxidation of phenol in aqueous solutions on electrochemically doped manganese dioxide was also studied. Iron (II) with hydrogen peroxide H_2O_2 in an aqueous medium (Fenton's reagent) was found to considerably strengthen phenol degradation. An assumption was made that the presence of the Fe^{2+}/Fe^{3+} redox pair in the oxide matrix of the electrode material can contribute to the activation of the anodic oxidation of phenol. A synergistic effect is expected due to the presence of mixed valence ions of different natures in the crystalline oxide matrix of manganese, along with anode generation of peroxide ions. The phenol (0.1 M) and sulfuric acid content of the electrolyte solution was applied. This electrolyte was used for electrolysis with a platinum anode covered with the iron-doped manganese dioxide film. The duration of electrolysis was one hour and the current density was 3.3 mA/cm^2. The iron-doped MnO_2 demonstrated advantages over the Pt electrode (Sokol'skii 2012).

In a study by Li and Sun (2018, 282), manganese dioxide was found to enhance the electrocatalytic generation of hydrogen peroxide and hydroxyl radicals for the degradation of phenol in wastewater. Modified MnO_2 nano-graphite (MnO_2/nano-G) and Pd loaded Ni-foam (foam-Ni/Pd) composites were prepared by the chemical redox and electrodeposition methods, respectively, and a two-layer type MnO_2/nano-G|foam-Ni/Pd composite cathode was prepared with chitosan as a binder. SEM and XRD results showed a crystal mix of MnO_2 (α-MnO_2 and γ-MnO_2) nanorods with lengths of 80–200 nm and widths of 20–50 nm uniformly loaded on the nano-G surface and that three-dimensional Pd° metal trees/crystals were tightly deposited on the foam-Ni substrate. The prepared cathode was applied in the electrocatalytic degradation of phenol in wastewater. The degradation efficiency of phenol by the MnO_2/nano-G|foam-Ni/Pd cathode was maximal. The removal efficiencies of phenol and total organic carbon (TOC) by the MnO_2/nano-G|foam-Ni/Pd cathode reached 98.7 % and 85.3 % after 120 min. of electrolysis

under conditions of oxygen aeration. The optimal reaction parameters were a current density of 39 mA• cm^{-2}, an electrolyte (Na_2SO_4) concentration of 0.1 mol• L^{-1}, an electrode distance of 4 cm, and an initial pH of 7.

Adsorption and petroleum removal. Manganese oxides have a high adsorption capacity. For example, δ-MnO_2 has a surface area of 260 m^2 g^{-1} and a pH_{zpc} of 2.25; it can therefore adsorb cations, such as Ni^{2+}, Cu^{2+}, and Zn^{2+}, from natural waters (Glasby 1986). The molecular sieve properties of the samples intensify and enhance the selectivity of processes focused on organic compounds. On the basis of the obtained data, we proposed and investigated some functional materials. Samples doped with ammonium ions were selected for water-soluble petrochemical removal due to their structural channels being able to absorb small size molecules of organic nature.

A high hollandite phase content was confirmed using X-ray and porometry methods. After heat treatment at 200 °C, this material showed greater efficiency in the removal of the water-soluble form of oil products compared to the standard sorbent (activated carbon, LLP Farm-Holding, Ukraine, R.02.03/05926). The residual concentration of oil products was lower in the case of manganese (IV) oxide. These model experiments were performed using the TC1 jet engine fuel as a test oil product (Sokol'skii 2012).

5.4.4 TiO_2-MnO_2 applications in PEC processes

Superfine manganese dioxide particles can increase the utilization rate of visible light irradiation due to their narrow bandgap, large surface area, and negatively charged surfaces (Xue and Huang 2008, 19; Ma and Wang 2017, 189). As such, MnO_2 deposition on the surface of a TiO_2 photoelectrode combines the advantages of wider visible light absorption and higher efficiency of electron-hole separation.

A MnO_2-TiO_2 nanotube array (MnO_2-TiO_2 NTA) photoelectrode was synthesized through anodization and electrodeposition. It was fabricated using a recycle pulse electrodeposition strategy in a traditional anode (TiO_2 NTA photoelectrode)-cathode (Pt plate) configuration. It should be noted that certain ratios of the solution mixture of $MnSO_4$ and Na_2SO_4 served as the supporting electrolyte. During electrodeposition, the deposition voltage (0.4 V, 0.6 V, 0.8 V, 1.0 V, and 1.2 V), the deposition content of the $MnSO_4$ solution, and the deposition time (0.0001 mol·L^{-1}, 5 min.; 0.001 mol·L^{-1}, 1 min.; 0.001 mol·L^{-1}, 3 min.; 0.001 mol·L^{-1}, 5 min.;

and 0.01 mol·L^{-1}, 1 min.) were controlled. After electrodeposition, the obtained samples were repeatedly washed with MQ water and calcined at 350 °C; 400 °C; 450 °C; 500 °C; and 550 °C for 2 h in a muffle furnace with a heating rate of 3 °C·min^{-1}.

The hydroxyl (OH) radicals generated at the photoilluminated MnO_2-TiO_2 NTA/water interface were able to be captured by terephthalic acid (TA) generating 2-hydroxyterephthalia acid (TAOH), which can emit unique fluorescent light with a spectral peak at 315 nm. As such, TAOH was employed to explain the trend of PEC activity in the obtained photoelectrodes for the photodegradation of MO. The initial TA concentration was 0.5×10^{-3} mol·L^{-1} in a 2×10^{-3} mol·L^{-1} sodium hydroxide (NaOH) aqueous solution. Afterwards the reaction solution was irradiated every hour and measured using a FP-6500 spectrometer with 315 nm excitation.

The volume solution of 30 ml with 5 mg·L^{-1} methyl orange (MO) was chosen as the compound for PEC activity evaluation because it is a representative dye that is harmful to humans. Typically, the PEC experiments were carried out in a cylindrical quartz reactor with magnetic stirring under a Xe-lamp with 350 W output power whose emission spectrum was similar to that of sunlight. The MnO_2-TiO_2 NTA photoelectrode and Pt plate served as the working electrode and cathode with a distance of 15 cm from the light source. Then, the MO solution was added to the reactor to establish the adsorption/desorption equilibrium. Afterwards, the MO solution was irradiated using a xenon lamp along with the supplied external potential (+2.0 V, vs SCE), which was controlled by a single output DC power supply (Agilent U8002A). Meanwhile, 0.1 mol·L^{-1} Na_2SO_4 solution served as the supporting electrolyte. During irradiation and the supply of external potential, approximately 2.0 mL of the mixture was withdrawn from the reactor at predetermined intervals and quantified using a UV-vis spectrophotometer (U-3900H) by checking the absorbance at its characteristic adsorption peak of 463 nm.

The enhanced PEC mechanism was further confirmed through the scavenging effect and photoluminescence (PL) spectra. The results showed that the highly ordered TiO_2 nanotube array photoelectrode had a uniform size with an inner diameter of 300 nm and well thickness of 60 nm and MnO_2 nanoparticles were successfully deposited. Furthermore, it was found that the novel MnO_2-TiO_2 NTA-photoelectrode does not only red-shift light absorption to the visible region between 400 nm and 700 nm, but also significantly enhances the generation of hydroxyl radicals, which play an important role in the PEC system. A MnO_2-TiO_2 NTA-photoelectrode made in optimized conditions exhibited much

higher PEC activity for MO degradation with an efficiency of up to 95.2 % within 1 h when an external potential (+2.0 V) was applied. These novel MnO_2-TiO_2 NTA-photoelectrodes have excellent stability and reusability, giving them great potential for organic contaminant degradation in wastewater treatment.

In Lei and Gou (2018, 220), a facile synthetic method combining the hydrothermal reaction with liquid phase deposition (LPD) was described in the preparation of MnO_2-TiO_2 composite materials from an aqueous solution. The prepared materials were analysed using X-ray diffraction (XRD), X-ray photoelectron spectroscopy (XPS), SEM, and TEM. It was found that the LPD-derived anatase TiO_2 nanocrystals were uniformly deposited on the α-MnO_2 nanorods, forming a core-shell microstructure. Additionally, cyclic voltammetry was used to evaluate the photoelectrochemical behaviour of the prepared materials. The results revealed that the MnO_2-TiO_2 composite materials exhibited larger anodic photocurrent density than pure MnO_2 materials when the electrolyte solution (Na_2SO_4, 0.1 M) was saturated with CO_2 gas.

Kim and Joshi (2020) designed and produced a hierarchical photocatalyst for water splitting by first fabricating ZnO nanorods using a chemical bath deposition (CBD) process in which ZnO seeds were electrosprayed onto In-doped tin oxide (ITO). The MnO_2 particles were then electrosprayed as a co-catalyst, and finally an ultrathin passivation layer of TiO_2 via atomic layer was deposited.

These hierarchical photocatalysts exhibit excellent photoelectrochemical properties and limited photocorrosion compared to materials without a TiO_2 coating. Moreover, MnO_2 garnished ZnO nanorods obtained at 550 °C -delivered a 1.7-fold enhancement in photocurrent density (0.95 mA/cm^2) at 1.2 $V_{Ag/AgCl}$ in a 0.5 M Na_2SO_3 solution compared to ZnO nanorods without MnO_2. This investigation presents a balanced nanoarchitecture for photoelectrodes, which favours the formation of effective photoelectrocatalytic sites while improving stability for potential large-scale water splitting applications.

Vertically oriented self-organized TiO_2-MnO_2 nanotube arrays were successfully obtained using one-step anodic oxidation of Ti-Mn alloys in an ethylene glycol-based electrolyte solution (Nevárez-Martínez and Kobylański 2017, 22). The prepared samples were characterized by SEM, energy-dispersive X-ray spectroscopy (EDX), UV-vis absorption, photoluminescence spectroscopy, XRD, and micro-Raman spectroscopy. The effects of the applied potential (30–50 V), the manganese content in the alloy (5–15 wt%), and the water content in the electrolyte (2–10 vol%) on the morphology and photocatalytic properties were investigated for the

first time. The photoactivity was assessed in the toluene removal reaction under visible light, using low-powered LEDs as the irradiation source (λ_{max} = 465 nm). Morphological analysis showed auto-aligned nanotubes over the surface of the alloy, with diameters of 76–118 nm, lengths of 1.0–3.4 μm, and wall thickness of 8–11 nm. All samples were photoactive under the influence of visible light and the highest degradation achieved was 43 % after 60 min of irradiation. The excitation mechanism of TiO_2-MnO_2 NTs under visible light was presented, highlighting the importance of MnO_2 species for generating e^- and h^+.

The recent interest in the TiO_2-MnO_2 system is down to its features of non-toxicity and natural abundance. These composites have been used primarily for capacitance applications (Zhou and Zhang 2014, 118) and, despite the narrow bandgap of MnO_2 (0.26–2.7 eV), they can absorb visible and, theoretically, even infrared light (Sakai 2008, 112). However, there exist few reports in the literature on the application of this system in photoelectrocatalysis.

A novel magnetic MnO_2-$MnFe_2O_4$ nanocomposite (Chen and Zhang 2019) was successfully fabricated by the hydrothermal method and characterized using X-ray photoelectron spectra (XPS), vibrating sample magnetometer (VSM), and Brunauer-Emmett-Teller (BET). Then, the material was used for Rhodamine B (Rh B) degradation. The results showed that the decomposition efficiency of a MnO_2-$MnFe_2O_4$ nanocomposite with a molar ratio of 7:1 was 90 % for Rh B within 5 min., which is significantly more than the values for the homogeneous catalysts (Fe^{3+} and Mn^{2+}), pure MnO_2, and pure $MnFe_2O_4$. The advantage of the MnO_2-$MnFe_2O_4$ nanocomposite is that it can be recycled in practical applications.

Our approach to TiO_2-MnO_2 composites was to combine both oxides, mechanically or electrochemically. The latter means that both components exist as soluble precursor species. We conducted electrodeposition using an 8 g/L TiO_2 electrolyte suspension, due to the low solubility of TiO_2 in an electrolyte solution containing 0.1 HF, 0.7 M $MnSO_4$ (1.5M $(NH_4)_2SO_4$). Each sample has an individual phase composition. For instance, the XRD-pattern obtained for the suspension electrolyte sample (with subtracted background in Match 2.0) demonstrated the presence of a ramsdellite phase with the main (110) peak of this phase component at 10 2θ degrees (fig. 5.19). The TiO_2 main (110) peak at d = 0.325 nm (12.5 2θ) was both broad and weak and we continue to investigate the titanium dioxide in the obtained samples.

The photoelectrocatalytic effect of TiO_2/C_{graf} in amino-azo dye degradation under UV irradiation in a salt electrolyte has been shown.

Low-power UV radiation (6 W) allows us to significantly increase the oxidation current at high scanning speeds (50 mV/s) and potentials of up to 500 mV for the formed nanostructured system based on anatase. This effect can be attributed to the influence of defective Ti^{3+} centres on the surface of the synthesized TiO_2 and the presence of oxygen vacancies due to the non-stoichiometry of the anatase modification by oxygen. A promising option is the doping of titanium dioxide with other cations, especially manganese. Composite materials based on TiO_2 and MnO_2 can be used during the creation of photoelectrocatalysts due to their complementary properties. The effect of graphite promotes the separation of charges on the defective surface of titanium dioxide due to the action of active centres of PEC-Ti^{3+}. Further research will focus on the search for and development of composites of titanium dioxide modified with Ti^{3+} surface states with other conductive carbon materials, such as carbon nanotubes etc., to stabilize the photocurrents in a wider range of potentials and with increased quantum yield.

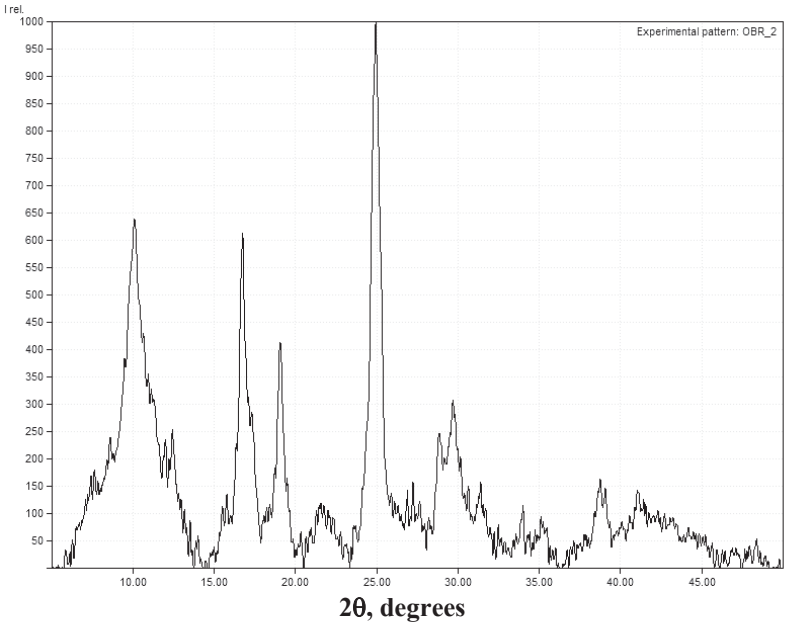

Fig. 5.19 XRD-pattern of EMD obtained from an 8 $g \cdot L^{-1}$ TiO_2 suspension containing fluoride-ion electrolyte.

We studied MO degradation with composite TiO_2-graphite, TiO_2-MnO_2-graphite electrodes. The IPM NASU TiO_2 sample displayed the lowest electrode potential for PEC currents and a potassium chloride medium is preferred for MO degradation. The other carbon materials were also tested in the degradation of organic compounds and water splitting. Contact with co-catalysts like manganese dioxide in a composite electrode material can decrease the bandgap value and shift the active range of the wavelengths of titanium dioxide into the visible and even into the IR spectrum.

SUMMARY

TiO_2 nanoparticles show high efficiency in water purification for the removal of toxic organic impurities and hydrogen synthesis. Furthermore, titanium dioxide nanoparticles display antiviral and bactericidal effects in the photocatalytic process.

The particular phase composition of the TiO_2 matrix and the morphology of composite nanoparticles and their optical properties has seen the $C_3N_4O_x$-TiO_2 photocatalyst used in various kinds of photochemistry-related applications. This new composite material ($C_3N_4O_x$-TiO_2) has been synthesized using an approach developed by Frantsevich Institute for Problems of Materials Science of NASU. This process involves the synthesis of oxygen-doped carbon nitride using a CVD method under the special reaction conditions (in the presence of a fixed volume of air) of melamine pyrolysis. $C_3N_4O_x$ is deposited on the surface of the TiO_2 matrix with different phase compositions—rutile or anatase. SEM images of the nanoparticles of both $C_3N_4O_x$-TiO_2 composites demonstrated the arrangement of TiO_2 nanoparticles and clusters between the plates, as well as in the channels of the porous scaly $C_3N_4O_x$ plates. The synthesized anatase phase nanoparticles show high dispersion and an average particle size of 10 nm. UV-vis spectroscopy shows a redshift at the long-wavelength edge of the fundamental absorption band in the spectra of TiO_2 (anatase); TiO_2 (rutile); C_3N_4, $C_3N_4O_x$-TiO_2 (anatase); and $C_3N_4O_x$-TiO_2 (rutile). The bandgap decrease was as follows: 3.2, 3.0, 2.6, 2.4, 2.25, and 2.1 eV, respectively. In this case, $C_3N_4O_x$-TiO_2 absorbs more visible light than both g-C_3N_4 and TiO_2, thereby generating more charges and contributing to the improvement in its photoactivity.

The *in situ* polymerization parameters of aniline affect the thickness and morphology of the polymer layer. Methods for obtaining powders and porous films formed by particles of 1D-structure lying parallel to the carrier plane (1D), or arranged perpendicular to the carrier plane (1D$^{\perp}$), as well as methods for obtaining continuous, uniform films, have been developed. The thickness of the layers is controlled in the range 30±10 nm to 300±30 nm. In the *in situ* method, the polymer layer is formed simultaneously with the growth of polymer chains at points of contact between the carrier and the polymerization medium. There is undoubted scientific and practical interest in the development of these

ideas about the management of polymer layer formation through the purposeful selection of *in situ* polymerization parameters.

A mechanism has been proposed for the oxidative polymerization of pyrrole to form a charge-transfer complex between the oxidized regions of the polypyrrole (PPy) chain and the monomer. The kinetic model of oxidative polymerization of pyrrole using ammonium persulfate, based on the proposed mechanism, is in qualitative and quantitative agreement with the results of experiments by the researchers. Due to its molecular structure, the conductivity of PPy varies over a wide range.

The prospects of using acrylate oligomers and rubber-methacrylate solutions for obtaining new composites through an *in situ* process under UV irradiation has been presented. There is practically no information on how nanoparticles influence the regularity of photopolymerization and the properties of the obtained composites. Methods for the modification of oxide nanoparticles are at the stage of preparing hybrid composites based on a polymer matrix.

The physicochemical conditions for hybrid polyaniline composite synthesis with metallic and oxide particles has been explained. As the silver content increases, aggregation of the metal particles occurs with the formation of microcrystalline regions. SEM and granulometric analysis has revealed that at a silver concentration of ~30 % can form ordered structures due to the mutual stabilization of the metal and the polymer, improving the catalytic activity of the hybrid composites.

Most of the currently proposed Me-N-C systems are an improvement on Fe-N-C catalysts. This can be explained by their higher ORR activity (in an acidic electrolyte solution) compared to, for example, cobalt-based analogues. At the same time, the stability problem of Fe-N-C catalysts during operation in real PE is acute. Me-N-C catalysts with low stability are due to the leaching of metal, unwanted interactions with H_2O_2 or free radicals, and the protonation of the active centres or N atoms adjacent to the centres, with subsequent adsorption of the anions. In the case of Fe-N-C catalysts, dissolved Fe^{2+} ions can interact with H_2O_2 by the Fenton reaction and generate active radical groups, which can further lead to the degradation of the catalysts.

For the efficient passage of electronic processes between oxide NPs and the PANI (PPy) matrix, there must be a strong bond, because the rate of generation of hydroxyl radicals, determining the rate of decomposition of organic and inorganic substances, depends on it. The development of new and effective composite nanocrystalline and nanoporous photocatalysts has been demonstrated. Composite powders show photocatalytic activity with increasing particle dispersion. The combination of PANI nanoparticles

with TiO_2 and $C_3N_4O_x$ will create an excited-state in electron (e-) and hole (h^+) pairs, which can react with O_2 and water vapour in the atmosphere to produce superoxide ions and hydroxyl radicals (OH•) under irradiation. Both O_2^- and OH• can act as agents for the destruction of toxic chemical compounds and bacterial cells, forming CO_2 and water. This process sees an increase in performance of the photocatalyst and the duration of its operation up to its regeneration. Due to their molecular structures and conductivity, PANI and PPy polymers produce important h^+ in the valence band.

Nanosized core-shell type composites containing iron oxide cores (magnetite or maghemite) and noble metal shells (in particular gold or silver) are some of the most promising materials for biomedical applications due to their combination of magnetic, optical, and colloid-chemical properties, as well as due to the possibility of biofunctionalization of the surface of the composite. Variation in the physicochemical characteristics of nanocomposites with ferrimagnetic cores and noble metal shells open up great possibilities for their use as a platform for the development of highly effective diagnostic and therapeutic tools, with significant selectivity at the level of individual cells and bio-macromolecules. The superparamagnetic properties of Fe_3O_4-Ag^0 shell composite particles and the photocatalytic properties of TiO_2 nanopowders, in combination with the bactericidal and antiviral activity of both, which can be significantly increased under the influence of UV radiation, provide a basis for the creation of new protective composite materials. Variation in the material composition of such a composite, the structure of the oxide particles, and the form of their modifying components can all optimize the photoactive composite system giving the greatest antiviral activity when initiated by the action of UV radiation. The nanocomposite obtained (in the form of a powder or film) can be used in the prevention of the spread of infectious diseases in confined air environments (transport, public places, and hospitals, etc.).

The influence of the gradient potential, the nature of the TiO_2 polymorph, and bandgap engineering on PEC phenomena of the TiO_2 composite semiconductor/electrolyte interface all need to be studied. Advantages of transition metal oxides and different TiO_2 doping strategies in PEC include a more complex co-doping strategy. The potential for organic contaminant degradation in wastewater treatment has been highlighted, with MO PEC degradation in an aqueous electrolyte providing an example. The presence of Ti^{3+} defects decreases the bandgap for TiO_2 nanocomposite electrodes and improves their PEC properties.

The recent interest in the TiO_2-MnO_2 system also has its origins in the features of MnO_2 non-toxicity and abundance. MnO_2 presents diversity in its open, tunnel structure and the unique complex behaviour of the defects in the oxide framework, PEC, and electrocatalytic activities under visible light. Successful strategies for PEC include the anodization of Ti with the formation of TiO_2-NTs, electrodeposition, and hydrothermal reactions with various attempt to modify TiO_2, as well as composite material design. The electrolytic doping procedure offers opportunities to obtain TiO_2 composites with different MnO_2 polymorphs, depending on the nature and concentration of the dopant-additive in the electrolyte solution.

GLOSSARY OF TERMS

The authors have included a glossary of terms used in this book. These terms are commonly used in industry, academia, and on scientific websites and Wikipedia; they can have multiple meanings. We hope that students of ceramics, material science, and chemistry can easily understand their meanings.

Absorbance is a measure of the quantity of light absorbed by a sample. It is also known as **optical density**, extinction, or decadic **absorbance**. Typical units of **absorbance** are called "**absorbance units**", have the abbreviation **AU**, and are dimensionless.

Adsorption is the adhesion of atoms, ions, or molecules from a gas, liquid, or dissolved solid to a surface. This process creates a film of the adsorbate on the surface of the adsorbent. **Adsorption** is a surface phenomenon, while **absorption** involves the whole volume of the material.

An **antimicrobial** is an agent that kills microorganisms or stops their growth. **Antimicrobial** medicines can be grouped according to the microorganisms they primarily act against; i.e. **antibiotics** are used against bacteria and antifungals are used against fungi.

An **antivirus** is an agent that kills a virus or that suppresses its ability to replicate and, hence, inhibits its ability to multiply and reproduce.

An **agglomerate** is a group of particles that behaves like a single particle. Mistler and others have noted that individual particles are held together by an electrical charge, with water on particle contact, and other short-range forces.

Anatase is a rare blue or black mineral that consists of titanium oxide in tetragonal crystalline form and occurs in veins in igneous rocks. Its formula is TiO_2 and it is also called octahedrite.

An **adenovirus** is a group of DNA-containing viruses that cause respiratory disease, including one form of the common cold. Adenoviruses

can also be genetically modified and used in gene therapy to treat cystic fibrosis, cancer, and, potentially, other diseases.

Bacteria are single-celled microorganisms that can exist either as independent (free-living) organisms or as parasites (dependent on another organism for life).

Biotransformation is the chemical modification (or modifications) made by an organism on a chemical compound. If this modification ends in mineral compounds like CO_2, NH_4^+, or H_2O, the biotransformation is called mineralization.

Biosafety is the application of knowledge, techniques, and equipment to prevent personal, laboratory, and environmental exposure to potentially infectious agents or biohazards. **Biosafety** defines the containment conditions under which infectious agents can be safely manipulated.

Bactericidal activity is a substance's ability to prevent the growth of bacteria with a subsequent decreasing concentration.

Bacteriophages (**phage**) are obligate intracellular parasites that multiply inside bacteria by making use of some or all of the host biosynthetic machinery (i.e., viruses that infect bacteria.). There are many similarities between **bacteriophages** and animal cell viruses.

Brookite is a form of titanium dioxide, TiO_2, occurring as a mineral in orthorhombic crystals. It is commonly translucent brown or opaque brown to black.

The **boiling point** is the **temperature** at which a specified liquid boils; the **temperature** at which the vapour pressure of a specified liquid equals atmospheric pressure, i.e. at sea level water boils at 212 °F or 100 °C; also the **point** at which one loses one's temper or matters get out of control.

A **charge carrier** is a particle or quasiparticle that is free to move, carrying an electrical **charge**, especially those particles that carry electrical **charges** in electrical conductors. Examples include electrons, ions, and holes.

The **conductive band (CB)** is the band of electron orbitals that electrons can jump up into from the **valence band** when excited.

Carbon nitride graphitic (g-C_3N_4) is a family of carbon nitride compounds with a general formula based on C_3N_4 (typically with non-zero amounts of hydrogen) and two major substructures based on heptazine and poly(triazine imide) units, which, depending on the reaction conditions, exhibit different degrees of condensation, properties, and reactivity.

Catalysis is the process of increasing the rate of a chemical reaction by adding a substance known as a **catalyst**, which is not consumed in the **catalysed** reaction and can be used repeatedly.

Condensation is a class of organic addition reaction that typically proceeds in a step-wise fashion to produce an addition product, usually in equilibrium, and a water molecule (hence it is named condensation).

A **covalent bond** is a chemical **bond** that involves the sharing of electron pairs between atoms. These electron pairs are known as shared pairs or **bonding** pairs, and the stable balance of attractive and repulsive forces between atoms when they share electrons is known as **covalent bonding**.

Crystallite is a single crystal in powder form. A grain is a single crystal within a bulk/thin-film form. A particle can also be thought of as an agglomerate. It is small enough in size to not be considered a bulk or thin film, but is composed of two or more individual **crystallites**.

CFU is a unit used in microbiology to estimate the number of viable bacteria or fungal cells in a sample.

Disinfection is a chemical or physical process that kills or inactivates microorganisms, such as bacteria, viruses, and protozoa. Common water **disinfectants** include chlorine, chloramine, ozone, and ultraviolet light.

A **dopant** is a trace impurity element that is introduced into a chemical material to alter its original electrical or optical properties. The amount of dopant necessary to cause changes is typically very low. When doped into crystalline substances, the dopant's atoms are incorporated into its crystal lattice.

Decomposition is a type of chemical **reaction** in which a single compound breaks down into two or more elements or new compounds. These **reactions** often involve an energy source, such as heat, light, or electricity, which breaks apart the bonds of compounds.

DNA is a double-stranded molecule held together by weak hydrogen bonds between base pairs of nucleotides.

An **energy bond** is defined as the amount of **energy** required to break apart a mole of molecules into its component atoms. It is a measure of the strength of a chemical **bond**. **Bond energy** is also known as **bond** enthalpy (H) or, simply, as **bond** strength.

Enthalpy is a thermodynamic quantity equivalent to the total heat content of a system. It is equal to the internal energy of the system plus the product of pressure and volume.

Filler materials are particles added to resin or binders (plastics, composites, and concrete) that can improve specific properties, make the product cheaper, or a mixture of both. Most of the **filler** materials used in plastics are mineral or glass-based **filler** materials.

Graphite is a crystalline form of the element **carbon** with its atoms arranged in a hexagonal structure. It occurs naturally in this form and is the most stable form of **carbon** under standard conditions. Under high pressures and temperatures, it is converted into diamond.

Graphene is the only form of carbon (or solid material) in which every atom is available for a chemical reaction from two sides (due to its 2D-structure). Atoms at the edges of a **graphene** sheet have special chemical reactivity. **Graphene** has the highest ratio of edge atoms of any allotrope.

Graphite oxide is a compound of carbon, oxygen, and hydrogen in variable ratios, obtained by treating **graphite** with strong oxidizers. The maximally oxidized bulk product is a yellow solid with the ratio C:O.

Gibbs energy is defined as the enthalpy of the system minus the product of the temperature times the entropy of the system: G = H-TS. The **Gibbs free energy** of the system is a state function because it is defined in terms of thermodynamic properties that are state functions.

A **hole** is the absence of an electron in a particular place in an atom. Although it is not a physical particle in the same sense as an electron, a **hole** can be passed from atom to atom in a semiconductor material. Electrons orbit the nucleus at defined energy levels called bands or shells.

The **inactivation of a pathogen** is a process designed to eliminate pathogens from water, air, or donated blood. Pathogens include viruses, bacteria, and fungi. One form of pathogen **inactivation** for blood uses a chemical that, when exposed to ultraviolet light, binds to genetic material.

Irradiation is a process where matter, for example food, is exposed to ionizing radiation, which causes chemical changes that destroy DNA and reduce microbial contamination (Hanis et al. 1988).

Molecular structure is the three-dimensional **structure** or arrangement of atoms in a **molecule**. Understanding the **molecular structure** of a compound can help determine its polarity, reactivity, phase of matter, colour, and magnetism, as well as its biological activity.

Metastable state. In physics and chemistry, this is a particular excited **state** of an atom, nucleus, or other system that has a longer lifetime than ordinary excited **states** and that generally has a shorter lifetime than the lowest, often stable, energy **state**, called the ground **state**.

A **monomer** is a molecule that can react together with other **monomer** molecules to form a larger polymer chain or three-dimensional network in a process called polymerization.

Nanoparticles are usually defined as particles of matter that are between 1 and 100 nanometres (nm) in diameter. The term is sometimes used for larger particles, of up to 500 nm, or fibres and tubes that are less than 100 nm in only two directions.

Noble metals are several **metals**, such as gold, silver, mercury, or platinum, that resist oxidation when heated in air and solution by inorganic acids.

An **oxidizer** is a substance that oxidizes another substance: an **oxidant**, **oxidizer**, or **oxidizing agent**. A chemical agent is an agent that produces chemical reactions.

An **oligomer** is a polymer molecule consisting of a small number of monomers.

A **pathogen** is an infectious agent or germ. The term **pathogen** came into use in the 1880s. Typically, the term is used to describe an infectious

microorganism or agent, such as a virus, bacterium, protozoan, prion, viroid, or fungus.

Photocatalysis is the acceleration of a photoreaction in the presence of a catalyst.

A **photocatalyst** is a material that absorbs light to bring it to a higher energy level and provides energy to a reacting substance to make a chemical reaction occur (from: Bioscience and Bioengineering of Titanium Materials (Second Edition) 2013).

A **polymer** a high molecular weight macromolecule made up of multiple repeating units. **Polymerization** is the chemical reaction in which high molecular mass molecules are formed from monomers. For example, polystyrene is a **polymer** commonly used in packaging.

Polyaniline (**PANI**) is a conducting polymer of the semi-flexible rod polymer family. Although the compound itself was discovered over 150 years ago, it has only been since the early 1980s that polyaniline has captured the attention of the scientific community. This interest is due to the rediscovery of its high electrical conductivity. Among the family of conducting polymers and organic semiconductors, polyaniline has many attractive properties. Because of its rich chemistry, polyaniline has become one of the most heavily studied conducting polymers of the past 50 years.

Polypyrrole (PPy) is a type of organic polymer formed by the polymerization of **pyrrole**. **Polypyrroles** are conducting polymers, with related members being polythiophene, polyaniline, and polyacetylene. The Nobel Prize for Chemistry was awarded in the year 2000 for work on conductive polymers including **polypyrrole**.

A **polaron** is a charged quasiparticle.

A **plasmon** is the collective oscillation of charged particles (a bound electromagnetic wave on charged particles).

A **precursor** is a compound that participates in a **chemical** reaction to produce another compound. In biochemistry, the term **precursor** often refers specifically to a **chemical** compound preceding another in a metabolic pathway, such as a protein **precursor**.

A **quinoid** is a six-member ring with one or more exocyclic double bonds resembling quinone.

Rutile is a reddish-brown to black mineral that consists of titanium dioxide, usually with a little iron, and has a brilliant metallic or adamantine lustre.

Self-assembly is a process in which a disordered system of pre-existing components forms an organized structure or pattern as a consequence of specific, local interactions among the components themselves, without external direction.

A **surfactant** is an additive used to change the chemical nature of a solid or liquid surface.

Synthesis is the creation of something. It is the process of combining two or more components to produce a new entity. In biochemistry, it refers to the production of an organic compound in a living thing, especially one aided by enzymes. Several synthesis processes occur in the cell or organism. The creation of an organic compound in a living organism is referred to as biosynthesis. One of these processes is photosynthesis: the synthesis of complex organic material using carbon dioxide, water, inorganic salts, and light energy (from sunlight) captured by light-absorbing pigments, such as chlorophyll and other accessory pigments.

TGA is an acronym for **thermogravimetric analysis**, which is used for measuring changes in mass with temperature changes.

Thermoplastics are plastic polymer materials that become pliable or mouldable at specific elevated temperatures and solidify upon cooling. Most **thermoplastics** have high molecular weight.

Toxicity is the degree to which a chemical substance or a particular mixture of substances can damage an organism.

Virucidal activity concerns the activity of interacting with and physically disrupting viral particles. In its broad definition, it includes activity to functionally inhibit (neutralize) viral infectivity without apparent morphological alterations of the viral particles.

BIBLIOGRAPHY

Introduction

Sabu, T. et al. 2018. “Nanoscale Materials in Water Purification”. *Elsevier*.

Zheng, Z., Murakamia, N., Liu, J., Teng, Z. et al. 2020. “Development of Plasmonic Photocatalyst by Site-selective Loading of Bimetallic Nanoparticles of Au and Ag on Titanium (IV) Oxide”. *Chem. Cat. Chem.*

Fujishima, Akira. 1972. “Electrochemical Photolysis of Water at a Semiconductor Electrode”. *Nature*, 238: 37-38.

Chapter 1

Shi, Hongbo & Magaye, Ruth. 2013. “Titanium dioxide nanoparticles: a review of current toxicological data”. *Particle and Fibre Toxicology*, 15: 1-33.

Woodruff, L.G., Bedinger, G.M., Piatak, N.M. 2017. “Titanium, chap”. T of Schulz, K.J., DeYoung, J.H., Jr., Seal, R.R., II, and Bradley, D.C., eds., Critical mineral resources of the United States—Economic and environmental geology and prospects for future supply: U.S. Geological Survey Professional Paper 1802, p. T1-T23.

Force, E.R. 1991. “Geology of titanium-mineral deposits: Geological Society of America”. Special Paper 259, 112 p.

Rudnick, R.L., & Fountain, D.M. 1995. “Nature and composition of the continental crust—A lower crustal perspective”. *Reviews of Geophysics,* No 3: 267-309.

Choudhury, Biswajit, Choudhary, Amarjyoti. 2013. “Local structure modification and phase transformation of TiO_2 nanoparticles initiated by oxygen defects, grain size, and annealing temperature”. *International Nano Letters*, No 3.

Satoh, Norifusa, Nakashima, Toshio, Yamamoto, Kimihisa. 2013. “Metastability of anatase: size dependent and irreversible anatase-rutile phase transition in atomic-level precise titania”. *Scientific Reports*, No 3: 1--6.

Yavorovsky, Olexander. 2016. “Nanomaterials and nanoparticles: Structure, physico-chemical and toxicological properties, impact on the organism of the workers”. *Environment & Health*, No 3: 29-36.

Zeinalov, Orkhan. 2016. “About the influence of metal oxide nanoparticles on living organism physiology”. *Reviews on clinical pharmacology and drug therapy,* No 3: 24-33.

Zaroddu, Maria & Medici, Serenella. 2014. “Toxicity of nanoparticles”. *Current Medicinal Cemistry,* No 33: 3837-3853.

Demetska, Oksana. 2010. “Problem of safety in the use of nanotechnologies”. *Environment & Health*, No 4: 8-12.

Zavgorodnii, Ivan & Dmuhovskaya, Tatyana. 2013. “Problems of hygiene and safety in the manufacturing and using nanotechnology”, 3: 52-56.

Balbus, John & Maynard, Andrew. 2007. “Meeting Report: Hazard Assessment for nanoparticles-Report from an Interdisciplinary Workshop”. *Environmental Health Perspectives*, No 11: 1654-1659.

Smith, Matthew & Brown, Jared. 2014. “From immunotoxicity to nanotherapy: the effects of nanomaterials on the immune system”. *Toxicological Sciences*, No 2: 249-255.

Koivitso, Antti & Kling, Kirsten. 2017. “First order risk assessment for nanoparticle inhalation exposure during injection molding of polypropylene composites and production of tungsten-carbide-cobalt fine powder based upon pulmonary inflammation and surface area dose”. *Nano Impact*, No 6: 30-38.

Ghosh, Saikat & Roy, Tanushree. 2014. “Nanoparticulate drug-delivery systems: lymphatic uptake and its gastrointestinal applications”. *Journal of Applied Pharmaceutical Science*, No 6.

Simon, Marina & Saez, Gladis. 2017. “In situ quantification of diverse titanium dioxide nanoparticles unveils selective endoplasmic reticulum stress-dependent toxicity”. *Nanotoxicology*, No 1: 134-145.

Bosquet, Alba & Guaita-Esteruelas, Sandra. 2016. “Exogenous FABP4 induces endoplasmic reticulum stress in HepG2 liver cells”. *Atherosclerosis*, No 249: 191-199.

Wojcik, Ewa & Szwajgier, Dominik. 2019. “Effects of Titanium Dioxide Nanoparticles Exposure on Human Health—a Review”. Biological Trace Element Research, 118-129.

Ostiguy, Claude & Lapointe, Gilles. 2006. “Health effects of nanoparticles”. *Studies and research projects. IRSST*, 52.

Jiang, Jinqkun & Oberdörster, Günter. 2008. “Does nanoparticle activity depend upon size and crystal phase?” *Nanotoxicology,* No 1: 33-42.

Ze, Yuguan, Hu, Renping, Wang, Xiaochun, Sang, Xuezi et al. 2014. “Neurotoxicity and gene-expressed profile in brain-injured mice

caused by exposure to titanium dioxide nanoparticles". *Journal of Biomedical Materials Research Part A*, No 2: 470-8.

Wang, J. & Lin, Z. 2008. "Freestanding TiO_2 Nanotube Arrays with Ultrahigh Aspect Ratio via Electrochemical Anodization". *Chemistry of Materials*, No 4: 1257-1261.

Ahn, J.Y., Cheon, H.K., Kim, W.D., Kang, Y.J. et al. 2012. "Aerosol-gel synthesis and photovoltaic properties of mesoporous TiO_2 nanoparticles". *Chemical Engineering Journal*, 188, 216-221.

Suciu, R.C., Marian, I., & Bratu, I. 2014. "Metal propionate synthesis of TiO_2 nanomaterials". *Journal of Alloys and Compounds*, 584, 159-166.

Khomane, R.B. 2011. "Microemulsion-mediated sol-gel synthesis of mesoporous rutile TiO_2 nanoneedles and its performance as anode material for Li-ion batteries. *Journal of Colloid and Interface Science*, No 1: 369-372.

Wang, X., Li, Z., Shi, J., & Yu, Y. 2014. "One-Dimensional Titanium Dioxide Nanomaterials: Nanowires, Nanorods, and Nanobelts". *Chemical Reviews*, No 19: 9346-9384.

Wei, F., Zeng, H., Cui, P., Peng, S., & Cheng, T. 2008. "Various TiO_2 microcrystals: Controlled synthesis and enhanced photocatalytic activities". *Chemical Engineering Journal*, No 1: 119-123.

You, Y., Zhang, S., Wan, L., & Xu, D. 2012. "Preparation of continuous TiO_2 fibers by sol-gel method and its photocatalytic degradation on formaldehyde". *Applied Surface Science*, No 8: 3469-3474.

El-Sherbiny, S., Morsy, F., Samir, M., & Fouad, O.A. 2013. "Synthesis, characterization and application of TiO_2 nanopowders as special paper coating pigment". *Applied Nanoscience*, No 3: 305-313.

Chigane, M., Shinagawa, T., & Tani, J. 2017. "Preparation of titanium dioxide thin films by indirect-electrodeposition". *Thin Solid Films*, 628, 203-207.

Amano, F., Nakata, M., Yamamoto, A., & Tanaka, T. 2016. "Rutile titanium dioxide prepared by hydrogen reduction of Degussa P25 for highly efficient photocatalytic hydrogen evolution". *Catalysis Science & Technology*, No14: 5693-5699.

Tian, Q., Luo, D., Li, X., Zhang, Z., Yang, L., & Hirano, S. 2016. "Elaborately prepared hierarchical structure titanium dioxide for remarkable performance in lithium storage". *Journal of Power Sources*, 313, 189-197.

Sakai, M., Kato, T., Ishizuka, N., Isobe, T., Nakajima, A., & Fujishima, A. 2015. "Bio-inspired highly hydrophobic surface with ecdysis behavior using an organic monolithic resin and titanium dioxide photocatalyst". *Journal of Sol-Gel Science and Technology,* No 1: 257-265.

Wang, J., Li, J., Liu, B., Xie, Y. et al. 2009. "Preparation of nano-sized mixed crystal TiO2-coated Er^{3+}:$YAlO_3$ by sol-gel method for photocatalytic degradation of organic dyes under visible light irradiation". *Water Science and Technology,* No 4: 917-926.

Muthukrishnan, K., Vanaraja, M., Boomadevi, S., Karn, R.K., Rayappan, J.B. B., Singh, V., & Pandiyan, K. 2015. "Highly selective acetaldehyde sensor using sol-gel dip coated nano crystalline TiO_2 thin film". *Journal of Materials Science: Materials in Electronics*, No 7: 5135-5139.

Huang, Y., Zhu, J., Ding, Y., Chen, S., Zhang, C. et al. 2016. TiO_2 "Sub-microsphere Film as Scaffold Layer for Efficient Perovskite Solar Cells". *ACS Applied Materials & Interfaces*, No 12: 8162-8167.

Khalifa, Z.S., & Mahmoud, S.A. 2017. "Photocatalytic and optical properties of titanium dioxide thin films prepared by metalorganic chemical vapour deposition". *Physica E: Low-Dimensional Systems and Nanostructures*, 91, 60-64.

Niemelä, J.P., Marin, G., & Karppinen, M. 2017. "Titanium dioxide thin films by atomic layer deposition: a review". *Semiconductor Science and Technology*, No 9: 093005.

Chapter 2

Mandal, B.K. 2016. "Scopes of green synthesized metal and metal oxide nanomaterials in antimicrobial therapy". *Nanobiomaterials in Antimicrobial Therapy*, 313-341.

Smirnova, O., Grebenyuk, A., Lobanov, V. 2017. "Titanium dioxide defect structures as catalytic sites". *Surface*, No 24: 44-56.

Francis, Hassard, Sharp, Jasmine H., Taft, Helen, Le Vay, Lewis et al. 2017. "Critical Review on the Public Health Impact of Norovirus Contamination in Shellfish and the Environment: A UK Perspective". *Food and Environmental Virology*, No 2: 123-141.

Teixeira, Juliana, Miranda, Sandra, Monteiro, Ricardo, Lopes, Filipe et al. 2012. "Assessment of indoor airborne contamination in a wastewater treatment plant". *Environmental Monitoring and Assessment*, No 1: 59-72.

Michałkiewicz, Michal. 2018. "Comparison of wastewater treatment plants based on the emissions of microbiological contaminants". *Environmental Monitoring and Assessment,* 190(11).

Gumy, D., Morais, C., Bowen, P., Pulgarin, C. et al. 2006. "Catalytic activity of commercial of TiO_2 powders for the abatement of the

bacteria (E. coli) under solar simulated light: Influence of the isoelectric point". *Applied Catalysis B: Environmental*, No 1-2: 76-84.

Nakano, Ryuichi, Ishiguro, Hitoshi, Yao, Yanyan, Kajioka, Jitsuo et al. 2012. "Photocatalytic inactivation of influenza virus by titanium dioxide thin film". *Photochemical & Photobiological Sciences*, No 8: 1293-1298.

Dong, Y., Xu, F., Zhou, Y. 2017. "Synthesis and photocatalytic activity of mesoporous-(001) facets TiO_2 single crystals". *Appl. Surf. Sci.*, 662-669.

Rodrigues-Silva, C. 2016. "Bacteria and fungi inactivation by photocatalysis under UVA irradiation: liquid and gas phase". *Environ. Sci. Polut. Res.*, 1-10. doi 10.1007/s11356-016-7137

Li, G., Liu, X., Zhang, H., Wong, P. 2014. "Adenovirus inactivation by in-situ photocatalytically and photoelectrocatalytically generated halogen viricides". *Chem. Engineer*, 1-37.

Bogdan, J., Zarzynska, J., Czarnak, J.P. et al. 2015. "Comparison of infectious agents susceptibility to photocatalytic effects of nanosized titanium and zinc oxides: A practical Approach". *Nanoscale Research Letters*, No 10: 1293-1298.

Liga, Michael, Bryant, Erika, Colvin, Vicki, Li, Qilin. 2011. "Virus inactivation by silver doped titanium dioxide nanoparticles for drinking water treatment". *Water Research*, No 2: 535-544.

Sagadevan, S. 2015. "Investigation of the Preparation and Characterization of Fe-doped TiO_2 Nanoparticles". *Journal of Material Sciences & Engineering*, No 3: 164.

Xiong, J., Ma, J., Jern, Ng, Wun, T. et al. 2011. "Silver-modified mesoporous TiO_2 photocatalyst for water purification". *Water Research*, No 5: 2095-2103.

Hayashi, Kenichiro, Nozaki, Kosuke, Tan, Zhenquan, Fujita, Kazuhisa et al. 2019. "Enhanced Antibacterial Property of Facet-Engineered TiO_2 Nanosheet in Presence and Absence of Ultraviolet Irradiation". *Materials*, No 1: 78.

Hoang, Nhung, Tran, Anh, Suc, Nguen, Nguyen, The Vinh et al. 2016. "Antibacterial activities of gel-derived Ag-TiO_2-SiO_2 nanomaterials under different light irradiation". *AIMS Materials Science*, No 2: 339-348.

Othman, S.H., Abd Salam, N.R., Zainal, N., Kadir Basha, R. 2014. "Antimicrobial Activity of TiO_2 Nanoparticle-Coated Film for Potential Food Packaging Applications". *International Journal of Photoenergy*, 1-6.

Altan, M., Yildirim, H. 2014. “Comparison of Antibacterial Properties of Nano TiO2 and ZnO Particle Filled Polymers”. *Acta Physica Polonica A*, No 2:645-647.

Shaili, T., Abdorreza, M.N., & Fariborz, N. 2015. “Functional, thermal, and antimicrobial properties of soluble soybean polysaccharide biocomposites reinforced by nano TiO_2”. *Carbohydrate Polymers*, 134, 726-731.

Kavoosi, F., Modaresi, F., Sanaei, M., Rezaei, Z. 2018. “Medical and dental applications of nanomedicines”. *APMIS*, No 10: 795-803.

Toledano-Osorio, M., Babu, J.P, Osorio, R., Medina-Castillo, A.L. et al. 2018. “Modified Polymeric Nanoparticles Exert In Vitro Antimicrobial Activity Against Oral Bacteria”. *Materials (Basel)*, No 6: 1013.

Park, D., Shahbaz H.M., Kim, S.H., Lee, M. 2016. **“**Inactivation efficiency and mechanism of UV-TiO_2 photocatalysis against murine norovirus using a solidified agar matrix**”**. *Int. J. Food Microbiol.*, No 238: 256-264.

Kryukov, A.I., Stroyuk, A.L., Kuchmiy, S.Ya., Pokhodenko V.D. [Nanofotokataliz]. Kiev: Akademperiodika. 2013. 618. Russian.

Khanal, S., Ghimire, P., Dhamoon, A.S. 2018. “The Repertoire of Adenovirus in Human Disease: The Innocuous to the Deadly”. Biomedicines, No 1: 30.

European Collection of Animal Cell Cultures Catalog. Porton Down: Salisbury (UK) PHLS Centre of Applied Microbiology and Research, 1990.

Mosmann, T. 1983. “Rapid colorimetric assay for cellular growth and survival: application to proliferation and cytotoxicity assays”. J. Immunol. Methods, No 1-2: 55-63.

Pichel, N., Vivar, M., & Fuentes, M. 2018. “The problem of drinking water access: A review of disinfection technologies with an emphasis on solar treatment methods”. *Chemosphere*.

Alrousan, D., Polo-López, M., Dunlop, P., Fernández-Ibáñez, P., Byrne, J. 2012. “Solar photocatalytic disinfection of water with immobilised titanium dioxide in re-circulating flow CPC reactors”. *App. Catal. B-Enviro*, 128, 126-134.

Matsunaga, T., Tomoda, R., Nakajima, T., & Wake, H. 1985. “Photoelectrochemical sterilization of microbial cells by semiconductor powders”. *FEMS Microbiology Letters,* No 1-2: 211-214.

Hoang, Nhung Thi-Tuyet, Tran, Anh Thi-Kim, Suc, Nguyen Van, Nguyen, The-Vinh. 2016. “Antibacterial activities of gel-derived Ag-

TiO2-SiO2 nanomaterials under different light irradiation". AIMS Materials Science, No 2: 339-

Madhumita B Ray, https://www.researchgate.net/figure/Photocatalytic-inactivation-of-E-coli-K-12-at-various-TiO-2-loadings-Each-point-is-an_fig4_223288914

Fujishima, A., Rao, Tata, Donald, Tryk. 2000. "Titanium dioxide photocatalysis". *Journal of photo chemistry and photobiology. Part C: Photochemistry reviews*, 1: 1-21.

Yalçın, Yelda, Murat, Kılıç, Cinar, Zekiye. 2010. "Fe^{+3}-doped TiO_2: A combinedexperimental and computational approach to the evaluation of visible light activity". *Applied Catalysis B Environmental*, No 3-4: 469-477.

Karakitsou, K.E., & Verykios, X.E. 1993. "Effects of altervalent cation doping of titania on its performance as a photocatalyst for water cleavage". *The Journal of Physical Chemistry*, No 6: 1184-1189.

Furubayashi, Y., Hitosugi, T., Yamamoto, Y., Inaba, K. et al. 2005. "A transparent metal: Nb-doped anatase TiO_2". *Applied Physics Letters*, No 25: 252101.

Wang, C., Zeng, T., Zhu, S., & Gu, C. 2019. "Synergistic Mechanism of Rare-Earth Modification TiO_2 and Photodegradation on Benzohydroxamic Acid". *Applied Sciences*, No 2: 339.

Choi, Wonyong, Termin, Andreas, & Hoffmann, Michael. 1994. "The Role of Metal Ion Dopants in Quantum-Sized TiO_2: Correlation between Photoreactivity and Charge Carrier Recombination Dynamics". *The Journal of Physical Chemistry*, No 51: 13669-13679.

Bondarenko, M.V., Khalyavka, T.A., Petrik, I.S., Camyshan S.V. 2018. "Photocatalytic activity of TiO_2-C nanocomposites in the oxidation of Safranin T under UV and visible light". *Theoretical and Experimental Chemistry*, No 1: 40-45.

Chen, Daimei, Siang, Zhongue, Geng, Jiaqing, Wang, Q. et al. 2007. "Carbon and Nitrogen Co-doped TiO2 with Enhanced Visible-Light Photocatalytic Activity". *Ind. Eng. Chem. Res.*, No 9: 2741-2746.

Peng, Feng Ã., Cai, Lingfeng, Huang, Lei, Yu, Hao. 2008. "Preparation of nitrogen-doped titanium dioxide with visible-light photocatalytic activity using a facile hydrothermal method". Journal of Physics and Chemistry of Solids, 1657-1664.

Li, X., Zhang, G., Wang, X., Liu, W. 2019. "Facile synthesis of nitrogen-doped titanium dioxide with enhanced photocatalytic properties". *Materials Research Express*.

Guo, Y., Zhang, Xi-wen, Weng, Wei-Hao, & Han, Gao-rong. 2007. "Structure and properties of nitrogen-doped titanium dioxide thin films

grown by atmospheric pressure chemical vapor deposition". *Thin Solid Films*, No 18: 7117-7121.

Ao, Y., Xu, J., Fu, D., & Yuan, C. 2009. "A simple method to prepare N-doped titania hollow spheres with high photocatalytic activity under visible light". *Journal of Hazardous Materials*, No 1-3: 413-417.

Chen, Daimei, Geng, Jiaqing, Jiang, Zhonqui, Zhu, Juhong. 2009. "A facile method to synthesize nitrogen and fluorine co-doped TiO_2 nanoparticles by pyrolysis of $(NH_4)_2TiF_6$". Journal of Nanoparticle Research, No 2: 303-313.

Guo, Y., Zhang, H.W., Weng, W.H., Han, G.R. 2007. "Structure and properties of nitrogen-doped titanium dioxide thin films grown by atmospheric pressure chemical vapor deposition". *Thin Solid Films*, No 18: 7117-7121.

Li, D., Haneda, H., Hishita, S., Ohashi, N., & Labhsetwar, N.K. 2005. "Fluorine-doped TiO2 powders prepared by spray pyrolysis and their improved photocatalytic activity for decomposition of gas-phase acetaldehyde**"**. *Journal of Fluorine Chemistry,* No 1: 69-77.

Rupa, A., Valentine, Divakar, D. Sivakumar, T. 2013. "Titania and Noble Metals Deposited Titania Catalysts in the Photodegradation of Tartazine". *Boston: Springer US*, No 1-2: 259-267.

Sakthivel, S., Shankar, M., Palanichamy, M., Arabindoo, B. et al. 2004. "Enhancement of photocatalytic activity by metal deposition: characterisation and photonic efficiency of Pt, Au and Pd deposited on TiO_2 catalyst**"**. *Water Research*, No 13: 3001-3008.

Papp, J., Shen, H.S., Kershaw, R., Dwight, K., Wold, A. 1993. "Titanium (IV) oxide photocatalysts with palladium". *Chemistry of Materials*, 284-288.

Kumar, Anod, Ramani, Vijay. 2014. "Strong Metal-Support Interactions Enhance the Activity and Durability of Platinum Supported on Tantalum-Modified Titanium Dioxide Electrocatalysts". *ACS Catalysis*, No 5: 1516-1525.

Wang, W.K. and Malati, M.A. 1986. "Doped TiO_2 for solar energy applications". *Solar Energy*, No 2: 163-168.

Zhang, Huanjun, Chen, Guohua, Bahnemann, Detlef. "Photoelectrocatalytic materials for environmental applications". *Journal of Materials Chemistry*, No 29: 24959-25506.

Roy, S.C., Varghese, O.K., Paulose, M., & Grimes, C.A. 2010. "Toward Solar Fuels: Photocatalytic Conversion of Carbon Dioxide to Hydrocarbons". *ACS Nano*, No: 3, 1259-1278.

Bondarenko, M.E., Silenko, P.M., Gubareni N.I., Khyzhyn, O.Yu. 2018. "Synthesis of multilayer azagraphene and carbon nitride oxide". *Chemistry, Physics and Technology of Surface*, No 4: 394-403.

Caputo, C.A., Gross, M.A., Lau, V.W., Cavazza, C., Lotsch, B.V., & Reisner, E. 2014. "Photocatalytic Hydrogen Production using Polymeric Carbon Nitride with a Hydrogenase and a Bioinspired Synthetic Ni Catalyst". *Angewandte Chemie*, No 43: 11722-11726.

Zahornyi, Maksym. 2017. "Nanosized powders as reinforcement for photoactive composites (Overview)". *Powder Metallurgy and Metal Ceramics*, 56: 130-147.

Devthade, V., Kulhari, D., & Umare, S.S. 2018. "Role of precursors on photocatalytic behavior of graphitic carbon nitride". *Materials Today: Proceedings*, No 3: 9203-9210.

Ragulya A.V., Kryachek V.M., Gudymenko T.V., Chernyshev L.I. 2017. "Nitride based materials—traditions and new solutions" Naukova Dumka, Kyiv, 560.

Ievtushenko, A., Karpyna, V. et al. 2018. "Effect of Ag doping on the structural, electrical and optical properties of ZnO grown by MOCVD at different substrate temperatures". *Superlattices and Microstructures*, 117: 121-131.

Chapter 3

Vidyasagar, Devthade, Dinesh, Kulhari, Suresh, S. Umare. 2018. "Role of precursors on photocatalytic behavior of graphitic carbon nitride". *Materials Today: Proceedings*, 9203-9210.

Liu, J., Liu, Y., Liu, N., Han, Yet et al. 2015. "Metal-Free Efficient Photocatalyst for Stable Visible Water Splitting via a Two-Electron Pathway". *Science*, No 6225: 970-974.

Tay, Q., Kanhere, P., Ng, C.F., Chen, S. et al. 2015. "Defect Engineered g-C3N4 for Efficient Visible Light Photocatalytic Hydrogen Production". *Chemistry of Materials*, No 14: 4930-4933.

Wang, X., Maeda, K., Thomas, A., Takanabe, Ket et al. 2009. "A Metal-Free Polymeric Photocatalyst for Hydrogen Production from Water under Visible Light". *Nature Materials*, No 8: 76-80.

Tyborski, T., Merschjann, C., Orthmann, S., Yang, F. et al. 2012. "Tunable Optical Transition in Polymeric Carbon Nitrides Synthesized via Bulk Thermal Condensation". *Journal of Physics Condensed Matter*, No: 16.

Wang, Yuong, Wang, Xinchen, Antonietti, Markus, Zhang, Yuanjian. 2010. "Facile One-Pot Synthesis of Nanoporous Carbon Nitride Solids by Using Soft Templates". *Chem. Sus. Chem*., No 4: 435-439.

Wang, X., Maeda, K., Thomas, A., Takanabe, K., Xin, G., Carlsson, J.M., Antonietti, M. 2008. "A metal-free polymeric photocatalyst for hydrogen production from water under visible light". *Nature Materials*, No 1: 76-80.

Cao, S., Low, J., Yu, J., & Jaroniec, M. 2015. "Polymeric Photocatalysts Based on Graphitic Carbon Nitride". *Advanced Materials*, No13: 2150-2176.

Zhu, J., Xiao, P., Li, H., & Carabineiro, S.A.C. 2014. "Graphitic Carbon Nitride: Synthesis, Properties, and Applications in Catalysis". *ACS Applied Materials & Interfaces*, No 19: 16449-16465.

Di Noto, Vito and Negro, Enrico. 2010. "Development of nano-electrocatalysts based on carbon nitride supports for the ORR processes in PEM fuel cells". *Electrochimica Acta*, No 26: 7564-7574.

Lee, Sung Pil. 2008. "Synthesis and Characterization of Carbon Nitride Films for Micro Humidity". *Sensors*, No 8: 1508-1518.

Hu, R., Wang, X., Dai, S., Shao, D. et al. 2015. "Application of graphitic carbon nitride for the removal of Pb (II) and aniline from aqueous solutions". *Chemical Engineering Journal*, No 260: 469-477.

Caputo, Christine, Gross, Manuela A., Lau, Vincent, Cavazza, Christine et al. 2014. "Photocatalytic Hydrogen Production using Polymeric Carbon Nitride with a Hydrogenase and a Bioinspired Synthetic Ni Catalyst". *Angewandte Chemie International Edition,* No 43, 11538-11542.

Lotsch, B.V., Schnick, W. 2006. "From Triazines to Heptazines: Novel Nonmetal Tricyanomelaminates as Precursors for Graphitic Carbon Nitride Materials". *Chem. Mater.*, No 18: 1891-1900.

Zheng, Y., Liu, J., Liang, J., Jaroniec, M. et al. 2012. "Graphitic carbon nitride materials: controllable synthesis and applications in fuel cells and photocatalysis". *Energy & Environmental Science*, No 5: 6717.

Takanabe, K., Kamata, K., Wang, X., Antonietti et al. 2010. "Photocatalytic Hydrogen Evolution on Dye-Sensitized Mesoporous Carbon Nitride Photocatalyst with Magnesium Phthalocyanine". *Phys. Chem. Chem. Phys.*, No 12: 13020-13025.

Liu, J., Zhang, Y., Lu, L., Wu, G., Chen W. 2012. "Self-Regenerated Solar-Driven Photocatalytic Water-Splitting by Urea Derived Graphitic Carbon Nitride with Platinum Nanoparticles". *Chem. Commun.*, 48: 8826-8828.

Zhang, G., Zhang, J., Zhang, M., Wang X. 2012. "Polycondensation of Thiourea into Carbon Nitride Semiconductors as Visible Light Photocatalysts". *J. Mater. Chem.*, No 22: 8083-8091.

Dong, G., Zhang, L. et al. 212. "Porous Structure Dependent Photoreactivity of Graphitic Carbon Nitride under Visible Light". *J. Mater. Chem.*, 22: 1160-1166.

Yang, H.; Zhao, D. 2005. "Synthesis of Replica Mesostructures by the Nanocasting Strategy". *J. Mater. Chem.*, *15*:1217-1223.

Dong F., Sun Y., Wu L., Fu M., Wu Z. Facile Transformation of Low Cost Thiourea into Nitrogen-Rich Graphitic Carbon Nitride Nanocatalyst with High Visible Light Photocatalytic Performance. *Catal. Sci. Technol.* 2012, *2*, 1332-1335.

Zhang, Y., Liu, J., Wu, G., & Chen, W. 2012. "Porous graphitic carbon nitride synthesized via direct polymerization of urea for efficient sunlight-driven photocatalytic hydrogen production". *Nanoscale*, No 17: 5300.

Dong, F., Wang, Z., Sun, Y., Ho, W.-K., & Zhang, H. 2013. "Engineering the nanoarchitecture and texture of polymeric carbon nitride semiconductor for enhanced visible light photocatalytic activity". *Journal of Colloid and Interface Science*, 401, 70-79.

Zhou, Jian, Hua, Zile, Liu, Zhicheng, Wu, Wei et al. 2011. "Direct Synthetic Strategy of Mesoporous ZSM-5 Zeolites by Using Conventional Block Copolymer Templates and the Improved Catalytic Properties". *ACS Catalysis*, No 4: 287-291.

Niu, P., Zhang, L., Liu, G., & Cheng, H.-M. 2012. "Graphene-Like Carbon Nitride Nanosheets for Improved Photocatalytic Activities". *Advanced Functional Materials*, No 22: 4763-4770.

Yang, S., Gong, Y., Zhang, J., Zhan, L. et al. 2013. Exfoliated Graphitic Carbon Nitride Nanosheets as Efficient Catalysts for Hydrogen Evolution Under Visible Light. *Advanced Materials*, No 17: 2452-2456.

Panasiuk, Y.V., Raevskaya, A.E., Stroyuk, O.L., Lytvyn, P.M., Kuchmiy, S.Y. 2015 "Preparation and Optical Properties of Highly Luminescent Colloidal Single Layer Carbon Nitride". *RSC Adv.*, No 5: 46843-46849.

Panasyuk, Y.V., Raevskaya, A.E., Stroyuk, A.L., Kuchmiy, S. Ya. 2014. "Nanoparticles of graphite-like carbon nitride: stabilization in aqueous solutions, spectral and luminescent properties". *Theor. Exp. Chem.*, No 5: 291-297.

Stroyuk, A.L., Panasiuk, Y.V., Raevskaya, A.E., Kuchmy, S.Y. 2015. "Spectral and Luminescent Characteristics of Products from

Exfoliation of Graphitic Carbon Nitride Produced at Various Temperatures". *Theor. Exp. Chem.*, 243-251.

Cui, Y., Zhang, J., Zhang, G., Huang, J. 2011 "Synthesis of Bulk and Nanoporous Carbon Nitride Polymers from Ammonium Thiocyanate for Photocatalytic Hydrogen Evolution". *J. Mater. Chem.*, No 21: 13032-13039.

Liang, Q., Li, Z., Yu, X., Huang, Z.-H. 2015. "Macroscopic 3D Porous Graphitic Carbon Nitride Monolith for Enhanced Photocatalytic Hydrogen Evolution". *Advanced Materials*, No 31: 4634-4639.

Li, X.-H., Zhang, J., Chen, X., Fischer, A. 2011. "Condensed Graphitic Carbon Nitride Nanorods by Nanoconfinement: Promotion of Crystallinity on Photocatalytic Conversion". *Chemistry of Materials*, No 19: 4344-4348.

Jin, X., Balasubramanian, V.V., Selvan, S.T., Sawant, D.P. 2009. "Highly Ordered Mesoporous Carbon Nitride Nanoparticles with High Nitrogen Content: A Metal-Free Basic Catalyst". *Angewandte Chemie International Edition*, No 42:7884-7887.

Li, Q. Yang, J., Feng, D., Wu, Z. 2010. "Facile Synthesis of Porous Carbon Nitride Spheres with Hierarchical Three Dimensional Mesostructures for CO_2 Capture". *Nano Res.*, 3: 632-642.

Zhong, R.-Y., Zhang, Z., Luo, S., Zhang, Z. C 2018. "Comparison of TiO2 and g-C3N4 2D/2D nanocomposites from three synthesis protocols for visible-light induced hydrogen evolution". *Catalysis Science & Technology*.

Lei, J., Chen, B., Lu, W., Zhou, L. 2019. "Inverse Opal TiO_2/g-C3N4 Composite with Heterojunction Construction for Enhanced Visible Light-driven Photocatalytic Activity". *Dalton Transactions*.

Zhang, J., Guo, F., Wang, X. 2013. "An Optimized and General Synthetic Strategy for Fabrication of Polymeric Carbon Nitride Nanoarchitectures".

Adv. Funct. Mater, 3008-3014.

Bondarenko, M.E., Silenko, P.M., Solonin, Yu.M., Gubareni, N.I. 2019. "Synthesis of O-g-C_3N_4/TiO_2 rutile composite material for photocatalytic application". *Him. Fiz. Tehnol. Poverhni.*, No. 4: 398.

Park, H.A., Choi, J.H., Choi, K.M., Lee, D.K. 2012. "Highly Porous Gallium Oxide with a High CO_2 Affinity for the Photocatalytic Conversion of Carbon Dioxide into Methane". *J. Mater. Chem.*, 22: 5304-5307.

Mori, K., Yamashita, H., Anpo, M. 2012. "Photocatalytic Reduction of CO_2 with H_2O on Various Titanium Oxide Photocatalysts". *RSC Adv.*, No 2: 3165-3172.

Zhao, Z., Sun, Y., Dong, F. 2015. "Graphitic Carbon Nitride Based Nanocomposites: A Review". *Nanoscale*, No 7: 15-37.

Niu, P., Yang, Y., Jimmy, C.Y., Liu, G., Cheng, H. M. 2014. "Switching the Selectivity of the Photoreduction Reaction of Carbon Dioxide by Controlling the Band Structure of a g-C3N4 Photocatalyst". *Chem. Commun.*, 50: 10837-10840.

Zhao, Z. Dai, Y., Lin, J. 2014. "Wang G. Highly-Ordered Mesoporous Carbon Nitride with Ultrahigh Surface Area and Pore Volume as a Superior Dehydrogenation Catalyst". *Chem. Mater.*, No 10: 3151-3161.

Min, B.H., Ansari, M.B., Mo, Y.H., & Park, S.E. 2013. "Mesoporous carbon nitride synthesized by nanocasting with urea/formaldehyde and metal-free catalytic oxidation of cyclic olefins". *Catalysis Today*, 204: 156-163.

Ansari, M.B., Min, B.H., Mo, Y.H., Park, S.E. 2011. "CO2 Activation and Promotional Effect in the Oxidation of Cyclic Olefins over Mesoporous Carbon Nitrides". *Green Chem.*, No 13: 1416-1421.

Bhadra, Sambu, Khastgir, Dipak, Singha, Nikhil, & Lee, Joong. 2009. "Progress in preparation, processing and applications of polyaniline". *Progress in Polymer Science*, No 8: 783-810.

Stejskal, J., & Gilbert, R.G. 2002. "Polyaniline. Preparation of a conducting polymer (IUPAC Technical Report)". *Pure and Applied Chemistry*, No 8: 857-867.

Stejskal, Jaroslav, Sapurina, Irina, & Trchová, Miroslava. 2010. "Polyaniline nanostructures and the role of aniline oligomers in their formation". *Progress in Polymer Science*, No 12: 1420-1481.

Nikolaeva, E. 2002. "Current is conducted by polymers here". *Rus. Chem. J.*, No 12: 28-31.

Tomczykova, Monica and Plonska-Brzezinska, Marta. 2019. "Conducting Polymers, Hydrogels and their Composites: Preparation, Properties and Bioapplications". *Polymers*, No 2: 350.

Li, Y., Zhao, X., Yu, P., & Zhang, Q. 2012. "Oriented Arrays of Polyaniline Nanorods Grown on Graphite Nanosheets for an Electrochemical Supercapacitor". *Langmuir*, No 1: 493-500.

Ko, Young, Tae, Do, Oh, Hyan, Lee, Hyun. 2015. "Line-patterning of polyaniline coated MWCNT on stepped substrates using DC electric field". *Scientific Reports*, 4, 6656.

Masters, J.G., Sun, Y., MacDiarmid, A.G., & Epstein, A.J. 1991. "Polyaniline: Allowed oxidation states". *Synthetic Metals*, No 1-2: 715-718.

Ray, A., Richter, A.F., MacDiarmid, A.G., & Epstein, A.J. 1989. "Polyaniline: protonation/deprotonation of amine and imine sites". *Synthetic Metals*, No 1: 151-156.

Green, Arthur, Woodhead, Arthur. 1910. "CCXLIII. Aniline-black and allied compounds. Part I". *J. Chem. Soc., Trans.*, 2388-2403.

MacDiarmid, A.G., Manohar, S.K., Masters, J.G., Sun, Y., Weiss, H., & Epstein, A.J. 1991. "Polyaniline: Synthesis and properties of pernigraniline base". *Synthetic Metals*, No 1-2, 621-626.

Khan, A., Inamuddin, & Jain, R.K. 2016. "Easy, operable ionic polymer metal composite actuator based on a platinum-coated sulfonated poly(vinyl alcohol)-polyaniline composite membrane". *Journal of Applied Polymer Science*, No 33.

Asaka, Kinji and Qkuzaki, Hidenori. 2019. "Soft Actuators: Materials, Modeling, Applications, and Future Perspectives", Springer, chapter 8.4.3, 180.

Patni, N., Jain, N., & Pillai, S.G. 2017. "Polyaniline-Based Sensors for Monitoring and Detection of Ammonia and Carbon Monoxide Gases". *Trends and Applications in Advanced Polymeric Materials*, 145-162.

Krinichnyi, V.I., Konkin, A.L., & Monkman, A.P. 2012. "Electron paramagnetic resonance study of spin centers related to charge transport in metallic polyaniline". *Synthetic Metals*, No 13-14: 1147-1155.

Zagorny, M.N. 2008. "Synthesis of textured polyaniline in the presence of organic and inorganic dopants of different chemical compositions". *Nanostructural materials*, No 1: 14-19.

Zahornyi, M. 2017. "Synthesis, structure and conductivity of polyaniline", *Book LAP LAMBERT Academic Publishing 61*.

Polyanilines / Trivedi D.C. // *Handbook of Organic Conductive Molecules and Polymers*, ed. Nalwa H.S., Wiley, Chichester, 1997, 505-72.

Gedela, Venkata, Srikansh, Valadi Venkata. 2014. "Polyaniline nanostructures expedient as working electrode materials in super capacitors". *Applied Physics A*, No 115: 189-197.

Chandrasekhar, P. 1999. "Conducting Polymers, Fundamentals and Applications: A Practical Approach". Kluwer Academic, Boston.

Sapurina, Irina, Riede, Andrea, & Stejskal, Jaroslav. 2001. "In-situ polymerized polyaniline films". *Synthetic Metals*, No 3: 503-507.

Shishov, M.A. 2013. "Self-organized layers of polyaniline for application in electronics", dissertation for a scientific degree by a candidate of technical sciences: 05.27.06/Shishov Mikhail Aleksandrovich. St. Petersburg, p. 23.

Shishov, Mikhail, Moshnikov, Vyacheslav, & Sapurina, Irina. 2013. "Self-organization of polyaniline during oxidative polymerization: formation of granular structure". *Chemical Papers*, No 8: 909-918.

Ding, Z., Sanchez, T., Labouriau, A., Iyer, S. 2010. "Characterization of Reaction Intermediate Aggregates in Aniline Oxidative Polymerization at Low Proton Concentration". *The Journal of Physical Chemistry B*, No 32: 10337-10346.

Sapurina, I.Y., & Stejskal, J. 2012. "Oxidation of aniline with strong and weak oxidants. *Russian Journal of General Chemistry*, No 2: 256-275.

Sapurina, I., Shishov M. 2012. "Oxidative polymerization of aniline: Molecular Synthesis of polyaniline and the formation of supramolecular structures". INTECH/Chapter 9 in *New Polymers for Special Applications*, ed. Ailton de Souza Gomes. 251-312.

Shishov, M.A. 2011. "Hierarchical supramolecular organization of globular polyaniline". 75th PPM Conducting polymers, Formations, Structure, properties and applications, Book of abstracts PC, Prague, p. 143.

Shishov, M.A. 2011. "The ordered structure of polyaniline films prepared by in situ polymerization method [et al.]". 7th International Symposium Molecular Mobility and order in polymer systems, Book of abstracts PC, St. Peterburg, p. 210.

Sapurina, I., Tenkovtsev, A.V., & Stejskal, J. 2015. "Conjugated polyaniline as a result of the benzidine rearrangement". *Polymer International*, No 4: 453-465.

Stejskal, J., Kratochvíl, P., & Jenkins, A.D. 1996. "The formation of polyaniline and the nature of its structures". *Polymer*, No 2: 367-369.

Wei, H., Dong, J., Fang, X. et al. 2019. "Ti3C2TxMXene/polyaniline (PANI) sandwich intercalation structure composites constructed for microwave absorption". *Compos. Sci. Technol.*, 52-59.

Sun, J., & Chen, L. 2019. "Novel capacitance properties of polyaniline with branch-like chains". *Reactive and Functional Polymers*, 138: 55-61.

Bhadra, J., Al-Thani, N.J., Karmakar, S., & Madi, N.K. 2016. "Photo-reduced route of polyaniline nanofiber synthesis with embedded silver nanoparticles". *Arabian Journal of Chemistry.*

Varga, M., Prokeˇs, J., Bober P., Stejskal, J. 2012. "Electrical Conductivity of Polyaniline-Silver Nanocomposites". WDS'12 *Proceedings of Contributed Papers, Part III*, 52-57.

Abbasi, M., Yu H., Wang L., Abdin, Z. 2015. "Preparation of silver nanowires and their application in conducting polymer nanocomposites". *Mater. Chem. Phys.*, 166: 1-15.

Shishov, M.A. 2013. “Self-organized layers of polyaniline for application in electronics”, dissertation obtaining a scientific degree by K.T. Sciences: 05.27.06/Shishov Mikhail Aleksandrovich. St. Petersburg., 20 p.

Root, Y., Koren, Ya., Carrier O. 2011. “Chemical synthesis and morphology of the surface of the arranged polyaniline”. *Visnyk Lviv*, 52: 317-321.

Kovalchuk, Ye. P., Koren, Ya., Transporter O. 2012. “Investigation of the surface morphology of polyaniline composites”. *Visnyk Lviv. Un-th Sir Khim*, Exp. 53: 309-314.

Han, T.H., Parveen, N., Shim, J.H., Nguyen, A.T.N. 2018. “Ternary Composite of Polyaniline Graphene and TiO_2 as a Bifunctional Catalyst to Enhance the Performance of Both the Bioanode and Cathode of a Microbial Fuel Cell”. *Industrial & Engineering Chemistry Research*, No 19: 6705-6713.

Jumat, N.A., Wai, P.S., Ching, J.J., & Basirun, W.J. 2017. “Synthesis of Polyaniline-TiO_2 Nanocomposites and Their Application in Photocatalytic Degradation”. *Polymers and Polymer Composites*, No 7: 507-514.

Meat processing technology for small-to medium-scale producers. Cleaning and sanitation in meat plants: http://www.fao.org/docrep/010/ai407e/ai407e26.htm. Accessed 04/02/2014.

Brooms, T.J., Otieno, B., Onyango, M.S., & Ochieng, A. 2017. “Photocatalytic degradation of P-Cresol using TiO_2/ZnO hybrid surface capped with polyaniline”. *Journal of Environmental Science and Health*, Part A, No 2: 99-107.

Ghazzal, M.N., Kebaili, H., Joseph, M., Debecker, D.P. et al. 2012. “Photocatalytic degradation of Rhodamine 6G on mesoporous titanium films: Combined effect of texture and dye aggregation forms”. *Applied Catalysis B: Environmental*, 115-116, 276-284.

Luna, A.L., Dragoe, D., Wang, K., Beaunier, P. et al. 2017. “Photocatalytic Hydrogen Evolution Using Ni-Pd/TiO_2: Correlation of Light Absorption, Charge-Carrier Dynamics, and Quantum Efficiency. *The Journal of Physical Chemistry C*, No 26: 14302-14311.

Zahornyi, M. (2017). “Nanosized powders as reinforcement for photoactive composites (Overview)”. *Powder Metallurgy and Metal Ceramics*, 3-4, 130-147.

Pankivska, Yu. B., Biliavska, L.O., Povnitsa, O. Yu., Zagornyi, M.M. et al. 2019. “Antiadenoviral activity of titanium dioxide nanoparticles”. *Microbiology Journal (Ukraine)*, No 5, 73-84.

Li, J., & Wu, N. 2015. "Semiconductor-based photocatalysts and photoelectrochemical cells for solar fuel generation: a review". *Catalysis Science & Technology*, No 3: 1360-1384.

Zahornyi, M. 2018. "Functional nanocomposites based on titanium dioxide". Monograph LAP Lambert Academic Publishing, 157.

Ghosh, S., Kouamé, N.A., Ramos, L., Remita, S. et al. 2015. "Conducting polymer nanostructures for photocatalysis under visible light". *Nature Materials*, No 5: 505-511.

Yunfeng, Zhu, Shoubin, Xu, Dan, Yi. 2010. "Photocatalytic degradation of methyl orange using polythiophene/titanium dioxide composites". Reactive and Functional Polymers, 70: 282-287.

Khalyavka, T.A., Shcherban, N.D., Shymanovska, V.V., Manuilov, E.V., Permyakov, V.V., & Shcherbakov, S.N. 2019. "Cerium-doped mesoporous BaTiO3/TiO2 nanocomposites: structural, optical and photocatalytic properties". *Research on Chemical Intermediates*.

Sokolsky, G.V., Zahornyi M.M., Lobunets T.F., Tyschenko N.I. 2019. "Photoelectrocatalytic degradation of amino-azodyes by titanium dioxide with surface states of Ti^{3+}". *Journal of Chemistry and Technologies (Dnipro)*, No 2: 130-139.

Adriana Zaleska-Medynska. 2018. *Metal Oxide-Based Photocatalysis 1st Edition Fundamentals and Prospects for Application*. Elsevier. 350.

Heshmatpour, F., & Zarrin, S. 2017. "A probe into the effect of fixing the titanium dioxide by a conductive polymer and ceramic on the photocatalytic activity for degradation of organic pollutants". *Journal of Photochemistry and Photobiology A: Chemistry*, 346: 431-443.

Marija, Radoičić, Gordana, Ćirić-Marjanović, VukSpasojević, Phil Ahrenkiel, Miodrag Mitrić. 2017. "Superior photocatalytic properties of carbonized PANI/TiO_2 nanocomposites". *Applied Catalysis B: Environmental*, 155-166.

Gnanaprakasam, A., Sivakumar, V.M., & Thirumarimurugan, M. (2015). "Influencing Parameters in the Photocatalytic Degradation of Organic Effluent via Nanometal Oxide Catalyst: A Review". *Indian Journal of Materials Science*, 2015, 1-16.

Burunkova, Y. É., Denisyuk, I. Y., & Sem'ina, S. A. 2013. "Structural self-organization mechanism of ZnO nanoparticles in acrylate composites". *Journal of Optical Technology*, No 3: 187.

Ren, H., Koshy, P., Chen, W.F., Qi, S. 2017. "Photocatalytic materials and technologies for air purification". *Journal of Hazardous Materials*, 325, 340-366.

Arora, R., Srivastav, A., Utam, M.K. 2012. "Polyaniline based polymeric nanocomposite containing TiO_2 and SnO_2 for environmental and

energy applications". *Internationsl journal of modern engineering research*, 2: 2384-2395.

Liu, Z., Zhou, J., Xue, H., Shen, L., Zang, H. et al. 2006. "Polyaniline/TiO_2 solar cells". *Synthetic Metals,* No 9-10, 721-723.

Li, Q., Zhang, C., & Li, J. 2010. "Photocatalysis and wave-absorbing properties of polyaniline/TiO_2 microbelts composite by in situ polymerization method". *Applied Surface Science*, No 3: 944-948.

Phang, S. W., Tadokoro, M., Watanabe, J., & Kuramoto, N. 2008. "Synthesis, characterization and microwave absorption property of doped polyaniline nanocomposites containing TiO_2 nanoparticles and carbon nanotubes". *Synthetic Metals*, No 6, 251-258.

Rajakani, P., & Vedhi, C. 2015. "Electrocatalytic properties of polyaniline-TiO_2 nanocomposites. *International Journal of Industrial Chemistry*, No 4: 247-259.

Chaturmukha, V.S., Naveen, C.S., Rajeeva, M.P., Avinash, B.S. et al. 2016. "Dielectrical properties of PANI/TiO_2 nanocomposites".

Zhang, L., Liu P., Su Z. 2006. "Preparation of PANI-TiO_2 nanocomposites and their solid-phase photocatalytic degradation". *Polymer Degradation and Stability*, No 9: 2213-2219.

Zhang, L., Wan, M., Wei, Y. 2005. "Polyaniline/TiO_2 microspheres prepared by a template-free method". *Synthetic Metals*, 151: 1-5.

Yatsishin, M.M. 2011. "Nanocomposite material polyaniline/TiO_2". *Nanostructured Materials Science*, 2011. 1. p. 81-86.

Zagorny, M., Bykov I., Melnyk A., Lobunets T. "Surface Structure, Spectroscopic and Photocatalytic Activity Study of Polyaniline/TiO_2 Nanocomposites". *J. Chem. Chem. Eng.*, 8: 118-127.

Phang, S.W., Tadokoro, M., Watanabe, J., Kuramoto, N. 2008. "Microwave absorbtion behaviors of polyaniline nanocomposites containing TiO_2 nanoparticles". *Current Applied Physics*, No 3-4: 391-394.

Song, X., Yan, C., Huang S., Zhang, M. 2013. "Synthesis of mesoporous polyaniline-TiO_2 composite microspheres for gas sensing application". *Advanced Materials Research*, 750-752, 1098-1103.

Moghaddam, H. M., Nasirian S. 2014. "Hydrogen gas sensing feature of polyaniline/titania (rutile) nanocomposite at environmental conditions". *Applied Surface Science*, 317: 117-124.

Choquette-Labbé, M., Shewa, W., Lalman, J., & Shanmugam, S. 2014. "Photocatalytic Degradation of Phenol and Phenol Derivatives Using a Nano-TiO_2 Catalyst: Integrating Quantitative and Qualitative Factors Using Response Surface Methodology". *Water*, No 6: 1785-1806.

Hirofumi, Harada, Akira Onoda, Taro Uematsu, Susumu Kuwabata, and Takashi Hayashi 2016. "Photocatalytic Properties of TiO_2 Composites

Immobilized with Gold Nanoparticle Assemblies Using the Streptavidin-Biotin Interaction". Langmuir, No 25: 6459-6467.

Burunkova, Yu.E., Denisyuk, N.Yu. 2013. "Mechanism of Structural Self-Organization of ZnO Nanoparticles in Acrylate Composites". *Optical Journal*, 80: 79-85.

Burunkova, Yu.E., Denisyuk, N.Yu., Semyina, S.A. 2012. "Investigation of the influence of SiO_2 nanoparticles on the self-organization of acrylate composites cured by ultrasonic light". *Optical Journal*, 79: 67-71.

Wang, H., Xu, P., Meng, S., Zhong, W. et al. 2006. "Poly(methyl methacrylate)/silica/titania ternary nanocomposites with greatly improved thermal and ultraviolet-shielding properties". *Polym. Degrad. Stab.*, 91: 1455-1461.

Sun, X., Chen, X., Fan, G., Qu, S. 2010. "Preparation and the optical nonlinearity of surface chemistry improved titania nanoparticles in poly(methyl methacrylate)-titania hybrid thin films". *Appl. Surf. Sci.*, 256: 2620-2625.

Chen, W.C., Lee, S. J., Lee, L.H. et al. 1999. "Synthesis and characterization of trialkoxysilane-capped poly(methyl methacrylate)-titania hybrid optical thin films". *J. Mater. Chem.*, 9: 2999-3003.

Lee, L.H., Chen, W.C. 2001. "High-refractive-index thin film prepared from trialkoxysilane-capped poly(methyl methacrylate)-titania materials". *Chem. Mater.*, 13: 1137-1142.

Federica De Riccards, M., Martina V. 2014. Hybrid conducting nanocomposites coatings for corrosion protection". *Developments in corrosion protection*, Chap. 13: 272-314.

Genies, E. M., Bidan, G., Dias, A.F. 1983. "Spectroelectrochemical study of polypyrrole films". *Journal of Electroanalytical Chemistry*, 149: 101-113.

Piskareva, A.I. 2012. "Kinetics and Mechanism of Oxidative Polymerization of Pyrrole by Ammonium Persulfate in Aqueous Solution". *Vestnik Voronezh State University*, No 2: 42-48.

Brezoi, D. 2010. "Polypyrrole films prepared by chemical oxidation of pyrrole in aqueous $FeCl_3$ solution". *Journal of Science and Arts*, 1: 53-58

Ourari, A., Aggoun, D., & Ouahab, L. 2014. "Poly(pyrrole) films efficiently electrodeposited using new monomers derived from 3-bromopropyl-N-pyrrol and dihydroxyacetophenone—Electrocatalytic reduction ability towards bromocyclopentane". *Colloids and Surfaces A: Physicochemical and Engineering Aspects*, 446, 190-198.

Wang, W.Y., Ting, P.N., Luo, S.H., & Lin, J.Y. 2014. "Pulse-reversal electropolymerization of polypyrrole on functionalized carbon

nanotubes as composite counter electrodes in dye-sensitized solar cells". *Electrochimica Acta*, 137, 721-727.

Mostafizur, Rahaman, Ali, Aldalbahi, Mohammed, Almoiqli, Shaykha Alzahly. 2018. "Chemical and Electrochemical Synthesis of Polypyrrole Using Carrageenan as a Dopant: Polypyrrole/Multi-Walled Carbon Nanotube Nanocomposites". *Polymers* 10, 632.

Huang, J., Yang, Z., Yang, B., Wang, R., Wang, T. 2014. "Ultrasound assisted polymerization for synthesis of ZnO/Polypyrrole composites for zinc/nickel rechargeable battery". *Journal of Power Sources*, 271: 143-151.

Arenas, M.C., Rodríguez-Núnez, L.F., Rangel, D., Martínez-Álvarez, O., Martínez-Alonso, C., & Castaño, V.M. 2013. "*Simple one-step ultrasonic synthesis of anatase titania/polypyrrole nanocomposites*". *Ultrasonics Sonochemistry*, No 2: 777-784.

Sundaram, M.M, Sangareswari, M., Muthirulan, P. 2014. "Enhanced Photocatalytic Activity of Polypyrrole/TiO_2 Nanocomposites for Acid Violet Dye Degradation under UV Irradiation". *International Journal of Innovative Research in Science & Engineering*, 1-4.

Batool, A., Kanwal, F., Imran, M., Jamil, T., Siddigi, S.A. 2012. "Synthesis of polypyrrole/zinc oxide composites and study of their structural, thermal and electrical properties". *Synthetic Metals*, No 23-24: 2753-2758.

Cao, S., Zhang, H., Song, Y., Zhang, J., Yang, H. et al. 2015. "Investigation of polypyrrole/polyvinyl alcohol-titanium dioxide composite films for photo-catalytic applications". *Applied Surface Science*, 342: 55- 63.

MacDiarmid, A.G. 2001. "Synthetic Metals: A Novel Role for Organic Polymers". *Angew. Chem. Int. Ed.*, No 14: 2581-2590.

Malinauskas, A., Malinauskiene, J., Ramanavicius, A. 2005. "Conducting polymer-based nanostructurized materials: electrochemical aspects". *Nanotechnology*, No R51-R62.

Khomenko, V.G., Barsukov, V.Z., Katashinskii, A.S. 2005. "The catalytic activity of conducting polymers toward oxygen reduction". *Electrochim. acta*, No 7/8: 1675-1683.

Qi, Z., Pickup, P.G. 1998. "A high performance conducting polymer supported oxygen reduction catalyst". *Chem. Commun*, No 21: 2299-2300.

Posudievsky, O.Yu., Kurys, Ya.I., Pokhodenko, V.D. 2004. "12-Phosphormolibdic acid doped polyaniline-V_2O_5 composite". *Synth. Met.*, No 2: 107-111.

Hasik, M., Pron, A., Kulszewicz-Bajer, I., Pozniaczek, A. et al. 1993. "Polyaniline doped with heteropolyanions: Spectroscopic and catalytic properties". *Synth. Met.*, No 55: 972-976.

Bashyam, R., Zelenay, P.A. 2006. "Class of non-precious metal composite catalysts for fuel cells". *Nat. Lett.*, 443: 63-66.

Yuasa, M., Yamaguchi, A., Itsuki, H., Tanaka, K. et al. 2005. "Modifying Carbon Particles with Polypyrrole for Adsorption of Cobalt Ions as Electrocatatytic Site for Oxygen Reduction". *Chem. Mater.*, 17: 4278-4281.

Millan, W.M., Thompson, T.T., Arriaga, L.G., Smith, M.A. 2009. "Characterization of composite materials of electroconductive polymer and cobalt as electrocatalysts for the oxygen reduction reaction". *Int. J. Hydrog. Energy*, 34: 694-702.

Reddy, A.L.M., Rajalakshmi, N., Ramaprabhu, S. 2008. "Cobalt-polypyrrole-multiwalled carbon nanotube catalysts for hydrogen and alcohol fuel cells". *Carbon*, 46: 2-11.

Dodelet, J.P. / ed. by J.H. Zagal, F. Bedioui, J.P. Dodelet // N4-macrocyclic metal complexes. New York: Springer Science + Business Media Inc., 2006.

Jasinski, R.A. 1964. "New Fuel Cell Cathode Catalyst". *Nature*, 201: 1212-1213.

Alt, H., Binder, H., Sandsted, G. 1973. "Mechanism of electrocatalytic reduction of oxygen on metal-chelates". *J. Catal*, *28*, 8-19.

Bezerre, C.W.B., Zhang, L., Lee, K., Liu, H. et al. 2008. "Novel carbon-supported Fe-N electrocatalysts synthesized through heat treatment of iron tripyridyl triazine complexes for the PEM fuel cell oxygen reduction reaction". *J. Electrochim. Acta*, *53*:7703-7710.

Shao, M., Chang, Q., Dodelet, J.-P., Chenitz, R. et al. 2016. "Recent advances in electrocatalysts for oxygen reduction reaction". *Chem. Rev*. *116*: 3594-3657.

Lefevre, M., Proietti, E., Jaouen, F., Dodelet, J.P. 2009. "Iron-Based Catalysts with Improved Oxygen Reduction Activity in Polymer Electrolyte Fuel Cells". *Science*, *324*: 71-74.

Shen, M., Wei, C., Ai, K., Lu, L. 2017. "Transition metal-nitrogen nanostructured catalysts for the oxygen reduction reaction: From mechanistic insights to structural optimization". *Nano Research*, 1449-1470.

Lee, K., Zhang, L., Lui, H., Hui, R. et al. 2009. "Oxygen reduction reaction (ORR) catalyzed by carbon-supported cobalt polypyrrole (Co-PPy/C) electrocatalysts". *Electrochim. Acta*, *54*: 4704-4711.

Feng, W., Li, H., Cheng, X. et al. 2012. “A comparative study of pyrolyzed and doped cobalt-polypyrrole electrocatalysts for oxygen reduction reaction”. *Applied Surface Science*, No 8: 4048-4053.

Jiang, S., Zhu, C., Dong, S. 2013. “Cobalt and nitrogen-cofunctionalized graphene as a durable non-precious metal catalyst with enhanced ORR activity”. *Journal of Materials A*, No 11: 3593-3599.

Hu, Y., Zhao, X., Huang, Y. et al. 2013. “Synthesis of self-supported non-precious metal catalysts for oxygen reduction reaction with preserved nanostructures from the polyaniline nanofiber precursor”. *Journal of Power Sources*, 225: 129-136.

Yuan, X., Zeng, X., Zhang, H-J. et al. 2010. “Improved Performance of Proton Exchange Membrane Fuel Cells with p-Toluenesulfonic Acid-Doped Co-PPy/C as Cathode Electrocatalyst”. *J. Am. Chem. Soc.*, No 6: 1754-1755.

Wu, G., More, K.L., Xu, P. et al. 2013. “A carbon-nanotube-supported graphene-rich non-precious metal oxygen reduction catalyst with enhanced performance durability”. *Chemical Communications*, No 32: 3291-3293.

Wu, G., Chen, Z., Artyushkova, K., Garzon, F.H. et al. 2008. “Polianiline-derived non-precious catalyst for the polymer electrolyte fuel cell cathode”. *ECS Trans*, 16: 159-170.

Wu, G., Artyushkova, K., Ferrandon, M., Kropf, A.J. 2009. “Performance Durability of Polyaniline-derived Non-precious Cathode Catalysts”. *ECS Trans.*, 25: 1299-1311.

Tran, T.N., Song, M.Y., Singh, K.P. 2016. “Iron-polypyrrole electrocatalyst with remarkable activity and stability for ORR in both alkaline and acidic conditions: a comprehensive assessment of catalyst preparation sequence”. *J. Mater. Chem. A*, No 22: 8645-8657.

Wang, Q., Zhou, Z-Y., Lai, Y-J. et al. 2014. “Phenilenediamine-Based FeNx/C Catalyst with High Activity for Oxygen Reduction in Acid Medium and Its Active-Site Probing”. *J. Am. Chem. Soc.*, No 31: 10882-10885.

Fu, X., Liu, Y., Cao, X., Jin, J. 2013. “Fe-Co-N_x embedded graphene as high performance catalysts for oxygen reduction recation”. *Applied Catalysis B: Environmental*, 130-131, 143-151.

Zhu, Y.S., Zhang, B.S., Feng, Z.D., Su, D.S. 2016. “Synthesis-Structure-Performance Correlation for Poly(phenylenediamine)S/Iron/Carbon Non-Precious Metal Catalysts for Oxygen Reduction Reaction”. *Catal. Today*, 260: 112-118.

Tetteh, E.B., Lee, H.Y., Shin, C.H., Kim, S., Ham, H.C., Tran, T.N., Yu, J.S. 2020. “A New PtMg Alloy with Durable Electrocatalytic

Performance for Oxygen Reduction Reaction in Proton Exchange Membrane Fuel Cell". *ACS Energy Letters*.

Neisi, Z., Ansari-Asl, Z., Jafarinejad-Farsangi, S., Tarzi, M. E., Sedaghat, T., & Nobakht, V. 2019. "Synthesis, characterization and biocompatibility of polypyrrole/Cu(II) metal-organic framework nanocomposites". *Colloids and Surfaces B: Biointerfaces*.

Belver, C., Bedia, J., Gómez-Avilés, A., Peñas-Garzón, M., & Rodriguez, J. J. 2019. "Semiconductor Photocatalysis for Water Purification". Nanoscale Materials in Water Purification, 581-651.

Chapter 4

Gilja, V., Novaković, K., Travas-Sejdic, J., Hrnjak-Murgić, Z., Kraljić Roković, M., & Žic, M. 2017. "Stability and Synergistic Effect of Polyaniline/TiO_2 Photocatalysts in Degradation of Azo Dye in Wastewater". *Nanomaterials*, No 12: 412.

Jumat, N. A., Wai, P. S., Ching, J. J., & Basirun, W. J. 2017. "Synthesis of Polyaniline-TiO2 Nanocomposites and their Application in Photocatalytic Degradation". *Polymers and Polymer Composites*, No 7: 507-514.

Heinz, Gunter, Hautzinger, Peter. 2007. "Meat processing technology for small-to medium-scale producers. Cleaning and sanitation in meat plants". http://www.fao.org/docrep/010/ai407e/ai407e26.htm. Accessed 04/02/2014.

Thabo, J., Brooms, Maurice S., Onyango, Aoyi Ochieng. 2014. "Photocatalytic Activity of Polyaniline/Tio_2/Zno Composite for Degradation of Aromatic Compounds in Abattoir Wastewater". *Intl. Conf. on Chemical, Integrated Waste Management & Environmental Engineering (ICCIWEE'2014)* 124-130.

Ghazzal, M.N., Kebaili, H., Joseph, M., Debecker, D.P., Eloy, P., De Coninck, J., & Gaigneaux, E.M. 2012. "Photocatalytic degradation of Rhodamine 6G on mesoporous titania films: Combined effect of texture and dye aggregation forms". *Applied Catalysis B: Environmental*, No 115-116, 276-284.

Luna, A.L., Dragoe, D., Wang, K., Beaunier, P. et al. 2017. "Photocatalytic Hydrogen Evolution Using Ni-Pd/TiO_2: Correlation of Light Absorption, Charge-Carrier Dynamics, and Quantum Efficiency". *The Journal of Physical Chemistry C*, No 26: 14302-14311.

Zahornyi, M. 2017. "Nanosized powders as reinforcement for photoactive composites (Overview)". *Powder Metallurgy and Metal Ceramics*, No

3-4: 130-147.
Olad, Ali, Behboudi, Sepideh, Entezami, Ali Akbar. 2012. “Preparation, characterization and photocatalytic activity of TiO_2/polyaniline core-shell nanocomposite”. *Bull. Mater. Sci.*, No5: 801-809.
Li, Jiangtian, Wu, Nianqiang. 2015. “Semiconductor-based photocatalysts and photoelectrochemical cells for solar fuel generation: a review”. *Catalysis Science & Technology*, No 3: 1360-1384.
Zahornyi M. 2017. *Synthesis, structure and properties of polyaniline* // Monograph LAP Lambert Academic Publishing, p. 61.
Ghosh, S., Kouamé, N.A., Ramos, L., Remita, S. 2015. “Conducting polymer nanostructures for photocatalysis under visible light”. *Nature Materials,* No 5: 505-511.
Zhu, Yunfeng, Xu, Shoubin, Yi, Dan. 2010. “Photocatalytic degradation of methyl orange using polythiophene/titanium dioxide composites”. *Reactive and Functional Polymers*, No 5: 282-287.
Gu, L., Wang, J., Qi, R., Wang, X. et al. 2012. “A novel incorporating style of polyaniline/TiO2 composites as effective visible photocatalysts”. *Journal of Molecular Catalysis A: Chemical*, 357: 19-25.
Xu, H., Jia, F., Ai, Z., & Zhang, L. 2007. “A General Soft Interface Platform for the Growth and Assembly of Hierarchical Rutile TiO2 Nanorods Spheres”. *Crystal Growth & Design*, No 7: 1216-1219.
Gopalakrishnan, K., Elango, M., Thamilselvan, M. 2012. “Optical studies on nano-structured conducting polyaniline prepared by chemical oxidation method”. *Archives of Physics Research*, No 4: 315-319.
Adriana Zaleska-Medynska. 2018. “Metal Oxide-Based Photocatalysis 1st Edition Fundamentals and Prospects for Application”. Elsevier.
Felora Heshmatpour, Saviz Zarrin. 2017. “A probe into the effect of fixing the titanium dioxide by a conductive polymer and ceramic on the photocatalytic activity for degradation of organic pollutants”. *Journal of Photochemistry and Photobiology A: Chemistry*, 431-443.
Marija Radoičić, Gordana Ćirić-Marjanović, VukSpasojević, Phil Ahrenkiel, Miodrag Mitrić, Tatjana Novaković, Zoran Šaponjić. 2017. “Superior photocatalytic properties of carbonized PANI/TiO_2 nanocomposites”. *Applied Catalysis B: Environmental*, 213: 155-166.

Chapter 5

Becquerel, H. 1839. On electric effect under the influence of solar radiation. CR *Acad. Sci. Paris*, 9, 561.
Garret C.G.B. and Brattain W.H. 1955. Physical Theory of Semiconductor Surfaces. *Physical Review*, 99(2), 376-387.

Fujishima A, Honda K. 1972. "Electrochemical photolysis of water at a semiconductor electrode". *Nature*, 238, 37-38.

Gerischer, H. 1972. "Electrochemical Surface-Reactions on Compound Semiconductors". *Journal of the Electrochemical Society*, 119(8) C241.

Gerischer, H. 1975. "Electrochemical Photo and Solar Cells - Principles and some Experiments". *Journal of Electroanalytical Chemistry*, 58(1): 263-74.

Pleskov Yu.V. 1984. "Solar Energy Conversion in Photoelectrochemical Cells with Semiconductor Electrodes". *Surface Science*, 15: 401-456.

Hagfeldt, A. and Grätzel, M. 2000. Molecular photovoltaics. *Acc. Chem. Res*., 33, 269.

Grätzel M. 2003. Applied Physics—Solar Cells to Dye For. *Nature*, 421, 586.

Grätzel M. 2004. "Conversion of Sunlight to Electric Power by Nanocrystalline Dyesensitised Solar Cells". *J. Photochem. & Photobio. A*, 164, 3.

Malato, S., Fernández-Ibanez, P., Maldonado, M.I., Blanco, J., Gernjak, W. 2009. "Decontamination and disinfection of water by solar photocatalysis: recent overview and trends". *Catal. Today*, 147: 1-59.

Bessegato, G.G., Guaraldo, T.T., de Brito, J.F., Brugnera, M.F., & Zanoni, M. V.B. 2015. "Achievements and trends in photoelectrocatalysis: from environmental to energy applications". *Electrocatalysis*, 6(5): 415-441.

Parkinson, B.A. 2002. Encyclopedia of Electrochemistry. Volume 6 Semiconductor Electrodes and Photoelectrochemistry. Edited by Stuart Licht (Israel Institute of Technology, Haifa, Israel). *4 Solar Energy Conversion without Dye Sensitisation* Wiley-VCH: Weinheim, p. 288.

Horiuchi, Y., Toyao, T., Takeuchi, M., Matsuoka, M., & Anpo, M. 2013. "Recent advances in visible-light-responsive photocatalysts for hydrogen production and solar energy conversion-from semiconducting TiO_2 to MOF/PCP photocatalysts". *Physical Chemistry Chemical Physics*, 15(32), 13243-13253.

Ding, Chunmei et al. 2017. "Photoelectrocatalytic water splitting: significance of cocatalysts, electrolyte, and interfaces". *ACS Catalysis* 7.1: 675-688.

Dotan, H., Sivula, K., Gratzel, M., Rothschild, A., Warren, S.C. 2011. *Energy Environ. Sci*., 4: 958-964.

Zaharieva, I., González-Flores, D., Asfari, B., Pasquini, C., Mohammadi, M. R., Klingan, K., Zizak, I., Loos, S., Chernev, P., Dau. 2016. *H. Energy Environ. Sci*., 9: 2433-2443.

Huynh, M., Bediako, D.K., Nocera, D.G. 2014. *J. Am. Chem. Soc.*, 136: 6002-6010.

Wieckowski, A., Savinova, E.R., Vayenas, C.G. 2003. *Catalysis and Electrocatalysis at Nanoparticle Surfaces*. CRC Press.

M. El Guindy, Platinum Group Metals: Alloying, Properties, and Applications. 2001. Editor(s): K.H. Jürgen Buschow, Robert W. Cahn, Merton C. Flemings, Bernhard Ilschner, Edward J. Kramer, Subhash Mahajan, Patrick Veyssière, Encyclopedia of Materials: Science and Technology, Elsevier, p. 7117-7121.

W. Tang, X. Chen, J. Xia, J. Gong, X. Zeng, Mater. 2014. *Sci. Eng. B*, 187, 39.

Haw, J.F., Song, W., Marcus, D.M., Nicholas, J.B. 2003. "The mechanism of methanol to hydrocarbon catalysis". *Acc. Chem. Res.*, 36: 317-326.

Suib, S.L. 2008. "Structure, porosity, and redox in porous manganese oxide octahedral layer and molecular sieve materials". *J. Mater. Chem*., 18: 1623-1631.

Kanke, Y., Takayama-Muromachi, E., Kato, K., Kosuda, K. 1995. "Synthesis and crystal structure of Priderite-type barium vanadium oxide BaxV8O16 (x = 1.09(1))". *J. Solid State Chem.*, 115:88-91.

Djerdj, I. et al. 2008. "Oxygen self-doping in hollandite-type vanadium oxyhydroxide nanorods". *J. Am. Chem. Soc.*, 130: 11364-11375.

Besnardiere, J., Ma, B., Torres-Pardo, A., Wallez, G., Kabbour, H., González-Calbet, J. M., Portehault, D. 2019. "Structure and electrochromism of two-dimensional octahedral molecular sieve h'-WO_3". *Nature communications*, 10(1), 327.

Coucou, A., Figlarz, M. 1988. "A new tungsten oxide with 3D tunnels: WO_3 with the pyrochlore-type structure". *Solid State Ion.*, 30: 1762-1765.

Gerand, B., Nowogrocki, G., Guenot, J., Figlarz, M. 1979. "Structural study of a new hexagonal form of tungsten trioxide". *J. Solid State Chem*., 29:429-434.

Anderson, M.W, Klinowski, J. 1990. "Layered titanate pillared with alumina". *Inorg. Chem.*, 17: 3260-3263.

Pless, J.D. et al. 2007. "Tunable conductivity of collapsed sandia octahedral molecular sieves". *Chem. Mater.*, 19: 4855-4863.

Kakazey, M., Ivanova, N., Boldurev, Y., Ivanov, S., Sokolsky, G., Gonzalez-Rodriguez, J.G., & Vlasova, M. 2003. "Electron paramagnetic resonance in MnO_2 powders and comparative estimation of electric characteristics of power sources based on them in the MnO_2-Zn system". *Journal of Power Sources*, 114(1): 170-175.

Shen, X., Morey, A., Liu, J., Ding, Y. 2011. "Characterization of the Fe-doped mixed-valent tunnel structure manganese oxide KOMS-2". *J. Phys. Chem. C*, 115: 21610-21619.

Chen, C.H. et al. 2015. "Structural distortion of molybdenum-doped manganese oxide octahedral molecular sieves for enhanced catalytic performance". *Inorg. Chem.*, 54: 10163-10171.

Vasconcellos, C.M., Gonçalves, M.L.A., Pereira, M.M., Carvalho, N.M.F. 2015. "Iron doped manganese oxide octahedral molecular sieve as potential catalyst for SOx removal at FCC". *Appl. Catal. A Gen.*, 498:69-75.

Ivanova, N.D., Ivanov, S.V., Boldyrev, E.I., Sokol'skii, G.V., & Makeeva, I.S. 2002. "High-performance manganese oxide catalysts for CO oxidation". *Russian journal of applied chemistry*, 75(9): 1420-1423.

Jin, L. et al. 2010. "Titanium containing γ-MnO_2 (TM) hollow spheres: one-step synthesis and catalytic activities in Li/Air batteries and oxidative chemical reactions. *Adv. Funct. Mater.*, 20: 3373-3382.

Said, S., El Maghrabi, H.H., Riad, M., & Mikhail, S. 2018. "Photocatalytic selective organic transformations by Fe-doped octahedral molecular sieves (manganese oxide) nano-structure". *Journal of Asian Ceramic Societies*, 6(2): 169-181.

Paramasivam, I., Jha, H., Liu, N., & Schmuki, P. 2012. "A review of photocatalysis using self-organized TiO_2 nanotubes and other ordered oxide nanostructures". *Small*, 8(20): 3073-3103.

Carbó, A.D. 2009. *Electrochemistry of porous materials*. CRC press.

Regonini, D., Bowen, C.R., Jaroenworaluck, A., & Stevens, R. 2013. "A review of growth mechanism, structure and crystallinity of anodized TiO_2 nanotubes". *Materials Science and Engineering: R: Reports*, 74(12), 377-406.

Shen, S., Chen, J., Wang, M., Sheng, X., Chen, X., Feng, X., & Mao, S.S. 2018. "Titanium dioxide nanostructures for photoelectrochemical applications". *Progress in Materials Science*, *98*: 299-385.

Liu, Z., Zhang, X., Nishimoto, S., Jin, M., Tryk, D. A., Murakami, T., & Fujishima, A. 2008. "Highly ordered TiO_2 nanotube arrays with controllable length for photoelectrocatalytic degradation of phenol". *The Journal of Physical Chemistry C*, 112(1): 253-259.

Grimes, C.A., & Mor, G.K. 2009. TiO_2 nanotube arrays: synthesis, properties, and applications. Springer Science & Business Media.

Hashimoto, K., Irie, H., & Fujishima, A. 2005. "TiO_2 photocatalysis: a historical overview and future prospects". *Japanese journal of applied physics*, 44(12R): 8269.

Fries, René & Simko, Myrtill. 2012. (Nano-)Titanium dioxide (Part I): Basics, Production, Applications. EFSA Panel on Food Additives and Nutrient Sources added to Food (ANS). "Re-evaluation of titanium dioxide (E 171) as a food additive". *EFSA Journal* 14.9 (016): e04545.

Weir, A., Westerhoff, P., Fabricius, L., Hristovski, K. and von Goetz, N. 2012. "Titanium dioxide nanoparticles in food and personal care products", *Environ. Sci. Technol.*, 46(4): 2242-50.

J. Gong, W. Pu, C. Yang, J. Zhang. 2013. *Catal. Commun.*, 36: 89.

K. Yang, W. Pu, Y. Tan, M. Zhang, C. Yang, J. Zhang. 2014. *Mater. Sci. Semicond. Process*, 27: 777.

H. Liu, G. Liu, J. Fan, Q. Zhou, H. Zhou, N. Zhang, Z. Hou, M. Zhang, Z. He. 2011. *Chemosphere* 82: 43.

W. Tang, X. Chen, J. Xia, J. Gong, X. Zeng, 2014. *Mater. Sci. Eng. B*, 187, 39.

H. Liu, G. Liu, X. Shi, Colloids Surf. 2010. *A Physicochem. Eng. Asp.*, 363, 35.

Sokolsky, G., Zudina, L., Boldyrev, E., Miroshnikov, O., Gauk, N., & Kiporenko, O. 2018. "ORR Electrocatalysis on Cr^{3+}, Fe^{2+}, Co^{2+}-doped Manganese(IV) oxides ". *Acta Physica Polonica A*, 133(4):1097-1102.

Li, K., Huang, Z., Zeng, X., Huang, B., Gao, S., & Lu, J. 2017. "Synergetic effect of Ti^{3+} and oxygen doping on enhancing photoelectrochemical and photocatalytic properties of TiO_2/g-C_3N_4 heterojunctions". *ACS applied materials & interfaces*, 9(13): 11577-11586.

W. Liao, J. Yang, H. Zhou, M. Murugananthan, Y. Zhang. 2014. *Electrochim. Acta* 136, 310.

N. Serpone. 2006. *J. Phys. Chem. B*, 110, 24287.

Rao, C.N.R., & Gopalakrishnan, J. 1997. *New directions in solid state chemistry.* Cambridge University Press.

Najafpour, M.M., Madadkhani, S., Akbarian, S., Hołyńska, M., Kompany-Zareh, M., Tomo, T., & Allakhverdiev, S.I. 2017. "A new strategy to make an artificial enzyme: photosystem II around nanosized manganese oxide". *Catalysis Science & Technology*, 7(19): 4451-4461.

Limburg, B., Bouwman, E. & Bonnet S.A. 2016. "Effect of Liposomes on the Kinetics and Mechanism of the Photocatalytic Reduction of Methyl Viologen". *Journal of Physical Chemistry B*, 120(28): 6969-6975.

Limburg, B., Wermink, J., Nielen, S.S. van, Kortlever R., Koper M.T.M., Bouwman, E. & Bonnet, S. 2016. "Kinetics of Photocatalytic Water Oxidation at Liposomes: Membrane Anchoring Stabilizes the Photosensitiser". *Acs Catalysis*, 6(9): 5968-5977.

J.H. Werner, S. Kolodinski and H.J. Queisser. 1994. *Phys. Rev. Lett.*, 72, 3851.

S. Singh, W. J. Jones, W. Siebrand, B.P. Stoicheff and W.G. Schneider 1965. *J. Chem. Phys.*, 42, 330.

Miller & E. Abrahams. 1960. *Phys. Rev.*, 120, 745.

D.L. Dexter. 1953. *J. Chem. Phys.*, 21, 836.

Lewerenz, H.J., Heine, C., Skorupska, K., Szabo, N., Hannappel, T., Vo-Dinh, T., Campbell, S.A., Klemm, H.W. and Munoz, A.G. 2010. "Photoelectrocatalysis: principles, nanoemitter applications and routes to bio-inspired systems". *Energy & Environmental Science*, 3(6): 748-760.

T.A. Egerton 2011. *J. Chem. Technol. Biotechnol.*, 86, 1024.

M. Pelaez, N.T. Nolan, S.C. Pillai, M.K. Seery, P. Falaras, A.G. Kontos, P.S.M.M. Dunlop, J.W.J.J. Hamilton, J.A.A. Byrne, K. O'Shea, M.H. Entezari, D.D. Dionysiou, K.O. Shea, M.H. Entezari, D.D. Dionysiou. 2012. *Appl Catal. B*, 125, 331.

G.G. Bessegato, T.T. Guaraldo, M.V.B. Zanoni. 2014. *Modern Electrochemical Methods in Nano, Surface and Corrosion Science*, ed. M. Aliofkhazraei (InTech, Rijeka,), pp. 271-319.

Papagiannis, G. Koutsikou, Z. Frontistis, I. Konstantinou, G. Avgouropoulos, D. Mantzavinos and P. Lianos. 2018. "Photoelectrocatalytic vs. Photocatalytic Degradation of Organic Water Born Pollutants". *Catalysts*, 8: 455.

H. Pan. 2015. "Bandgap engineering of oxygen-rich TiO_{2+x} for photocatalyst with enhanced visible-light photocatalytic ability". *Journal of Materials Science*, 50: 4324-4329.

Wang H.M., Tan X., Yu.T. 2014. *Appl. Surf. Sci.*, 321: 531.

Dai J., Yang J., Wang X. H., Zhang L., Li Y. 2015. *J. Appl. Surf. Sci.*, 349: 343.

T. Gao, M. Glerup, F. Krumeich, R. Nesper, H. Fjellvag, and P. Norby. 2008. *J. Phys. Chem. C*, 112, 13134.

J. Georgieva, E. Valova, S. Armyanov, N. Philippidis, I. Poulios, S. Sotiropoulos, 2012. *J. Hazard Mater.*, 211, 30.

J. Georgieva, S. Sotiropoulos, S. Armyanov, N. Philippidis, I. Poulios. 2010. *J. Appl. Electrochem.*, 41, 173.

M. Zhang, C.Yang, W. Pu, Y. Tan, K. Yang, J. Zhang. 2014. Electrochim Acta, 148: 180.

L.C. Almeida, M.V.B. Zanoni. 2014. *J. Braz. Chem. Soc.* 25: 579.

An, T.C, Chen, J.Y, Nie, X., Li, G.Y, Zhang, H M, Liu, X.L, Zhao, H. J. 2012.*ACS Appl. Mater. Inter.*, 4: 5988.

Chen, J. C., Luo, H.Y., Shi, H. X., Li, G. Y., An T. C. 2014. *Appl Catal A*, 485: 188.

Dong, Y. M., Tang, D. Y., Li, C.S. 2014. *Appl. Surf. Sci.*, 296: 1.

Yu, Y., Yu, J.C., Chan, C.Y., Che, Y.K., Zhao, J.C., Ding, L., Ge, W.K., Wong, P.K. 2005. *Appl. Catal. B*, 61: 1.

Wang, P., Wang, J., Ming, T.S., Wang, X.F., Yu, H.G., Yu, J.G., Wang, Y.G., Lei, M. 2013. *ACS Appl. Mater. Inter.*, 5: 2924.

Wang, P., Wang, J., Wang, X.F., Yu, H.G., Yu, J.G., Lei, M., Wang, Y.G. 2013. *Appl. Catal. B*, 132-133: 452.

Tan, L.L., Cha,i S.P., Mohamed, A.R. 2012. *Chem. Sus. Chem.*, 5: 1868.

Cong, Y., Li, X.K., Dong, Z.J., Yuan, G.M., Cui, Z.W., Zhang, J. 2015. *Mater. Lett.*, 138: 200.

Yu, G., Chen, Z.Y., Zhang, Z.L., Zhang, P.Y., Jiang, Z.P. 2004. *Catal. Today*, 90: 305.

Wang, Y.J., Lin, J., Zong, R.L., He, J., Zhu, Y.F. 2011. *J. Mol. Catal. A*, 349: 13.

Zhang, L. W., Fu, H.B., Zhu, Y. F. 2008. *Adv. Funct. Mater.*, 18: 2180.

Chai, B., Peng, T.Y., Zhang, X.H., Mao, J., Li, K., Zhang, X.G. 2013. *Dalton Trans*, 42: 3402.

Lian, Z.C., Xu, P.P., Wang, W.C., Zhang, D.Q., Xiao, S.N., Li, X., Li, G.S. 2015. *ACS Appl. Mater. Inter.*, 7: 4533.

Litter, M.I. 1999. "Heterogeneous photocatalysis-transition metal ions in photocatalytic systems". *Appl. Catal. B-Environ*., 23: 89-114.

Ge, M.Z., Cao, C.Y., Huang, J.Y., Li, S.H., Zhang, S.N., Deng, S., & Lai, Y.K. 2016. "Synthesis, modification, and photo/photoelectrocatalytic degradation applications of TiO_2 nanotube arrays: a review". *Nanotechnology Reviews*, 5(1): 75-112.

Murray, J.L. & Wriedt, H.A. 1987. The O-Ti (Oxygen-Titanium) system JPE. 8: 148.

U. Kuylenstierna & A. Magneli. 1956. "A New Modification of Titanium Monoxide". Acta Chem. Scand., 10(7):1195-1196.

Wang, G., Liu, Y., Ye, J., & Qiu, W. 2017. "Synthesis, microstructural characterization, and electrochemical performance of novel rod-like Ti_4O_7 powders. *Journal of Alloys and Compounds*, 704: 18-25.

Ma, Y., Wang, X.L., Jia, Y.S., Chen, X.B., Han, H.X., Li, C. 2014. *Chem. Rev.*, 114: 9987.

Liu, L. & Chen, X.B. 2014. *Chem. Rev.*, 114: 9890.

Wen, J., Li, X., Liu, W., Fang, Y., Xie, J., & Xu, Y. 2015. „Photocatalysis fundamentals and surface modification of TiO_2 nanomaterials". *Chinese Journal of Catalysis*, 36(12): 2049-2070.

Y. Liu, X.Gan, B. Zhou, B.Xiong, J. Li, C.Dong, J. Bai,W. Cai. 2009. *J. Hazard. Mater.*, 171: 678.

J.C. Cardoso, M.V. Boldrin Zanoni. 2010. *Sep. Sci. Technol.*, 45: 1628.

Z. Miao, D.S. Xu, J.H. Ouyang, G.L. Guo, X.S. Zhao, Y.Q. Tang. 2002. *Nano Lett.*, 2: 717.

Y. Li, H.Yu, C. Zhang, L. Fu, G. Li, Z. Shao, B. Yi. 2013. *Int. J. Hydrogen Energy*, 38: 13023.

F. Wang, Z. Zheng, F. Jia. 2012. *Mater. Lett.*,71, 141.

C.A. Grimes, G.K. Mor. 2009. *TiO_2 Nanotube Arrays: Synthesis, Properties, Applications*, Springer, New York.

G.K. Mor, O.K. Varghese, M. Paulose, K. Shankar, C.A. Grimes. 2006. *Sol. Energy Mater. Sol. Cells*, 90, 2011.

Qiu, L., Wang, Q., Liu, Z., Zhao, Q., Tian, X., Li, H., & Gao, S. 2018. "Preparation of 3D TiO_2 nanotube arrays photoelectrode on Ti mesh for photoelectric conversion and photoelectrocatalytic removal of pollutant. *Separation and Purification Technology*, 207: 206-212.

X.W. Cheng, H.L. Liu, Q.H. Chen, J.J. Li, X.J. Yu. 2013. "Preparation and photoelectrocatalytic performance of TiO_2 nano-tubes arrays electrode". *Nanotechnology and Material Engineering Research*, 661, 11.

Feng, Y., Yang, L., Liu, J., & Logan, B.E. 2016. "Electrochemical technologies for wastewater treatment and resource reclamation". *Environmental Science: Water Research & Technology*, *2*(5): 800-831.

Rocha, J.B., Gomes, M.S., dos Santos, E.V., de Moura, E.M., da Silva, D.R., Quiroz, M.A., & Martínez-Huitle, C.A. 2014. "Electrochemical degradation of Novacron Yellow C-RG using boron-doped diamond and platinum anodes: Direct and Indirect oxidation". *Electrochimica Acta*, 140: 419-426.

Oturan, N., Ganiyu, S.O., Raffy, S., & Oturan, M.A. 2017. "Sub-stoichiometric titanium oxide as a new anode material for electro-Fenton process: application to electrocatalytic destruction of antibiotic amoxicillin". *Applied Catalysis B: Environmental*, 217: 214-223.

He, W., Liu, Y., Ye, J., & Wang, G. 2018. "Electrochemical degradation of azo dye methyl orange by anodic oxidation on Ti_4O_7 electrodes". *Journal of Materials Science: Materials in Electronics*, 29(16): 14065-14072.

Qiu, L., Wang, Q., Liu, Z., Zhao, Q., Tian, X., Li, H., & Gao, S. (2018). "Preparation of 3D TiO_2 nanotube arrays photoelectrode on Ti mesh for photoelectric conversion and photoelectrocatalytic removal of pollutant". *Separation and Purification Technology*, 207: 206-212.

Ensaldo-Rentería, M.K., Ramírez-Robledo, G., Sandoval-González, A., Pineda-Arellano, C. A., Álvarez-Gallegos, A. A., Zamudio-Lara, Á., & Silva-Martínez, S. 2018. "Photoelectrocatalytic oxidation of acid green 50 dye in aqueous solution using Ti/TiO_2-NT electrode". *Journal of environmental chemical engineering*, 6(1): 1182-1188.

Wang, H., Liang, Y., Liu, L., Hu, J., & Cui, W. 2018. "Highly ordered TiO_2 nanotube arrays wrapped with g-C_3N_4 nanoparticles for efficient charge separation and increased photoelectrocatalytic degradation of phenol". *Journal of hazardous materials*, 344: 369-380.

Sokolsky, G.V., Zahornyi, M.N., Lobunets, T.F. Tyschenko, N.I. Shyrokov A.V. et al. 2019. "Photoelectrocatalytic degradation of amino-azodyes by titanium dioxide with surface states of Ti^{3+}". *Journal of Chemistry and Technologies*, 27(2): 130-140.

Qu, Xin, Xiaomin, Zhao, and Zhihua Chen. 2016."A new in vitro method to determine sun protection factor." *Journal of cosmetic science,* 67(2): 101-108.

L. Xiong, J. Li, B. Yang and Y. Yu. 2011. "Ti^{3+} in the Surface of Titanium Dioxide: Generation, Properties and Photocatalytic Application". *Journal of Nanomaterials*, 2012:13

J. Tauc. 1968. "Optical properties and electronic structure of amorphous Ge and Si". *Materials Research Bulletin*, 3: 37-46.

K. Dai et al. 2007."Photocatalytic degradation of methyl orange in aqueous suspension of mesoporous titania nanoparticles". *Chemosphere*, 69: 1361-1367.

Zahornyi, M. 2017. "Nanosized powders as reinforcement for photoactive composites (Overview)". *Powder Metallurgy and Metal Ceramics*, 56: 130-147.

A. Kryukov, O. Stroyuk, S. Kuchmiy, V. Pokhodenko. 2013. *Nanophotocatalysis*. Monograph, Kyiv: Academic Periodicals, 619 p. (in Russian).

M. Zahornyi. 2018. *Functional nanocomposites based on titanium dioxide, Monogr*. Lambert Academic Publishing, 157 p.

M. Xue, L. Huang, J.Q. Wang, Y. Wang, L. Gao, J.H. Zhu, Z.G. Zou. 2008. "The direct synthesis of mesoporous structured $MnO_{(2)}$/$TiO_{(2)}$ nanocomposite: a novel visible-light active photocatalyst with large pore size". *Nanotechnology*, 19(18): 185604.

Ma, Q., Wang, H., Zhang, H., Cheng, X., Xi,e M. et al. 2017." Fabrication of MnO_2/TiO_2 nano-tube arrays photoelectrode and its enhanced visible light photoelectrocatalytic performance and mechanism". *Separation and Purification Technology*, 189: 193-203.

K. Ishibashi, A. Fujishima, T. Watanabe, K. Hashimoto. 2000. "Detection of active oxidative species in TiO_2 photocatalysis using the fluorescence technique". *Electrochemistry Communications*, 2: 207-210.

Gao, Tao et al. 2008. "Microstructures and spectroscopic properties of cryptomelane-type manganese dioxide nanofibers". *The Journal of Physical Chemistry C*, 112(34): 13134-13140.

Chan, Yim Leng et al. Photocatalytic degradation of Rhodamine B using MnO_2 and ZnO nanoparticles. *Materials Science Forum*. Vol. 756. Trans Tech Publications Ltd, 2013.

Lungemeister, D.A., Korolev, R.I., Serzhan, S.L., Isaev, A.I., & Borodkin, E.O. 2020, July. Materials of devices and equipment for deep-sea mining of manganese resources. In *Journal of Physics: Conference Series*. Vol. 1582, No. 1, p. 012098. IOP Publishing.

Ali, S., Iqbal, Y., & Fahad, M. 2019. "A comprehensive phase, minero-chemical and microstructural investigation of low-grade manganese ore". *Materials Research Express*, 6(11): 115527.

Glasby, G.P. 2006. Manganese: predominant role of nodules and crusts. In *Marine geochemistry* (pp. 371-427). Springer, Berlin, Heidelberg.

Vereshchagin, O.S., Perova, E.N., Brusnitsyn, A.I., Ershova, V. B., Khudoley, A.K., Shilovskikh, V.V., & Molchanova, E.V. 2019. "Ferro-manganese nodules from the Kara Sea: Mineralogy, geochemistry and genesis. *Ore Geology Reviews*, 106: 192-204.

Morgan, J.J. 2000. "Manganese in natural waters and earth's crust: its availability to organisms. *Metal ions in biological systems*, 37: 1-34.

Taylor, R.M., McKenzie, R.M., Norrish, K. 1964. *Austr. J. Soil Res.*, 2: 235-248.

Golden, D.C., Dixon, J.B., Kanehiro, Y. 1993. *Austr. J. Soil Res.*, 31: 51-66.

Emsley, John. 2001. Manganese. Nature's Building Blocks: an A-Z Guide to the Elements. Oxford, UK: Oxford University Press. pp. 249-253.

Varentsov, I.M., Grasselly G., Crerar, D.A., Cormick, R.K., Barnes, H.L. 1980. *Geology and Geochemistry of Manganese*, eds. Varentsov I.M., Grasselly Gy. (E. Schweizerbart'sche Verlagsbuchhandlung, Stuttgart), 1, pp. 293-334.

Corathers, L.A. 2009. Mineral Commodity Summaries 2009: Manganese. United States Geological Survey. Retrieved 30 April 2009.

Brian J. Skinner. 2015. Mineral Deposits. Encyclopædia Britannica, Encyclopædia, Britannica Inc. Access date: August 24, 2020.

Rziha, T. 1997. *Synthese, Charakterisierung und Kristallchemie von Manganoxidphasen* (Doctoral dissertation, Ph. D. Thesis, Fakultät für Geowissenschaften der Ruhr-Universität Bochum, Bochum, Germany).

Veblen, D.R. 1991. "Polysomatism and polysomatic series: A review and applications". *Amer. Mineralogist*, 76: 801-826.

Wells, A.F. 2012. *Structural inorganic chemistry*. Oxford university press.

Shannon, R.D. 1976. Revised effective ionic radii and systematic studies of interatomic distances in halides and chalcogenides. *Acta crystallogr.*, A32: 751.

De Wollf, P.M. 1959. "Interpretation of Some γ-MnO_2 Diffraction Patterns". *Acta Cryst.*, 12(N 4): 341-345.

Brenet, J. 1979. "Electrochemical behaviour of metallic oxides". *J. Power Sources*, 4: 183-186.

Ruetschi, P. (1984) Cation Vacancy Model for MnO_2. *J. Electrochem. Soc.*, 131, N12: 2737-2444.

Turner, S., Buseck, P.R. 1983. "Defects in Nsutite (γ-MnO_2) and Dry Cell Efficiency". *Nature*, 304: 143-146.

Shao-Horn, Y., Hackney, S.A., Johnson, C.S., Thackeray, M.M. 1998. "Microstructural Features of Alpha-MnO_2 Electrodes for Lithium Batteries. *J. Electrochem. Soc.*, No 2: 582-587.

Chabre, Y., Pannetier, J. 1995. "Structural and electrochemical properties of the proton/γ-MnO_2 system". *Prog. Solid State Chemistry*, No 1: 101-105.

Li, X., Ma, J., Yang, L., He, G., Zhang, C., Zhang, R., & He, H. 2018. "Oxygen vacancies induced by transition metal doping in γ-MnO_2 for highly efficient ozone decomposition". *Environmental science & technology*, 52(21): 12685-12696.

Zou, Y., Zhang, W., Chen, N., Chen, S., Xu, W., Cai, R., & Yao, X. 2019. "Generating oxygen vacancies in MnO hexagonal sheets for ultralong life lithium storage with high capacity". *ACS nano.*, 13(2): 2062-2071.

M. Kakazey, N. Ivanova, Y. Boldyrev, S. Ivanov, G. Sokolsky et al. 2003. "Electron Paramagnetic Resonance in MnO_2 Powders and Comparative Estimation of Electric Characteristics of Power Sources Based on them in the MnO_2-Zn System. *Journal of Power Sources*, 114: 170-175.

M. Kakazey, N. Ivanova, G. Gonzalez-Rodriguez, G. Sokolsky. 2001. Electron Paramagnetic Resonance in Disperse MnO_2. *Electrochemical and Solid-State Letters*, 4 J1-J4.

P. Ruetschi, R. Giovanioli. 1988. *J. Electrochem. Soc.*, 135, 2663.

Zhang, J., Burnham, C. 1994. "Hollandite-type phases: Geometric consideration of unit-cell size and symmetry". *American Mineralogist*, 79: 168-174.

Fritsch, S., Post, E.J., Navrotsky, A. 1997. *Geochim. Cosmochim. Acta*, 61, 13, 2613-2616.

Laberty, C., Suib, S.L., Navrotsky, A. 2000. "Effect of Framework and Layer Substitution in Manganese Dioxide Related Phases on the Energetics". *Chem. Mater.*, N6: 1660-1665.

Fritsch, S., Post, E.J., Suib, S.L., Navrotsky, A. 1998. *Chem. Mater.*, 61, 13, 2613-2616.

Petrovic, I., Navrotsky, A., Davis M.E., Zones, S.I. 1993. *Chem. Mater.,* 5 : 1805-1813.

Parc, Sylvie et al. 1989. « Estimated solubility products and fields of stability for cryptomelane, nsutite, birnessite, and lithiophorite based on natural lateritic weathering sequences". *American Mineralogist*, 74(3-4): 466-475.

Takahashi, K. 1981. "Dry cell and battery industry and battery technology with emphasis on powdered manganese dioxide. *Electrochim. Acta*, N10: 1467-1476.

R.L. Paul, A. Cartwright. 1986. "The mechanism of the deposition of manganese dioxide: Part III. Rotating ring-disc studies". *J. Electroanal. Chem*., 201 123-131.

C.J. Clarke, G.J. Browning, S.W. Donne. 2006. "An RDE and RRDE study into the electrodeposition of manganese dioxide. *Electrochim. Acta*, 51(26): 5773-5784.

N.D. Ivanova, I.S. Makeeva. 1999. "Manganese dioxide electrodeposition kinetics in fluoride electrolytes. *Theoretical and Experimental Chemistry*, 35(5): 280-285.

Sokolsky, G.V., Boldyrev, Y.I., Ivanova, N.D., Ivanov, S.V., Kolbasov, G.Y., Lazzara, G. & Chivikov, S.V. 2020. "Effects of electrolyte doping on electrodeposited nanostructured manganese oxide and chromium oxide". *Surface and Coatings Technology*, 126211.

Boldyrev, Y.I., Ivanova, N.D., Sokolsky, G.V., Ivanov, S.V., & Stadnik, O.A. 2013. "Thin film nonstoichiometric chromium oxide-based cathode material for rechargeable and primary lithium batteries". *Journal of Solid State Electrochemistry*, 17(8): 2213-2221.

M. Massaro, C.G. Colletti, G. Lazzara, S. Milioto, R. Noto, S. Riela. 2017. "Halloysite nanotubes as support for metal-based catalysts". *J. Mater. Chem*. A., No5: 13276-13293.

G. Cavallaro, G. Lazzara, S. Milioto. 2011. "Dispersions of nanoclays of different shapes into aqueous and solid biopolymeric matrices: extended physicochemical study. *Langmuir*, 27: 1158-1167.

G. Cavallaro, A. Danilushkina, V. Evtugyn, G. Lazzara, S. Milioto, F. Parisi, E. Rozhina, R. Fakhrullin. 2017. "Halloysite Nanotubes:

Controlled Access and Release by Smart Gates". *Nanomaterials*, 7, 199.

Heyes, P.J., Anastasakis, K., De Jong, W., Van Hoesel, A., Roebroeks, W., & Soressi, M. 2016. "Selection and use of manganese dioxide by Neanderthals. *Scientific reports*, 6(1): 1-9.

Jeffrey E. Post. 1999. Manganese oxide minerals: Crystal structures and economic and environmental significance. *PNAS* March 30, 96(7), 3447-3454.

Yoshizuka, K., Fukui, K., & Inoue, K. 2002. "Selective recovery of lithium from seawater using a novel MnO_2 type adsorbent". *Ars Separatoria Acta*, 79-86.

Ryu, T., Shin, J., Ghoreishian, S.M., Chung, K.S., & Huh, Y.S. 2019. "Recovery of lithium in seawater using a titanium intercalated lithium manganese oxide composite". *Hydrometallurgy*, 184: 22-28.

Xhaxhiu, Kledi. 2015. "Synthetic birnessites and buserites as heavy metal cation traps and environmental remedies". *Journal of Metallomics and Nanotechnologies*, 3: 23-32.

Ivanova, N.D., Ivanov, S. V., Boldyrev, E.I., Sokol'skii, G.V., & Makeeva, I.S. 2002. "High-performance manganese oxide catalysts for CO oxidation". *Russian journal of applied chemistry*, 75(9): 1420-1423.

Ringwood, A.E., Reid, A.F. 1967. *Acta Crystallogr.*, 23: 1093-1099.

Sokol'skii, G.V., Ivanova, S.V., Ivanova, N.D., Boldyrev, E.I., Lobunets, T.F., & Tomila, T.V. 2012. "Doped manganese (IV) oxide in processes of destruction and removal of organic compounds from aqueous solutions". *Journal of Water Chemistry and Technology*, 34(5): 227-233.

Débart, A., Paterson, A.J., Bao, J., & Bruce, P.G. 2008. "α-MnO_2 nanowires: A catalyst for the O_2 electrode in rechargeable lithium batteries". *Angewandte Chemie International Edition*, 47(24): 4521-4524.

Sokolsky, G., Zudina, L., Boldyrev, E., Miroshnikov, O., Gauk, N., & Kiporenko, O. 2018. "ORR Electrocatalysis on Cr^{3+}, Fe^{2+}, Co^{2+}-doped Manganese(IV) oxides ". *Acta Physica Polonica A*, 133(4): 1097-1102.

C. Song, and J. Zhang, eds. J. Zhang. 2008. *PEM Fuel Cell Electrocatalysts and Catalyst Layers: Fundamentals and Applications*, Springer, London, p. 89.

Takahashi, Kusuhiko. 1981. "Dry cell and battery industry and powder technology with emphasis on powdered manganese dioxide". *Electrochimica Acta,* 26(10): 1467-1476.

Desmond, Ng, Jia, Wei et al. 2013. "A Precious-Metal-Free Regenerative Fuel Cell for Storing Renewable Electricity". *Advanced Energy Materials*, 3(12): 1545-1550.

Liu, G., Zeng, C., Wang, X., Zhang, L., & Qiao, S.Z. 2019. "3D Hollow α-MnO_2 Framework as an Efficient Electrocatalyst for Lithium-Oxygen Batteries". *Small*, 15(10): 1804958.

Zhu, Lihua et al. 2019. "MnO_2 and Reduced Graphene Oxide as Bifunctional Electrocatalysts for Li-O_2 Batteries". *ACS Applied Energy Materials*, No10: 7121-7131.

Xiaoshi Lang, Lan Li, Qingguo Zhang. 2020. "Novel Ni and Al doped manganese oxide ($Ni_xAl_yMn_zO_2$) ternary catalyst materials synthesized by a homogeneous precipitation method for high performance air electrodes of lithium-oxygen batteries". Sustainable Energy & Fuels, 10.1039/D0SE00981D.

Mo, Zhao et al. 2019. "Construction of MnO_2/Monolayer g-C_3N_4 with Mn vacancies for Z-scheme overall water splitting". *Applied Catalysis B: Environmental,* 241: 452-460.

Sherin, J.S.,. Thomas, J.K, and Shiney, Manoj. 2015. "Facile Synthesis and Characterization of Pyrolusite, β-MnO_2, Nano Crystal with Magnetic Studies". *Int. J. Sci. Eng. Appl.*, 4(5): 250-252.

Huo, Ge, et al. 2020. "γ-MnO_2 nanorod-assembled hierarchical microspheres with oxygen vacancies to enhance electrocatalytic performance toward the oxygen reduction reaction for aluminium-air batteries". *Journal of Energy Chemistry*, 51: 81-89.

Chen, G., Zhang, X., Gao, Y., Zhu, G., Cheng, Q., & Cheng, X. 2019. "Novel magnetic MnO_2/$MnFe_2O_4$ nanocomposite as a heterogeneous catalyst for activation of peroxymonosulfate (PMS) toward oxidation of organic pollutants. *Separation and Purification Technology*, 213: 456-464.

Sokolsky, G., Ivanova, N., Ivanov, S., Tomila, T., & Boldyrev, Y. 2007. "Phase composition and crystallinity degree of nanostructured products of anode oxidation of manganese (II) ions doped by ions of lithium and cobalt (II)". *Science of Sintering*, 39(3): 273-279.

Sakai, N., Fukuda, K., Omomo, Y., Ebina, Y., Takada, K., & Sasaki, T. 2008. "Hetero-nanostructured films of titanium and manganese oxide nanosheets: photoinduced charge transfer and electrochemical properties". *The Journal of Physical Chemistry C*, 112(13): 5197-5202.